SHIBAURA INSTITUTE OF TECHNOLOGY

Graduate School of Engineering and Science

AGH UNIVERSITY OF SCIENCE AND TECHNOLOGY

Faculty of Physics and Applied Computer Science

DOCTORAL DISSERTATION

Hydrogen storage properties of magnesium hydride nanocomposites with graphite and transition metals

Kamil Goc

Supervisor: Prof. Akito Takasaki

Supervisor: Prof. Czesław Kapusta

TOKYO, CRACOW 2018

For final review

A heartfelt thanks to Prof. ***Akito Takasaki*** *for comprehensive support and assistance during my scientific work.*

A heartfelt thanks to Prof. ***Czesław Kapusta*** *for comprehensive support and assistance during my scientific work.*

Thanks also to all those who contributed to this work: friends, family, coworkers, lab members both in Poland and in Japan.
Dr. hab. ***Janusz Przewoźnik*** *(Faculty of Physics and Applied Computer Science, AGH University of Science and Technology),*
Dr. hab. inż. ***Agnieszka Radziszewska*** *(Faculty of Metals Engineering and Industrial Computer Science, AGH University of Science and Technology),*
Dr. hab. ***Łukasz Gondek*** *(Faculty of Physics and Applied Computer Science, AGH University of Science and Technology),*
Kentaro Mineo, Satoshi Hasegawa, Ntumba Lobo *and* ***Witold Prendota*** *for cooperation in this study*

ABSTRACT

Recently, metal hydrides are widely considered and studied as materials for use as the hydrogen storage materials in mobile and on-boards applications. One of the most interesting is the magnesium hydride, because of high storage capacity (~7.5 wt. %, or 110 g/L), low cost and availability. However, its applications are limited by poor reaction kinetics and high decomposition temperature. Several methods, such as nanostructuring, alloying or addition of catalyst are often used to improve MgH_2 performance.

This dissertation is focused on designing and development of a new method of introducing catalytic elements by forming a thin layer of catalyst on the surface of magnesium hydride particles using technology of magnetron sputtering on powdery substrates. Thin films of nickel, niobium and vanadium were successfully deposited on the as-purchased and the ball milled magnesium hydride powders. SEM observations and EDS elements mapping show metallic layers of 80-320 nm thickness formed on hydride particles. It was proven by measurements with Sievert's method that such surface modification increases the H_2 dissociation/recombination speed and effectively enhances hydrogenation/dehydrogenation reaction rate. The DSC study performed shows a reduction of the activation energy and a decrease of the decomposition temperature.

In order to improve the heat transfer during hydrogen charging/discharging, special anisotropic composites of magnesium hydride and graphite, with thermal conductivity enhanced through their anisotropy, were prepared. Interaction of graphite flakes with the applied strong electric field gives rise to an induced polarization which results in a torque acting on the graphite particles and causes their reorientation and alignment. Samples of magnesium hydride with graphite suspended in a special high temperature proof resin were prepared in this way. A study of their thermal conductivity compared with hydrogenation/dehydrogeneration kinetic measurements shows that alignment enhances heat transfer in such composite materials making them prospective candidates for applications.

LIST OF CONTENT

1. INTRODUCTION

Recently, hydrogen has been a widely studied and developed material to be used as the energy carrier. It offers a high energy density and provides clean and ecologic power with limited amount of pollution. Much research work is performed in areas of hydrogen production and its convertion to electric energy in fuel cells. The key technology for practical applications, especially for mobile and on-boards use is the efficient and safe storing of hydrogen, which a lot of studies is focused on. Chapter 1 of this Disseration contains a review of hydrogen storage methods, starting from simple mechanical options, such as compressing the gas and liquefaction, physisorption on high surface materials, or storage via chemical reactions in metal hydrides. Each method has some advantages and drawbacks.

Mechanical methods are simple, but require advanced materials to withstand low temperatures or high pressure. They also require a good thermal insulation, possessing low permeability for small hydrogen molecules. Also the mechanical work needed to compress or liquefy hydrogen gas is large and can reach ~20-40 % of hydrogen heating value (the amount of energy released in reactions such as combustion or fuel cell conversion). Van der Waals based adsorption is limited by small binding energy, but low temperature options and high surface metal organic frameworks can be considered for application.

Finally, a variety of metal hydrides, both binary, intermetallic and complex compounds, are possible to use. They are characterized with wide range of capacities and operating temperatures. One of the most interesting is the magnesium hydride. It possesses relatively high storage capacity (~7.5 wt. %, or 110 g/L) it is light, low cost and magnesium is easy available element. However, its applications are limited by two problems: poor reaction rate coming from thermodynamic (high enthalpy of formation) and kinetical (high activation barrier for hydrogen dissociation on magnesium surface) constrains.

Several methods for improvement of the MgH_2 performance have been developed. Nanostructuring or nanocofinement can decrease particle size and, thus, increase active area, improving reaction kinetics and reducing decomposition temperature. Another approach is to form magnesium based alloy with less stable hydride forming element, such as nickel, silicon, or titanium. By changing the reaction pathway the effective enthalpy of reaction can efficiently be decreased. The main disadvantage here stems from the fact, that the introduction of large amounts of heavy elements makes the hydrogen capacity smaller (1-3 wt. %).

It was found, that doping even few percent of additives can improve hydrogen kinetics through catalytic reduction of the activation energy via spillover method (Chapter 1). Transition

metals and their compounds, as well as other inorganic materials are effectively applied for this purpose.

The method most commonly used for introducing catalytic elements is their ball milling in rotary mills together with magnesium hydride powder. It causes improvements not only through catalytic effects, but also through nanostructurization. The disadvantage is a low repeatability of the process and a need of using large amounts of dopants to achieve good contact between magnesium hydride and catalyst.

This Dissertation is focused on designing and developing new methods of introduction of catalytic elements to magnesium hydride and preparation of its composite enabling effective hydrogen charging-discharging. Catalytic elements were deposited onto magnesium hydride powders with magnetron sputtering. This method was previously used to produce magnesium thin films, often covered with the other layer of a catalytic material. Such sandwiched structures exhibit good reaction kinetics at acceptable pressure and temperature conditions. However, their applications are limited to switchable mirrors and sensors and it is difficult to use them as a bulk hydrogen storage material. The main idea developed in this Thesis is to form a thin layer of a catalyst on the surface of magnesium hydride grains (to coat hydride particles). Such a surface modification should reduce the kinetic barrier on the magnesium/magnesium hydride surface and improve reaction rate while keeping the amount of dopant low. The advantage is a precise control of film thickness, uniform coating and possibility of sputtering of different elements, alloys and compounds.

A special equipment for deposition on powdery substrates was designed and constructed as a part of the work presented in the Dissertation (Chapter 2). The key issue here is the proper mixing of powder during sputtering in order to get uniform coating. It was achieved by using a special, round shaped cup, set in circular motion in vertical plane, below magnetron target, by an electric motor. The entire device was placed in the chamber of the magnetron sputtering setup, designed and constructed within this Thesis work.

Thin films with submicron thickness of nickel, niobium and vanadium were sputtered (Chapter 3) on the magnesium hydride powder, both raw and ball milled. Differential Scanning Calorimetry was applied to determine the decomposition point and the activation energy. Next, volumetric, Sievert's type apparatus was used to analyze the reaction kinetics of coated powders, as well as to collect the Pressure-Composition-Temperature dependences and to obtain thermodynamic parameters. The uniformity of layers and their thickness were studied with electron microscopy, and the phase composition, together with the structure of materials

was determined with X-Ray Diffraction method. As the problems occurred with the particles agglomeration and the oxidation of magnesium hydride, the experimental setup was modified in order to perform all the experimental procedures without exposing magnesium hydride sample to air, to obtain well defined, good quality materials. A thorough study has been carried out to determine if the proposed method of magnetron sputtering on powder substrates can be an effective way to introduce catalytic elements to metal hydrides and to determine usefulness of the materials obtained for hydrogen storage.

Aiming of improvement of the heat transfer during hydriding/dehydriding, special composites of magnesium hydride and graphite were prepared, aiming at an improvement of the heat transfer (Chapter 4). Graphite has a very specific, layered crystal structure resulting in strong anisotropy of its electrical and thermal transport properties. This enables ordering of graphite flakes by application of a strong electric field. Interaction of graphite flakes with the applied strong electric field gives rise to an induced polarization which results in a torque acting on the graphite particles and causing their reorientation and alignment. Samples of magnesium hydride with graphite suspended in a special, high temperature proof, resin were prepared in this way. A study of their thermal conductivity compared with hydrogenation/dehydrogeneration kinetics measurements was carried out to check if the alignment can enhance heat transfer in such composite materials making them suitable for applications.

2. HYDROGEN ECONOMY AND STORAGE METHODS

Hydrogen gas is widely considered as the future energy carrier and as an alternative to the fossil fuels. Its use produces carbon and nitrogen oxides free waste, which fulfills the most restricted emission norms and fits into the preferred tendency of using low carbon fuels. Moreover, hydrogen is abundant and widely distributed in the world in different compounds (e.g. water, organic compounds) providing security in energy supply. It can be used for power generation either by burning in an internal combustion engine or electrochemically used in a fuel cell. It possesses high gravimetric energy content of 120 MJ/kg (33 kWh/kg), which is almost three times greater than diesel and gasoline (Fig. 2.1). The difference is even higher if we take into account the efficiency of internal combustion engine (~30%) and maximal efficiency obtained from the fuel cell (~80%). The main disadvantage is the fact that hydrogen does not occur in a form of natural resources as coal/oil do, so that an efficient and cheap way of conversion/production of H_2 gas has to be developed. It is worth noting that hydrogen should not be referred to as a fuel, but as the energy carrier. Another its disadvantage is a low energy density per volume, compared to conventional fuels, which limits all mobile/onboard application.

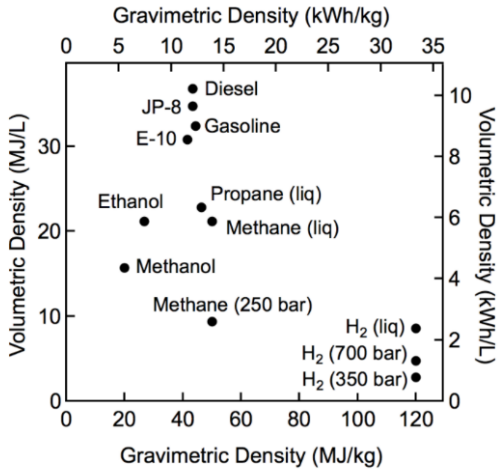

Fig. 2.1. Comparison of the energy densities of different fuels.[1]

The key issue the most of research work is focused on, is a proper method for storing of the hydrogen. In the next paragraphs basic methods of hydrogen storage are overviewed. There are two main parameters characterizing each method: the gravimetric capacity (density), expressed in % describing the mass of H_2 which can be stored in the unit mass of the vessel; and the volumetric capacity, expressed in kg/L, describing the mass of H_2 which can be stored inside the unit of the volume of the tank. Another parameters used, are related to the power obtained

from hydrogen stored in the mass unit (1 kg) or the volume unit (1 L) of the tank. Desired operating parameters and conditions, suggested by the US Department of Energy as targets for mobile applications are presented in the Table 2.1. The ideal hydrogen tank should be able to store at least 2.2 kWh/kg and 1.7 kWh/L, which is equivalent to gravimetric and volumetric capacity of 6.5% and 50 g/L respectively. The operating temperature should be close to the room temperature (-40 to -60°C) and the filling time should be not more than 5 minutes.

Table 2.1 DOE Technical Targets for Onboard Hydrogen Storage for Light-Duty Vehicles[1]

Storage Parameter	Units	2020	2025	Ultimate
System Gravimetric Capacity				
Usable, specific-energy from H_2 (net useful energy/max system mass)	kWh/kg ($kg\ H_2$/kg system)	1.5 (0.045)	1.8 (0.055)	2.2 (0.065)
System Volumetric Capacity				
Usable energy density from H_2 (net useful energy/max system volume)	kWh/L ($kg\ H_2$/L system)	1.0 (0.030)	1.3 (0.040)	1.7 (0.050)
Durability/Operability				
Operating ambient temperature	ºC	-40/60 (sun)	-40/60 (sun)	-40/60 (sun)
Min delivery pressure from storage system	bar (abs)	5	5	5
Max delivery pressure from storage system	bar (abs)	12	12	12
Charging/Discharging Rates				
System fill time	min	3–5	3–5	3–5

2.1. Overview of hydrogen storage methods

Hydrogen storage methods can be classified into two main categories (Fig. 2.2): Physical (mechanical) based, where the change of physical conditions, such as pressure and temperature, is used to densify the hydrogen; and material based, where hydrogen is bonded to the active material of vessel. The first group includes compressing of the gas, liquefaction and combination of these methods in cryo-compressed tanks. On the other side – hydrogen can be adsorbed on carbon surfaces or in other materials, bonded to the elements and to the organic or inorganic compounds to form different types of hydrides.

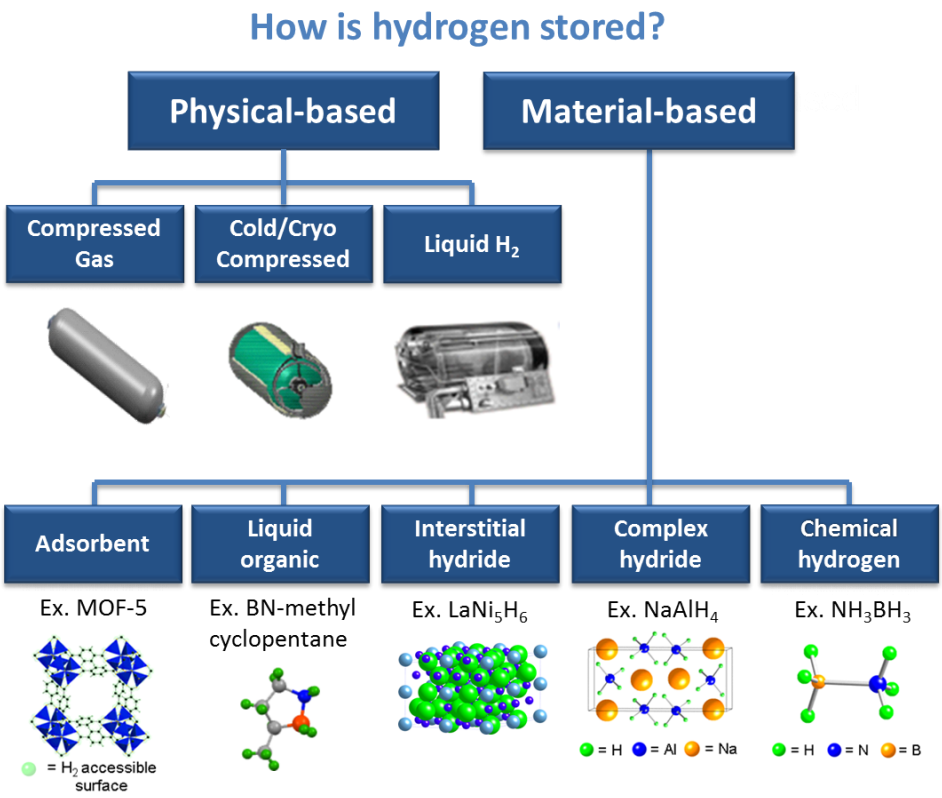

Fig. 2.2. Overview of different hydrogen storage methods [1].

Compressed gas

The most conventional way to store hydrogen is to compress the gas [2]–[9] in cylindrical bottles at high pressure. It is the simplest and the most natural way, with fast fill/release properties (80% in 5min), however, it requires specific technology and materials. Depending on the tank design (Fig. 2.3, Table 2.2), the maximal safe pressure varies typically from 50 to 70MPa. Type I vessels made from stainless steel have the pressure limited to 50MPa because of the limit being the strength of the walls. Type II is additionally reinforced by partial metal or composite wrapping. Pressure tanks made from metal liner fully wrapped with the fiber resin composites can also be used. When the metal liner inside the vessel contributes to the mechanical resistance, the vessel is of type III, and when the mechanical strength is provided by the polymers we can talk about the type IV pressure vessel. In that case, metal layer is responsible mainly for limiting the hydrogen diffusion through walls. Type V containers, whole made from light composites are at present at the research stage [2]. Type II and IV vessels provide high pressure, enabling us to achieve higher volumetric concentrations, however the cost of such vessels is high because of using expensive carbon fiber composites for their construction[5].

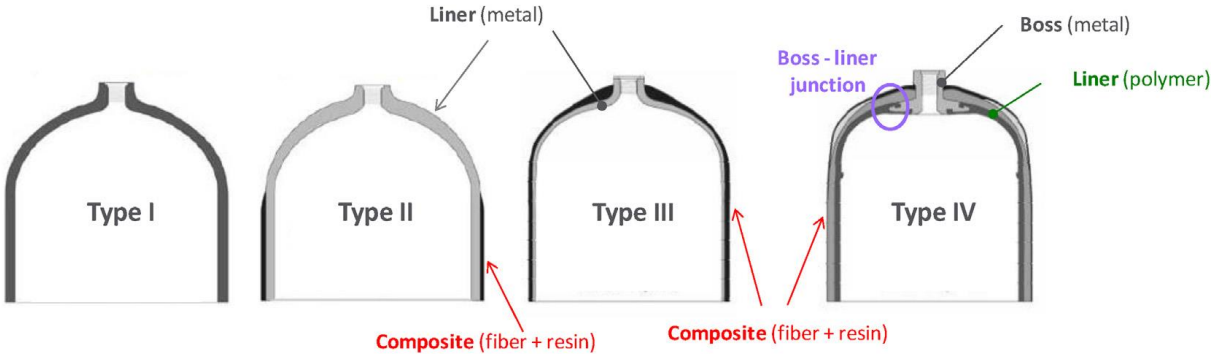

Fig. 2.3. Representation of different types of hydrogen gas pressure tanks [2].

Table 2.2. Key characteristics of pressure vessels for compressed gas storage [2].

Type	Technology maturity
Type I	Pressure limited to 50 MPa
Type II	Pressure not limited
Type III	For P _ 45 MPa (difficulty to pass pressure cycling requirements for 70 MPa,
Type IV	For P _ 100 MPa First commercial series to be further studied

The volumetric density of stored hydrogen increases with pressure and reaches a maximum above 70-100MPa depending on the materials used [8]. On the other hand, the gravimetric density is going low because of the weight of the vessel walls. Therefore, the increase in volumetric storage density is obtained on the cost of a reduction of the gravimetric density in pressurized gas systems. At a pressure of 30-70 MPa the gravimetric density is found to be 4.5-5 wt. %, and volumetric capacity is 26.3-36 g/L[4], [8], [9]. Another issue is the need to compress the gas from atmospheric to high pressure of ~100 MPa. Currently, reciprocating (piston or membrane) compressors with multistage setups are used. Dynamic compressors (centrifugal and axial) are not yet available for hydrogen because of the high number of compressor stages required (in comparison with positive displacement machines) due to the low density of hydrogen gas, the corresponding complexity and cost. Main problem is the amount of energy needed to compress the hydrogen. Because the machines are using nearly isothermal process, the energy in the form of the compression heat is usually transferred to environment (cooling water or cooling air) and is therefore lost. The compression of H_2 gas from 0.1 to ~70-100 MPa consumes around 2.2-3.6 kWh/kg, which is between 6 and 10% of the lower heating value for hydrogen burning reaction (~33 kWh /kg). Taking into account the efficiency of compressing process and tendencies for move for adiabatic process, the energy loses can reach 15% of the energy stored in hydrogen gas [5], [8], [9]. There is also a significant concern related to the very high pressure in the system causing safety problems and leakage

risk. To sum up, the relatively low hydrogen density and compression problems make storing hydrogen as a compressed gas not the most practical method, especially in mobile applications, however it is well established on the laboratory scale.

Liquid hydrogen

Hydrogen gas can be liquefied at the temperature below 21 K at ambient pressure. A high volumetric density of hydrogen (70.8 g/L) can easily be achieved [4], [5], [8]. The gravimetric capacity depends strongly on the size of the vessel, but values about 10-12% can be successfully reached[3]. Except of the price and material requirements, liquid hydrogen tanks have considerable limitations and disadvantages. First of all, there is no way to prevent the boiling off of liquid hydrogen because of the residual heat inflow through the walls of the container. Despite using special technologies (including the double wall, vacuum insulated constructions and thin metal films preventing thermal radiation), the leakage rate is relatively high for long-term storage. It depends strongly on the size of the vessel and ranges between 0.4% per day for 50 m^3 tanks and 0.06% for 20 000 m^3 tanks [5], [6], [8]. In addition to that, as hydrogen has a critical temperature of 33K [4]–[6], above which it behaves as a non-condensable gas, it is necessary to keep the liquid hydrogen (LH) in open dewars for safety reasons. Overheated hydrogen can expand its volume 10^4 times. Second problem is related to the energetic efficiency of liquefaction of the hydrogen gas. Hydrogen cannot be liquefied with conventional Linde cycle (isoenthalpic expansion) because of low inversion temperature [4]. It is usually precooled with liquid nitrogen and then goes through several expansion cycles. The theoretical energy used is 3.23 kWh/kg and the mechanical work is about 15.2 kWh/kg which is of 45% of the lower heating value of hydrogen combustion [2], [5], [8]. Because of these two effects, combined with high price of the cryogenic vessels, this technology has applications limited to the space programs, stationary storage and short-term onboard storing. Further development of insulation technology and cooling systems may open this technology for wider mobile applications.

Cryo-compressed gas

Cry-compressed gas tanks are one of the improvements of high pressure tank technology by combining it with cryogenic technologies. Compressed hydrogen tank is connected to cooling system keeping the temperature around 50K [6], which allows increasing the volumetric density of H_2 by a factor of ~2 comparing to ambient temperature compressed gas (Fig. 2.4). The key

feature is that tank walls can withstand high pressure, which allows keeping hydrogen at these conditions, over the boiling point, in order to limit the boil-off loses present in the liquid hydrogen technology. Moreover, the cryogenic gas possesses 27% larger density than that in the LH tank. Cryo-compressed tanks can be filled with hydrogen at any temperature between the ambient one and 20K, which is more flexible, effective and less expensive than filling the tank with liquid H_2. BMW Group have started development of such tanks for mobile applications, especially for cars and other vehicles [2], [5]. The tank consists of a type III composite pressure vessel with a metallic liner that is encapsulated in a secondary, insulating jacket, which role is to limit heat transfer between the hydrogen and the environment.

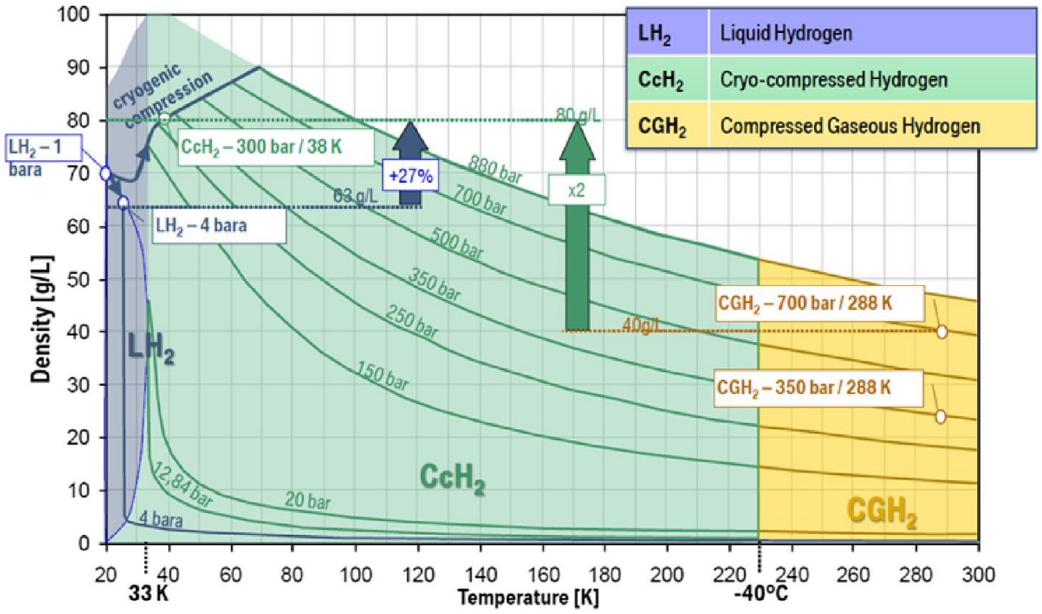

Fig. 2.4. Hydrogen density versus pressure and temperature from BMW report [2]

Storage by physisorption

Hydrogen particles can be adsorbed with van der Waals forces to the high specific area porous materials [4]–[6], [8]. The binding energy is generally low, in range of 0.1-10 kJ/mol [8]. Because of the weak interaction, the effective capacity depends strongly on the active surface area, operating pressure and temperature, since the bonding is getting more effective with cooling the system. The room temperature and ambient pressure yield unsatisfactory results – usually there is no significant adsorption. However, it turns out that the use of not very high pressures (5–15 MPa) and liquid nitrogen temperatures (77 K) can increase the capacity to 5-7.5 wt. % [4], [6], [8]. Materials suggested for applications here include activated carbon, nanotubes, graphene/graphite, zeolites and metal-organic frameworks (MOFs). Carbon based

structures exhibit maximum sorption of 2 wt. % for the highest specific area graphene sheets [6]. Recent works are focused on catalyst assisted adsorption via spillover mechanism. Metals and their oxides are suggested to be used as dopants to increase the binding energy to 15 kJ/mol [10] in order to make the material more stable. Zeolites, usually alumosilicates or aluminophosphates are used here to build microporous frameworks. The adsorption energies in the narrow pores are very low, allowing for thermal cycling to be used for adsorption and desorption of hydrogen. The capacities of 1.5% were reported, and maximal expected capacities are of 2.5 wt. % [6]. Metal-organic frameworks are compounds formed of metal ions connected by organic molecules such as e.g. carboxylic acids. They posses very high specific area, in the range of 5000m^2/g [4] leading to high capacities up to 7.5-11 wt. % at 77 K [1], [6]. Such physisorption materials also exhibit short hydrogen absorption and desorption times and are fully reversible, which attracts large interest in this type of tanks. In addition, these materials work in cryogenic storage tanks at liquid nitrogen temperature, 77 K, which is much less demanding than direct liquid state storage of hydrogen in tanks, at 21 K. Storing physisorbed hydrogen in porous materials solves the boil-off problem, but since the physisorption process is exothermic, thermal management issues arise with respect to the adsorption process. All these reasons make physisorbed hydrogen unsuitable for mobile applications.

Chemical hydrogen storage

The name "chemical hydrogen" is usually used for description of the group of materials with hydrogen bonded by strong covalent bonds [1], [5], [6], [8]. They generally have the highest density of hydrogen. Typical examples are: amino borane (NH_3BH_3 – 6.5 wt. %) or alane (AlH_3 -10%) and a variety of amides and imides [6], [8]. The dehydrogenation can be accomplished either by reaction with water or thermolytically by heating the compound to temperatures of 363-373 K. Some of these materials exhibit multistage decomposition (NH_3BH_3 – 363/420/970 K) which causes problems with handling of the material because of possible reaction pathways that may not be easily predicted. In addition to solids, many liquid organic hydrogen carriers (LOHC) have been studied. The reaction of hydrogenation/dehydrogenation is based on hydrogen saturation of organic unsaturated carbon-carbon bonds. The examples are the toluene/metylcyclohexane (6.1 wt. % H_2), n-ethylcarbazole (5.7 wt. %) and methyl-cyclopentane (4.7 wt. %) with the reaction temperatures around 120-200 °C [5], [11], [12]. The reactions have usually exothermic or weak endothermic character, thus rehydrogenation requires special chemical processes performed off-board. This limits applications to single use

cycle. In addition, some of the difficulty in working with these materials is that the material can solidify/liquefy during different decomposition stages.

Metal hydrides

Hydrogen reacts with many metals at elevated pressure and temperature conditions to form the hydrides [2], [3], [5], [6], [8], [13]. Instead of weak adsorption on the surface, hydrogen atoms are bonded with ionic, metallic or covalent bond to the metal host. It is possible to achieve high volumetric and good mass capacities and long lasting thermodynamic stability, while providing full reversibility of reaction. Moreover, metal hydride tanks can filter most of the impurities from gaseous hydrogen, providing clean fuel for powering fuel cells which are very sensitive to the pollutions.

Single, elemental metals, such as Mg, Li, Ti, V, Ni, La, Fe, etc. form the group of binary hydrides. Most of them are formed at temperatures and pressures well beyond the range for any application (Fig. 2.5) or have capacities too low to prove useful. It ranges around 2 wt. %, because of a high density of these metals. There exist some light metal hydrides: MgH_2, LiH with reasonable theoretical capacities of 7.5 and 12.7 wt. %, however, their applications are limited because of high desorption temperatures (450 °C and 910 °C respectively). Most of the research there is focused on decreasing the decomposition temperature of magnesium hydride.

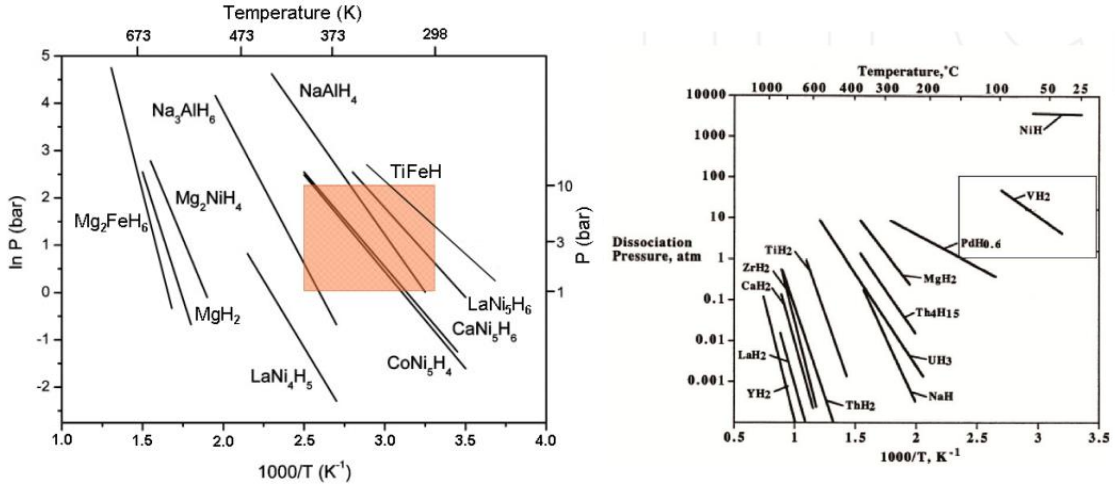

Fig. 2.5. Van't Hoff plots for various metal hydrides, showing hydrogen dissociation pressures and temperatures (rectangular area represents desirable operating conditions).[6], [13]

Except of the binary hydrides, in attempt to alter extreme conditions of reaction caused either by their low or high stability, hydriding of alloys is possible. The materials used generally consist of two metals: metal A (stable), exothermically reacting with hydrogen, (typically Mg,

Ti, La); and metal B (unstable) with endothermic reaction type, typically Ni, Fe, Co, Mn. Stoichiometric alloys (intermetallic compounds) include the types: AB_5, AB_2, AB, A_2B (Fig. 2.5, Table 2.3) and others, but it is possible to obtain non-stoichiometric compositions, such as e.g. vanadium solutions or doped intermetallics, which give opportunity to tune alloy properties to get suitable reaction conditions near ambient temperatures. The hydrides formed with intermetallics are generally characterized by low hydrogen storage capacities (~ 2 wt. %) due to the mass of heavy elements they are composed of.

Table 2.3. Examples of different interstitial, metal alloys hydrides.[6], [13]

Type	A	B	Compounds	Example	H_2 capacity (wt. %)	Temperature (K) for desorption
A_2B	Mg, Zr	Ni, Fe, Co	Mg_2Ni, Mg_2Co, Zr_2Fe	Mg_2Ni	3.6	528
AB	Ti, Zr	Ni, Fe	TiNi, TiFe, ZrNi	TiFe	1.86	265
AB_2	Zr, Ti, Y, La	V, Cr, Mn, Fe, Ni	$LaNi_2$, YNi_2,YMn_2, $ZrCr_2$, $ZrMn_2$,ZrV_2, $TiMn_2$	$ZrMn_2$	1.77	440
AB_5	Ca, La, Ce	Ni, Cu, Co, Pt, Fe	$CaNi_5$, $LaNi_5$, $CeNi_5$, $LaCu_5$, $LaPt_5$, $LaFe_5$	$LaNi_5$	1.49	285

Light elements from groups 1, 2 and 3 form a family of complex hydrides, such as borohydrides and alanates. They are built from complex anions containing hydrogen as terminal ligand, such as the BH_4^- or AlH_4^- anions and counter-anions such as Mg, Na, K, Li, etc. This storage method offers very high gravimetric and volumetric densities (up to 18.4 wt. %, Table 2.4) due to the use of lightweight metals, however, due to the strong character of the bonds, kinetics are very slow and high temperatures (200-300 ˚C) are required to achieve hydrogen desorption. Reaction reversibility is also poor because of exothermic reaction character, multistage decomposition process and high pressure needed.

Table 2.4. Overview of characteristics of some of the borohydrides and alanates for hydrogen storage[6]

Material	H_2 capacity (wt. %)	Dehydrogenation temperature (K)	Dissociation enthalpy (kJ/mol H_2)
$NaBH_4$	10.8	670	-217 to -270
$LiBH_4$	13.4	650	-177
$Mg(BH_4)_2$	13.7	530-670	-39.3 to -50
$Ca(BH_4)_2$	9.6	620	32
$NaAlH_4$	5.6	480-490 (I step) >525 (II step)	37 (I step, 3.7 mass% H_2) 42 (II step, 1.9 mass% H_2)
$LiAlH_4$	7.9	430-450 (I step) 450-490 (II step)	-10 (I step, 5.3 mass% H_2) 25 (II step, 2.6 mass% H_2)
$Mg(AlH_4)_2$	9.3	380-470 (I step)	41 (I step, 7 mass% H_2)

		510-650 (II step)	76 (II step, 2.3 mass% H_2)
$KAlH_4$	5.7	570 (I step) 610 (II step) 650 (III step)	55 (I step, 2.9 mass% H_2) 70 (II step, 1.4 mass% H_2)
$Ca(AlH_4)_2$	5.9	400 (I step) 520 (II step)	-7 (I step, 2.9 mass% H_2) 28 (II step, 2.9 mass% H_2)

2.2. Hydrogen in metal hydrides

The process of absorption of gaseous hydrogen molecule is usually described with classical repulsive/attractive Lennard-Jones potential, plotted in Fig. 2.6.

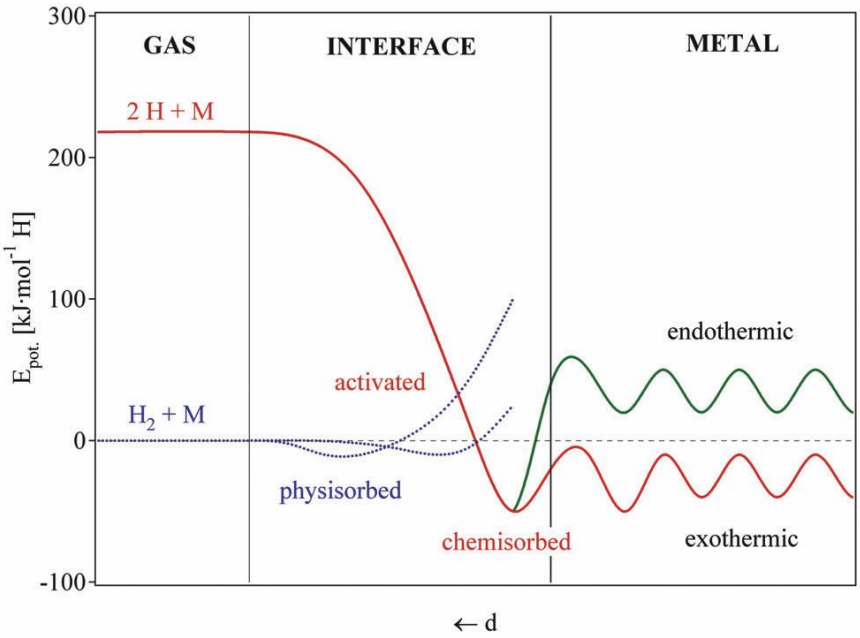

Fig. 2.6. Potential energy of the hydrogen molecule during the absorption in metal[8].

Far from the metal surface, the potential of a hydrogen molecule and that of two hydrogen atoms are separated by the dissociation energy (435.99 kJ/mol H_2). The first attractive interaction of the hydrogen molecule approaching the metal surface is the Van der Waals force, leading to a physisorbed state. The physisorption energy is typically about 6 kJ/mol H_2. The interaction is composed of an attractive term, which diminishes with increasing distance of the hydrogen molecule and the solid metal in the power of 6, and a repulsive term diminishing in the power of 12. In result, the minimum of the potential energy of the molecule appears, approximately at a distance of one molecular radius (~0.2 nm).

When the hydrogen particle is getting closer to the surface, the potential energy increases and it is energetically preferable to dissociate into two atoms. Hydrogen atoms sharing their

electron with the metal atoms at the surface are then in the chemisorbed state. The chemisorption energy is typically in the range of ~50 kJ/mol H_2 and, thus, significantly higher than the respective energy for physisorption. Hydrogen has to overcome the activation barrier for dissociation and formation of the hydrogen metal bond. The height of the activation barrier depends on the surface elements involved. The chemisorbed hydrogen can jump into the subsurface layer and diffuse through the bulk metal to form solid solution referred to as α-phase. In the conventional room temperature metals / metal hydrides, hydrogen occupies interstitial sites (usually tetrahedral or octahedral) in the metal host lattice (Fig. 2.7). After the hydrogen content corresponding to its maximum solubility the α-phase is reached, hydride phase (β-phase) begins to form.

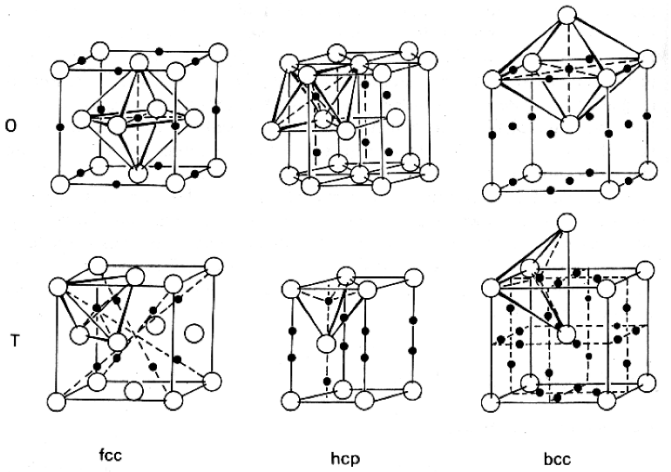

Fig. 2.7. Octahedral (O) and tetrahedral (T) interstitial sites in fcc-, hcp- and bcc-type metals.

From the thermodynamic point of view, the hydride formation from gaseous hydrogen and solid metal is possible when the standard Gibbs free energy of products is equal or lower than that of substrates. The change of the standard Gibbs free energy is related to the pressure and temperature of the system with the equation [14]:

$$\Delta G^0 = RT \ln \frac{p_{H_2}}{p^0}$$

where p^0 is the reference pressure (1 bar), p_{H_2} is the real hydrogen pressure, T is the temperature and R is gas constant. It is also defined as:

$$\Delta G^0 = \Delta H^0 - T\Delta S^0$$

where ΔH^0 and ΔS^0 are the change of enthalpy and entropy, respectively. From conjunction of the above equations we can derive the van't Hoff formula,

$$\ln \frac{p_{H_2}}{p^0} = \frac{\Delta H^0}{RT} - \frac{\Delta S^0}{R}$$

which is the basic law describing thermodynamics of hydrides, used for estimation of thermodynamic parameters such as entropy and enthalpy of reaction and to estimate the equilibrium pressure and temperature conditions, including often used parameter $T_{1\,bar}$,

$$T_{1\,bar} = \frac{\Delta H^0}{\Delta S^0}$$

i.e. the temperature of desorption under ambient pressure. The entropy change [3], [8] is similar for most metal hydrides as it describes the entropy change from gaseous (~130 J /(mol K)) to solid state (~0 J/(mol K)). To reach an equilibrium pressure of 1 bar at a moderate temperature of 25 °C the decomposition enthalpy should be ~40 kJ/mol.

To determine experimentally the reaction enthalpy and entropy, the pressure-composition-temperature (PCT) plot is created (Fig. 2.8). The PCT curve shows how the equilibrium pressure depends on the hydrogen content at given temperature.

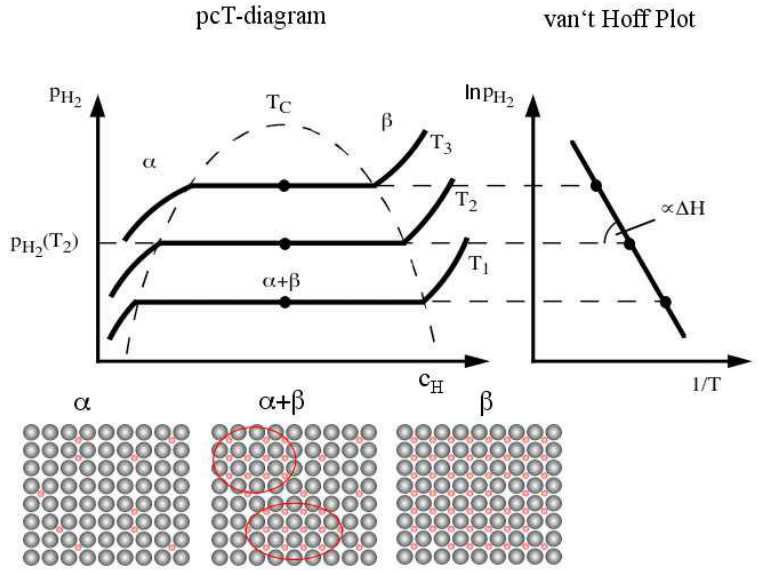

Fig. 2.8. Schematic PCT-diagram and van't Hoff plot.

At low pressures, a solid solution is formed between the metal and hydrogen (the α-phase), then nucleation and growth of the metal hydride initiate. The two phases coexist, with the amount of β-phase increasing very fast with further uptake of hydrogen at a constant pressure and the PCT curve is in the plateau region. The length of the plateau determines practical amount of hydrogen stored. As the content of the β-phase reaches saturation point, the pressure starts to

increase strongly. By plotting the data of $\ln \frac{p_{H_2}}{p^0}$ versus $\frac{1}{T}$ from the mid-points of the plateau (Fig. 2.8), the enthalpy and entropy of the dehydrogenation reaction can be derived from the slope and intercept of the straight line fitted to the data points (van't Hoff plot).

There are two interesting phenomena of practical importance regarding PCT curves: hysteresis and sloping of the plateau region. The absorption plateau is located at a higher pressure than the desorption one. This is caused mainly by stresses which appear in the course of growth of hydride phase inside the metal matrix. For practical on-board vehicular applications, hysteresis would increase the required service (recharge) pressure. Thus, it is desirable that the magnitude of hysteresis would be as small as possible. Sloping originates from inhomogeneity in the sample. The negative impact of plateau sloping is a reduction in reversible capacity, defined by the width of the plateau region. That is, the amount of hydrogen to be extracted (introduced) is dependent on the on-board operation pressure range. Significant plateau sloping results in a reduction of the amount of hydrogen accessible in the prescribed operating pressure window.

2.3. Properties of magnesium hydride and their tuning strategies

Magnesium hydride is one of the most promising materials proposed to be used for hydrogen storage. It possesses a high gravimetric and volumetric capacity (~7.5 wt. % and 110 g/L respectively), low specific gravity and easy availability. The main application limits are its poor reaction kinetics and high decomposition temperature (T_{dec} ~ 470 °C). The reasons causing those problems are:

- High thermodynamic stability – enthalpy of hydride formation is very high (ΔH = -74.5 kJ/mol) – high amounts of energy are required to deliver/dissipate during dehydrogenation/hydrogenation reaction. Together with a low thermal conductivity of powdered hydride (0.09-0.4 W/m·K) it leads to unsatisfactory heat management [16]. Also, basing on van't Hoff equation, to obtain material with the decomposition point near ambient conditions, the enthalpy should be not higher than 50 kJ/mol.
- Slow diffusion of hydrogen through the surface, limits reaction rate for bigger Mg particles due to MgH_2 forming. Diffusion constants are $1.5 \cdot 10^{-16}$ m^2/s for MgH_2 and $4 \cdot 10^{-13}$ m^2/s for Mg [15].
- Effectiveness of dissociation/recombination of hydrogen at the magnesium metal surface is slow due to a high activation energy of hydrogen on magnesium surface (E_a = 156-206 kJ/mol) [15].

- Easy oxidation of magnesium surface causes formation of surface oxides shells affecting both the activation energy and the diffusion of hydrogen atoms.

There exists several methods to enhance thermodynamic and kinetic properties, such as nanoscaling, alloying and use of additives affecting hydride kinetics, thermodynamic and heat transfer performance [4], [15]–[19].

First approach lies in the extreme reduction of Mg/MgH_2 particle size, which increases effective contact surface, decreases diffusion distance for hydrogen and changes hydride thermodynamics – the surface energy of the nanostructure contributes in the van't Hoff equation. Additionally, grain boundaries act as favorable nucleation sites for the formation and decomposition of the hydride phase. It results in a reduction of the activation energy and the enthalpy of reaction and in better sorption kinetics [4], [15], [16], [18]. Large specific surface increases the rate of surface reaction with hydrogen. The small powder particle size may also be a solution to the problem of the 'blocking' layer of MgH_2 as the Mg powder can be fully hydrogenated. On the other hand, the smaller particle size and therefore larger surface area of the Mg powder causes the material to be more susceptible to oxidation. Technologies used for nanostructuring of the magnesium include ball milling, melt spinning, chemical vapor deposition *etc.*.. By comparing of the properties of different size MgH_2 (from 60 µm to 3 nm) it was found that reaction was faster when the particle size was smaller [17] (Fig. 2.9). Also the enthalpy of reaction was going down to 55 kJ/mol while decreasing the particle size[18]. Magnesium nanowires [19], as well as fibered magnesium [20] of 30 nm thickness were found to have the lower activation barrier of 33.5 kJ/mol and 116 kJ/mol, respectively. A high surface energy of nano-magnesium may result in aggregation problem during the cycling.

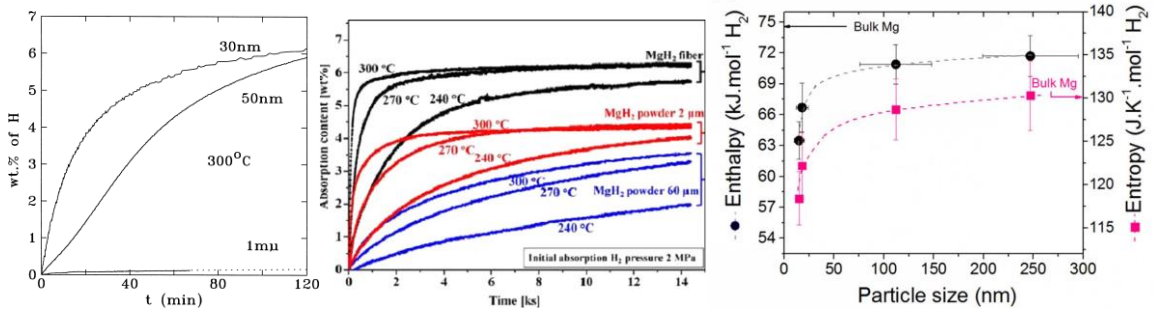

Fig. 2.9. Effect of grain size on hydrogen absorption of ball-milled magnesium powders and fibers [17], [18], [20].

The other method proposed to keep magnesium in nanoscale is the nanocofinement, which relies in embedding the magnesium nanoparticles into a stable scaffold. The most scaffolds used are porous carbons, metal-organic frameworks, porous polymers, etc. Scaffold material is required to be chemical resistant (not reacting with many reactants) and it should be stable during hydriding cycling. Additionally, high surface area, high volume ration and uniform pore size distributions will help to tolerate higher loadings of active materials. For example, carbon aerogels (CA) with the pore size from 6 nm to 20 nm were successfully used as a scaffold for magnesium nanoparticles with size closed to the size of the pores [21] . They release hydrogen at temperatures of 140 °C lower than the bulk MgH_2 and the existence of CA effectively protects the particles from aggregation during the cycling. The other examples here are graphene nano-sheets decorated with TiB_2 (T_{dec}=319 °C, E_a =90.8 kJ/mol)[24], NiCo (T_{Dec}=313 °C, E_a =105 kJ/mol) [25], Mg (T_{Dec}=334 °C, E_a =76.2 kJ/mol) [26] or multi-walled carbon nanotubes with Ni and TiF_3 supported on them [27]. In [22] the authors reported on the synthesis of monodispersed magnesium hydride nanoparticles on graphene sheet (Fig. 2.10). When doped with Ni, the material demonstrates better hydrogen storage performance with ultra-long cycling life and fast sorption kinetics. Basic reasons for improved hydrogen storage performance are: enlarged contact surface of reactants, increased grain boundaries, decreased diffusion distance and resistance to the particle agglomeration. The hydrogen capacity of nanoconfined MgH_2 is, however, decreased due to its limited loading ability. The kinetics is also relatively poor compared with e.g. the catalyzed MgH_2.

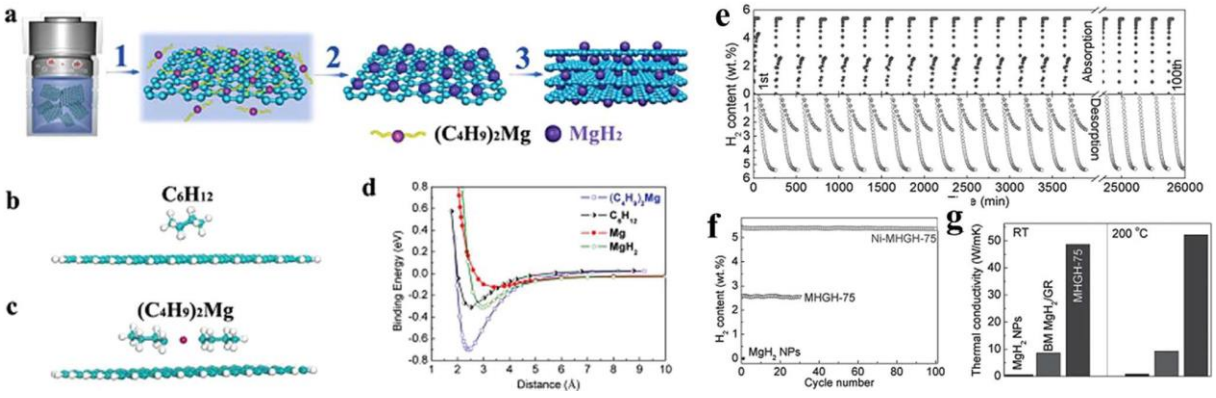

Fig. 2.10. (a) Schematic illustration of the self-assembling MgH_2 nanoparticles on graphene, (b) C_6H_{12} and (c) $(C_4H_9)_2Mg$ on a graphene sheet under the most stable configuration, (d) binding energy curves based on density functional theory (DFT) calculations. (e) Reversible H_2 sorption, (f) cycling of Ni doped MgH_2 nanoparticles on graphene, pure MgH_2 nanoparticles

on graphene and ball milled magnesium hydride at 200 °C. (g) thermal conductivity of MgH_2 nanoparticles on graphene [22].

Another approach is the formation of a metastable γ-phase of magnesium hydride. During hydrogenation, the hydrogen atoms are introduced into the hexagonally close-packed (HCP) magnesium metal lattice (Fig. 2.11).

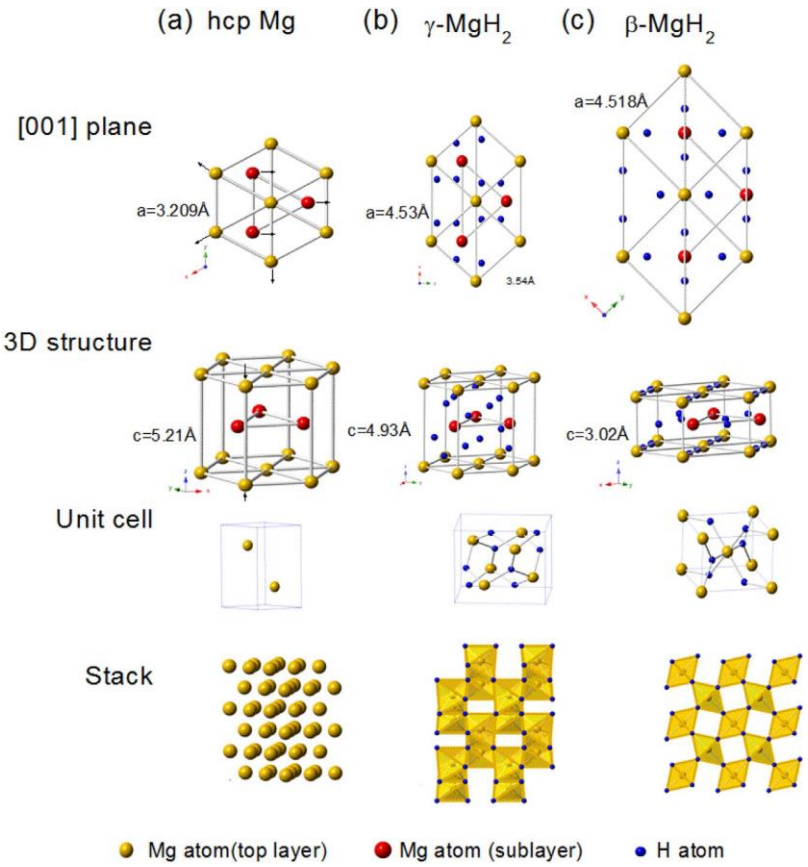

Fig. 2.11. Evolution of the crystalline structure of (a) hcp Mg when it is transformed to (b) γ-MgH_2, and (c) β-MgH_2 upon hydrogen absorption. As the hydrogen atoms are introduced, the Mg atoms of the A and B stacking slide, as indicated by the arrows in result the length of the Mg-Mg bond increases.

The hydrogen atoms first occupy the tetrahedral interstitial sites, forming the α-phase, then addition of hydrogen leads to the formation of the β-phase with tetragonal lattice structure (Fig. 2.11) of α-TiO_2 type, of the space group $P4_2/mnm$ and lattice parameters: a=0.452 nm and c=0.302 nm. At the high pressure (0.39 GPa) [23]–[25] the compound forms orthorhombic structure (α-PbO_2) of γ-MgH_2 with the space group *Pbcn* and lattice parameters: a=0.450 nm,

b=0.542 and c=0.492 nm. The volume of hcp lattice of magnesium expands by approximately 31.4 % for α-MgH_2 and 29.1 % for γ-MgH_2. Due to the differences in the crystal structure, faster hydrogen diffusion and lower formation enthalpy (44.6 kJ/mol [26]) for γ-MgH_2 are predicted [27], [28]. This phase can be formed by mechanical stressing of the β-phase. It is usually achieved in high energy ball milling process [16], [23], [26], [29]. Unfortunately, it is not stable during hydrogen cycling and reverts back to β-phase.

The next effective method to reduce the thermodynamic barrier of high enthalpy of reaction is alloying of magnesium with elements forming less stable hydride, including mainly rare earth and transition metals. Formation of such alloys changes the reaction path and may reduce the enthalpy (Fig. 2.12) to practical ranges of 30-60 kJ/mol [4], [15], [30]. Examples of magnesium based alloys are listed in Table 2.5. Typical examples are here Mg_2Ni (64.5 kJ/mol [31]), and Mg_2Si (36.4 kJ/mol[32]). However, alloying was found to reduce the hydrogen capacity to 3.6 wt. % and 5.0 wt. % respectively.

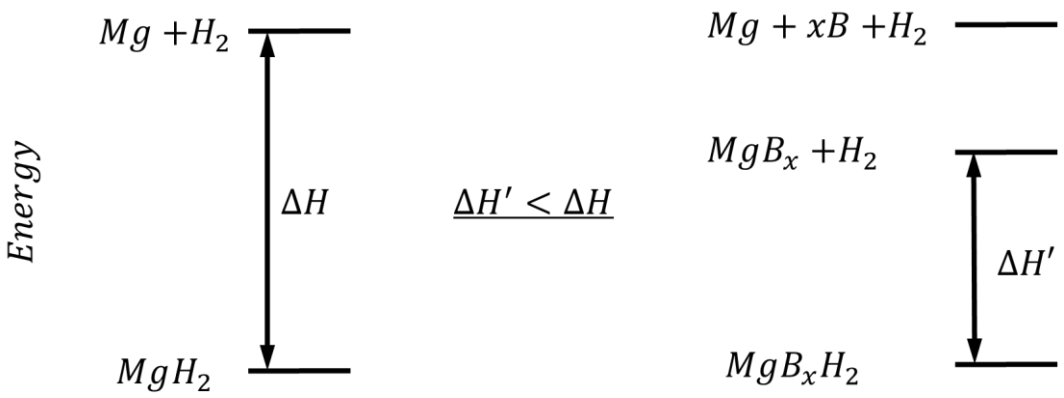

Fig. 2.12. A scheme of destabilization of metal hydrides through alloy formation.

Table 2.5. Examples of magnesium-based hydrogen storage alloys and their fundamental properties [15].

Name	E_a (kJ/mol)	ΔH (kJ /mol H_2)	Capacity (wt. %)	T (°C)
Mg	–	74.5	7.6	300
Mg (2–7 nm)	–	71.2	7.6	276
$Mg_{90}Ce_{10}Ni_{10}$	109.2	77.9	5.4	284
Mg_2Ni	–	64.5	3.6	254
$Mg_3LaNi_{0.1}$	–	81	2.73	284
Mg_3Cd	69	65.5	2.8	–
MgH_2-Ti	30.8	75.2	6.7	278
$Mg_{0.95}In_{0.05}$	–	68.1	5.3	–
Mg_3Ag	–	68.2	2.1	–
Mg_2Si	–	36.4	5.0	–
Mg_5Ga_2	149	68.7	5.7	300

Another approach for enhancing the hydride properties is adding catalysts. Small amounts of dopants can reduce the activation barrier owing to the spillover mechanism: after the hydrogen molecule dissociate on the catalyst, some hydrogen atoms attach to the catalyst, and some atoms diffuse through, gradually penetrating and interacting with the metal (Fig. 2.13) [15], [33], [34].

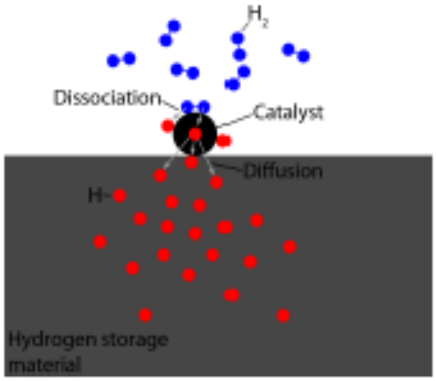

Fig. 2.13. Diagram illustrating the spillover mechanism.

Numerous materials such as transition metals metal oxides, halides and other compounds have been successfully applied. Doping of 5% of Ti, V, Mn, Ni and Fe improved reaction kinetics (Fig. 2.14) by reducing the activation energy down to 62.3-88.1 kJ/mol[35] . Pressure-composition – temperature test suggests that the thermodynamic s of samples is not changed, so the improvement of the kinetic is directly connected with the reduction of activation energy.

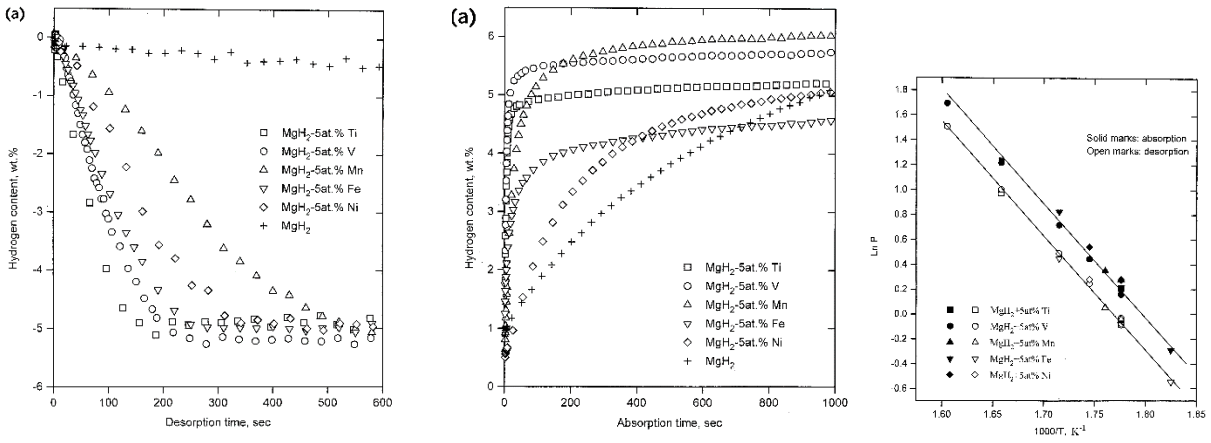

Fig. 2.14. Hydrogen desorption - absorption curves of Mg–Tm composites at 473 K and van't Hoff plots for Mg–Tm composites [35];

Metal oxides systems, including Nb_2O_5 [36]–[38], Cr_2O_3 [36], [39] and CeO_2 [39], as well as non-metallic compounds such as silica and silicon carbide [40], [41] are often considered as effective catalysts. Different types of Ti-based materials (Ti-metal, TiO_2, TiF_3, TiN) ball milled with MgH_2 lower the onset temperature down to 257 °C, 216 °C, 173 °C, 280 °C and decrease the kinetic barrier to 103.9 kJ/mol, 118.9 kJ/mol, 75,0 kJ/mol and 144.7 kJ/mol for Ti-metal, TiO_2, TiF_3 and TiN, respectively[42]. The most common way to introduce the catalytic elements and compounds is the ball milling, but chemical methods, such as reaction in THF solution[43], sol-gel [44] and nanoparticles precipitation [45] were also successfully applied. These methods usually combine with nanoscaling effects due to the preparation route used. Carbon-based materials show a great potential in improving MgH_2 performance. Graphite, MWCNTs, nanofibers and activated carbon were milled with magnesium hydride [46], [47] and the best results obtained for nanofibers show a shift of the decomposition peak temperature from 363 °C to 322 °C. Carbon nanostructures may serve both as catalyst and dispersion matrix/support (as mentioned before in nano-confinement part) for magnesium, catalytic metals and their compounds.

Nanostructured metal hydrides may also be manufactured in the form of thin films. It offers a different path of achieving a high surface area that will enhance hydrogen storage properties and the application of catalytic thin film overlayer provides additional benefits by enhancing the sorption kinetics. The study of pure magnesium films has been carried out [48]–[50] as well as different multilayered structures of Mg with Ti, Ni and Pd . It was shown that thin film multilayered structures of Pd and Mg [51]–[54], exhibit remarkable enhancement of thermodynamic and kinetic properties. The presence of the uniform thin catalytic film on the surface of magnesium hydride increases among others the H_2 dissociation rate by reduction of the activation energy of hydrogen desorption. The formation of a multilayered thin film complex has been shown to lower the temperature of hydrogen desorption for magnesium as well as boost the sorption kinetics. A tri-layered (Pd/Mg/Pd) hydrogen storage system (Fig. 2.15) [51] which absorbs ~ 5 wt.% hydrogen at 100 °C under 1 bar pressure and is fully dehydrogenated at about 90 °C. The authors suggested that the reduced temperature of hydrogen desorption is effect of interaction between the Pd and Mg layers in their interface regions: Hydrogen is initially desorbed from the Pd films because of the lower desorption temperature of Pd, as compared to Mg. This causes a contraction of the Pd films and induces compressive stress on both sides of the Mg layer, which causes destabilization of hydrogenated magnesium.

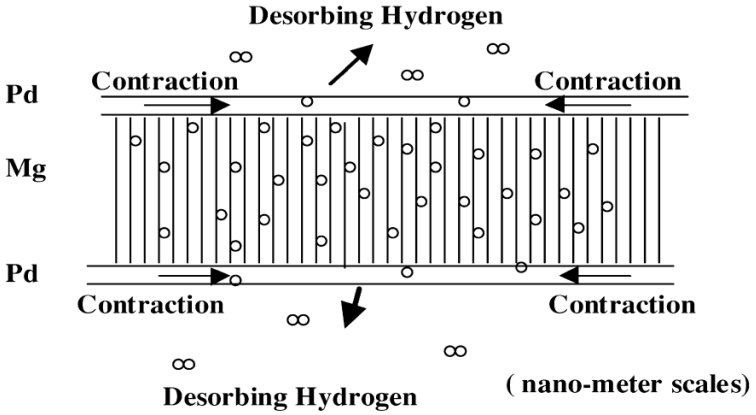

Fig. 2.15. Schematic diagram of the cooperative phenomena on a hydrogenated Pd/Mg/Pd film [51].

What is interesting, increasing the thickness of the magnesium layer results in a decrease in the temperature of dehydrogenation (Fig. 2.16). This is confirmed by the thermal desorption spectroscopy (TDS) profiles showing a shift of the peak position to lower temperatures with increasing thickness of Mg. On the other hand, no dependence on the thickness of Pd film has been observed for the hydrogen sorption properties of Mg.

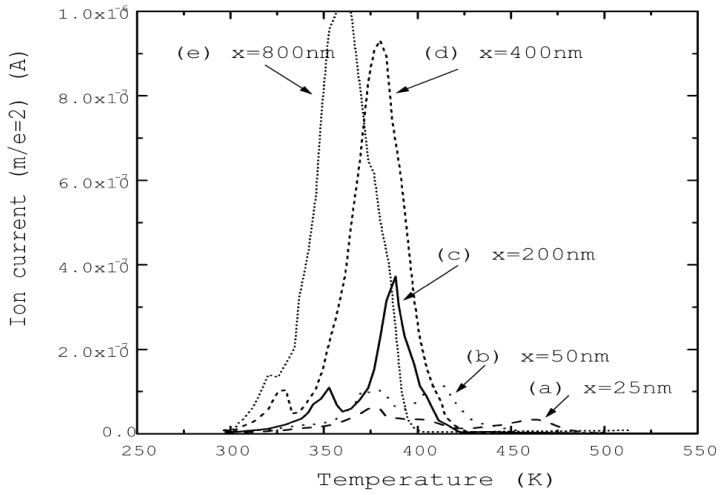

Fig. 2.16. TDS spectra of several hydrogenated Pd (50nm)/Mg(x nm)/Pd (50nm) films with x = 25, 50, 200, 400 and 800nm [51]

An interesting approach was proposed by Cui and Wang [43], where ball milled magnesium hydride was coated with the multi-valence, titanium-based film. The coating of 10 nm thickness (Fig. 2.17a) was prepared by chemical reaction between Mg particles and titanium chloride solution in THF.

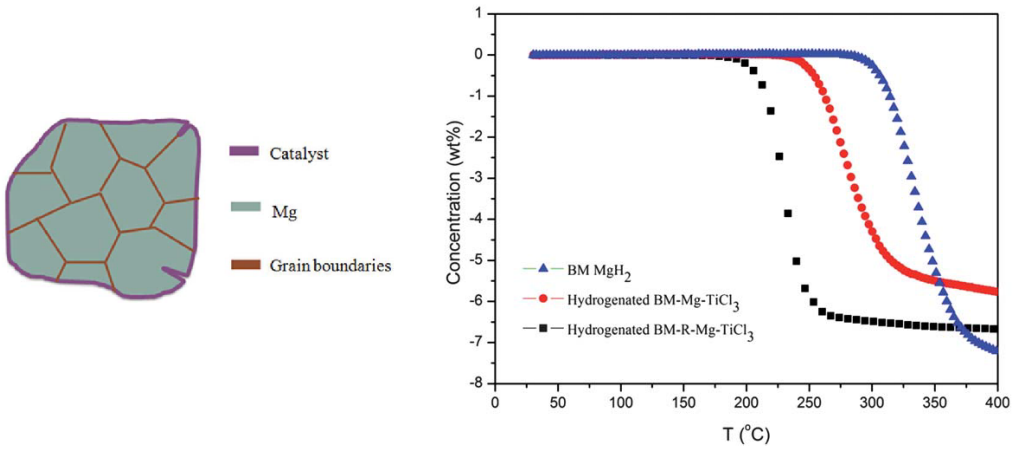

Fig. 2.17. a) Schematic illustration of magnesium particle coated with the catalyst layer. b) TPD profiles for undoped ball milled MgH_2 (BM - blue points), MgH_2 ball milled with $TiCl_3$ (BM-Mg-$TiCl_3$ – red points) and ball milled MgH_2 coated with catalyst layer (BM-R-Mg-$TiCl_3$ – black points) [43].

Properties of obtained samples were compared there with more conventional ball milling technology: temperature programmed desorption (Fig. 2.17b) shows that the decomposition of coated powders starts at the temperature of 175 °C, about 60 °C lower than for ball-milled sample and gives 6.7 wt. % hydrogen storage capacity. The activation energies were derived to be 30.8 kJ/mol for titanium-coated and 77.6 kJ/mol for titanium-milled one. This work was a direct motivation for this Thesis. The main is to modify of the surface of each particle in magnesium hydride powder by coating of the particle with the transition metal layer using magnetron sputtering. It should reduce the kinetic barrier on the magnesium/magnesium hydride surface and improve reaction rate while keeping dopant amount low. Nickel, vanadium and niobium metals were chosen to sputter. The key advantages of using magnetron sputtering are easy control of thickness of the films, which allows to introduce precise amount of dopants and possibility to achieve very uniform coating. Also, this technology is clean, does not require volatile chemicals and it is possible to sputter different alloys and catalytic materials combinations.

Large enthalpy of reaction for magnesium hydride leads to large amount of heat needed to be dissipated or supplied. When hydrogen is required, heat is supplied to the metal hydride bed and the reaction is reversed. Dissipation of the released heat and absorption of the supplied heat (about 2 kJ/mol per second to keep the magnesium hydride powder at constant temperature) controls the chemical equilibrium and hence the rate of absorption/desorption of hydrogen.

Therefore, effective heat transfer is essential for improving the performance of a metal hydride storage system. There are several factors governing this phenomena coming from basic heat transport and convection equations for heat flux q [55]:

$$q = kA\frac{\Delta T}{\Delta x}$$

$$q = h\Delta T$$

where: Δx – distance, A – exchange surface area, k – thermal conductivity, h – convection coefficient, ΔT – temperature difference.

Methods of improvement of heat transfer in metal hydride based tanks can be classified according to them:

- Optimization of the tank geometry (Δx, A)
- Optimization of mass and heat flow (h, ΔT)
- Enhancement of thermal conductivity (k)

First method is to reduce the distance and increase the heat transfer area by addition of cooling pipes, radiators, exchange fins and other structures [56]–[60], which helps to take away waste heat from the hydride. For example, Askri et al. [57] carried out a numerical analysis of four cylindrical metal hydride tanks (Fig. 2.18):

a) normal, cylindrical tank that loses heat through its surfaces,
b) tank with plate fins on its lateral surface,
c) cylindrical tank with the inner, concentric cooling/heating tube,
d) similar to c), but with the addition of fins to the heat exchanger tube.

On comparing the designs it was found that the time required for 90% storage reduced remarkably. An improvement of 10%, 56% and 80% in the hydrogenation profiles over the basic case was registered.

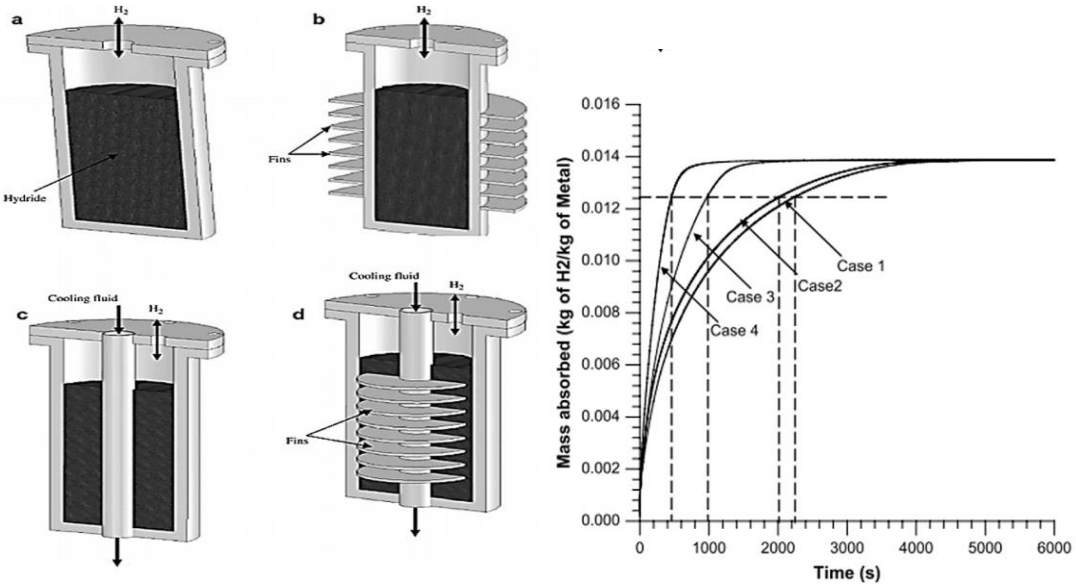

Fig. 2.18. Comparative study of four types of metal hydride reactors [57]

Optimization or forcing of gas and mass flow is the next attempt. An interesting example is physical mixing of metal hydride in the tank (Fig. 2.19 [61]). Because of the fact that hydrogenation reaction starts faster in regions of the tank which are close to the gas inlet, a wide distribution of hydride temperature can be observed. The movement (which can be treated as convection) of the powdered material beds inside the vessel causes averaging of the temperature and "self-cooling" effect, which enhances the reaction rate.

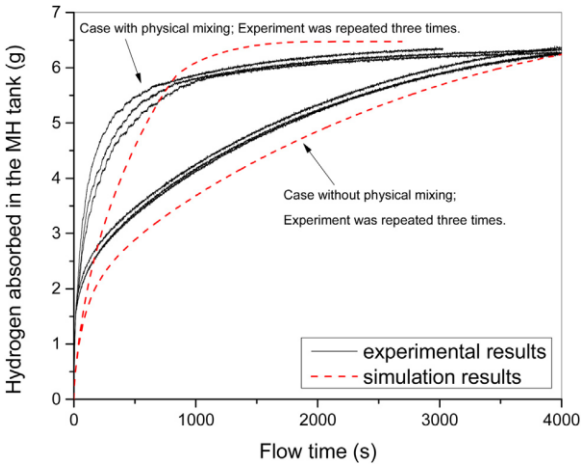

Fig. 2.19. Comparison of experimental and computed hydrogen absorption curves in the metal hydride tank with and without mixing [61]

The key parameter in heat transfer phenomena is the thermal conductivity of hydride forming material. Despite the fact that conductivity of magnesium is relatively high because of its

metallic character, for the dielectric hydride the thermal conductivity is two orders of magnitude lower (Table 2.6). Moreover, because of the stress caused by the unit cell expansion/shortening a cracking effect is observed (Fig. 2.20) which causes the reduction of grain size of the metal hydride and limits the thermal conductivity to the level of 0.1 W/m·K.

Table 2.6. Thermal conductivity of different magnesium hydride structures.[62]

Material type	*Thermal conductivity [W/m·K]*
Magnesium, bulk	156
MgH_2, as-received powder	0.11
Ball milled MgH_2, powder	0.09
Compressed MgH_2 pellets	1.21

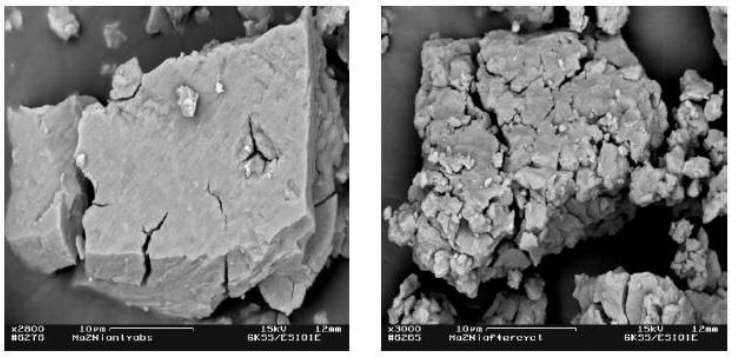

Fig. 2.20. MgNi sample surface before and after the six hydriding cycles[63]

Highly conductive dopants, such as Al powders and foams [64]–[66], Cu powders and coatings[67], Ni foams[67] were applied to boost the thermal conductivity of metal hydrides. Many type of graphite-based materials were successfully used [68]–[72]. Graphite powders (up to 25 wt. %) are introduced to hydride by high pressure compacting to pellets. Fig. 2.21 presents thermal conductivity of magnesium hydride and sodium alanate composites with graphite flakes. It was shown, that thermal conductivity is increased by more than one order of magnitude and it can be tuned up to 40 W/m·K. The pellets have good volumetric and gravimetric hydrogen storage capacity and are very stable during the reaction cycling. Especially, hydralloy based composites (Fig. 2.22) were found to be stable up to 85 cycles in a wide range of pressure/temperature conditions. Hydrogen gas permeability can be kept at sufficient level due to porosity of compacted pellets (~30%). High gas permeability and thermal conductivity in combination with a stable pellet structure indicate a high potential to use such materials composites for hydrogen storage.

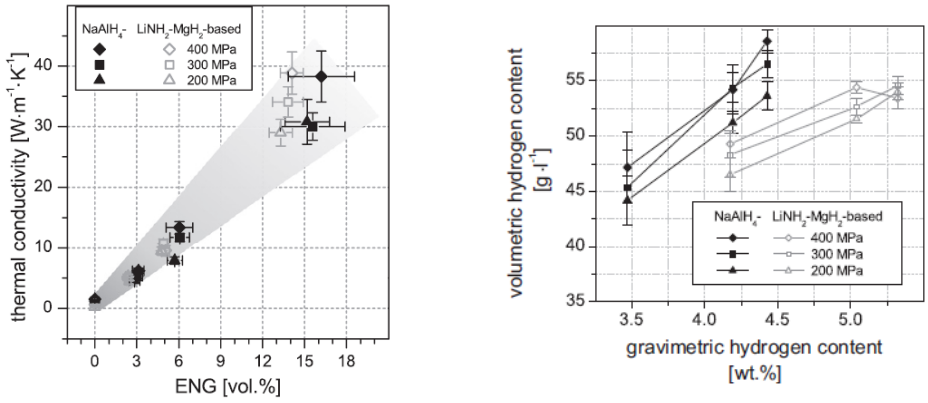

Fig. 2.21. Thermal conductivity of chosen hydride based graphite composites pellets and the influence of cycling [68]

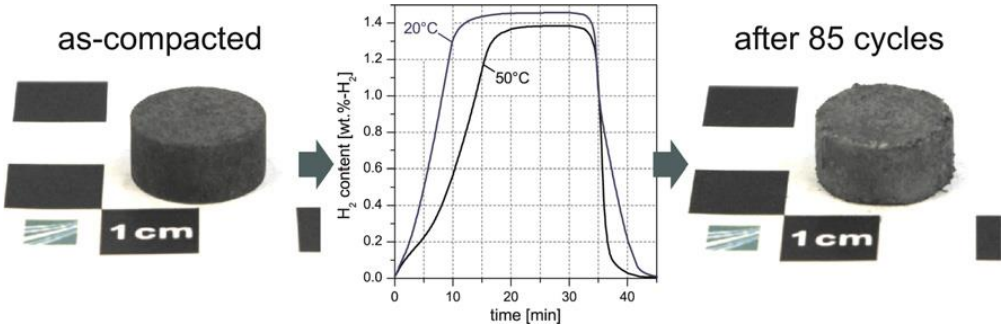

Fig. 2.22. Hydrogen de- and absorption behavior of a hydralloy-ENG pellet with 12.5 wt.% ENG compacted at 75 MPa[69].

Graphite has a very interesting crystal structure leading to unusual transport properties. It is composed on stacked parallel layers (Fig. 2.23a) with carbon atoms arranged in a honeycomb lattice with their separation of 0.142 nm, and the distance between planes is 0.335 nm. Each atom in the plane is bonded covalently (σ-bond) to the three neighbors, owing to the *sp2* hybridization. Only three of the four potential bonding sites satisfied. The fourth electron is free to delocalize in the plane, making graphite electrically conductive. However, it does not conduct in the direction perpendicular to the plane. The adjacent two layers are bonded by van der Waals forces. Bonding between layers is much weaker (7 kJ/mol) comparing to the covalent bond (534 kJ/mol) which allows layers of graphite to be easily separated, or to slide past each other. The spacing between the layer planes is relatively large, approximately twice of the van der Waals radius of carbon. The stacking layers order in two slightly different ways: hexagonal and rhombohedral (Fig. 2.23b). In the hexagonal α-graphite layers are superimposed over each in

A-B-A-B stacking order. The crystallographic description is given by the space group $P6_3/mmc$ space group. It is the most thermodynamically stable form of graphite and is found in all synthetic materials. The other structure is rhombohedral β-graphite with the stacking order A-B-C-A-B-C and the space group $R\bar{3}m$. The carbon atoms in every third layer are superimposed. It makes graphite thermodynamically unstable (can be considered as an extended stacking fault of hexagonal phase) at it always occurs always in combination with hexagonal graphite, up to 40% in some natural and synthetic materials. It usually reverts to the hexagonal form during heat treatment above 1300°C

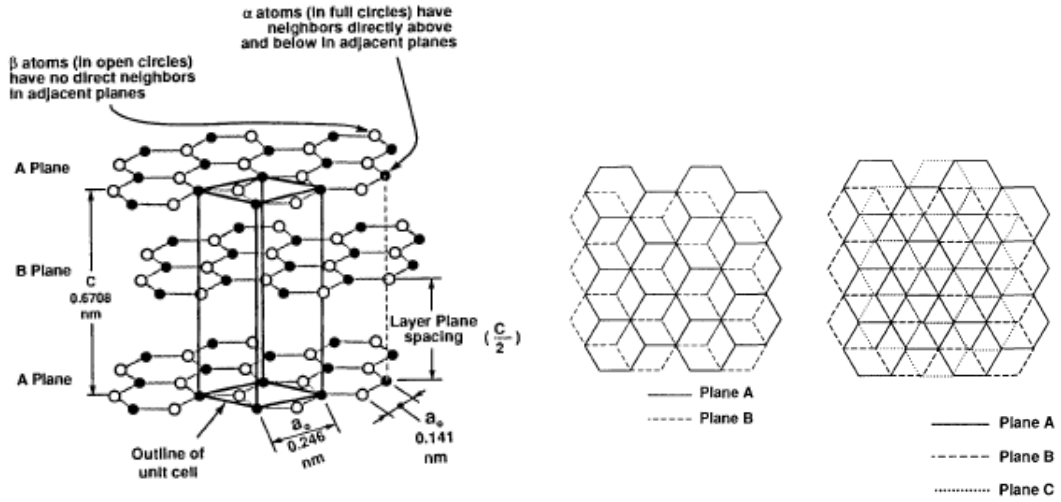

Fig. 2.23. Crystal structure of graphite showing ABAB stacking sequence and unit cell (a). Perpendicular view of hexagonal and rhombohedral graphite crystal (b) [73].

Different form of graphite, such as flaked, pyrolytic, carbon fibers, carbon black and others are actually aggregates of graphite crystallites and forms of polycrystalline graphites. These crystallites and their aggregates may vary considerably in size from nanometers to submillimeter scale. The thickness of the single crystallite or aggregate (along c-axis) is usually much smaller than particle size in the ab direction, which leads to common flake/plate/fiber shape of particles. Within each crystallite, a different types of imperfections, vacancies, stacking faults and declinations of the planes may be found. The size, shape, numbers of imperfections, orientation of crystallites, as well as bulk characteristics, such as porosity and amount of impurities, may vary considerably from one material to another causing differences in the properties of these materials. Aggregates may be large, with limited number of defects and essentially parallel to each other, in this case its properties are close to the ideal graphite crystal. Such large aggregates are often found in pyrolytic graphite. When the aggregates, are

composed of small and randomly oriented crystallites (such as amorphous carbon) their properties are usually isotropic. The planar structure of graphite results in a considerable anisotropy, especially in electrical and thermal properties. The properties of the material differ when measured along the *ab* directions (within the plane) or the *c* direction (perpendicular to the planes). It is worth to note, that in case of powdered graphites, such as natural or flake graphite, the anisotropy occurs in microscale, in point of view of single grain, but in macroscale, a powder can be considered as an isotropic material [73].

Heat conduction in graphite is usually dominated by phonons, despite the presence of delocalized electrons. This is explained by the strong covalent *sp2* bonding resulting in efficient heat transfer by lattice vibrations. However, electron conductivity can become significant in doped materials [74]. Thermal conductivity depends on the specific heat (Debye equation), group speed of phonons and mean free path related to their scattering. In polycrystalline materials, phonons are scattered by crystallite boundaries, defects, and other phonons. In the basal plane, the mean free path is high and thermal conductivity is high in the ab directions. On the other hand, in the direction perpendicular to the basal plane (*c* direction), the conductivity is two orders of magnitude lower since the amplitude of the lattice vibration in that direction is much lower than in the *ab* directions. The room temperature thermal conductivity of a graphite crystal has been reported as ~4200 W/m·K in the *ab* directions and ~10 W/m·K in the c direction for highly crystalline pyrolytic graphite (Fig. 2.24).

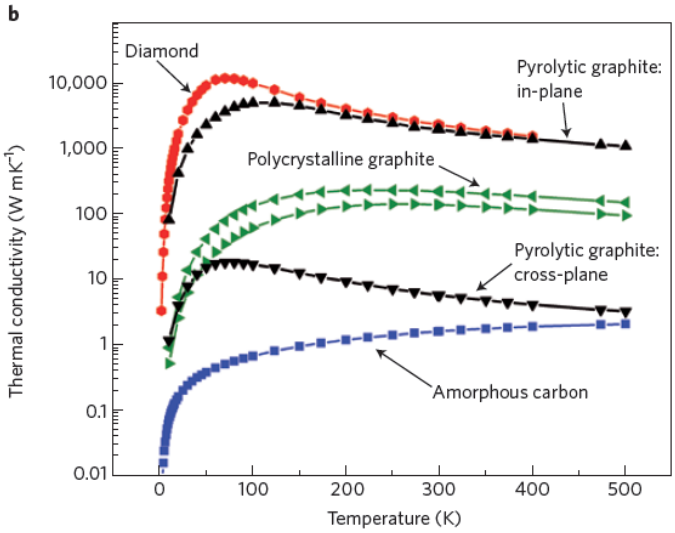

Fig. 2.24. Thermal conductivity of bulk carbon allotropes as a function of temperature.

The average value for commercial pyrolytic graphite is near 400 W/m·K. The temperature dependence of the thermal conductivity clearly shows that with decreasing of graphite

crystallite size from pyrolytic, through flaked, to amorphous carbon the heat conduction characteristics changes from typical dielectric like curve with a maximum below 100 K to a flat curve typical for polycrystalline and amorphous materials.

As mentioned before, graphite particles are introduced usually using pelletization methods. During the compacting of the plate/flake–like shape particles reorganize and become mostly orientated with normal directions to their planes parallel to the compression axis. Such alignment results in anisotropy of the thermal conductivity and thus, of hydrogen permeability through material. In the case of commonly used cylindrical pellets the thermal conductivity is enhanced in radial direction due to the better conductivity along graphitic planes. An example is shown on Fig. 2.25a [70]. Magnesium hydride was compressed with the expanded natural graphite under pressure of 100 MPa. Effective thermal conductivity increases with ENG contentment and for radial direction is nearly four times higher than along the pellet axis.

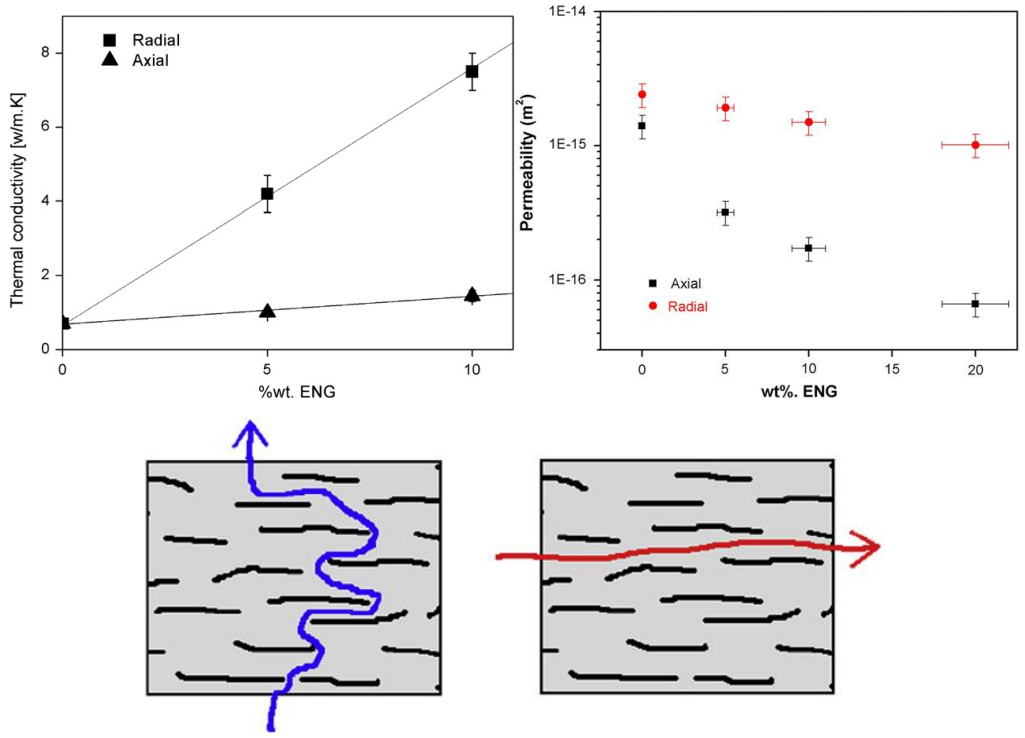

Fig. 2.25. Axial and radial thermal conductivities: (a) and permeabilities (b) of compacted disks versus expanded natural graphite. Diffusion path of hydrogen in compacted disks containing ENG (c): axial flow (d) radial flow [70].

Hydrogen gas permeability (Fig. 2.25b) is poorer in axial direction, because the hydrogen molecules in motion face the non-permeable graphite flakes on their way this direction (Fig. 2.25c,d). Varying of these two factors i.e. thermal conductivity and permeability to hydrogen

by changing the vessel geometry and graphite orientation degree allows to optimize effective heat and mass flow in metal hydride composites and to achieve the best reaction kinetics. Ordering of graphite flakes can achieved by using of strong electric field. Magnesium hydride with graphite particles were suspended in a special, high temperature silicone resin. Electric field induces torque acting on graphite particles suspended in the fluid and causing their reorientation and alignment in final composite material.

3. EXPERIMENTS AND SAMPLE PREPARATION

Two main parts of the experimental work have been carried out: the one focused magnetron coating of magnesium hydride with catalytic layers and the other concerning composites of magnesium hydride and graphite with the thermal conductivity enhanced by electric field alignment of graphite flakes. This Chapter presents experimental methodology, as well as properties of starting materials. Morphology of the samples was examined with X-Ray diffraction method and Scanning Electron Microscopy. The study of hydrides thermodynamics and kinetics was performed using volumetric Sievert method followed by Thermogravimetry and Differential Scanning Calorimetry. Additionally, thermal conductivity of composites was evaluated using Thermal Transport Option of the PPMS apparatus.

3.1. Magnetron sputtering of thin films on the powdery substrates

Magnetron sputtering using powder substrates was recently reported in several papers [75]–[86]. The key aspect is to get uniform coverage of each grain surface. In order to achieve that, the material particles need to be continuously mixed during the sputtering. There are three main approaches solving the problem: to place the powder in a rotating cup (Fig. 3.1a), polygonal barrel called Polygonal Barrel Sputtering (Fig. 3.1b) or to get fluidized particle bed by applying low or high frequency vibrations (Fig. 3.1c).

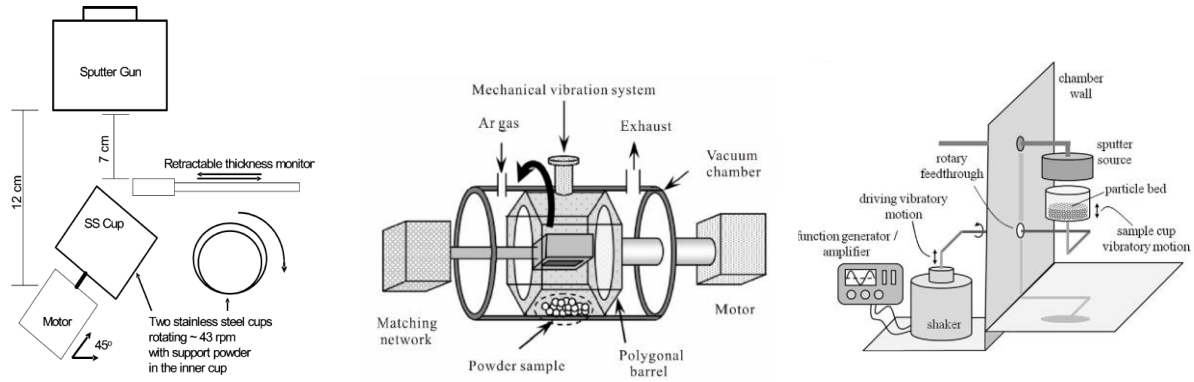

Fig. 3.1. Scheme of magnetron sputtering equipment using rotating cup (a) [84], polygonal barrel (b) [75] and vibrational stirrer (c) [77].

It was found that each technique has some advantages and disadvantages. Methods using rotating vessels work-well for big particles, but the finest particles get stick to the walls of the container and tend to agglomerate, which leads to a non-uniform coverage and presence of uncoated grains. It also requires specific construction of magnetron cathode placed inside the

rotating vessel. High frequency vibrations may prevent agglomeration, but the limitation is a relatively small amount of stirred powders (few milligrams) and problems with low efficiency of ultrasonic transducer working in vacuum.

The laboratory equipment constructed in the course of realization of this Thesis (basic parameters in Table 3.1) consists of the magnetron cathode and powder mixer placed in the vacuum chamber (Fig. 3.2). In conventional magnetron sputtering the substrate has a form of bulk material, typically a plate placed near to the cathode. In this study we used a container in the shape of a small bowl set in circular motion in the vertical plane by an electric motor connected with arm and crank mechanism (Fig. 3.2bc). It enables efficient shaking of relatively large amount of powder (~500 mg) with reduced effect of its sticking to container walls. The shaking frequency (up to 5 Hz) and amplitude (up to 10 mm) is controlled by adjustment of the motor speed and crank length. To reduce the problem of particle agglomeration a small metal ball is placed inside the vessel, which hits and disperses the agglomerates during motion of the container. The vacuum chamber was evacuated with diffusion pump (Tepro PDO-300) and filled with 6N purity Ar gas. Maximal level of vacuum achieved was 10^{-3} mbar and the working pressure was 10^{-3} mbar. After coating, the chamber was vented with argon gas and the samples were immediately closed in glass jars under argon in a glove-box. However the contact of powder with air could not be avoided during initial stage of pumping and while moving it into glove box. The pumping system and shaking device was modified in the second stage of experiments, after oxidation problems were spotted (Chapter 4). A special, remote opened, sealed cover for powder container was developed and allowed to conduct entire process in argon atmosphere, starting from measuring of powder weight, to closing the sample in glass jars. Also, pumping system was changed and cleaned, so that higher vacuum ($< 10^{-4}$ mbar) could be reached.

Table 3.1. Overview of sputtering experiment conditions.

Powder mass	500 mg
Sputtering time	Adjustable, with 5 min break after 15 min of sputtering
Magnetron power	260 W
Cathode-substrate distance	5 cm
Working pressure	3-5·10-3 mbar
Pumping pressure	< 10-3 mbar
Argon flow	~ 25 ml/min
Shaking amplitude	~ 5 mm
Shaking frequency	~ 3 Hz

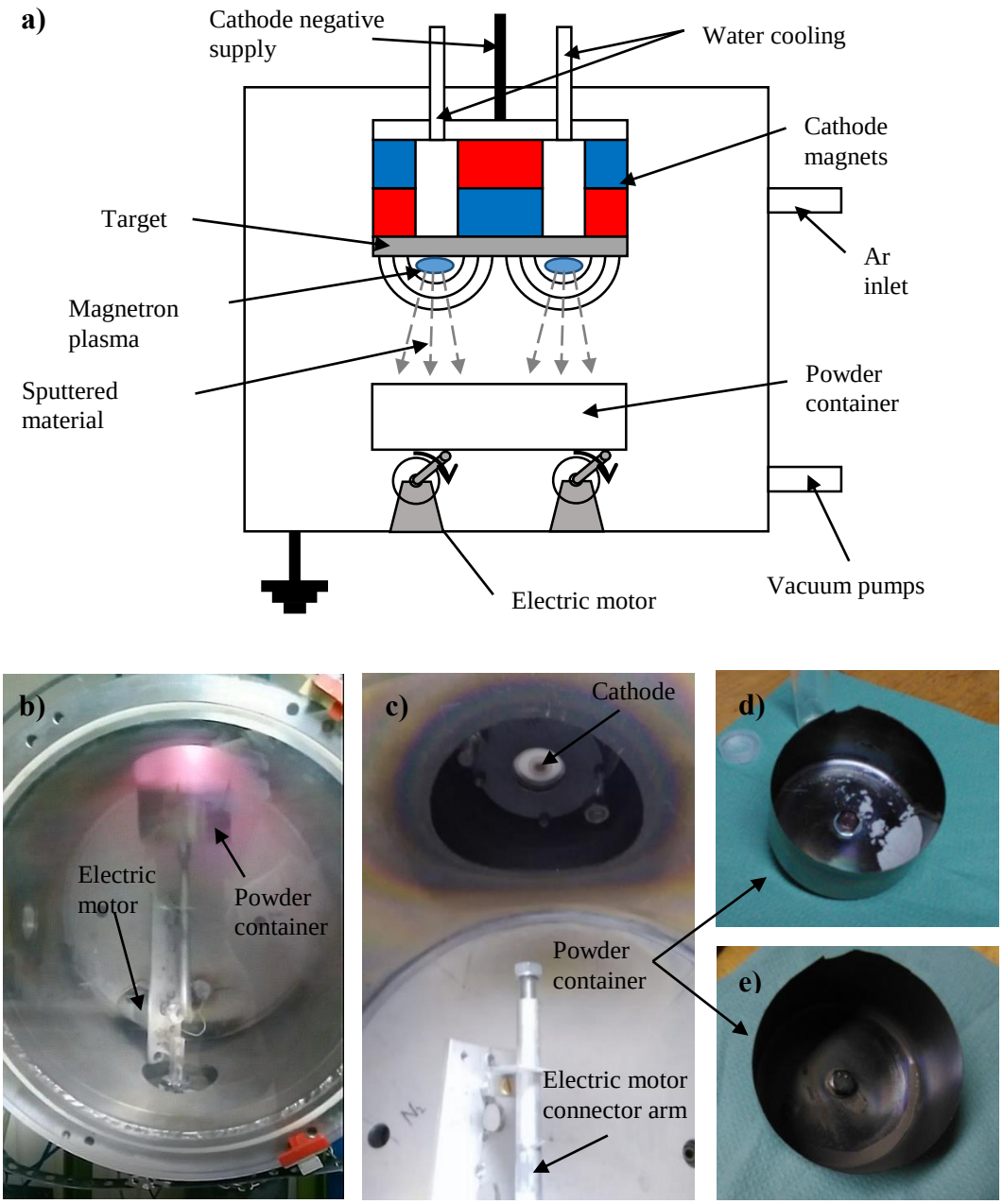

Fig. 3.2. Scheme of the equipment used for sputtering (a) and photo of practical realization. Photos presents general view of vacuum chamber (b), close view for cathode (c) and powder shaker – the cup (d) is mounted on the top of electric motor connector arm. Picture (e) shows powder container after the sputtering process.

The magnetron is a planar source cathode placed 5cm above the stirrer. Designing and constructing of the sputtering source was a part of this PhD project. Its scheme is presented in Fig. 3.3a. Main body has the shape of a cylinder with one base hollow and it is made from copper to provide good electrical and thermal contact. Front wall is 1.5 mm thick and lateral surface is threaded. The target is mounted to the front by a threaded cap. The size of the cap

allows to use targets in the shape of disks with 25–30 mm diameter and 2–5 mm thickness. There is a permanent magnet (N50 grade) and a soft steel yoke placed inside the main body. Magnets produce magnetic field with its lines bending over the cathode front surface (Fig. 3.3b). Radial component of the field induction depends on the distance from the center and to the cathode surface (Fig. 3.3c). Its value ranges from 80 to 120 mT for 5-3 mm distances from the cathode surface, which is sufficient for efficient plasma confinement. The maximum field intensity is located on the circle with ~19 mm diameter, so the plasma is confined only on the target surface and no sputtering of copper parts occurs. Main body is attached to PTFE insulating part with brass screw and then mounted in vacuum chamber wall. All parts are sealed with high vacuum O-rings. The cooling is provided by continuous water flow.

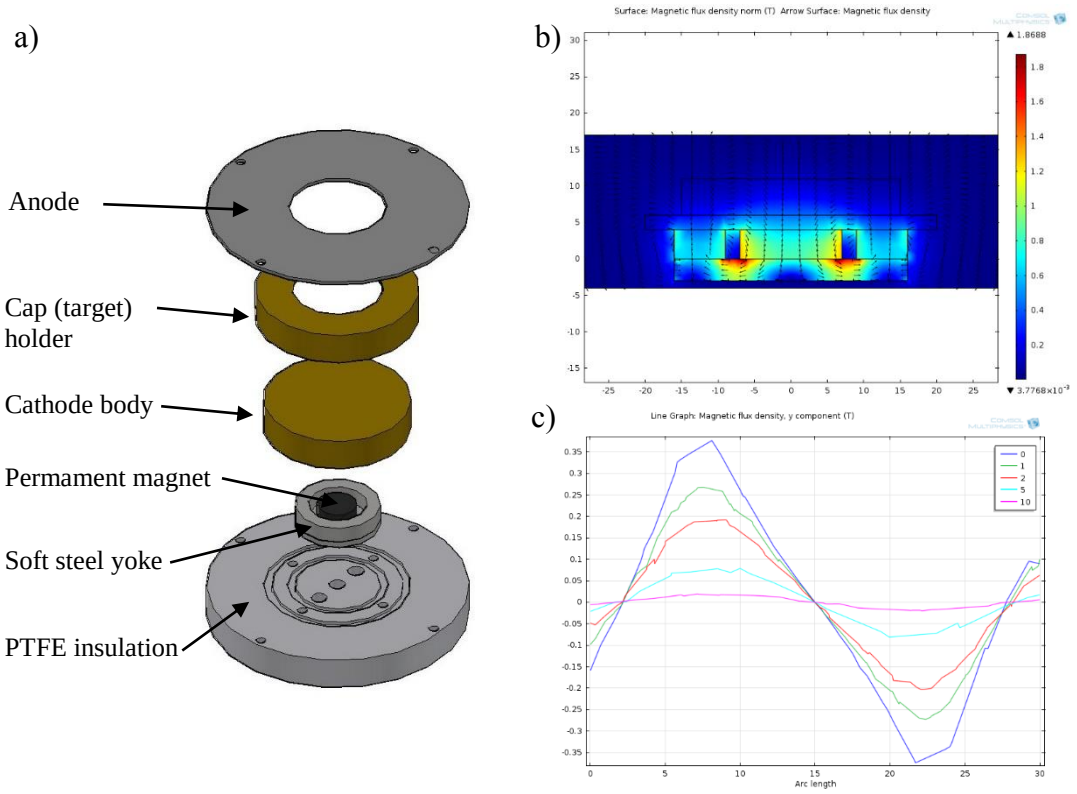

Fig. 3.3. Scheme of magnetron source constructed for the experiments (a), magnetic field distribution around the cathode surface (b) and distance from the center dependence of the radial magnetic field component, at different positions from the cathode surface (c)

The basics of magnetron sputtering process are as follows: A target made of the material desired to be deposited, is bombarded with energetic ions, typically of inert gas, such as e.g. argon (Ar^+). Argon gas is introduced into a vacuum chamber at a pressure of 1 to 10 mTorr. A DC

voltage is placed between the target and substrate which ionizes argon atoms and creates a plasma in the process accompanied with the so called glow discharge due to the light emitted. These argon ions are now charged and they are accelerated towards the cathode target. The forceful collisions of these ions onto the target eject target atoms into the space. The ejected atoms then travel some distance until they reach the substrate being at the ground potential and start to condense into a film. Electrons released during argon ionization are accelerated to the anode, subsequently colliding with additional argon atoms, creating more ions and free electrons in the process, continuing the cycle. The strong magnetic field of a proper configuration present near the target area causes traveling electrons to spiral along magnetic flux lines near the target instead of being attracted toward the anode. The advantage of this is that the plasma is confined to an area near the target, without causing damages to the thin film being formed. Also, in such a way the electrons travel for a longer distance, increasing the probability of further ionizing argon atoms. This tends to generate a stable plasma with high density of ions near the target. More ions mean more ejected atoms from the target and, thus, increased efficiency of the sputtering process.

The cathode in this set-up is driven with a pulsed DC DORA Power Systems magnetron power supply, which has specific construction and characteristics. The power stage of the supply generates high voltage (1200V) pulses (85-100 kHz), current stabilized with group modulation at 0.1-4 kHz frequency (Fig. 3.4). Pulse duration modulation within group is controlled by a feedback loop to maintain constant current power. The supply responses to varying process conditions by change of number of pulses inside the group and by pulse peak voltage. Application of pulsed magnetron supply allowed for stable and repeatable conditions of the sputtering process

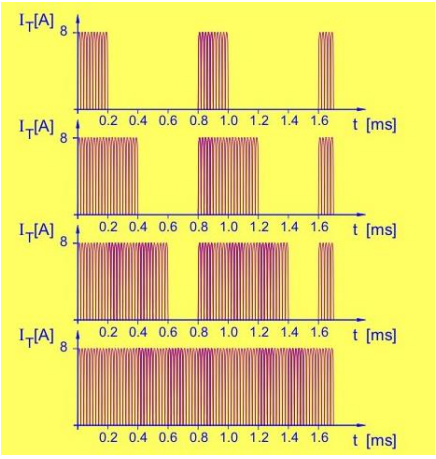

Fig. 3.4. Current signal for DORA DPS pulsed magnetron power supply [87].

For the power generated on the output two components are distinguished: the effective, which is the power transferred to plasma, and the circulating, which appears when the load impedance is unmatched (short circuit, change of the magnetic field, reactive process etc.). Monitoring of the circulating power may inform on the target surface state during the sputtering process.

3.2. Electric field aligned graphite composites with enhanced thermal conductivity

The anisotropy of composite material can be obtained by rearrangement of the filler particles in the liquid, uncured matrix by applying an aligning force. Properties of magnetic field aligned composites based on polymer resins and magnetic fillers, such as carbonyl iron [88], ferrite [89] and magnetite [90] were previously discussed. The aggregation of the filler particles into long, parallel chain-like structure enhances the effective thermal conductivity in the direction along the applied field. The alignment is poorer for higher filled (>40 vol. %) composites because the interparticle interactions becomes stronger than the influence of the external field. On the other hand, the enhancement of the thermal conductivity (TC of aligned composited compared to isotropic) is getting higher while increasing the filler content. This is because the distances between the filler particles become smaller thanks to the magnetic attraction and conduction paths can be created. In the case of graphite, its magnetic susceptibility is generally too low (-6.1×10^{-4} for *ab* plane and -1.4×10^{-5} for *c*-axis [91]) and strong magnetic field (9-16 T) would be necessary to use to generate magnetic torque and forces strong enough to achieve good alignment [92], [93]. However, literature reports successful alignment of nanotubes in high magnetic field [94]–[96] but no data for graphite/graphene structures are found. The presence of magnetic impurities, typically Fe, which is the most abundant element in graphite or graphene, may increase actual susceptibility and promote effective reorientation [92]. Many works were focused on alignment of carbon structures (nanotubes, graphene) decorated with magnetic nanoparticles of iron oxide (magnetite, maghemite, magnetite) [97]–[100]. Graphene nanosheets (GNS) functionalized with Fe_3O_4 were fabricated by coprecipitation method and aligned in epoxy resin under field of 0.3 T induction (Fig. 3.5). Effective thermal conductivity measurements show better performance of aligned composites. Samples conduct heat more efficiently along the direction parallel to the applied aligning field.

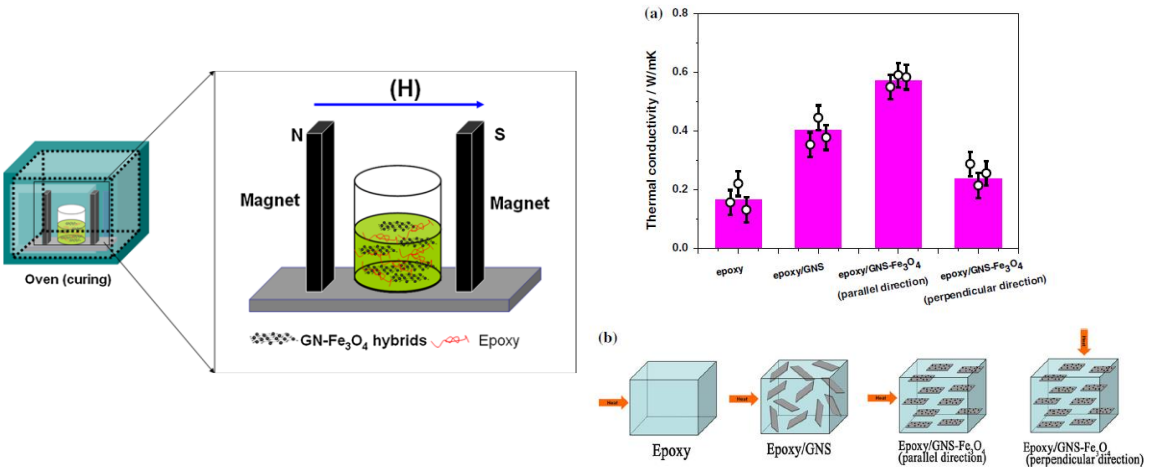

Fig. 3.5. A scheme for the synthesis of epoxy/GNS–Fe_3O_4 composites by magnetic alignment and thermal conductivity for pure epoxy and graphene nanosheets (GNS) measured in different directions [99].

Electric field-induced alignment approach is an efficient and direct route to prepare materials with aligned filler particles and has successfully been applied to reorientation of pure graphite/graphene flakes in liquid polymer resin matrix [101]–[106]. Both, alternating (AC) and direct current (DC) electrical fields with amplitude in the range of 20-200 V/mm can be used to orient the GNs. Under the electric field the graphite structures undergo a polarization. Because of the crystalline anisotropy the component of polarization parallel to the graphite layers is larger than the perpendicular one. Such a polarization leads to a field-induced torque (Fig. 3.6) acting on the flake. This torque rotates the graphite flakes against the viscous drag of the resin matrix in the direction of the electric field. In addition, Coulombic attraction is generated among the oppositely charged ends of different graphite flakes, causing formation of chain like structures [103].

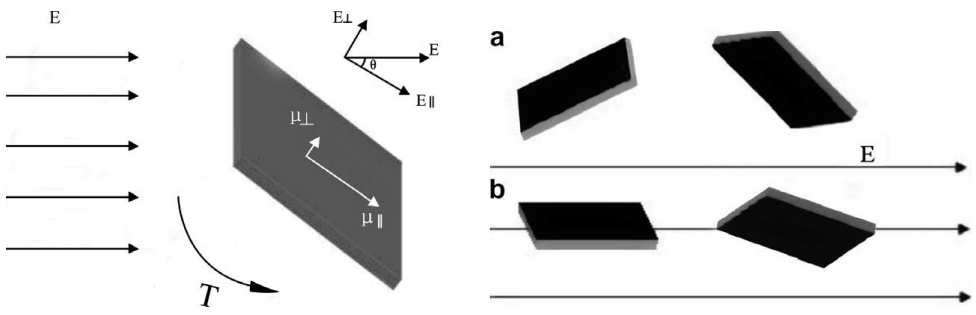

Fig. 3.6. Schematic illustration of polarization of a flake in the electric field. Cross-sectional schematic illustration of electric field-induced orientation of the GNs. [101]

It has to be noticed, that for graphite flakes, which are 2-dimensional structures, the alignment along the field direction does not mean, that the graphite plates are parallel to each other (Fig. 3.6). To achieve highly aligned composite, the process shown in Fig. 3.7 has to be applied. At the beginning, the graphite flakes were randomly dispersed in the polymer matrix (Fig. 4a). Directed by the first direction electric field, the graphite flakes were oriented along the electric field as an intermediate state (Fig. 4b). After being polarized by another electric field, the graphite flakes were highly aligned with their flakes parallel to each other (Fig. 4c). In practice, changing the direction of the field can be done by rotating of the electrodes or sample mold between them [102], [103].

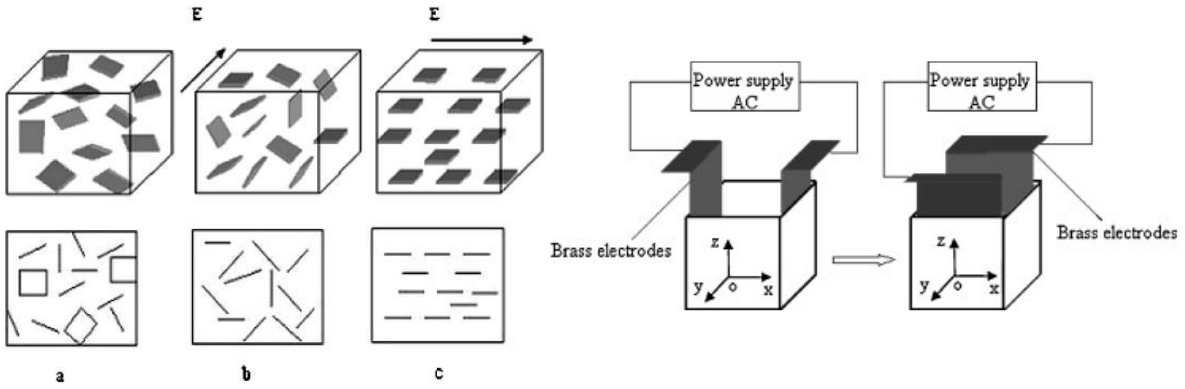

Fig. 3.7 Schematic illustration of alignment of graphite flakes induced by the electric field. (a), (b), and (c) exhibit the initial random state, intermediate state and aligned state, respectively [102].

Electrically oriented composites poses anisotropic transport properties (electric and thermal conductivity). Fig. 3.8 presents how the electrical resistivity of graphite filled composites depends on the filler content and direction of measurement. The resistivity along the plate plane is 2-3 orders of magnitude lower than perpendicularly to it. Usually, the structure anisotropy is evaluated using X-ray diffraction method, because of the fact, that the peak intensity depends on the sample texture. In the case of graphite plate-like structures, the <002> line intensity is boosted when the radiation scattering vector is perpendicular to the alignment direction. This indicates ordering of the flakes with their planes along the alignment direction. For well aligned materials, big differences in the <002> reflection intensity for different sample orientation are observed (Fig. 3.9).

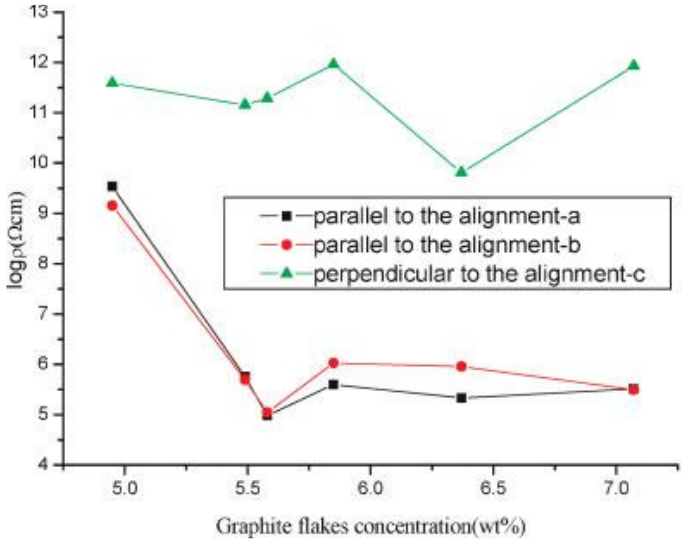

Fig. 3.8. Resistivity of the composites with the anisotropy induced by the alignment of the conductive graphite flakes [102].

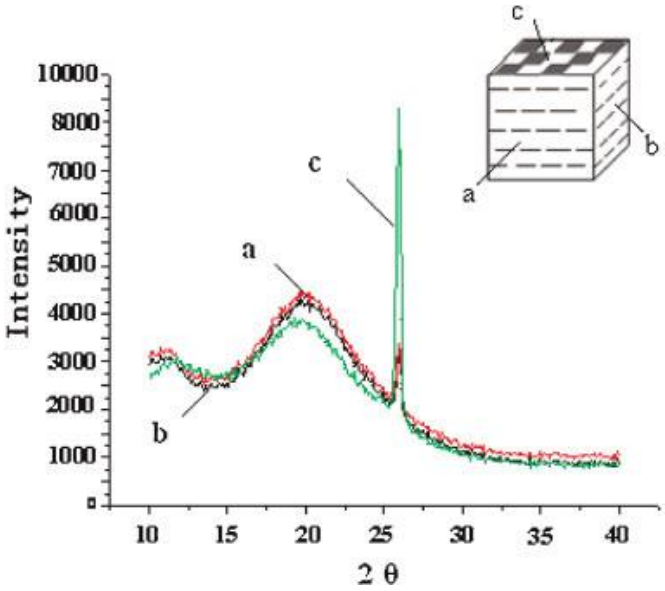

Fig. 3.9. XRD patterns for different planes of the aligned composite containing 5.0 wt. % graphite flakes. (a) and (b) show that the planes of graphite flakes in the sample were mostly parallel to the X-ray scattering direction during measurements; (c) represents the perpendicular sample plane case [102].

Experimental setup for sample preparation was designed and constructed at the AGH University. It consists of (Fig. 3.10):

- high dc voltage supply – based on high frequency, pulse transformer, producing adjustable voltage in range 200 – 1300 V,

- copper electrodes – rectangular plates, separated by 15mm distance, providing uniform electrical field, like in a flat capacitor,
- PTFE molds for composites – they allow to cast cylindrical samples with 6mm diameter and 6-10 mm height,
- Electric motor – rotates the molds with 6 rpm speed to obtain uniform alignment.

The device was supplied from 9 V rechargeable battery and was designed to work inside argon filled chamber.

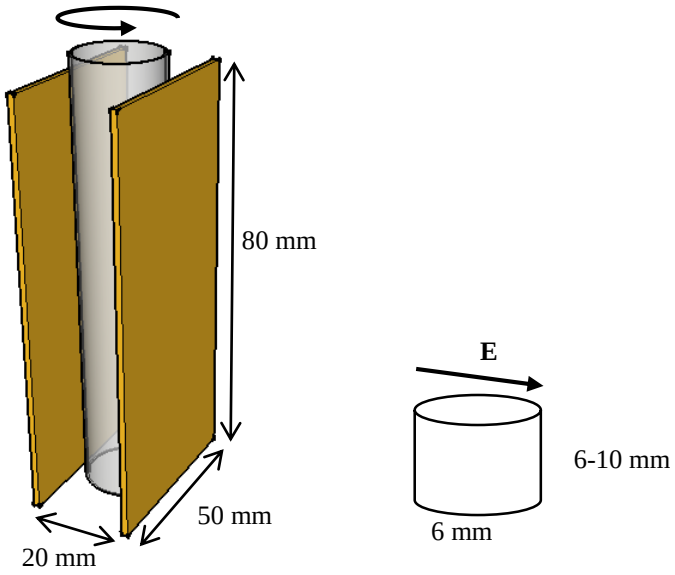

Fig. 3.10. Scheme and photo of the setup constructed for aligned composites fabrication.

Composites were manufactured from flake graphite, magnesium hydride and silicone resin. A detailed description of their properties is presented in paragraph 3.4. The experimental procedures are as follows: at first, the proper amounts of uncured silicon resin, filler powders and a thinner are mixed for 15 min (Fig. 3.11a). Using thinner, which is a silicone oil, is necessary to reduce high viscosity of resin in order to get better wetting of filler grains and to get easy castable mixture. Then hardener is added to the pot and mixed again for 15 min (Fig. 3.11b). Next, the most important step is the curing of the resin (Fig. 3.11). The mixture is transferred to the PTFE molds, placed between parallel copper electrodes And connected to high voltage supply of 1.2 kV generating uniform electric field of intensity 80 V/mm passing cross the sample. Electric motor rotates the sample with 6 rpm speed to obtain high and uniform alignment. The curing process is performed in room temperature and it takes 24 hours. High voltage and rotation are on during entire process. The last step is outgassing of the hardened

composite (Fig. 3.11d) in vacuum at the temperature of 80 °C for 24 hours in order to remove remaining, non-cured of the sample. After that samples are cut and closed in argon-filled, sealed containers.

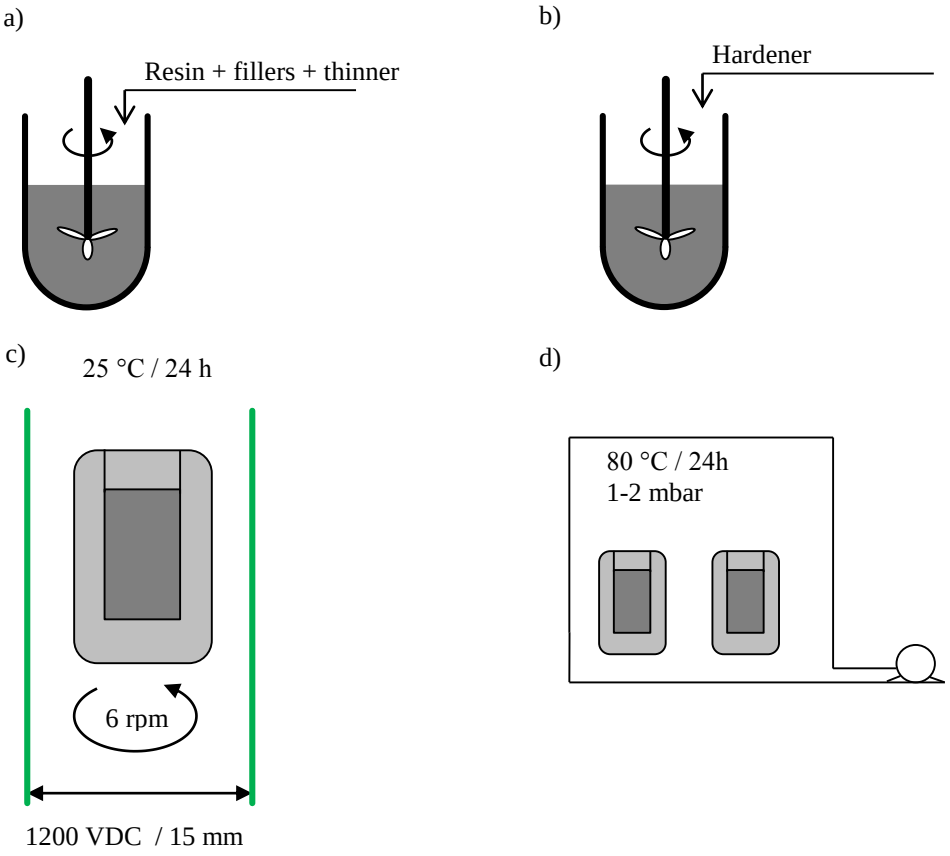

Fig. 3.11. Sample preparation method for electric field aligned graphite composites.

3.3. Methods of characterization

X-Ray diffractometry

The microstructure of coated powders and composites was examined by X-Ray diffraction method. Its principle is based on Bragg's law. A monochromatic X-ray beam, typically Cu- Kα radiation with wavelength λ=1.5406 Å, is directed to the surface of the sample at a Bragg angle θ. This incident beam is diffracted by the atomic planes of the crystalline sample. The diffracted beam is then monitored by a moving detector measuring the reflexes at the θ angle, corresponding to different plane spacings, d. These are derived from the observed reflections through Bragg's equation:

$$n\lambda = 2d \sin\theta$$

Fitting and simulations of crystal structure to the experimentally obtained XRD peaks using Rietveld refinement method [107] provides a wide range of information about the sample phase composition, lattice constants and strain , crystallite size, orientation, etc.) Full fitting results (data, calculated profile, background and difference plots) are listed in the Appendix. In this work Rigaku Smartlab machine was used for the measurements [108]. It is equipped with 3 kW sealed X-ray tube with 20 – 60 kV accelerating voltage and a high resolution 2D detector. Measurements were performed at room temperature, with 2θ in the range of 10-120° and with 40 kV voltage.

Scanning Electron Microscopy and Energy Dispersive Spectrometry

Scanning electron microscopy works by moving the electron beam (Thermionic or Field emitted), accelerated with high voltage (~30 kV) and confined with magnetic lenses, across the surface of a sample. The interaction between electrons and the sample material results in emission of different radiation and particles, including secondary electrons, backscattered electrons and X-rays. Low energy (<50 eV) secondary electrons, coming from inelastic scattering of the beam electrons from the area of few nanometers depth from the sample surface, provide information about the sample topography (SEI – Secondary Electrons Image). The electrons are detected by a scintillator-photomultiplier detector. The brightness of the signal depends on the number of secondary electrons reaching the detector. If the beam scans the sample perpendicular to the surface, the activated region is uniform about the axis of the beam and a certain number of electrons "escape" from this region the sample. As the angle of incidence increases, the interaction volume increases and the "escape" distance of one side of the beam decreases, resulting in more secondary electrons being emitted from the sample. Thus, steep surfaces and edges tend to be brighter than flat surfaces, which provides a well-defined image of surface topology. Backscattered electrons images (BEI) give information about sample composition according to the Z-number of scattering element. They are used to detect contrast between areas with different chemical compositions. High-energy electrons originating from the electron beam, are reflected or backscattered from the sample by elastic scattering interactions with specimen atoms. The heavy elements (high atomic number Z) backscatter electrons much more effectively than light elements and appear brighter in the image. Detection of BSE is limited in SE detectors because of energy and emitting angle range, and, to overcome this problem, dedicated backscattered electron detectors are used. They are positioned above the sample in a toroidal arrangement, concentric with the beam. When all parts of the detector

are used to collect electrons symmetrically about the beam, atomic number contrast is produced. It is possible to use asymmetric, directional detector to produce topographic images. Backscattered electrons can also be used to form an electron backscatter diffraction (EBSD) image that can be used to determine the crystallographic structure of the specimen.

An important method connected with SEM is the elemental analysis of characteristic X-rays from the specimen with Energy-dispersive X-ray spectroscopy (EDS, EDX). The incident beam excites an electron from inner atomic electron shell, ejecting it and creating an electron hole. Then, an electron from an outer, higher-energy shell fills the hole, and the difference in energy between two shells is released in emitted X-rays. Energy and intensity of the X-rays emitted from a specimen can be measured by an energy-dispersive or wavelength dispersive spectrometer. As the emission lines are characteristic for the emitting element, EDS allows the elemental composition of the specimen to be analyzed. By scanning the beam in a television-like raster and displaying the intensity of a selected X-ray line, element distribution images or "maps" can be produced. The accuracy of quantitative analysis of the sample composition is possible, however, it requires the application of correction procedures, which are sometimes referred to as matrix corrections. Three main effects need to be taken into account and to be corrected (called ZAF correction):

- Atomic number effect (Z) - penetration range of electrons into the specimen and the X-ray intensities depend on the atomic numbers of the elements.
- Self-absorption effect (A) - measured X-ray intensities are a function of the escape depth and of the absorption characteristics of the specimen. Especially, for the specimens with higher Z and the X-rays at lower energies, this correction becomes even more important.
- Fluorescence effect (F). - X-ray emission of low-Z elements (with low energy X-rays) is increased because of the presence of radiation of high-Z elements (with characteristic X-rays of a high energy) and the concentration of the low-Z elements can be overestimated, while the concentration of the high-Z elements can be underestimated.

In this work two types of SEM equipment were used: Thermionic emission JSM-5900LV type and field-emission JSM 7100F. Basic parameters of both systems are described in Table 3.2. Two types of samples were used: plain powders and cross-sections of powders and composites suspended in epoxy resin. Plain powders were stick to conductive carbon tape and placed directly on the sample holder. Observation of their surfaces, as well as EDS analyzing of panoramic view was performed. EDS element mapping, performed on chosen powder particles allowed us to determine the uniformity of the coating. In order to measure the thickness and

morphology of the layers, SEM images and EDS line scans of cross sections of powder grains were taken. Powders were prior suspended in liquid epoxy resin, then cured and polished with series of different grades sandpapers and diamond pastes. After outgassing and coating with conductive carbon layer samples were ready for the measurements. The same process was performed for preparation of composite samples.

Table 3.2. Basic parameters of scanning electron microscope systems used for sample characterization

Type	JSM-5900LV	JSM-7100F
Resolution	3 nm (30 kV, SEI) 5 nm (30 kV, BEI)	1.2 nm (30 kV, SEI), 3.0 nm (1 kV, SEI)
Magnification	×180 to ×300 000	×10 to ×1 000 000
Accelerating voltage	0.3 to 30 kV	0.2kV to 30kV
Specimen stage	8" max., 125 mm X, 100 mm Y Tilt: -10 to +90°, Rotation: 360°	5 axes specimen stage X-Y: 70 mm to 50 mm, Z: 3 mm to 41 mm Tilt: -5 to +70°, Rotation: 360°

Thermal transport measurements with Physical Properties Measurement System.

Thermal conductivity measurements for composite samples were performed by means of PPMS (Physical Property Measurement System) manufactured by Quantum Design Inc., using thermal transport option (TTO). Its basic parameters are listed in the Table 3.3. The cylindrical or cuboid sample is mounted in two probe configuration, with two copper leads glued to the parallel base planes by the electrically and thermally conductive epoxy adhesive. One lead is connected to the heater and hot thermometer, the opposite one - to the cold foot (ground) and the cold thermometer. Heat is provided by Joule heating and time response of two thermometers is monitored. Four point probe configuration is also available to use. Additionally, electrical resistivity measurements are possible to make. Current pulse (I+/-) flowing through the sample was monitored using leads (V+/-).

Table 3.3. Basic parameters of Thermal Transport option of the PPMS apparatus [109].

Thermal Conductivity	0.03 to 100 W/m·K
Thermal Diffusivity	Correlating limit mm2/s
Specific Heat Capacity	Correlating limit MJ/m3K
Measurement Time	2.5 to 640 seconds
Reproducibility	Typically better than 2%
Accuracy	Better than 5%
Temperature Range	Cryogenic to 200 °C
Min. Sample Dimensions	3 mm High, 13 mm Diameter or Square.
Sensor Types Available	Kapton insulated with or without cable (from cryogenic temperatures up to 180 °C).

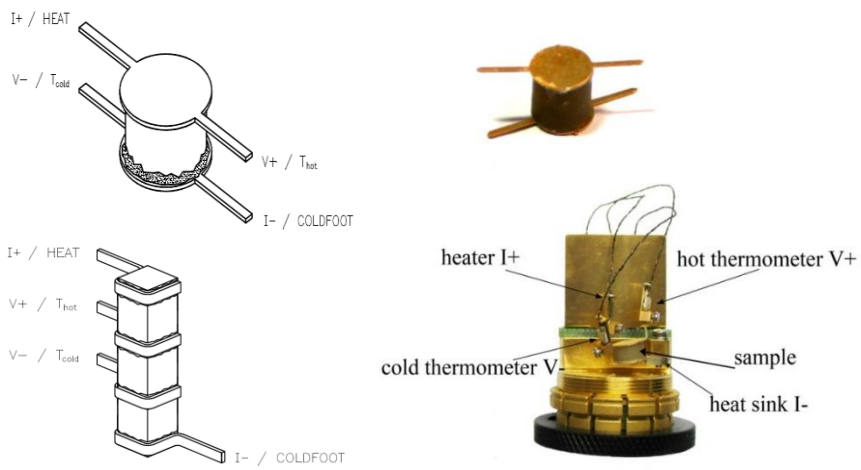

Fig. 3.12. Sample puck with thermal and electrical connections [110]

The thermal conductivity measurements have been performed using longitudinal steady-state method in the high vacuum conditions (10^{-4} Torr) at room temperature and additionally in temperature dependence from 4K to 300 K. During measurements the software uses algorithms which help to optimize parameters such as heater power or heat pulse duration. After the constant power heat pulse is applied (Fig. 3.13), the temperatures on both, the hot and the cold thermometers, as well as the sample chamber temperature is measured during the pulse duration and during cooling time. Within the heat pulse lifetime the temperature difference between the leads ΔT vs time is calculated using least-squares fitting routine and the equation below:

$$\Delta T = \Delta T_{\infty}\left(1 - \frac{\tau_1 e^{-t/\tau_1} + \tau_2 e^{-t/\tau_2}}{\tau_1 + \tau_2}\right)$$

where ΔT_{∞} represents the asymptotic temperature drop across the sample, τ_1 and τ_2 are the long and short time constants. The heat flux cannot be measured directly. The conducted heat through the sample is presented as the power in the heater resistor I^2R with the radiation losses on leads subtracted. Radiation loses are calculated with the Stefan-Boltzmann low:

$$P_{rad} = \sigma_T \frac{S}{2} \varepsilon (T_{hot}^4 - T_{cold}^4)$$

where S is total surface area, ε – infrared emissivity of the radiating surface, $T_{hot/cold}$ - temperatures of thermometers during measurements, σ_T - Stefan-Boltzman constant. Finally, the thermal conductivity is calculated using conducted heat, sample length and cross-section area and the asymptotic temperature drop:

$$\lambda = \frac{I^2R - P_{rad}}{\Delta T_{\infty}} \frac{l}{S}$$

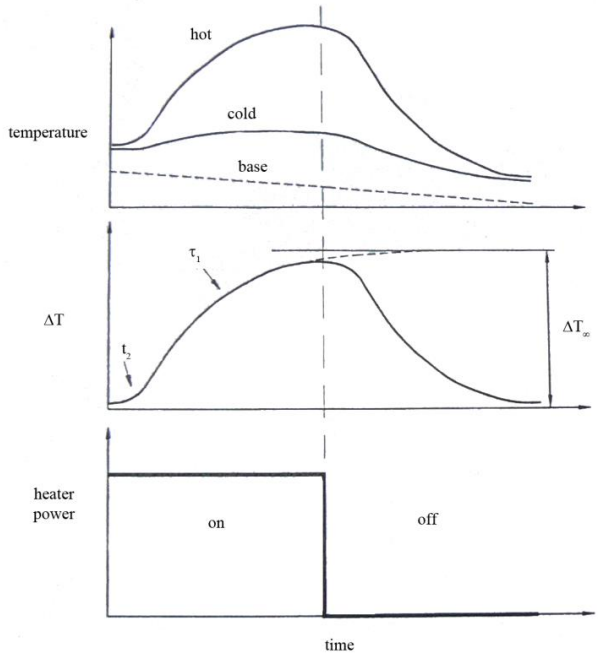

Fig. 3.13. Heat pulse, temperature response at the hot and the cold thermometer shoes in an idealized sample [110].

Thermogravimetry

Amount of hydrogen released from the material can be measured using thermogravimetric method (TG). The mass of the sample is continuously measured while its temperature is changed over the time. A typical thermogravimetric analyzer consists of a precision balance with a sample pan located inside a furnace. It is usually sealed, which allows to use vacuum or gas atmosphere, typically neutral argon, but for some applications, reactive gases such as oxygen or hydrogen are used. The thermogravimetric data (mass, temperature, and time) are collected and plot of mass versus either temperature or time is drawn and referred as TG curve. Differential thermal analysis (DTA) is often coupled with TG experiments. A small amount of reference material (Al_2O_3) is placed next to the sample, under the same conditions and the difference of the temperature between sample and reference is measured by very accurate thermocouples. The signal (expressed as voltage difference in μV) is plotted versus the temperature or time and informs us about changes in the sample, either exothermic or endothermic, such as e.g. glass transitions, decomposition, crystallization, melting, etc.

An ULVAC TGD9600 [111] apparatus was used. The samples consist of 20 mg of material, placed in Al_2O_3 cup under constant high purity argon flow. The temperature is generally increased at a constant rate, typically 5 K/min.

Differential Scanning Calorimetry.

A Differential Scanning Calorimetry (DSC) measures the difference in heat flux going into and out of a sample and the reference material during the heating with programmed temperature run. It provides an information about the exothermic and/or endothermic nature and thermodynamics of a process. It generally consists of one or two furnaces with controlled atmosphere and temperature. The samples and reference material (Al_2O_3) is placed inside aluminum or copper pans, usually sealed by crimping. Two types of the DSC approaches are used:

- Heat Flow (or Power Compensation) DSC – the temperature difference between the sample and reference is maintained constant during the scan. The resulting power difference is proportional to heat flow. It generally uses two independently heated furnaces – when a heat-consuming process takes place in the sample, the sample furnace increase the heating power to keep the temperature program. The signal measured in this type of apparatus is the heating power.
- Heat Flux DSC – Single furnace, the temperature difference is allowed to vary, and the temperature difference signal is converted to heat flow through the mathematical calculations, knowing the thermal resistance of the transducer.

A power compensation instrument can generally heat or cool faster (>200K/min), and provides better resolution for sharp peaks, but the signal is less stable, the baseline is less flat and the short-term noise is higher. A heat flux instrument cannot achieve the rapid scan rates of a power compensation design, but baseline is usually straighter and more stable, providing higher sensitivity for subtle events. While DSC measurements are often used for directly reporting the enthalpy values of hydrogen storage reactions, the process of extracting accurate information is often complicated by the multi-phase nature of the reaction, which can involve simultaneous heat and mass transfer (release/uptake of H_2 gas) events.

The laboratory equipment used was a heat flux Shimadzu DS-60 Differential Scanning Calorimeter [112]. Its basic parameters are listed in Table 3.4. Samples of 1 mg of hydride were sealed in aluminum pans in argon-filled glove box chamber. DSC scan was performed from room temperature to 500 °C with typically 5 °C/min heating rate. For chosen samples,

measurements with different heating rate (1-20 °C/min) were done in order to estimate the activation energy for hydrogen on the metal surfaces using the Kissinger method [113], [114].

Table 3.4. Basic parameters of the differential scanning calorimeter [112].

Heat Flow Range	± 40μW
Hold Time	0 - 999 min, hour
Noise level	1μW
Temperature Range	-150 to 600 ° C
Program Rate	0 – 99 K/min, K/hour
Cooling Time	about 6 min from 600 °C to 40 °C with LN_2
Atmosphere	Inert gas or air

Study of hydrogen absorption/desorption with Sievert's type apparatus.

An important part of this work are measurements of hydrogen desorption performance done with volumetric Sievert method [115]. This method allows us to determine the amount of hydrogen absorbed or released from material under equilibrium conditions, as well as to observe the reaction kinetics. The equipment (Fig. 3.14) consists of a set of reference tanks (called the dosing or reference) of known volume V_{ref}, and sample chamber with volume V_{cell}. The volume V_{cell} is calculated as the difference between the volume of empty chamber and volume of the sample. Both volumes are connected by the valve V_S.

The system is complemented with vacuum pumps, pressure sensor and hydrogen tank. The measurement starts with removing of the air by vacuum pumps and checking if there aren't any leakages in the system. Next, a dose of hydrogen is let into the reference tank until reaching given pressure p_{ref}. The sample chamber pressure p_{cell} is the pressure obtained by vacuum pump (first step) or the equilibrium pressure from previous step. The valve separating the sample from the system (V_S) opens and the pressure in the system changes, and reaches a stable level p_{sys}. After the system reached equilibrium the amount of hydrogen adsorbed or desorbed can be calculated from real gas equation. The molar amount of gas n is given by:

$$n = \frac{pV}{zRT}$$

where p is the pressure, V the gas volume, T gas temperature, z the compressibility factor and R is gas constant. Thus, the amount of hydrogen reacted in a single step is calculated as:

$$\Delta n = \frac{p_{sys}\left(V_{cell} + V_{ref}\right)}{zRT} - \frac{p_{cell}V_{cell} + p_{ref}V_{ref}}{zRT}$$

At the end of each step, the valve is closed, and the reference volume is prepared with a new amount of gas for the subsequent step. Changing pressure in the chamber requires expansion or

compression of the gas but this causes temperature changes due to the partly adiabatic conditions. The heated or cooled gas returns to the original temperature through contact with the walls of the pipes and the tanks. A suitable time delay for temperature equilibration is needed to be set.

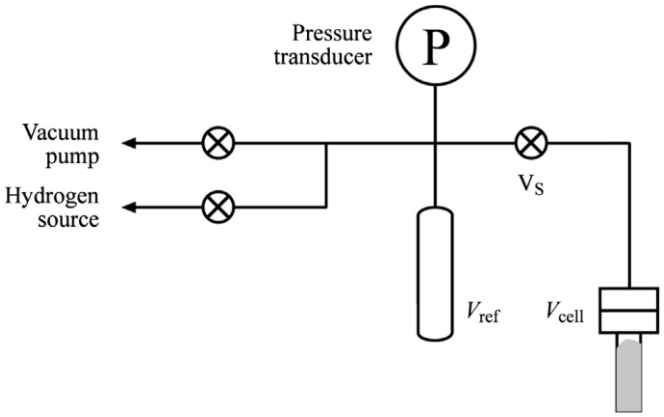

Fig. 3.14. A simplified scheme of Sieverts apparatus [115].

Sieverts apparatus allows us to observe reaction kinetics by plotting the amount hydrogen reacted versus time, to perform cycling of hydrogenation/dehydrogenation reaction or to obtain Pressure-Composition-Temperature (PCT) curves in order to analyze the thermodynamics of the active material. The experimental procedure involves a series of small step-change in pressure and allows us to establish the equilibrium in each step (Fig. 3.15a). Then, the data points of different hydrogen content from zero to full capacity are obtained until the full PCT curve is shown (Fig. 3.15b). In the next step, the series of similar experiments are performed for a set of temperatures (Fig. 3.15c). Finally, using middle points of the plateau regions the van't Hoff plot is constructed (Fig. 3.15d). The above steps are repeated both for adsorption and desorption process.

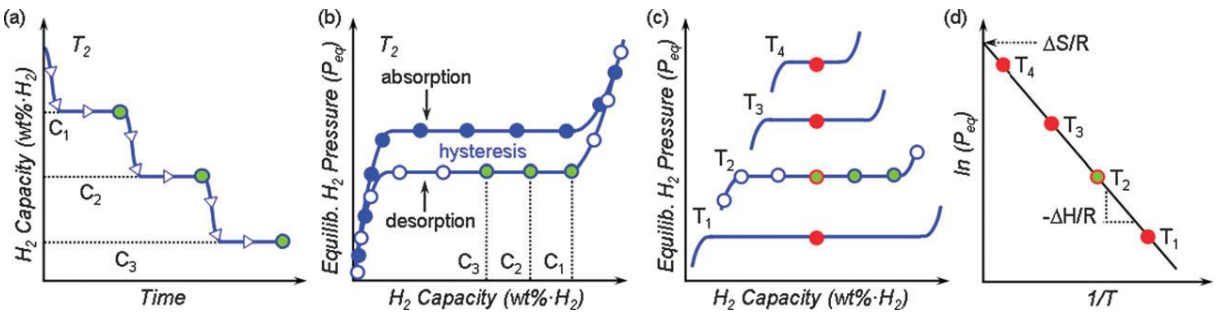

Fig. 3.15. Schematic summary of the experimental determination of thermodynamic properties using pressure-composition isotherms [10].

In this work, two types of machines were used. For kinetics and cycling test the Japan Metals & Chemicals Co. Ltd (JMC) manufactured one [116] and for PCT measurements a Setaram PCT-Pro [117] apparatus were used. The experimental procedures are as follows:

- Kinetic and cycling:
    1. Preparation of 150-200 mg samples under argon atmosphere.
    2. Removing air with vacuum pumps for 1 hour, until 10^{-2} mbar vacuum is reached.
    3. Filling the system with 7 bars of hydrogen and pumping again in order to remove the residual gases. This step was repeated three times.
    4. Filling the system with 15 bars of hydrogen and monitoring the pressure for 30 min to detect eventual leakage.
    5. Activation of the hydride sample at 300 °C for 12 hours in continuous vacuum.
    6. Measurements of absorption/desorption/cycling at the temperature of 300 °C with initial pressure of 1 MPa and 0.001 MPa for absorption and desorption respectively. Measurements were continued until the equilibrium was reached and sample was fully hydrogenated/dehydrogenated at given conditions.
- PCT curves:
    1. Preparation of ~30 mg samples under argon atmosphere.
    2. Flushing with helium gas and pumping for 30 hours.
    3. Activation of the hydride sample at 300 °C in continuous vacuum.
    4. Collecting of PCT curves for temperatures from 300 °C to 340 °C and pressures from 0.1 to 100 MPa. For single data point on the PCT plot it takes from 5 min. to 30 min. to reach the saturation level.

3.4. Characterization of starting materials

Flaked graphite

Graphite powder, a MG-1599 grade was purchased in Sinograf company [118]. It contains at least 99.5 wt. % of pure carbon and consist of 10 μm flakes (Fig. 3.16). Main impurity fraction represents silicon, which is not typical for natural based graphite, where iron is the most commonly occurring element. Crystal structure parameters obtained from the Rietveld refinement of XRD patterns (Fig. 3.17) are consistent with the literature data The pattering is characterized of strong c-plane reflection near 27º and the lattice parameters are 2.46 Å and º6.71 for hexagonal cell.

Table 3.5. Impurities in graphite powder [119].

Element	Content [wt. %]	Element	Content [wt. %]	Element	Content [wt. %]
C	99.5 — 99.99	Ca	0.0 — $5.0E^{-5}$	Pb	0.0 — $1.0E^{-5}$
Si	0.0016	Cr	0.0 — $5.0E^{-5}$	Sb	0.0 — $1.0E^{-5}$
Mo	$1.2E^{-4}$	Fe	$3.2E^{-5}$	Zn	0.0 — $1.0E^{-5}$
V	$8.1E^{-5}$	Al	$1.0E^{-5}$	Co	0.0 — $5.0E^{-6}$
S	$8.1E^{-5}$	Cu	0.0 — $1.0E^{-5}$	Ni	0.0 — $5.0E^{-6}$

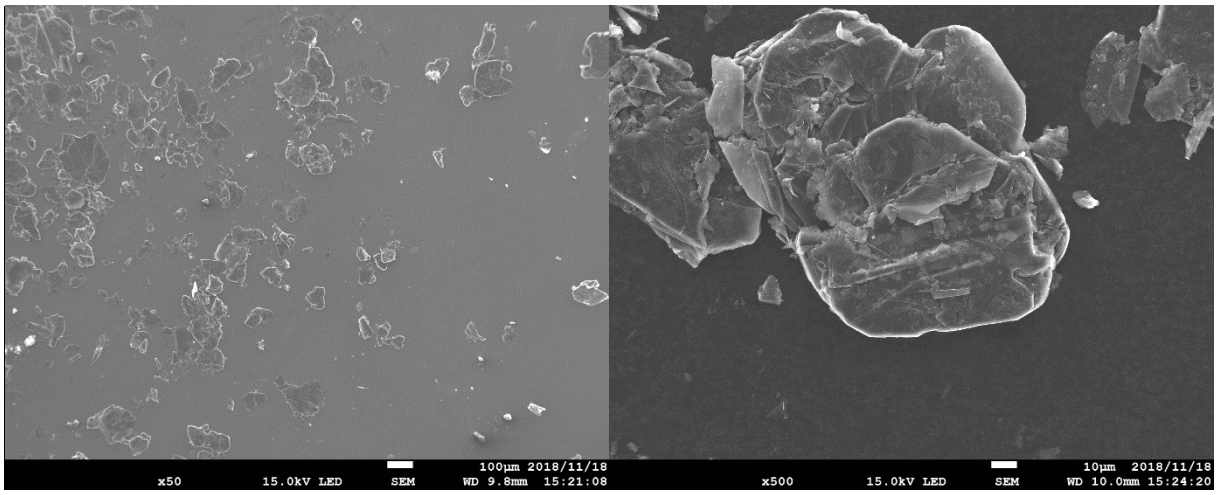

Fig. 3.16. SEM image of graphite powder used.

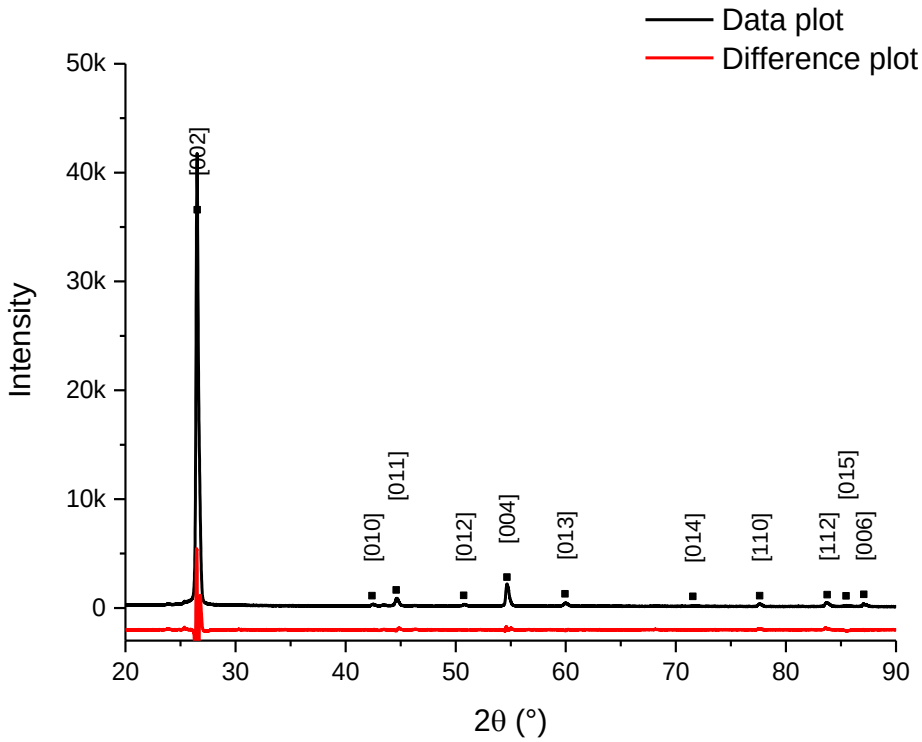

Fig. 3.17. XRD pattern of MG1599 graphite used as high thermal conductivity dopant

Magnesium hydride

Magnesium hydride was purchased from Bio Coke Lab company. It was used in powder form, with nearly Gaussian grain size distribution of average size around 95 µm, however there is large fraction of small (< 30 µm) particles present (Fig. 3.18). The grains have very irregular shape. The surface of the grains is also decorated with small grains, which can belong to small particles fraction or be the effect of oxidation occurring during SEM sample preparation.

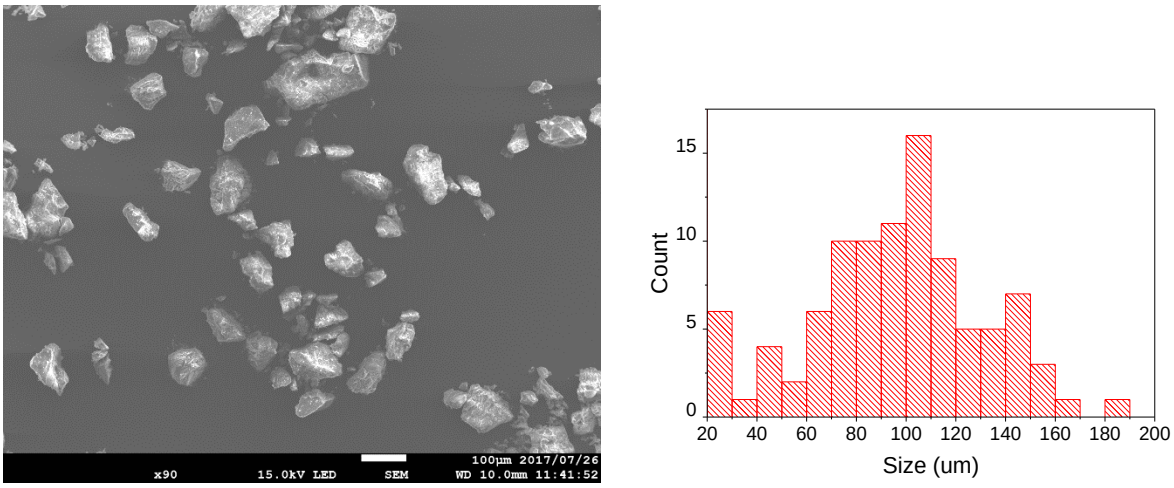

Fig. 3.18. SEM images of the pure magnesium hydride powder and its grain size distribution.

The EDS spectra (Fig. 3.19) measured on panoramic view show only small signals from aluminum and silicon impurities - elemental analysis estimates their content at below 0.2 wt. %.

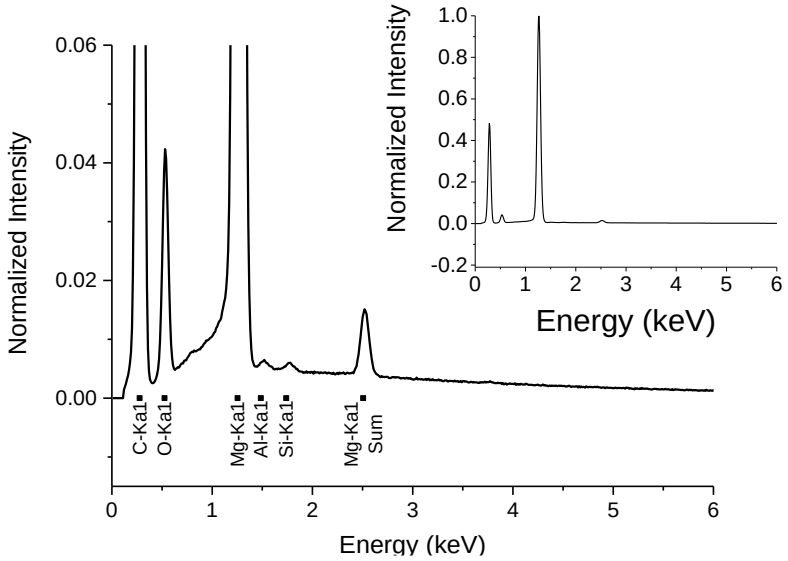

Fig. 3.19. EDS spectrum of the as received magnesium hydride

X-ray diffraction patterns (Fig. 3.20, Table 3.6) were collected for the as-received material. The results suggest, that there is a small amount of unreacted magnesium (~2 wt. %) remaining in the material. No visible oxidation effects are present. The peaks of the hydride phase are sharp, which suggest low amount of defects and stress inside the sample grains. Crystal structure parameters are consistent with the literature data – our magnesium hydrides consist of pure tetragonal β-MgH_2 phase.

Table 3.6. Rietveld refinement results for pure, as received magnesium hydride powder.

Phase	Parameter	Value	Error
MgH_2	Content [wt. %]	97.9	
	a [Å]	4.51633	0.00005
	b [Å]	4.51633	0.00005
	c [Å]	3.02040	0.00005
Mg	Content [wt. %]	2.1	
	a [Å]	3.2118	0.0002
	b [Å]	3.2118	0.0002
	c [Å]	5.2113	0.0006

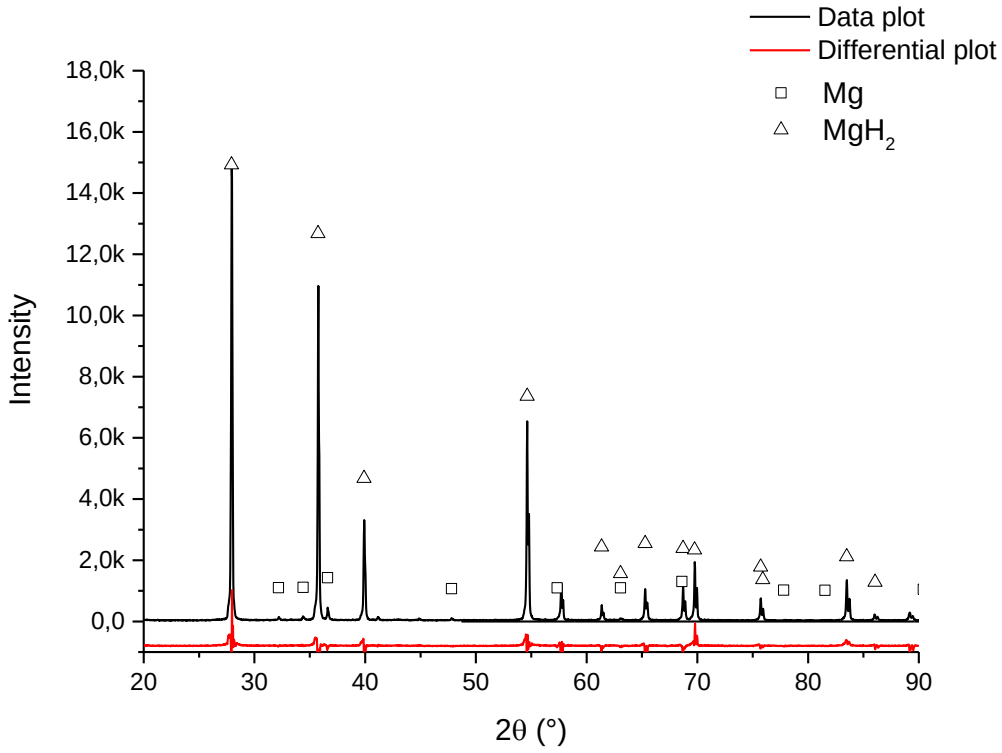

Fig. 3.20. XRD pattern of the magnesium hydride from Bio Coke Lab company.

The decomposition temperature, one of the most important parameters of the hydride, was evaluated using two methods: DSC and TG (Fig. 3.21). From thermogravimetry we know that magnesium hydride starts to decompose near 400 °C and the amount of desorbed hydrogen is

close to the theoretical capacity. Differential scanning calorimetry shows a sharp decomposition peak above 460 °C.

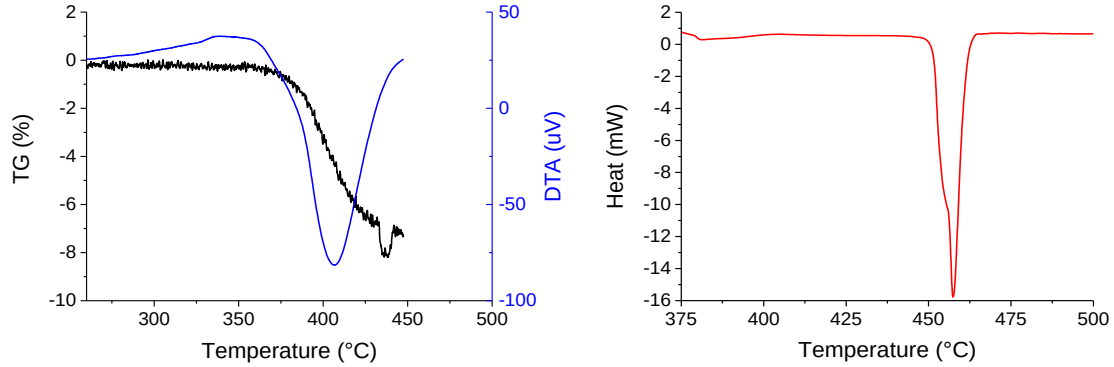

Fig. 3.21. DSC and TGA curves of the pure, as received, magnesium hydride.

Decomposition peaks on DTA and DSC curves are shifted because of slightly different measurements setups. DTA (on TG device) uses open alumina pans with continuous argon gas flow, whereas DSC samples are sealed in closed aluminum containers. In result, during thermogravimetry experiment the pressure stays nearly constant, but when the calorimetric scan is taken pressure growths because of the hydrogen release, which increases effective decomposition temperature. Moreover, when the decomposition of MgH_2 occurs, the temperature varies (usually drops) due to large amount of heat absorbed by the decomposing hydride. Together with possible unsealing of sample cells it causes that strongly asymmetrical and double decomposition peaks are present in the temperature plot.

Part of the experiments was carried out using ball milled magnesium hydride (BM-MgH_2). Powders were milled using rotary mill with 10 mm diameter steel balls, with 1:10 powder/ball ratio. Mill speed was set to 300 rpm and after each 30 min. of milling the process was paused for 30 min. in order to prevent the powder from overheating. 20 cycles were performed, which gives 10 hours of total milling time. The results of the X-ray diffraction measurement and pattern refinement are presenten on Fig. 3.22 and Table 3.7. MgH_2 reflections are charactersited with wider peaks what suggests reduction of the crystalline size and introduction of strains during the milling. Williamson-Hall analysis shows reduction of the crystalline size from 1880 nm to 278 nm due to the milling. Except of the tetragonal β phase, orthorhombic γ-MgH_2 phase, with 5.8 wt. % content is present. A partial oxidation occurs during the milling, but the mount of the MgO do not exceed 5 wt. %.

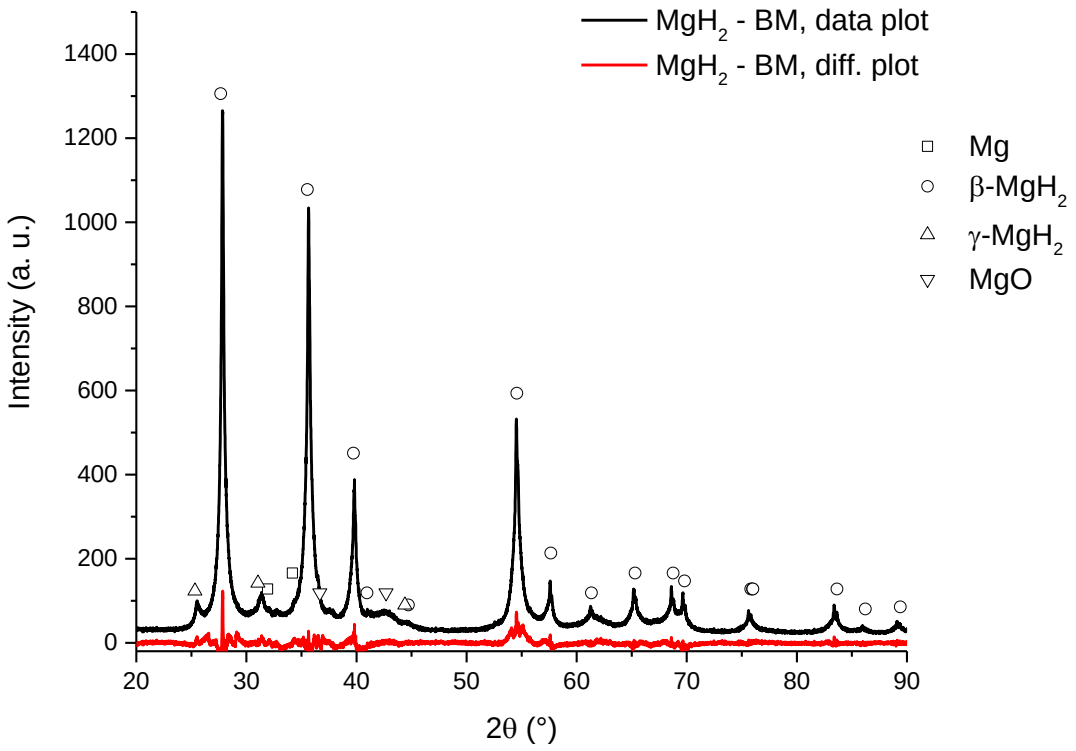

Fig. 3.22. XRD pattern of the magnesium hydride after the ball milling.

Table 3.7. Rietveld refinement results for ball milled magnesium hydride.

Phase	Parameter	Value	Error
β-MgH_2	Content [wt. %]	86.2	
	a [Å]	4.517	0.002
	b [Å]	4.517	0.002
	c [Å]	3.020	0.001
γ-MgH_2	Content [wt. %]	5.8	
	a [Å]	4.531	0.003
	b [Å]	5.389	0.004
	c [Å]	4.987	0.007
Mg	Content [wt. %]	2.9	
	a [Å]	3.251	0.003
	b [Å]	3.251	0.003
	c [Å]	5.122	0.004
MgO	Content [wt. %]	5.0	
	a [Å]	4.217	0.003
	b [Å]	4.217	0.003
	c [Å]	4.217	0.003

SEM photos were taken in order to study the particle shape and size. Fig. 3.23 shows that a wide distribution of particles can be found after the milling. Nanoparticles of MgH_2 are mixed together with their agglomerates and bigger, not milled grains. A Surface of such grains is usually decorated with a smaller nanoparticles. Size distribution, obtained using the computer software from the first picture of big grains and agglomerates, possesses maximum near 10 μm

(Fig. 3.24). On the other hand, when analysing a close-up photos of nanoparticles, their average grain size stay around 130 nm. A wide size distribution and the agglomeration tendency may affect on the sputtering process and the uniformity of the coating.

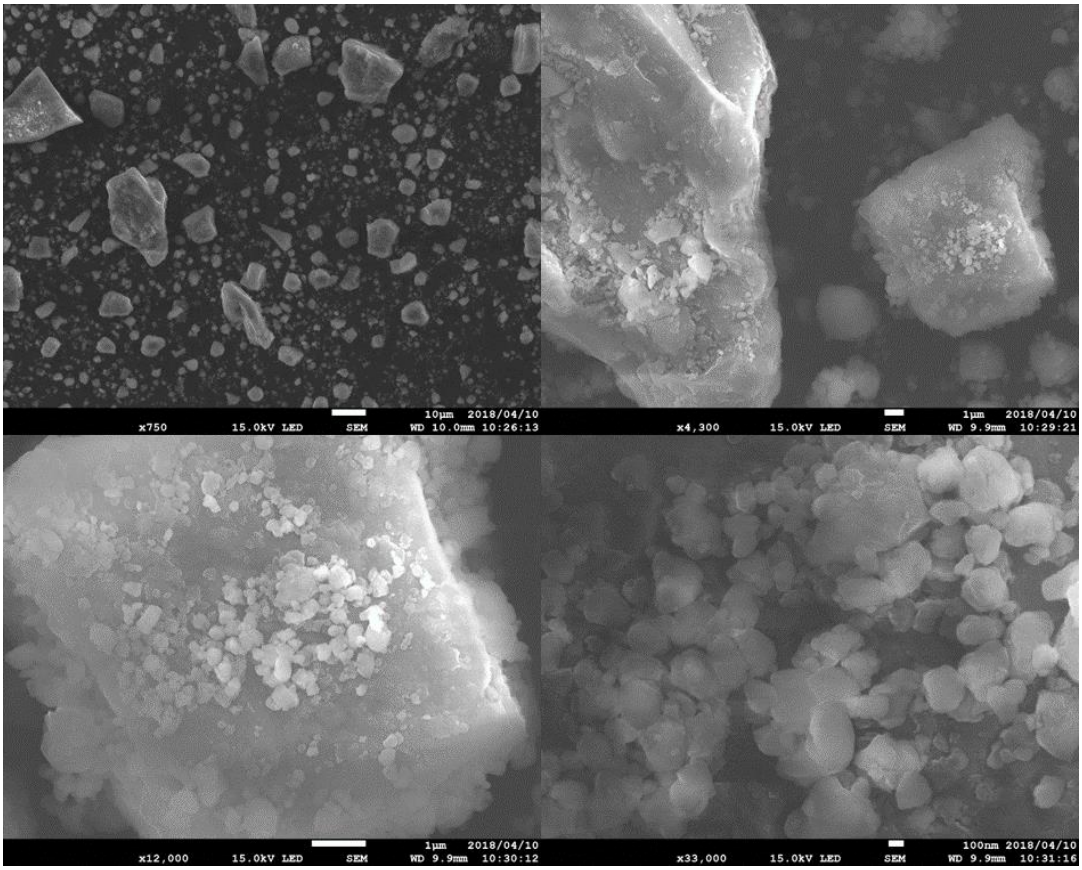

Fig. 3.23. SEM images showing ball milled powder of MgH_2 under the different magnifications.

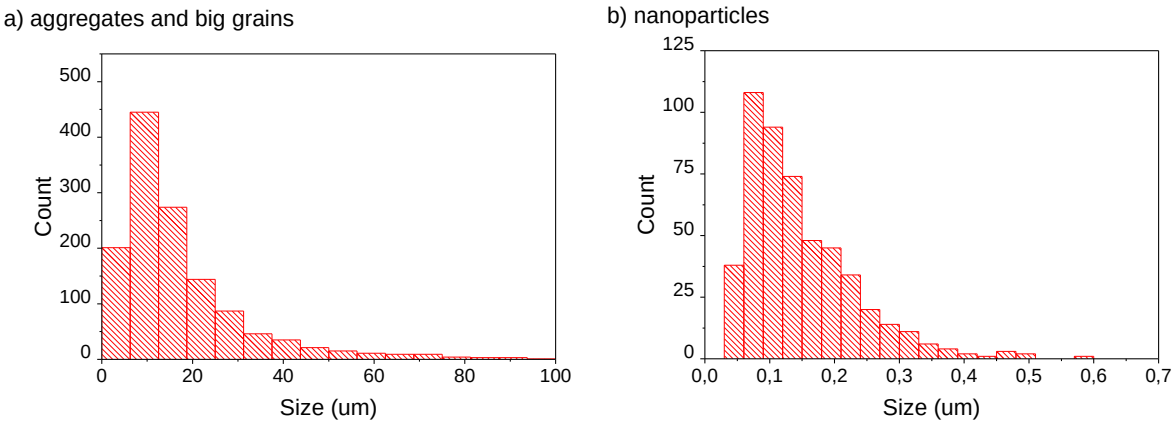

Fig. 3.24. Particle size distribution of the ball milled magnesium hydride, obtained from SEM images of agglomerates (a) and nanoparticles (b).

Results of the decomposition tests for BM-MgH_2, performed with TG and DSC methods, are presented in Fig. 3.25. The decomposition occurs in lower temperatures comparing to as received one. Thermogravimetry and DSC shows the decomposition point near 365 °C and 376 °C respectively, which is 35-84°C lower. A hydrogen capacity obtained from TG plot is near 5.8 wt. %, which is slightly samaller than non-modified MgH_2 (7 wt. %). This is an effect of changed in phase content caused by the ball milling (Table 3.6).

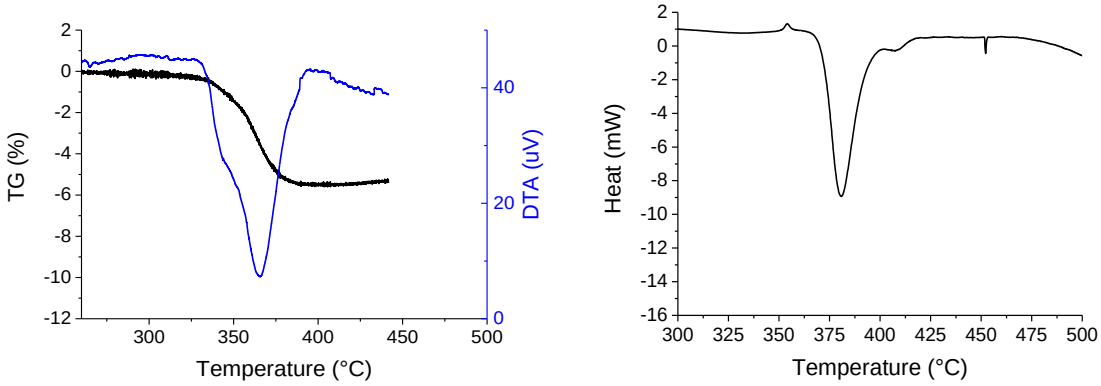

Fig. 3.25. DSC and TGA curves of the ball milled magnesium hydride.

Silicone resin

Silicones are inorganic–organic polymers with the chemical formula $[R_2SiO]_n$, where R is an organic group such as methyl, ethyl, phenyl, etc., which are polymerized siloxanes or polysiloxanes [120]. Silicone consist of an inorganic silicon-oxygen backbone chain (Fig. 3.26) with organic side groups attached to the silicon atoms. The (-SiO-) repeat unit is called as the "siloxane" bond.

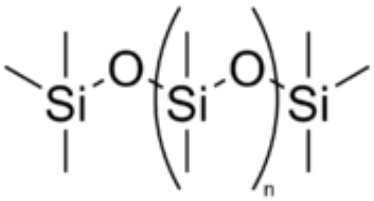

Fig. 3.26. Chemical structure of polysiloxane chain.

Since the polymer backbone is "inorganic" in nature, while the substituents attached to the silicon atom are generally "organic" radicals, silicones form an important bridge between inorganic and organic polymers. Compared to the carbon-based polymers, silicone polymers display an unusual combination of physical and chemical properties, such as high backbone

flexibility and very low glass transition temperatures (around −120 °C), good thermal and oxidative stability, high gas permeability, and good dielectric properties. The differences are coming from different properties of the (-C-O-) and (-SiO-) bonds. The siloxane bond displays an ionic character due to the large electronegativity difference between silicon and oxygen atoms and, at the same time, partially double bond character, due to pπ–dπ interaction between the silicon and oxygen atoms. It results in a large bond angle (142.5°) and provides flexibility of the chain and low glass transition temperature by reduction of rotation energy for organic groups attached to Si atom. (-Si-O-) bonds are also stronger (dissociation energy of 460 kJ/mole, compared with the (-C-O-) (345 kJ/mole) bond) which makes silicone polymers more chemically inert and more thermally stable.

The partial ionic nature of the (-Si-O-) bond also provides great flexibility to chemists for the preparation of a wide range of backbone compositions. By varying the (-Si-O-) chain lengths, side groups, and crosslinking, silicones can be synthesized with a wide variety of properties and compositions from liquid to gel to rubber to hard plastic. One of the most common is linear polydimethylsiloxane (PDMS, a silicone oil). The oldest classical synthesis methods is the hydrolysis of dimethyldichlorosilane precursor:

$$n\ Si(CH_3)_2Cl_2 + n\ H_2O \rightarrow [Si(CH_3)_2O]_n + 2n\ HCl$$

The polymerization produces linear chains capped with Si-Cl or Si-OH (silanol) groups. Today, acetates are used instead of chlorides. The hydrolysis of the acetates produces the less dangerous acetic acid as the reaction product of a much slower curing process.

A large group of silicone materials is based on the silicone resins, which are formed by branched and cross-linked cage-like structures (Fig. 3.27). Silicone resins represent a broad range of products. Polysiloxane polymers with reactive side group functionality such as vinyl, acrylate or epoxy - are used to create thermoset polymer matrix composites, coatings and adhesives.

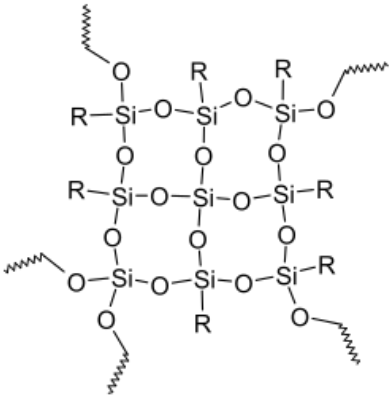

Fig. 3.27. Chemical structure of the silicone resin. R is usually organic group: Methyl (Me) or Phenyl (Ph), or a functional group: Hydrogen (H), Hydroxyl group (OH), Chlorine (Cl) or Alkoxyl group (OR).

In its uncured state, silicone rubber is a highly-adhesive gel or liquid. In order to convert to a solid, it must be cured, vulcanized, or catalyzed. There are two main approaches: condensation and addition curing.

- Addition curing – it is based on reaction between two different chemical groups, usually with non-saturated carbon bonds, to form an ethyl bridge [CH_2- CH_2] and there are no byproducts. The reaction occurs only in presence of platinum catalyst, typically two separate components are mixed: one component contains platinum; the second component contains a siloxane polymer. Such silicone rubbers cure quickly, though the rate of or even ability to cure is easily inhibited in the presence of elemental tin, sulphur, and many amine compounds. For the platinum-catalyzed cure system, the curing process can be accelerated by adding heat or pressure.
- Condensation curing – consists of two types: one-part and two-part systems. In one-part system a cross-linker exposed to ambient humidity undergoes hydrolysis reaction and is left with a hydroxyl or silanol group, which condenses with another group from the other polymer or cross-linker and the process continues until the system is fully cured. The reaction occurs at room temperature, so the materials are usually called RTV – Room Temperature Vulcanizing. The crosslinkers used in condensation cure systems are typically alkoxy, acetoxy silanes. Two-part condensation systems combine the cross-linker and condensation catalyst together in one part, while the polymer and any fillers or pigments are in the second part. Mixing of the two parts causes the curing to take place.

In this work, room temperature addition cured Shin-Etsu K1310ST silicon molding resin was used as a composite matrix. It can withstand temperatures over 350 °C, cures at room temperature for 24 h but that process can be faster when the heat is provided. Pot life time for uncured resin, when the mixture stays in liquid form is around 80 min. Cured material exhibits expected mechanical strength, and, because of its elastic, rubber-like properties it can absorb tensions coming from the hydride expansion during the reaction. In the uncured state, the viscosity of the liquid is very high (75 Pa·s) and during the sample preparation it is mixed with a silicone based thinner to tune the viscosity down to 0.1 Pa·s, which allows to get better wetting of the filler particles and to achieve higher loading.

Sputtering targets

Sputtering targets of vanadium, nickel and niobium were supplied by the Changsha Xinkang Advanced Materials Co. Ltd. [121]. They are of a disk shape (30mm x 3mm) and 3N purity. In the case of nickel, which is a ferromagnetic material and it cannot easily be sputtered using magnetron technology, a special, paramagnetic alloy of nickel and 7 wt. % of vanadium was used.

4. MAGNETRON COATING OF MAGNESIUM HYDRIDE POWDERS – RESULTS AND DISCUSSION

This chapter presents results of the research focused on coating of magnesium powders with catalytic layers using magnetron sputtering technology. Thin films of nickel, vanadium and niobium were successfully produced and observed with the SEM microscopy. The structure and phase composition, as well as element content was analyzed with XRD and EDS methods. Thermodynamics and kinetics of coated magnesium hydride was studied using differential scanning calorimetry, thermogravimetry and volumetric Sieverts method. At the end, the hydrogenation/dehydrogenation cycling was studied.

4.1. Samples overview

Three series of samples, which differ in the substrate form, type of sputtered material and conditions were prepared (summary in Table 4.1):

- Series 1- As received magnesium hydride was coated with the nickel and vanadium layers. Three samples with different sputtering times were produced for each target – 15, 30, 45 min for nickel and 30, 60 and 90 min for vanadium. Times of sputtering are chosen using a previously prepared calibration curve of magnetron to obtain layers with similar thickness. Because the sputtering of the pure nickel is not possible with magnetron technology, due to its strong ferromagnetic properties, a special $NiV_{7wt.\ \%}$ alloy, with paramagnetic properties was used. In this work, that materials will be called just “nickel” to simplify the samples nomenclature.
- Series 2 - Magnesium hydride was ball milled in order to nanostructurize material, which results with its better kinetic and thermodynamic performance (Chapter 2). Powders were coated again with the nickel, but instead of vanadium, which had weaker impact on the reaction kinetics, more promising niobium was used. A three samples for each material were sputtered. Unfortunately, ball milled powders were much more reactive than the as-received one and easy getting oxidized during experiment, which provided a motivation to modify the equipment. However, basic measurements were also performed for this group of materials.
- Series 3 - Sputtering equipment (Chapter 3) had been modified by adding remotely controlled, sealed cover for powder container and by improving high vacuum pumps, which can generate one order of magnitude better vacuum. Experiment could then be carried out without exposing MgH_2 to the air. One sample for both niobium and nickel

target was prepared, with 60 and 30 min sputtering times, respectively. Moreover, to reduce agglomeration effect, which occurred for ball milled powder, metal balls crushing agglomerates during powder mixing were added.

Table 4.1. Preparation parameters and naming of coated samples.

Series	Substrate type	Coating material	Sputtering time [min]	Code
1	As received MgH_2	Ni	15	#1a
			30	#1b
			45	#1c
		V	30	#1d
			45	#1e
			90	#1f
2	Ball milled MgH_2 (MgH_2 – BM)	Nb	30	#2a
			45	#2b
			90	#2c
		Ni	15	#2d
			30	#2e
			45	#2f
3	Ball milled MgH_2 (MgH_2 – BM)	Nb	60	#3a
		Ni	30	#3b

4.2. Structural studies with X-Ray diffraction

Right after the sputtering XRD patterns for all samples were collected in order to examine composition changes during the sputtering and to analyse sputtered material structure. Results for Series 1 powders are presented in Fig. 4.1 (nickel) and in Fig. 4.2 (vanadium). In addition, phase composition determined from the Rietveld refinement are listed in Table 4.1. Full fitting results (data, calculated profile, background and difference plots) are listed in the Appendix. There is no significant reflections of nickel or vanadium metal present (blue dots), which is possibly due to amorphous/nanocrystalline character and/or very low thickness of the sputtered films. To prove the presence of metal layers on the surface of the grains the EDS mapping was performed, as described in the next subsection. It is worth noting, that magnesium hydride does not oxidize during experiment. No significant reflections from MgO or $Mg(OH)_2$ (black dots) were found. Also the decomposition of hydride resulting from plasma heating in vacuum is negligible. Rietveld refinement of the diffractograms shows that the samples contain from 2.6 to 6.5% of pure magnesium, which is slightly more than in pristine MgH_2 material. It is caused by the decomposition of magnesium hydride due to plasma bombardment or it could be the effect of presence of the catalyst on the surface grains. Partial decomposition is slightly stronger for nickel samples, which is the result of its good catalyzing performance.

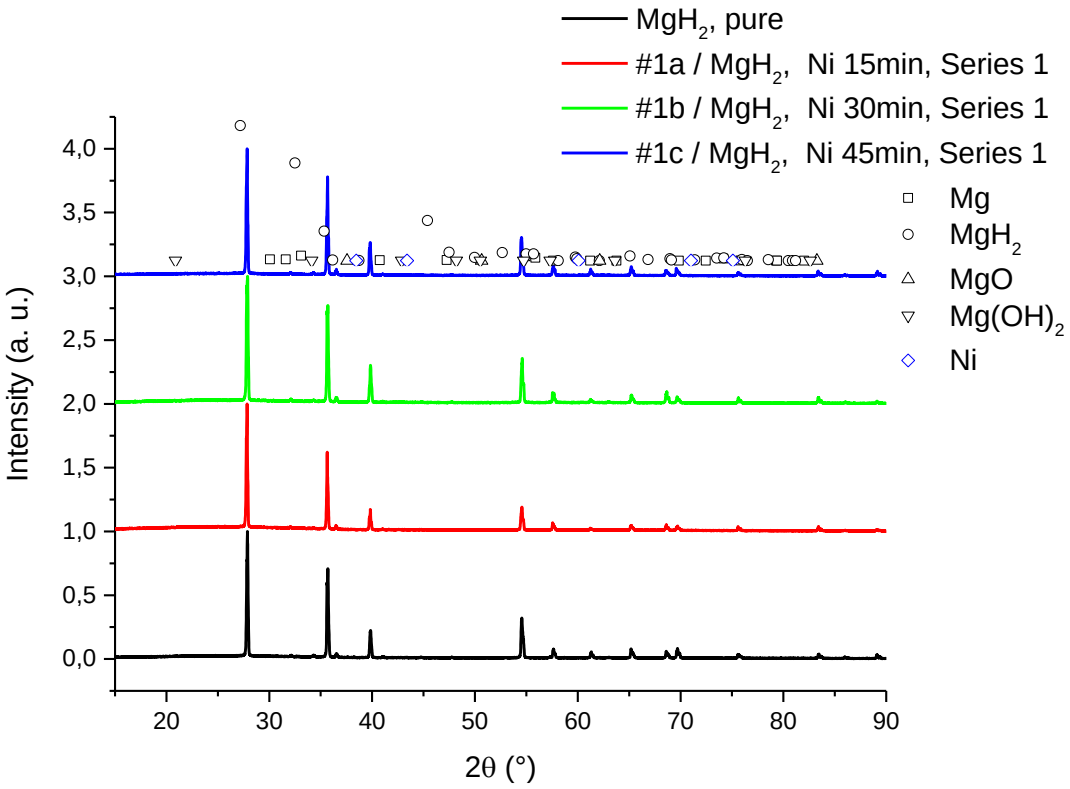

Fig. 4.1. XRD pattern of the nickel coated magnesium hydride powders (Series 1).

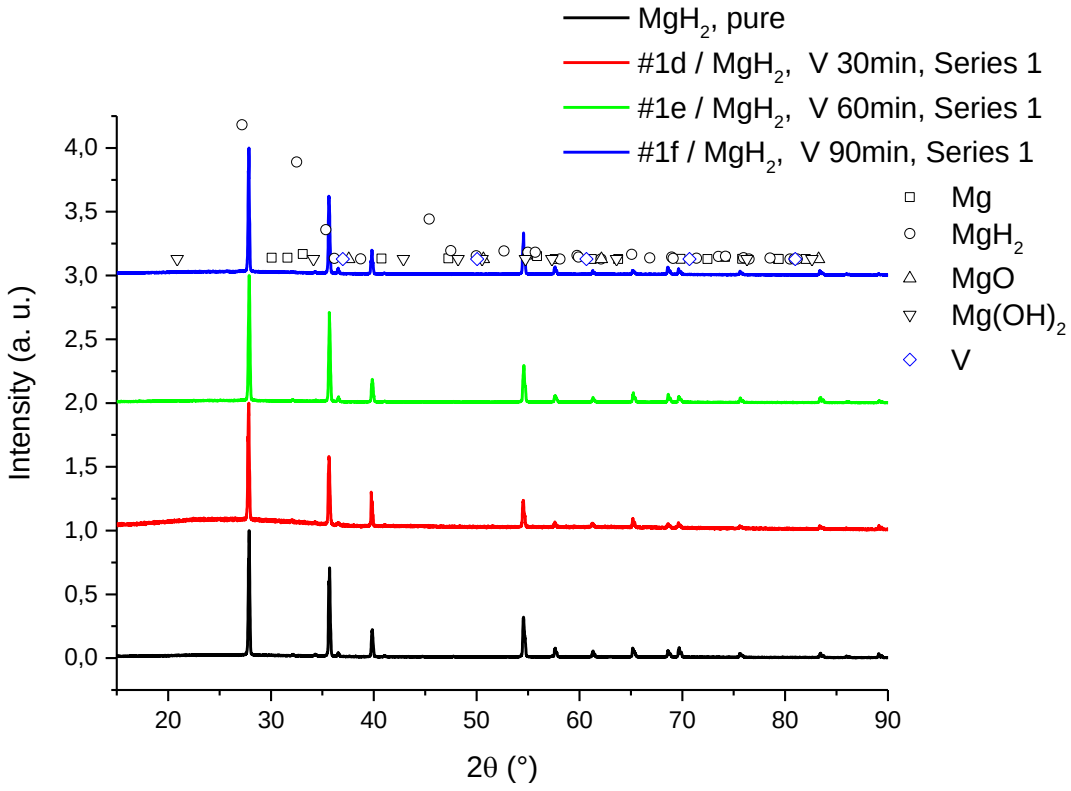

Fig. 4.2. XRD pattern of the vanadium coated magnesium hydride powders (Series 1).

Table 4.2. Series 1samples - composition obtained from Rietveld refinement of XRD pattern.

Code	Sample Name	Sample composition [wt. %]	
		Mg	β-MgH_2
#1a	MgH_2, Ni 15min, Series 1	2.1	97.9
#1b	MgH_2, Ni 30min, Series 1	3	97
#1c	MgH_2, Ni 45min, Series 1	6.5	93.5
#1d	MgH_2, V 30min, Series 1	1.2	98.8
#1e	MgH_2, V 60min, Series 1	2.2	97.8
#1f	MgH_2, V 90min, Series 1	3	97

Series 2 composed of coated ball milled powders exhibits more complex structure. Peaks coming from both sputtered materials, niobium (Fig. 4.3) and nickel (Fig. 4.4), are negligible like in Series 1 materials. What is new a strong magnesium oxide reflection (near $2\theta = 42°$) is present. Its wide shape is characteristic to surface shell oxidation layer present on oxidized magnesium and magnesium hydride. For niobium the amount of oxide keeps on the level of 20-30 wt. %, but in case of nickel it is stronger, it can reach content near 70 wt. % (Table 4.3). The mount of MgO for Ni coated powders growths while increasing of sputtering time, what suggest, that the main problem may be related with proper vacuum level and impurities of the working gas during the sputtering. Other interesting observation is the partial decomposition of the MgH_2 to pure magnesium, which is stronger in case of ball milled powders. Coated hydride poses lower activation energy, which enhances desorption kinetics and magnesium hydride may partially decompose due to plasma heating.

Table 4.3. Series 2 composition obtained from Rietveld refinement of XRD pattern.

Code	Sample Name	Sample composition [wt. %]			
		Mg	β-MgH_2	γ-MgH_2	MgO
#2a	MgH_2-BM, Nb 30min, Series 2	1.1	77.9	2.4	18.6
#2b	MgH_2-BM, Nb 60min, Series 2	20.8	46.8	0.4	32.0
#2c	MgH_2-BM, Nb 90min, Series 2	11.2	61.9	0.7	26.2
#2d	MgH_2-BM, Ni 15min, Series 2	5.3	57.7	2.6	34.4
#2e	MgH_2-BM, Ni 30min, Series 2	10.1	28.9	2.6	58.4
#2f	MgH_2-BM, Ni 45min, Series 2	3.5	11.5	0.4	84.7

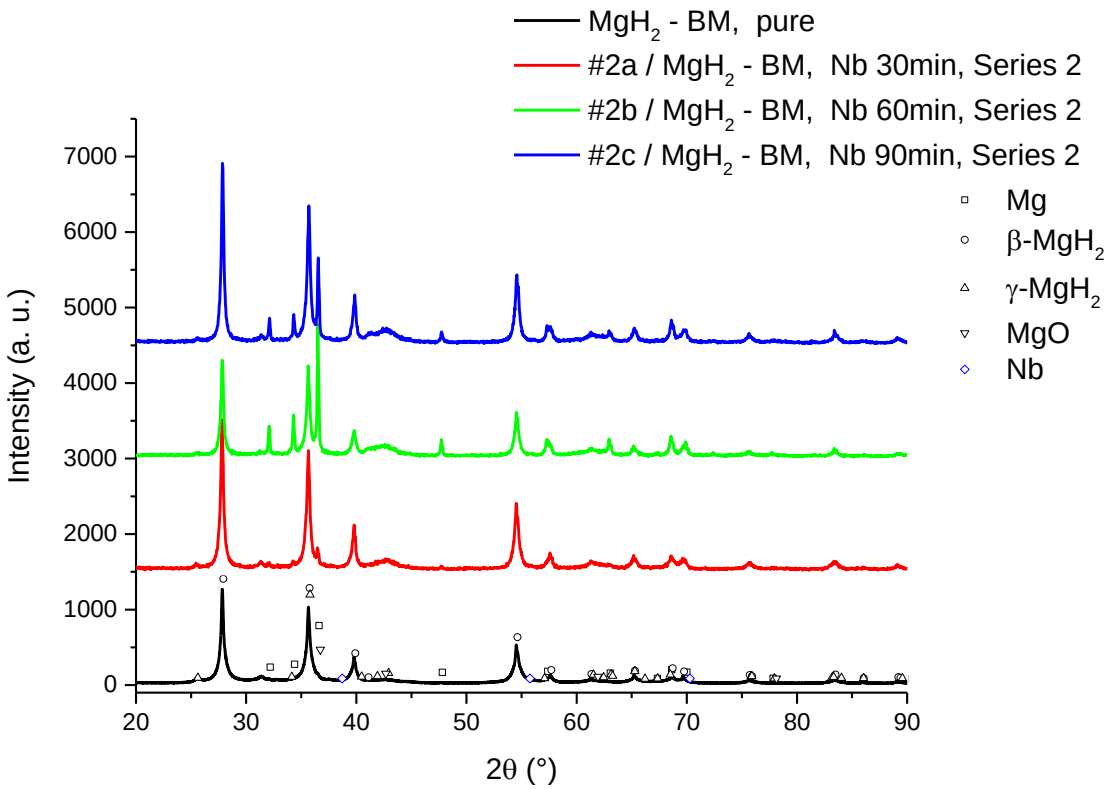

Fig. 4.3. XRD pattern of the niobium coated, ball milled magnesium hydride powders (Series 2).

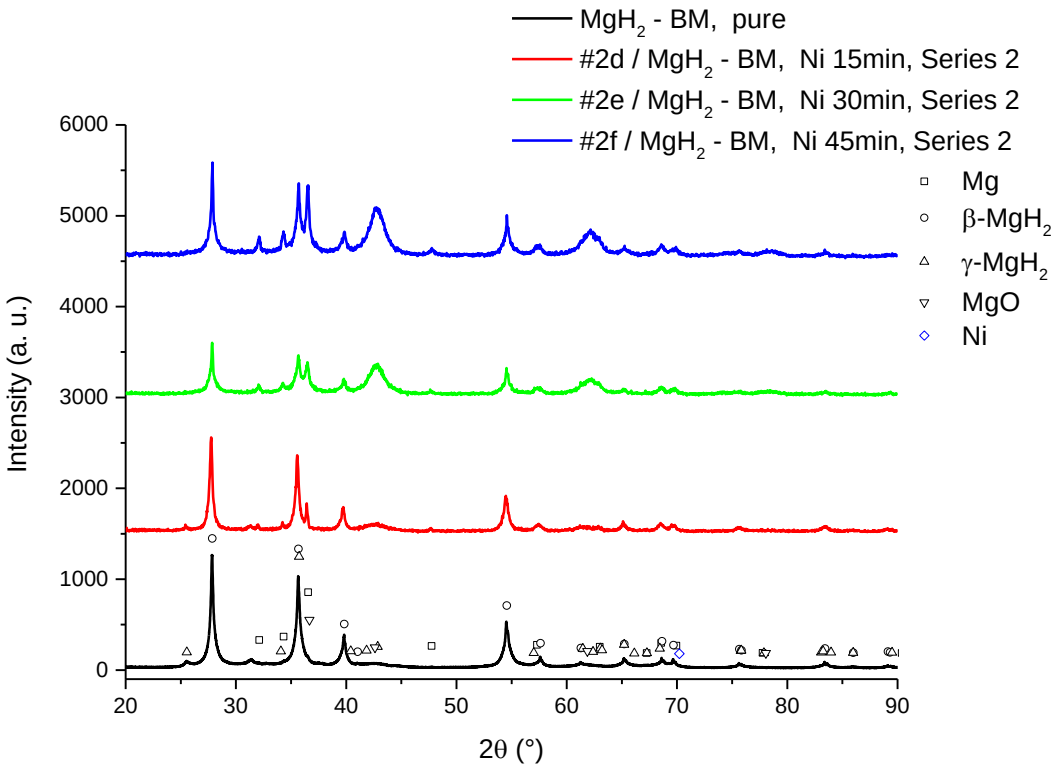

Fig. 4.4. XRD pattern of the nickel coated, ball milled magnesium hydride powders – (Series 2).

Modification of the experiment equipment for Series 3 samples results in reduction of the oxidation problem, especially for nickel coated materials (Fig. 4.5 and Table 4.4). The decomposition of magnesium hydride is also stopped, what is probably unexpected result of improving of the vacuum level – plasma heating is weaker. For niobium samples from both of Series 2 and 3 decomposition effect of magnesium hydride is slightly greater, what may result in better kinetic for hydride coated with that catalyst. On the other hand, nickel samples are more sensitive for presence of oxygen. The amount of Nb and Ni metals was too low to observe its diffraction peaks.

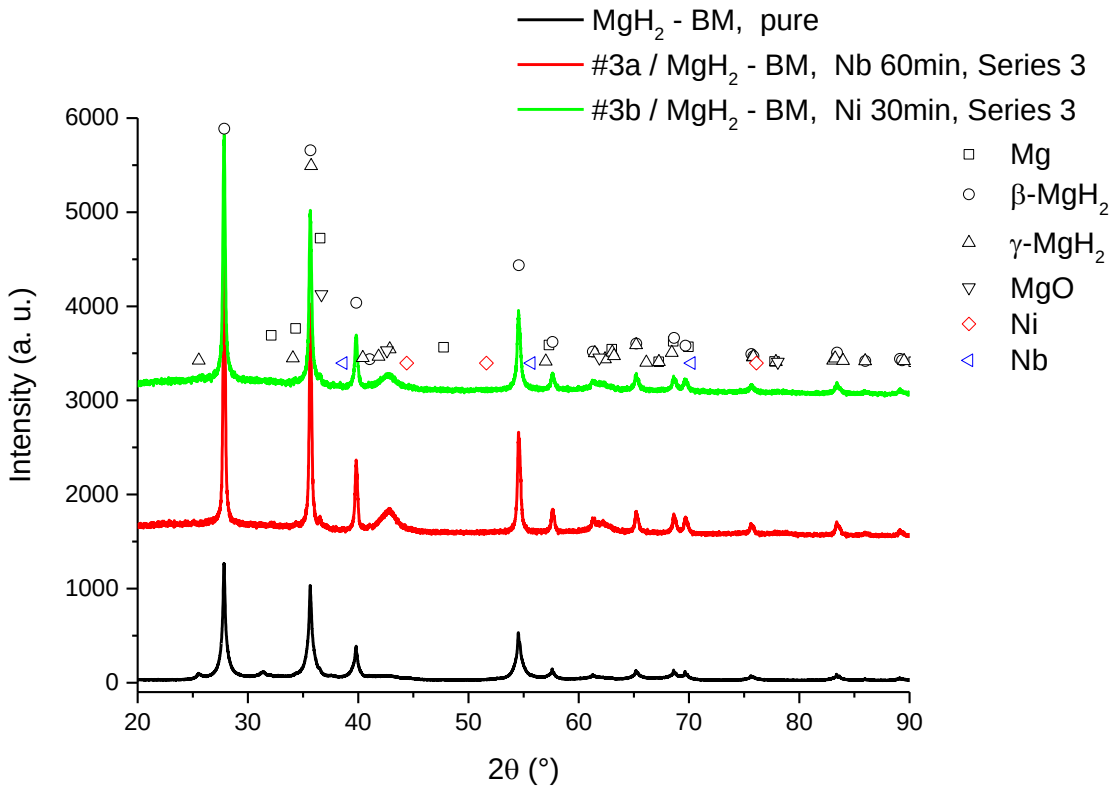

Fig. 4.5. XRD pattern of the nickel and niobium coated, ball milled magnesium hydride powders (Series 3).

Table 4.4. Series 3 composition obtained from Rietveld refinement of XRD pattern.

Code	Sample Name	Sample composition [wt. %]			
		Mg	β-MgH_2	γ-MgH_2	MgO
#3a	MgH_2-BM, Nb 60min, Series 3	4.3	71.1	0.2	24.3
#3b	MgH_2-BM, Ni 30min, Series 3	1.7	78.6	0.5	19.2

4.3. Observations of surface element distribution

In order to prove the presence of thin films of Ni, V and Nb metal on the surface of magnesium hydride particles an EDS mapping was performed. Moreover, SEM observation allowed to check the character of films, i.e. if they are built from nanoparticles or flakes attach to the grain surface or if they are continuous layer. It also allows to estimate the thickness of coatings and to analyze the distribution of elements (Subsection 4.4). Elemental analysis of EDS spectra of panoramic photos (containing many particles, not single grain) was used to estimate effective catalyst amount in the samples – obtained valued are presented on the plots together with the spectra. For as received coated powders (Series 1), results are shown on Fig. 4.6. Nickel and vanadium K-lines are clearly seen in the spectra, but their intensity is around 1-2% of the intensity of magnesium line. It gives between 0.18 wt. % and 1.21 wt. % of nickel and 0.23 wt. % to 0.95 wt. % of vanadium in the sample. Based on literature data (Chapter 2) amounts of dopant are relatively low compared to the typical values reported in publications (5-15 wt. %). Magnesium, nickel and vanadium distribution maps for single, random picked grain are presented in Fig. 4.7 and Fig. 4.8. They show that the catalytic elements fully cover the surface of the grains and the intensity of catalytic metal signal increases with sputtering time, which indicates increasing layer thickness. The coating can be assumed as uniform – variations in the Ni or V intensity are related to the grain topography – edges, cracks, slopes poses slightly higher or lower signal intensity.

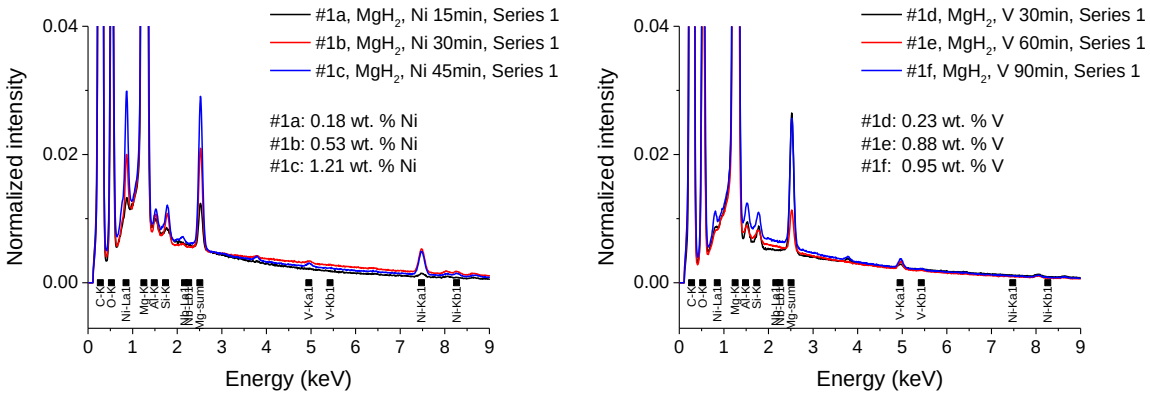

Fig. 4.6. EDS spectra of Series 1, nickel and vanadium coated powders.

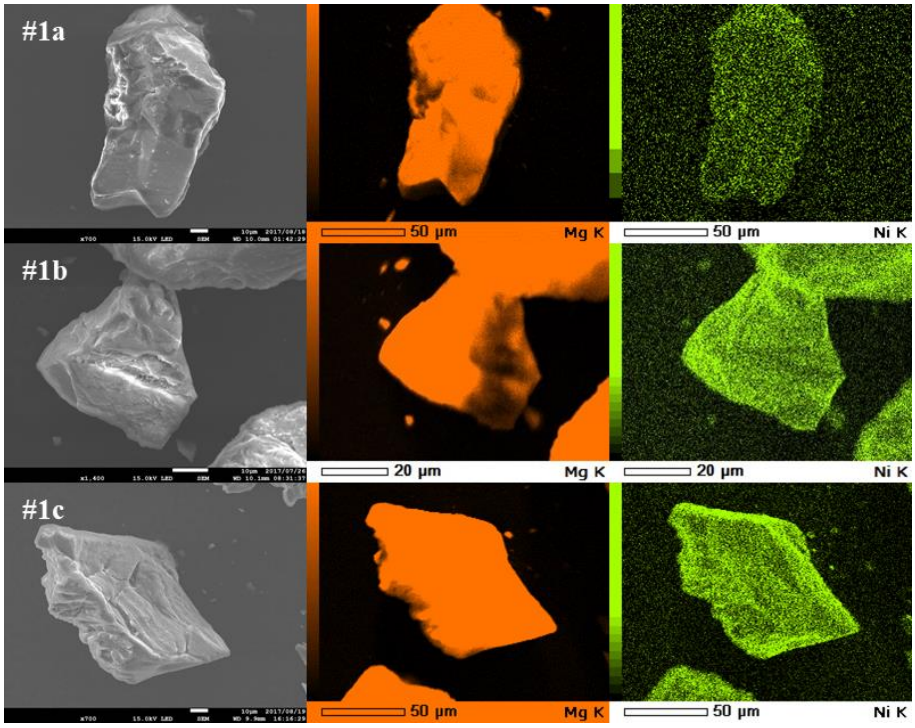

Fig. 4.7. SEM image and EDS element map of the nickel coated magnesium hydride powder (Series 1).

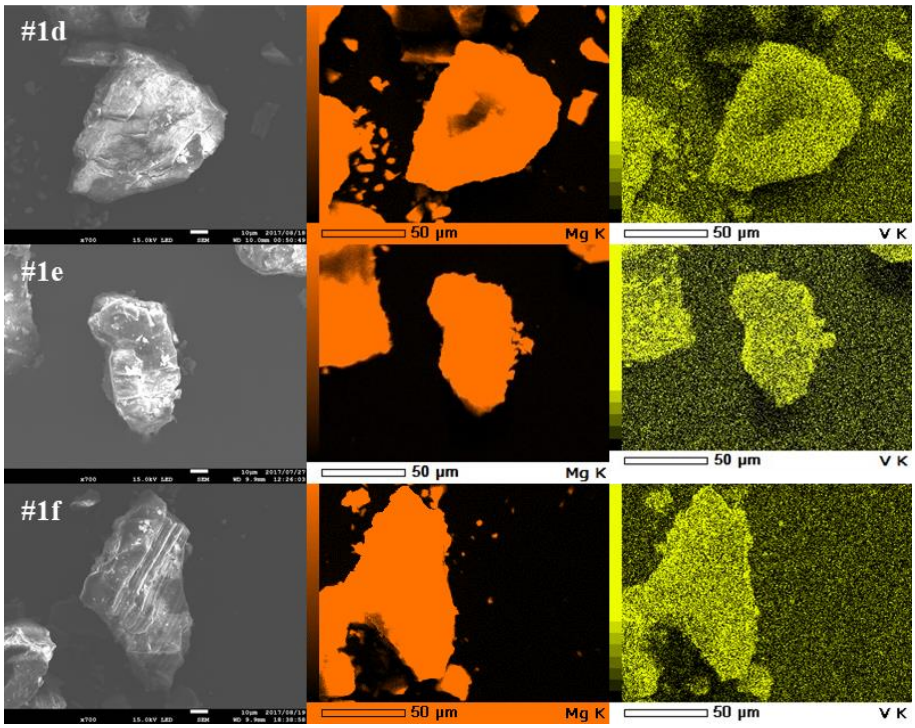

Fig. 4.8. SEM image and EDS element map of the vanadium coated magnesium hydride powder (Series 1).

A higher magnification image of single grain shows interesting phenomena. There are two types of particles: with the clear surface and with the surface decorated with ~60 nm size nanoparticles (Fig. 4.9). To check the possibility that nickel and vanadium are present in form of nanoparticles on the surface instead of a continuous layer the EDS measurements at different points were performed in order to check the chemical composition of observed structured (Fig. 4.10). Vanadium lines are present on spectra collected for both clear surface and nanoparticle points. Line intensity on clear surfaces is stronger than for nanoparticle, so it can be assumed, that metal layer lays under the nano grains and is continuous. Visible nanoparticles can be results of surface oxidation occurring during SEM sample preparation, when powder is exposed to the air. Bigger grains (~1μm) present on the surface are coming from the finest phase of original, as received MgH_2 powder. Observation confirming that theory is the strong peak of silicon visible on Fig. 4.10a – Si impurities were found in the origin magnesium hydride powder (Chapter 3).

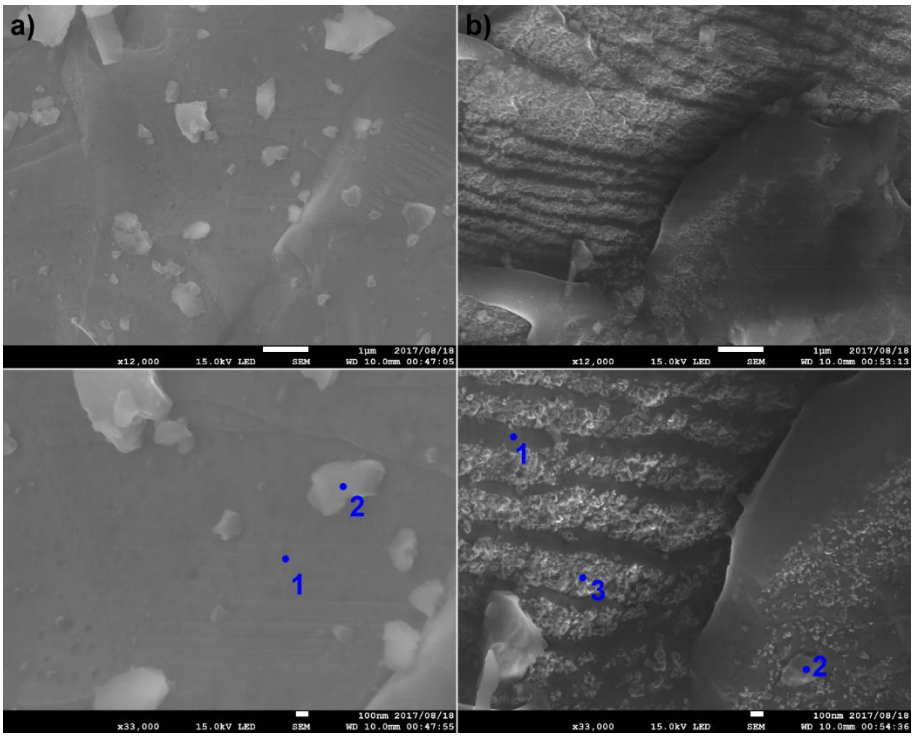

Fig. 4.9. SEM close up images of V #1e sample showing vanadium coated grains with clear (a) and nanoparticle decorated surface (b).

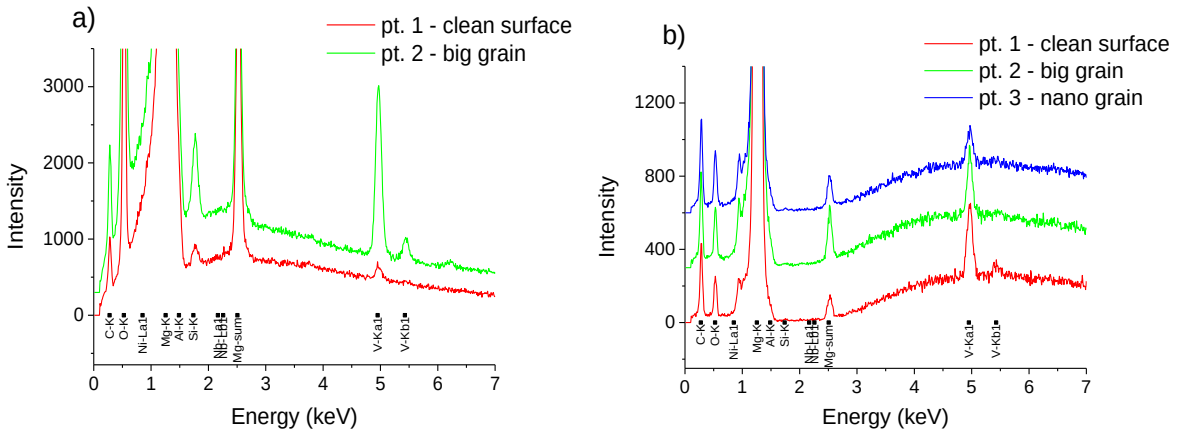

Fig. 4.10. EDS spectra of #1e vanadium coated grains with clear (a) and nanoparticle decorated surface (b).

Because the grains size was strongly reduced for the ball milled magnesium hydride, different effects are observed. First of all, fine powders easy undergo agglomeration while mixing during the sputtering – large conglomerates (~10-50 µm) of smaller (100 nm) grains are formed. Fig. 4.11shows SEM images of #2d sample taken under different magnifications. On the two panoramic views (a, b) a wide distribution of particles, staring from fine nanoparticles to 100 µm grains can be observed. More detailed images (c, d) shows that there are two type of structures with similar, nearly 10 µm size: clear not milled grains (c) and aggregates (d) build of 100 nm nanoparticles (f). Except of conglomerates, a lot of irregular shape nanoparticles lays in the background of bigger structures (e).

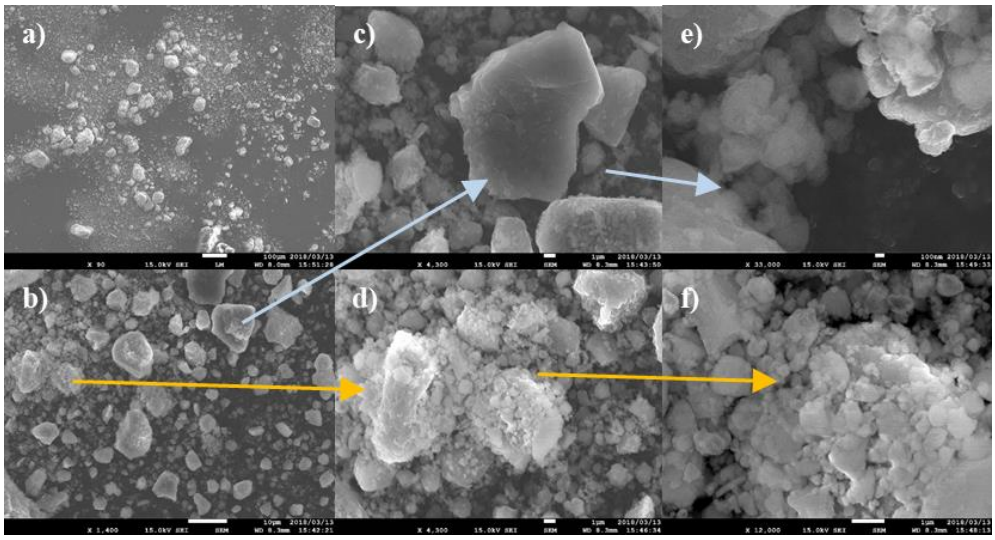

Fig. 4.11. SEM photos of #2d (MgH_2 –BM, Ni 15min, Series 2) powders taken under different magnification to observe different particle types, size, and structures.

Coating of such agglomerates and structures is strongly not uniform. Fig. 4.12 and Fig. 4.14 presents elements distribution maps for niobium and nickel samples. It is clearly seen that catalyst lines intensities poses very wide distribution – some of magnesium grains are fully covered with Ni or Nb, some of them are only partially covered. When agglomerates are crushed, particles from their interior can be even clean. In result of pure uniformity, influence of catalyst on the magnesium hydride properties will be varied for different particles and the average properties and parameters of coated samples will poses wide range of values and large uncertainty. An example is the effective amount of dopant introduced to the MgH_2 (Fig. 4.13), for nickel it is between 0.77 and 1.73 wt. %, but for niobium it is overestimated - it can reach 7.6 wt. %, despite the fact, that the sputtering times were set using calibration curve to achieve similar thickness.

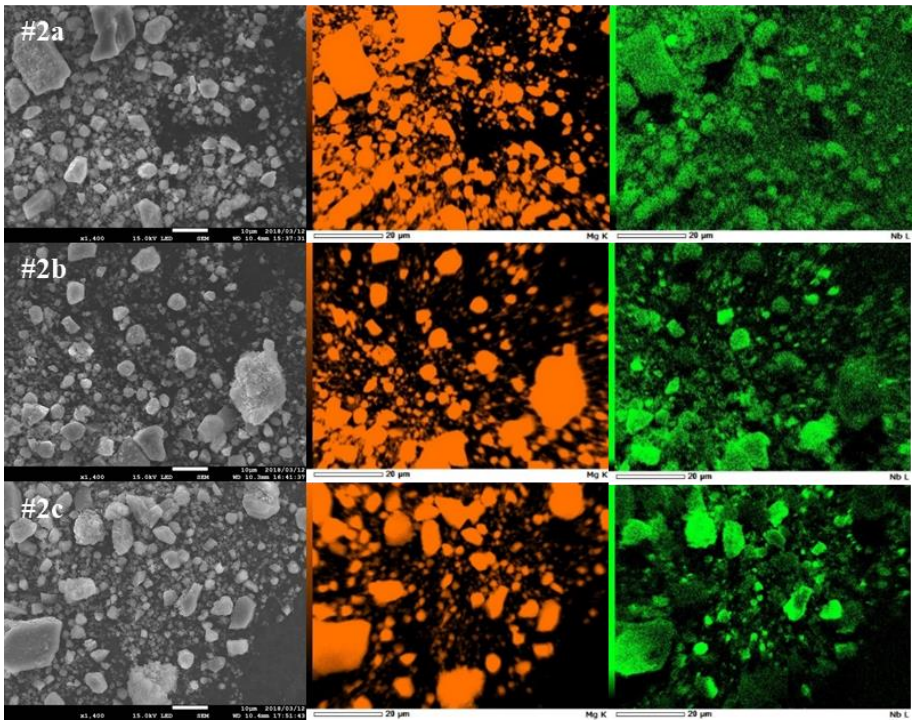

Fig. 4.12. SEM image and ED's element map of the niobium coated, ball milled magnesium hydride powder (Series 2).

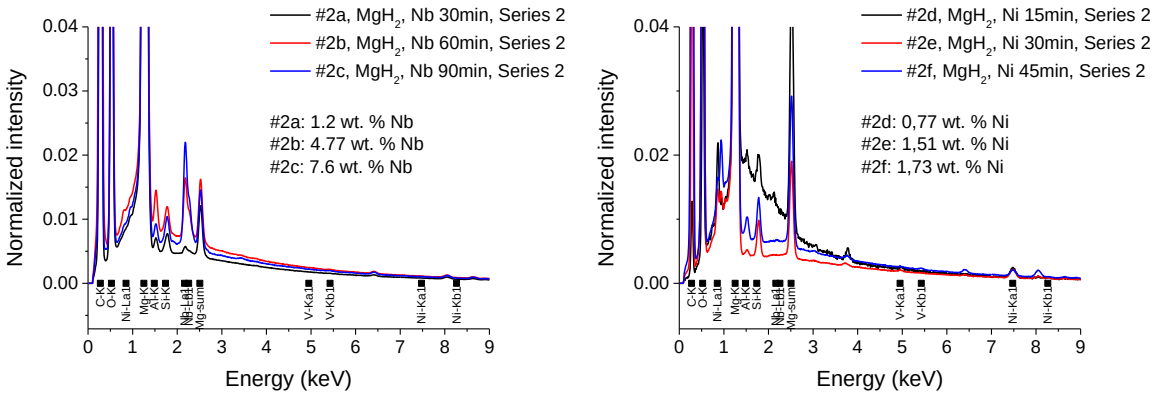

Fig. 4.13. EDS spectra of Series 2, nickel and niobium coated, ball milled powders.

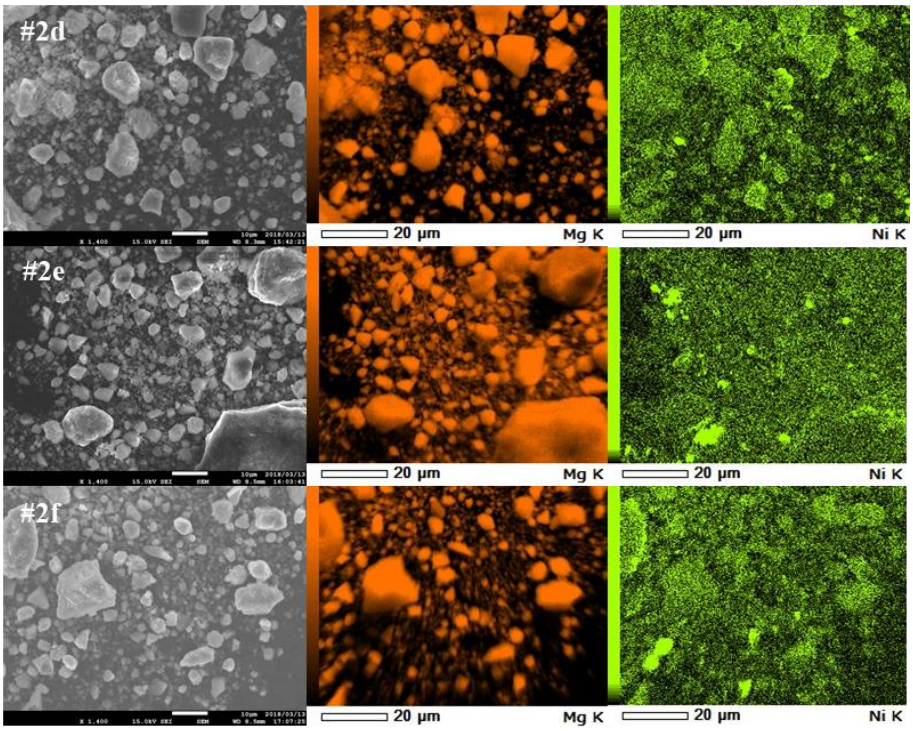

Fig. 4.14. SEM image and EDS element map of the nickel coated, ball milled magnesium hydride powder (Series 2).

After the modification of sputtering equipment by adding metal balls crushing the conglomerates samples of Series 3 were produced and studies (Fig. 4.15 and Fig. 4.16). The uniformity of the coating is better, however it still exists – future studies about the mixing process and development of anticaking system suited to work in high vacuum are needed. Effective amount of dopant calculated from EDS spectra are 1.58 and 0.27 wt. % for niobium and nickel respectively. Nickel amount is much lower than expected (~1.5 wt. %), despite using the same conditions of time and power as in previous samples. This could be

effect of the target erosion, because this experiment was performed at last. Presence of deep race track on the target surface enhances redeposition of sputtered atoms on the target and in results, reduces the sputtering rate. This is confirmed when we look on the results of elemental analysis for #2d-#2f samples (Fig. 4.13). Sputtering times were growing linearly (15, 30 and 45 min), but the difference in nickel content between #2e and #2f sample is three time lower than the difference between sample #2d and #2e, which has to be caused by erosion of the target.

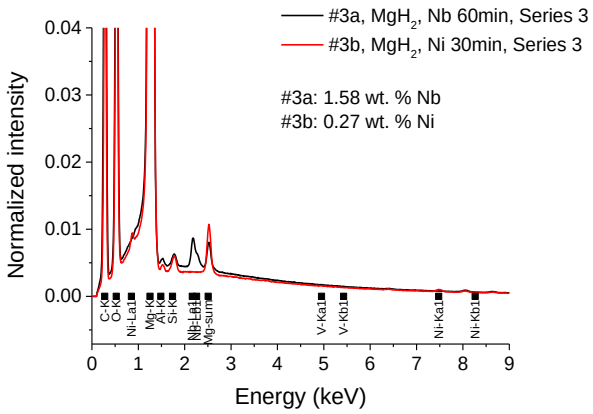

Fig. 4.15. EDS spectra of Series 3, nickel and niobium coated, ball milled powders.

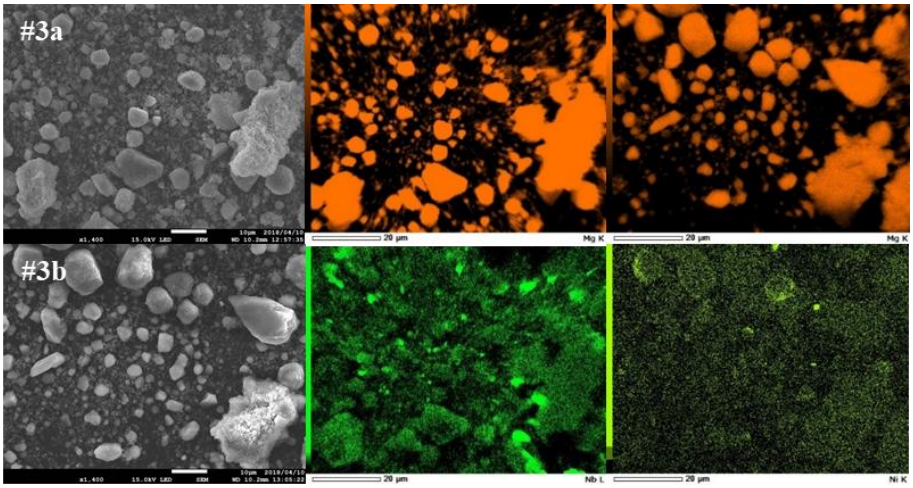

Fig. 4.16. SEM image and EDS element map of the niobium and nickel coated, ball milled magnesium hydride powder (Series 3).

4.4. Measurements of the coating films thickness and its variation

In order to determine the thickness of sputtered films, the cross-sections were prepared and their SEM images were obtained. Powder samples were suspended in the epoxy resin, cured, then cut and polished with the sandpaper and diamond pastes. Fig. 4.17 and Fig. 4.18 present the images of a single nickel-coated grain of the samples #1b and #1c. A glossy layer visible on the grain edge corresponds to Ni film and the EDS mapping confirms its metallic character

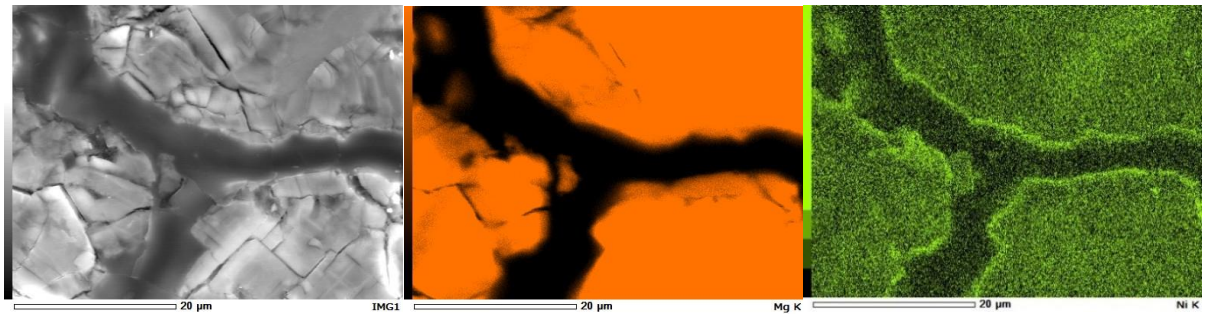

Fig. 4.17. Cross section image of #1b powder and EDS mapping results showing magnesium and nickel distribution.

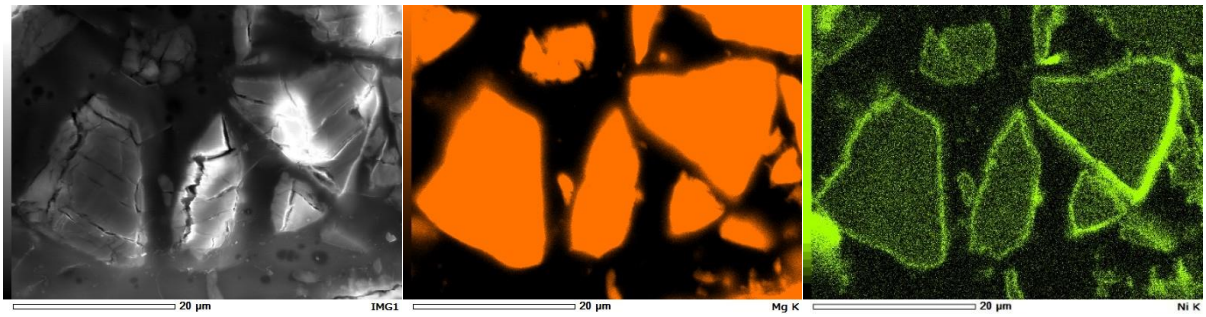

Fig. 4.18. Cross section image of #1c powder and EDS mapping results showing magnesium and nickel distribution.

Some may notice, that interior of the grains on the Ni – maps poses stronger intensities than inter-particle, resin filled spaces. It is due to the higher background coming from stronger electron interactions with magnesium than with the carbon from resin. To prove that, point EDS measurements were taken at point near glossy layer, in the interior and between the grains (Fig. 4.19). On the pt. 1 spectra, nickel line is present in contrast to the pt. 2 and 3, which is result of thin film of nickel formed on the surface of magnesium hydride. On spectra taken in pt. 2, which is interior of the particle, magnesium, as well as related impurities (Al, Si) only are present. Space between particles, is filled with resin, so except the carbon only chlorine and fluorine

lines are visible. Small magnesium peak in that point is coming probably from magnesium particles in deeper parts of the cross-section.

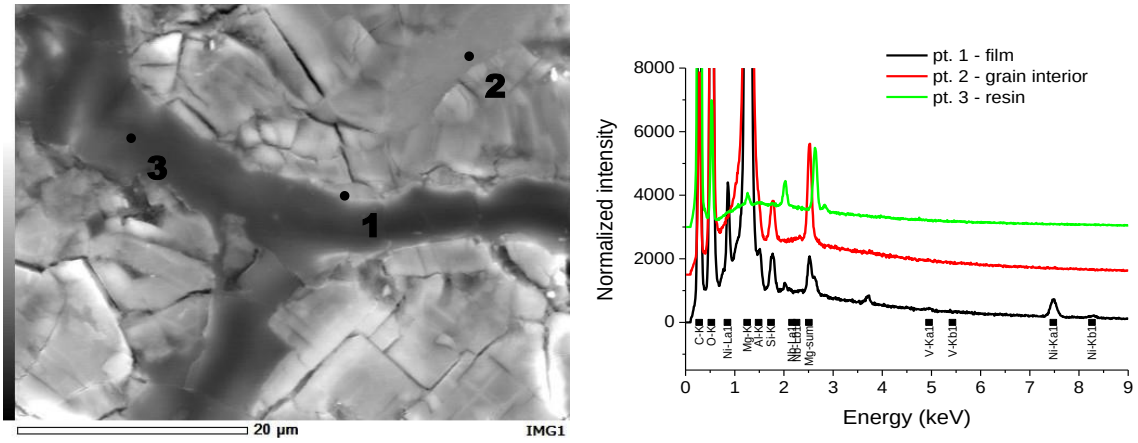

Fig. 4.19. EDS spectra of the cross-section of particles from #1b, nickel coated sample, collected at points on the layer, in thee grain interior and between the particles.

The thickness was calculated using computer software, basing on nickel intensity profile along line coming through background, the layer and grain interior, perpendicularly to the layer (Fig. 4.20). However, the exact measurement and thickness distribution cannot be collected. The main reason is that the metal film is scrapped form the hydride surface during polishing process. Moreover, the effective thickness measured depends on the grain position and orientation and low electrical conductivity of the resin limits image resolution and EDS signal.

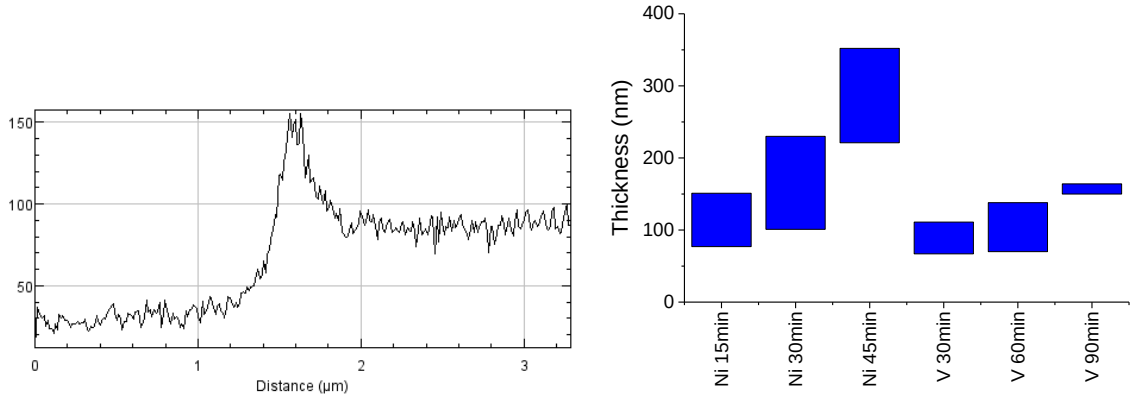

Fig. 4.20. Relative nickel intensity profile along line passing through the background, metal layer and interior of hydride grain and approximate thickness distribution calculated for Series 1 samples.

Estimated results are presented in Fig. 4.20. The thickness of both sputtered metals, nickel and vanadium grows with increasing sputtering time, and it is in the range of 80-320 nm and 60-170 nm for hydride coated with Ni and V respectively. It has to be noted, that vanadium layers are thinner even if sputtering time is two times longer than for nickel films. This effect can be related to a lower diffusion rate of vanadium atoms in argon plasma. In case of ball milled coated powders, thickness analysis could not be performed due to sample preparation problem during the polishing and the fact, that the is strongly not uniform and very thin.

4.5. Study of thermodynamic properties and thermal decomposition

DSC measurements were performed on 0.5 mg samples at the 1, 5 and 10 °C/min heating rates. As shown in Fig. 4.21, nickel coating reduces hydrogen desorption temperature by about 50 °C comparing to the pure hydride, moreover the temperature decreases with increasing sputtering time, which can be related to larger amount of dopant added. Endothermic decomposition peaks have asymmetric shape, suggesting two reactions occurring at the same time and giving overlapping peaks. This may be an effect of intermetallic alloys formed at the interface between the hydride and nickel layer, as the asymmetry is stronger for thicker coatings.

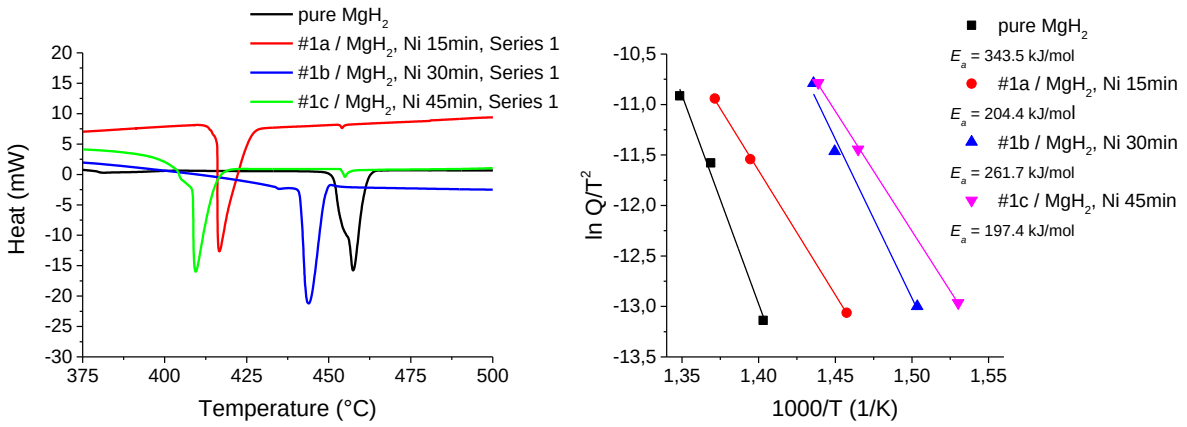

Fig. 4.21. DSC curves obtained at 5°C/min heating rate and the activation energies derived from Kissinger plots for DSC curves obtained at 1, 5 and 10 °C/min heating rates - for nickel coated samples (Series 1).

Activation energy of hydrogen dissociation on the surface of the materials could be determined using the Kissinger method (Chapter 3) based on the DSC peak shift due to different heating rates (1 to 10 °C/min). The energy barrier is found to be of 90-150 kJ/mol lower than that of

the raw magnesium hydride, but no clear dependence between the coating thickness and the activation energy could be observed. Kinetic barriers for samples #1a (15min) and #1c (45min) are similar, but the decomposition temperatures differ by ~40 °C. An interesting fact is that the activation energy of medium coated sample is higher than others – we believe that it is caused by cracking or falling off the thick layers (sample Ni #3) during the sample preparation, but they could not be found during SEM observations. To solve this problem further study is needed.

In case of vanadium samples different results were obtained (Fig. 4.22). The decomposition temperature is similar, or even slightly higher than the pure hydride, as for 30min sample, but the activation energy is still reduced by ~100 kJ/mol. Again, no dependence between the catalyst amount and the activation energy can be derived.

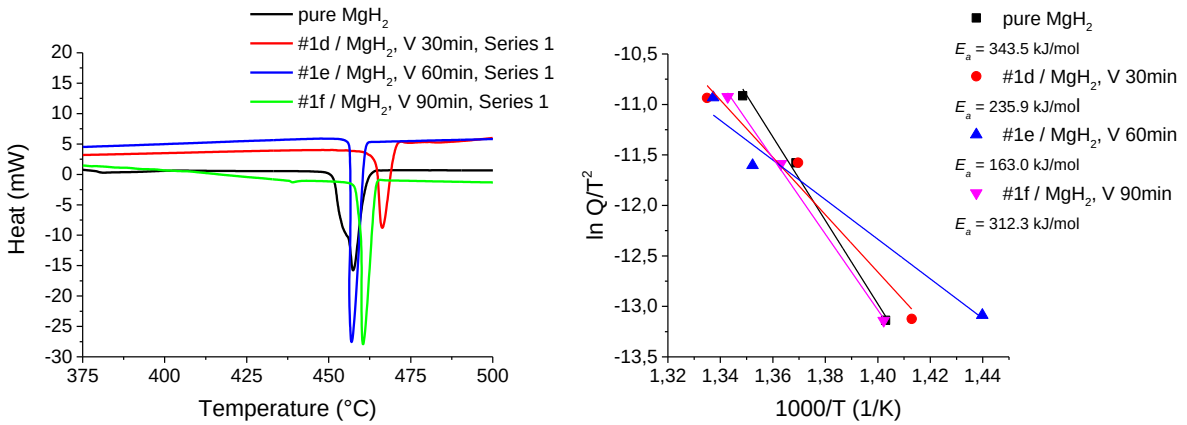

Fig. 4.22. DSC curves obtained at 5°C/min heating rate and the activation energies derived from Kissinger plots for DSC curves obtained at 1, 5 and 10 °C/min heating rates - for vanadium coated samples (Series 1).

To distinguish the effects of thin film catalyst on the decomposition temperature shift and the reduction of the activation energy the following model of the influence of the coating thickness on the kinetic properties is proposed: The dissociation with spill-over mechanism on the coating is the most effective, when the surface of the hydride grain is completely covered and all hydrogen gas molecules approaching the magnesium surface can meet the catalyst atoms. As long as the layer covers whole surface, further increase of its thickness will no more affect the activation energy. On the other hand, thicker coating may lead to formation of magnesium alloys on the surface of magnesium, which allows to start decomposition at lower effective temperatures due to enhanced nucleation and phase growth. For both nickel and vanadium

samples activation energy is lowered because the layers cover whole surface of the MgH_2 particles, but the nickel rather form hydrogen storage alloys with magnesium than vanadium, thus the decomposition temperature can be reduced.

Because of the oxidation effect, DSC curves collected for ball milled, coated powders (Fig. 4.23 – black curve represents data for the pure, ball milled magnesium hydride) have unusual course. At first, the peak area varies because of lower content of magnesium hydride. Some of samples, especially with mean amount of dopant (blue lines), shows very weak decomposition peaks, near 490 °C for Nb and 395 °C for Ni. Only niobium samples with 30 and 90 sputtering times poses typical shape of the plots with decomposition occurring near 452 °C and 469 °C. Other samples have very irregular, or composed of multiple peaks, heat flow dependence. It is an effect of strongly uniform coating - particles covered with different amount of dopant exhibits different reaction kinetics. Because the coating distribution is wide, but continuous, it can produce very wide peaks, noises and changes of shape of DSC baseline (e. g. sample Ni 15min and Ni 45min). Such artefacts make data analysis and material characterization uncertain. Last observed effect is higher desorption temperature for all prepared samples. The simplest explanation is the presence of the oxidation shells on the surface of magnesium hydride, but no clear dependence between the MgO content (Table 4.3) and shift in the decomposition temperature – magnesium oxide layer may cover the grain with different thickness because of different reactivity of not uniformly coated powder.

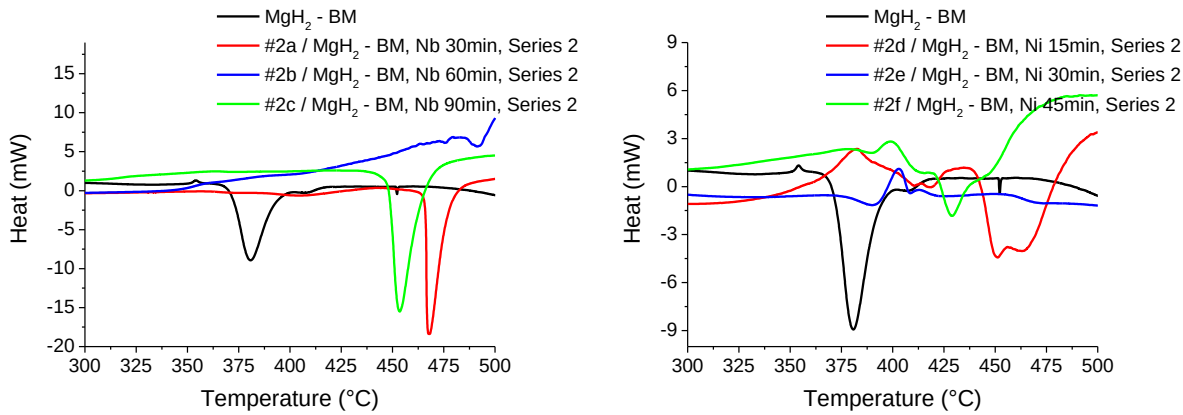

Fig. 4.23. DSC curves obtained at 5°C/min heating rate for niobium and nickel coated, ball milled samples (Series 2).

Last series (Series 3) of materials was prepared in covered powder container with presence of metal balls limiting agglomeration. The DSC plots (Fig. 4.24) consist of the single

decomposition peak, near 381 °C for nickel and 404 °C for niobium. Powder poses more uniform properties than the previous sample group, but the effect of oxidation still affects on the decomposition temperature - comparing with the pure ball milled MgH_2 it is around 1 °C and 14 °C for the nickel and niobium respectively. It must be notice, that despite the oxidation and smaller effective amount of nickel in the sample (Fig. 4.15) the peak shift is lower than niobium, which confirms postulate of stronger catalysis capabilities of nickel. The activation energy has been reduced for both samples, but is slightly lower (161.7 kJ/mol) for Nb sample than nickel one (168.8 kJ/mol).

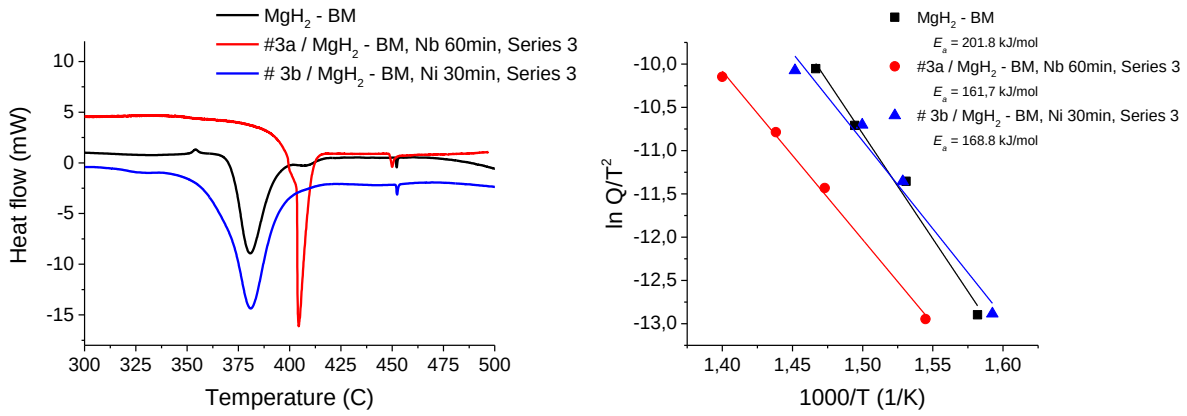

Fig. 4.24. DSC curves obtained at 5°C/min heating rate and the activation energies derived from Kissinger plots for DSC curves obtained at 1, 5, 10 and 20 °C/min heating rates - for nickel and niobium coated, ball milled samples (Series 3).

4.6. Measurements of the hydrogenation/dehydrogenation reaction rate

Hydrogen absorption and desorption kinetics were studied using a Sieverts apparatus. 100mg of hydride sample was initially activated for 20h at 300 °C. Then, it has been dehydrogenated and hydrogenated under 0.01 and 10 bar pressure, respectively. Fig. 4.25 and Fig. 4.26 show time dependence of reacted hydrogen content for the first 150 min of the reaction for nickel and vanadium coated magnesium hydride powder from Series 1 group of samples. Nickel can effectively enhances hydrogenation and dehydrogenation rates, reducing time needed for charging and discharging of the tank. One of the method to estimate the reaction kinetic is to compare times needed to desorb or absorb of 90% of maximal capacity for the sample (Table 4.5).

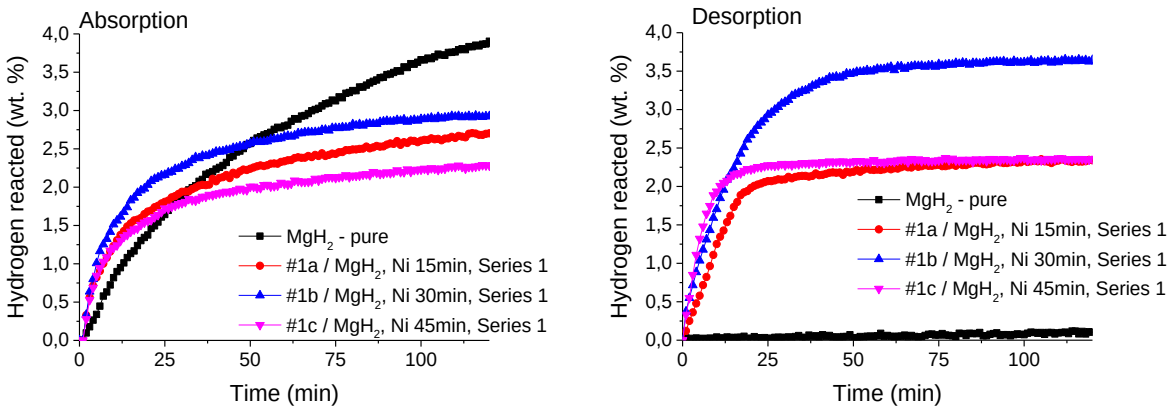

Fig. 4.25. Hydrogenation and dehydrogenation curves of the nickel coated magnesium hydride powders – Series 1.

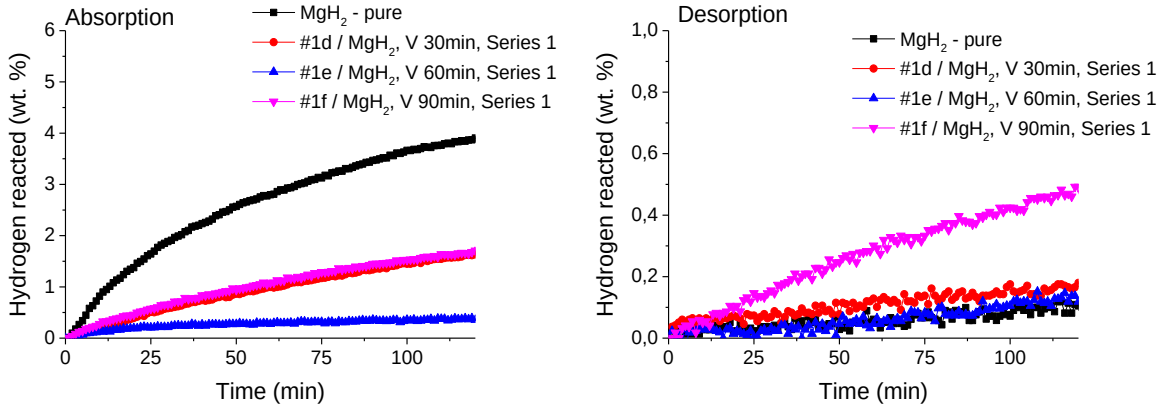

Fig. 4.26. Hydrogenation and dehydrogenation curves of the vanadium coated magnesium hydride powders – Series 1.

Table 4.5. Time needed to react of 90% of hydrogen for Series 1, nickel coated powders.

Code	Sample name	Time to react of 90% of hydrogen [min]	
		Absorption	Desorption
-	MgH_2 - pure	>500	>700
#1a	MgH_2, Ni 15min, Series 1	97	31
#1b	MgH_2, Ni 30min, Series 1	64	38
#1c	MgH_2, Ni 45min, Series 1	69	15

Time reduction effect is much stronger for desorption process - to completely decompose the sample it needs 15-38 min for coated samples and more than 12h for pure, as received magnesium hydride. Absorption process is also enhanced, but weakly. Vanadium coating causes some improve in dehydrogenation rate, but the influence is very small and in case of absorption reaction it is even slower than the pure MgH_2 – there is a postulate, that vanadium layer is too dense at limits hydrogen diffusion to and from the magnesium metal, but there is

not experimental method to confirm that statement. What is important, the equilibrium hydrogen capacity of samples differs between them and does not reach the theoretical value (7.5%), it reaches around 2 – 3.5 wt. % which is 2-3 times lower than expected level. XRD measurements performed after the desorption stage have confirmed, that samples are only partially decomposed. Additional trials and studies are needed in order to find the proper pressure/temperature conditions for the reaction (Subsection 4.7).

Ball milled magnesium hydride generally exhibits better reaction kinetics (Table 4.6). For the pure MgH_2, it takes around 25 minutes to absorb and 235 min to desorb of 90% of stored hydrogen. Series 2 niobium coatings have very small impact for reaction kinetics, the desorption time stays on similar level (233-219 min) and the absorption is longer than the pure hydride (26-33 min). Obtained results suggest great enhancement of hydrogenation (11-4 min) and dehydrogenation (103-62) speed for nickel samples, but it must be pointed out, that nickel samples contains smaller amounts of the hydride (~11-5 wt. %, Table 4.3). On the other hand, larger oxide shells should reduce the diffusion rate and reaction speed. Further analysis is needed to distinguish effects of mounts of the hydride and oxide to reaction kinetics.

Table 4.6. Time needed to react of 90% of hydrogen for Series 2 and Series 3, ball milled, niobium and nickel coated powders.

Code	Sample name	Time to react of 90% of hydrogen [min]	
		Absorption	Desorption
-	MgH_2 - BM	25	235
#2a	MgH_2 - BM, Nb 30 min, Series 2	32	233
#2b	MgH_2 - BM, Nb 60 min, Series 2	33	229
#2c	MgH_2 - BM, Nb 90 min, Series 2	26	212
#2d	MgH_2 - BM, Ni 15 min, Series 2	9	103
#2e	MgH_2 - BM, Ni 30 min, Series 2	11	100
#2f	MgH_2 - BM, Ni 45 min, Series 2	4	62
-	MgH_2 - BM	25	235
#3a	MgH_2 - BM, Nb 60 min, Series 3	19	277
#3b	MgH_2 - BM, Ni 30 min, Series 3	31	228

Hydrogen capacities (Fig. 4.27 and Fig. 4.28) are different than expected value (6-7.5 wt. %), due to the changes in sample composition and changes in optimal reaction conditions. Effective measured hydrogen content is near 1.5-3.5 wt. % and 1.2 – 1.7 wt. % for niobium and nickel coated samples.

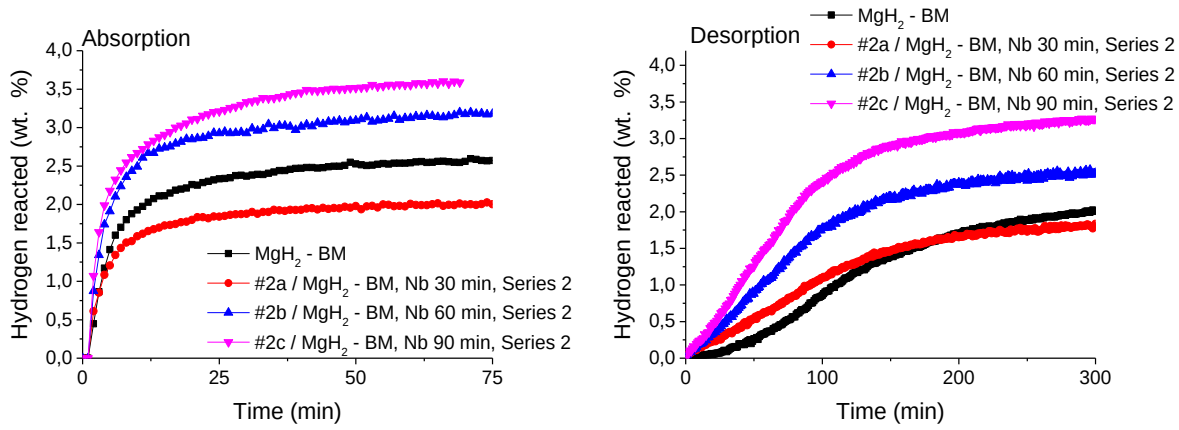

Fig. 4.27. Hydrogenation and dehydrogenation curves of the niobium coated, ball milled magnesium hydride powders – Series 2.

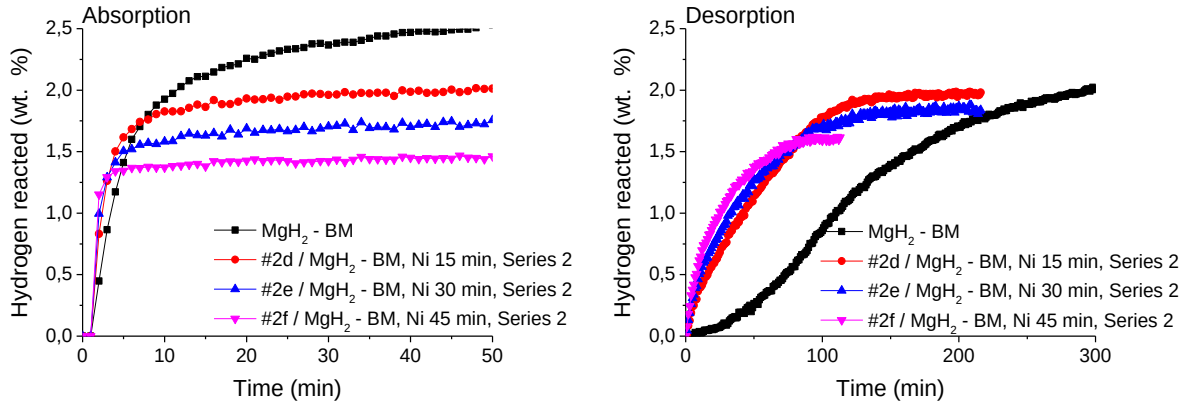

Fig. 4.28. Hydrogenation and dehydrogenation curves of the nickel coated, ball milled magnesium hydride powders – Series 2.

Except of comparing times of reaction and achieved capacities, a reaction speed changes can be studied. For open system, e.g. with the hydrogen inflow, it is usually calculated as the derivative of the amount of reacted (Absorbed or desorbed) hydrogen versus the time. Results in the initial minutes of the reaction are shown on plots below (Fig. 4.29 and Fig. 4.30). Absorption plots have typical exponential shape, where reaction starts rapidly and slowly extinguishes when the saturation area is reached. The desorption for niobium coated and for the pure hydride looks different: it poses a maximum point after several minutes for the start of reaction. It can be related to heat transfer problem – it is necessary to deliver large amount of heat to the sample to star the reaction, thus the reaction rate on the begging is slow. In case of absorption, heat also have to be dissipated, but the active material can store some amount of heat until it is removed. Moreover, on beginning of the process it is in metallic form, so the thermal conductivity is more than two orders of magnitude greater (Chapter 2), so heat can be

transferred faster. When the amount of MgH_2 in sample is lower, heat transfer is more negligible and its influence on desorption character is weaker. It can be observed for the nickel desorption derivative, there is some raise near 75 min reaction time but the dependence is more close to the exponential one.

Both of nickel and niobium samples have higher rate for absorption but the difference is higher for Nb coated powders (0.7 wt. %/min compared to 0.03 wt. %/min) than Ni one (0.7 wt. %/min compared 0.09 wt. %/min). Nickel doped materials poses also much better kinetics for the desorption than niobium samples, but the absorption kinetics is slightly lower.

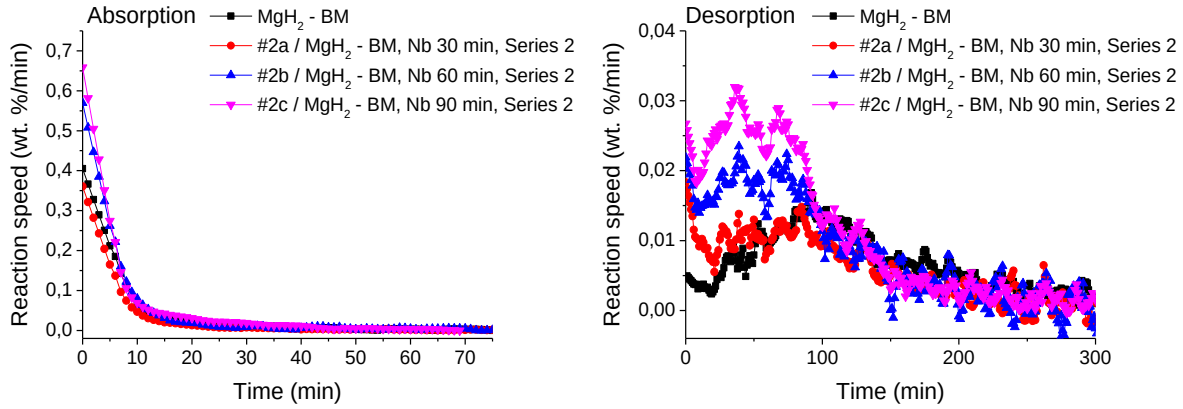

Fig. 4.29. Reaction speed, calculated as the derivative of the reacted hydrogen plot, for Series 2, ball milled, niobium coated magnesium hydride.

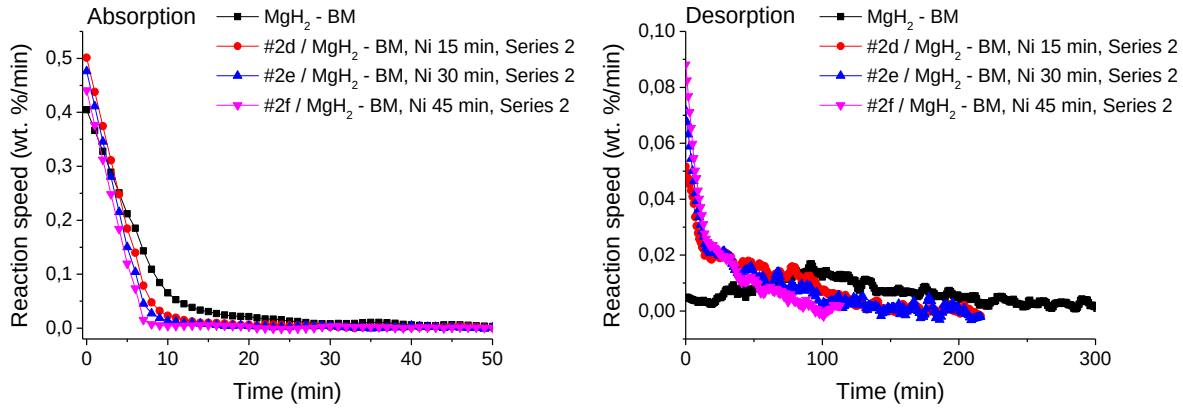

Fig. 4.30. Reaction speed, calculated as the derivative of the reacted hydrogen plot, for Series 2, ball milled, nickel coated magnesium hydride.

Series 3 ball milled, Nb- and Ni-coated materials (Fig. 4.31) exhibits similar effects, but there is an interesting observation for desorption plot. When it starts, it is relatively fast, then the increase suddenly stops and the amount of reacted hydrogen poses nearly linear time

dependence until it saturates. It is clearly seen on the derivative plot (Fig. 4.32). It starts with rate of 0.05 – 0.07 wt. %/min, then the reaction slows down (in case of pure MgH_2 and nickel coated it almost stops) and then the reaction rate raises to 0.01 wt. %/min and falls again when the reaction is close to the saturation point.

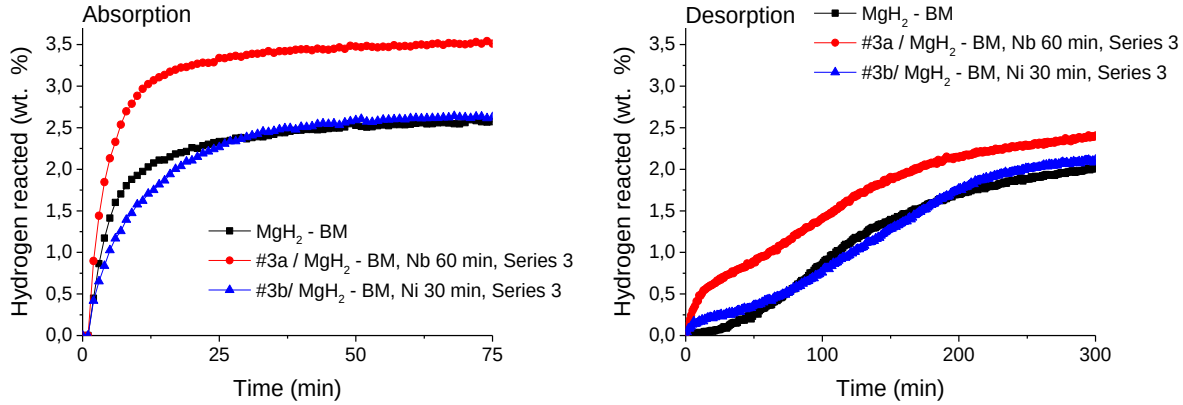

Fig. 4.31. Hydrogenation and dehydrogenation curves of the nickel and niobium coated, ball milled magnesium hydride powders – Series 3.

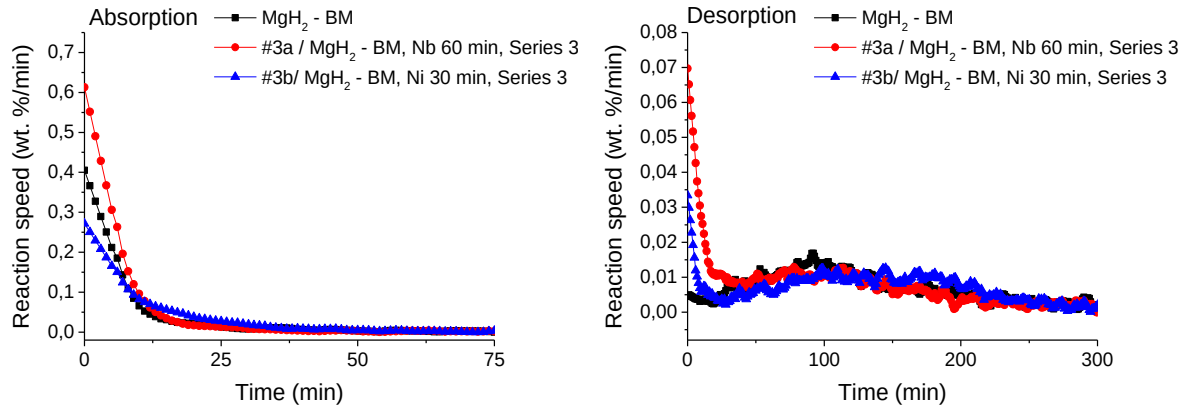

Fig. 4.32. Reaction speed, calculated as the derivative of the reacted hydrogen plot, for Series 3, ball milled, niobium and nickel coated magnesium hydride.

4.7. Analysis of the Pressure-Composition-Temperature dependencies

Pressure-Composition-Temperature curves for both absorption and desorption were taken at first for raw MgH_2 and nickel coated sample from Series 1 (Fig. 4.33). The hydrogen concentration saturates at 6.5 wt. % for the uncoated and at 5-6.5% for the nickel coated sample, where additionally a stronger dependence of the maximal hydrogen capacity on temperature and a higher slope of the plateau for the coated sample can be observed. A pressure position of the plateau is around 2 bars lower for coated sample, which suggests that coating allows

hydrogen to effectively transfer to magnesium at lower pressures. The thermodynamic parameters of the reactions were derived using van't Hoff equation. There is no significant difference in their values between uncoated and Ni coated samples - the amount of nickel introduced to the hydride is not large enough to form an alloy in large part of the sample, not only on the surface. In case of desorption process the entropies and enthalpies are overestimated for the nickel sample.

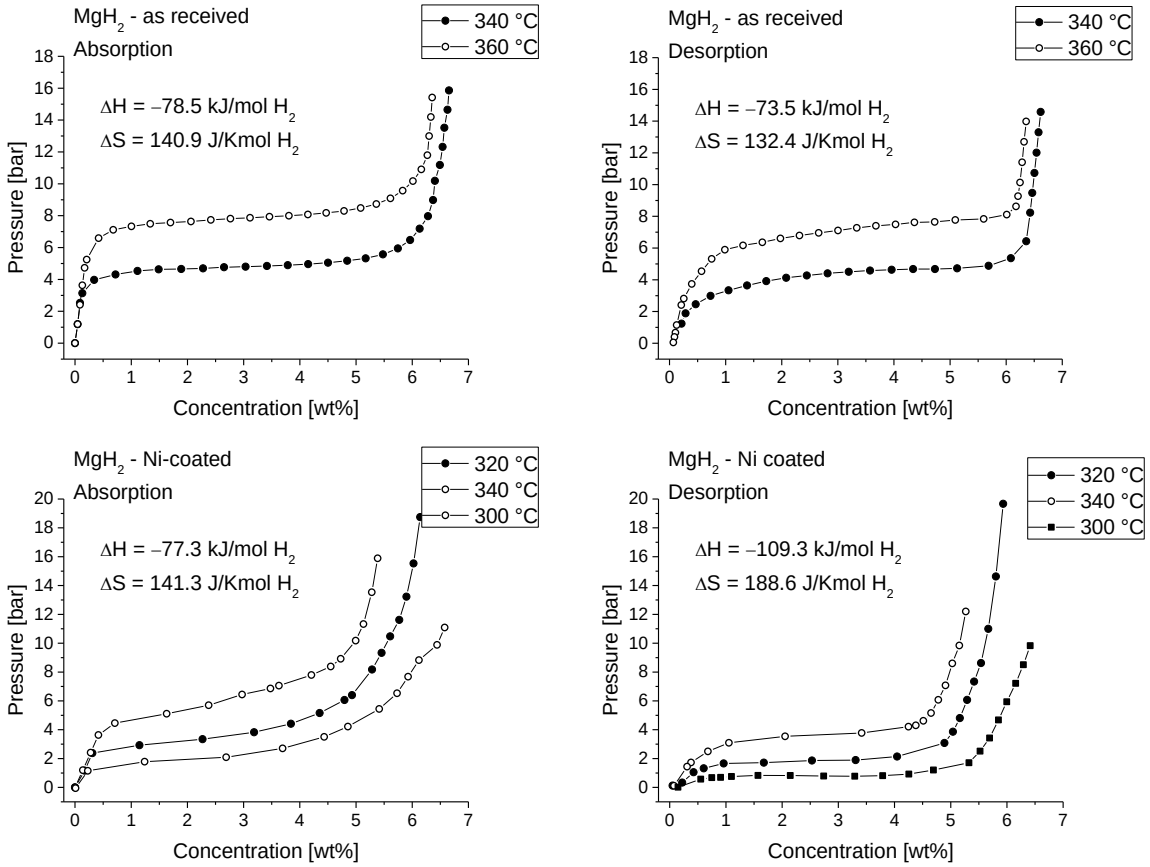

Fig. 4.33. Absorption and desorption PCT curves for uncoated MgH_2 and #1b (30min) nickel coated sample.

In addition, PCS measurement were performed also for one of the niobium materials (#3a, Nb 30min). Results (Fig. 4.34) indicates the increase of both of entropy (to ~200 kJ/mol) and enthalpy of reaction (to ~110 kJ/mol), probably due to the oxidation effects. It is interesting, that the increase in the enthalpy of the decomposition can be also noticed from the deeper peak for that sample on the DSC plot (Fig. 4.24), because of grater heat of reaction. I can be achieved 4.5-4.8 wt. % hydrogen concentration for that material and the plateau is more flat than for the nickel one. Desorption and absorption plateaus are shifted by 3 bars, and there is interesting

difference in the plot for low and high hydrogen concentrations. In case of absorption, transition from α to (α+β) phase (Chapter 2) is very sharp but or the desorption is more smooth. Opposite effect can be observed for when the amount of β increases.

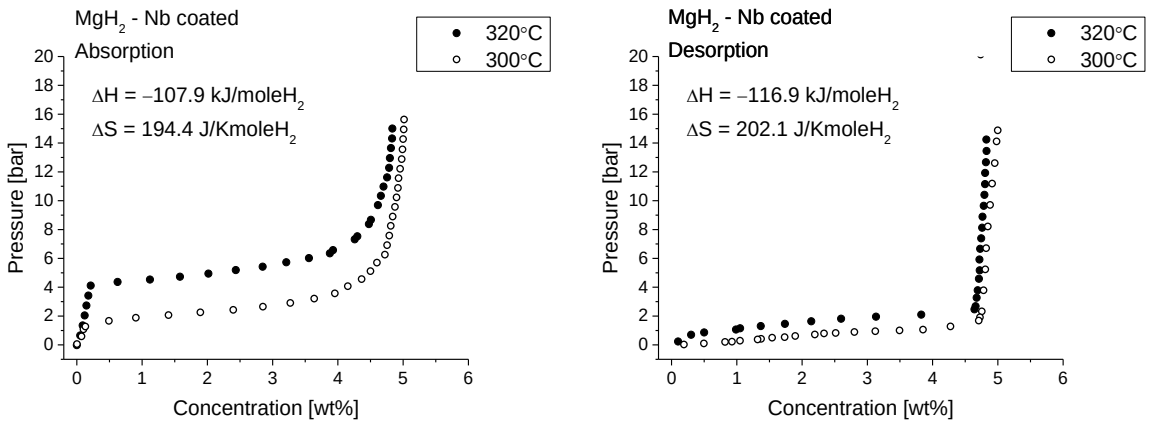

Fig. 4.34. Absorption and desorption PCT curves #3a niobium coated sample

4.8. Study of the influence of reaction cycling on the properties of coated powders

Previously described measurements were repeated for #1b nickel coated sample after ten dehydriding/hydriding cycles in order to check the layer quality and tolerance for cycling. Cycling was performed under 300 °C, with absorption pressure of 1 MPa and continuous vacuum for desorption. Hydrogenation curves and maximal capacity versus the cycle number are presented in Fig. 4.35. Coated powder has stable reaction kinetics (except of first cycle) and stable hydrogen capacity of ~2.85 wt. %.

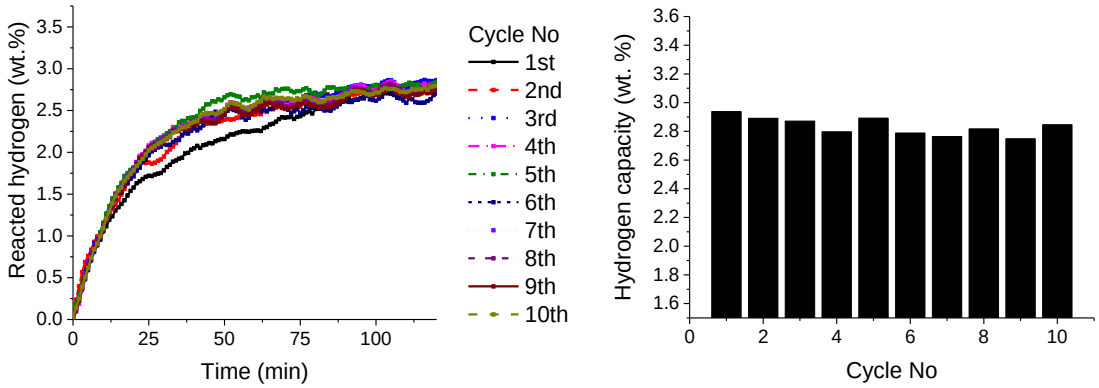

Fig. 4.35. Hydrogenation curve for ten cycles of reaction for sample #1b, and maximum capacity of the sample versus cycle number

Because maximal amount of reacted hydrogen is below predicted value, XRD measurements were performed in order to determine sample composition. Fig. 4.36 presents XRD pattern of material after the cycling. Only 38 wt. % of magnesium is in hydride form, the rest stays in metallic stage, probably because of too low pressure of reaction. No oxidation effect during cycling occurred.

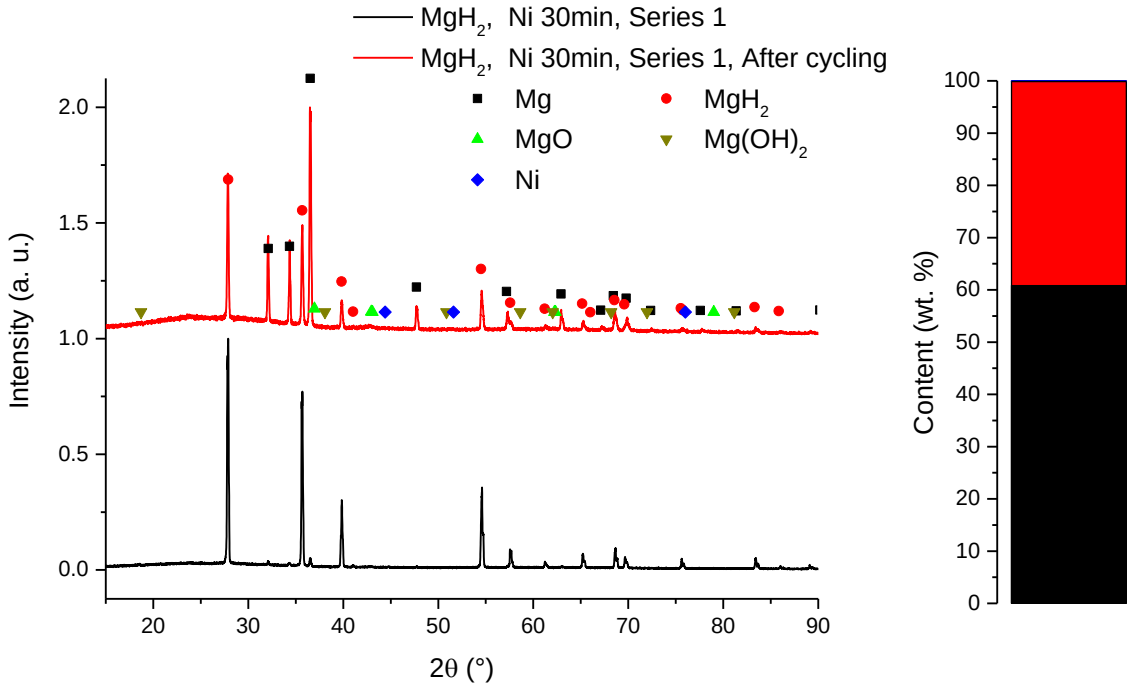

Fig. 4.36. XRD pattern and phase content of #1b nickel coated magnesium hydride after several reaction. Last cycle ended with absorption.

Fig. 4.37 presents SEM image and nickel distribution map on the surface of hydride grain. Metal coating is still present on the exemplary particle but the layer is cracked and partly detached, which is confirmed by EDS point measurements (Fig. 4.38) performed in points at the particle edge, interior and on visible rupture. The Ni-K line intensity is poorer on the crack comparing to the interior area. Apparently higher nickel content on the edges is an effect of slope coming from particle shape and orientation.

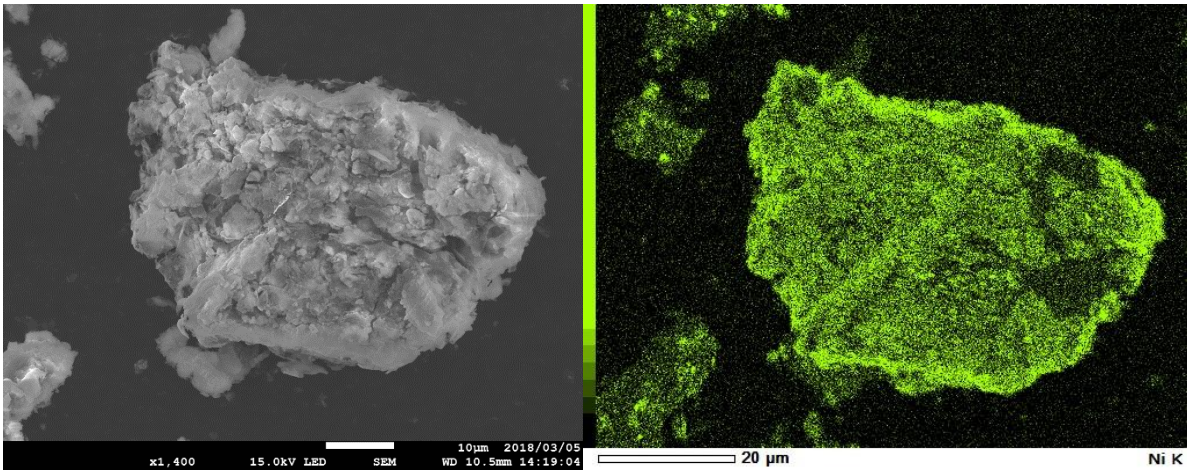

Fig. 4.37. SEM images and EDS map of nickel distribution for a particle of #1b, nickel coated sample after the hydriding/dehydriding cycling.

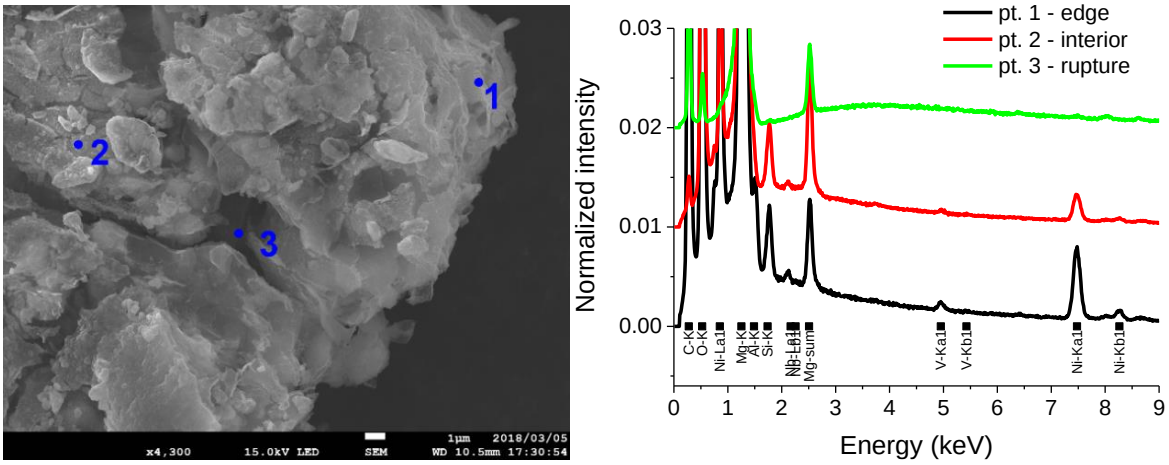

Fig. 4.38. SEM image and EDS spectra of Ni #1b nickel coated grains after reaction cycling. Spectra were collected at the edge layer area (pt. 1), internal layer (pt. 2) and at a hole in cracked layer (pt. 3)

The DSC spectra of raw, nickel coated and cycled hydrides, as well as their activation energies, are collected in the Fig. 4.39. What is interesting, the decomposition peak tends to shift back to pure MgH_2 level, which could be explained by cracking of the metal layer. On the other hand, the activation energy for the cycled sample is almost two times lower than for pure hydride and 45% lower than for initial run. We realize that, when the number ruptures on the layer surface grows and the interface between the magnesium and metal film is more open and exposed for the hydrogen gas, the dissociation, diffusion and penetration of hydrogen atoms through the nickel layer is more effective.

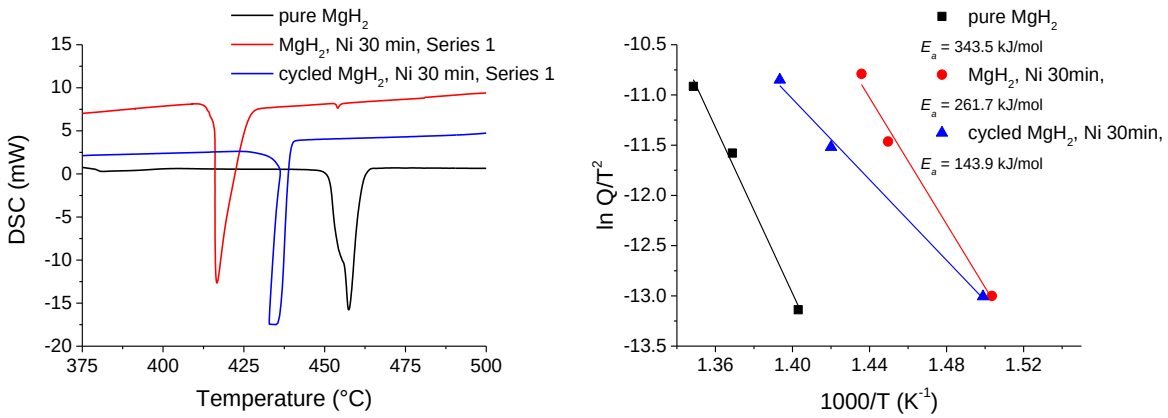

Fig. 4.39. The DSC plots and activation energies for the uncoated, the nickel coated hydride and for the sample after few reaction cycles.

4.9. Summary of the results obtained for coated magnesium hydride powders

The aim of the study was test of the possibility of introducing the catalytic elements to the magnesium hydride using magnetron sputtering. Instead of ball milling of MgH_2 and catalyst, deposition of a thin film of metal on the surface of each hydride grain. Thin films of the nickel, niobium and vanadium were successfully deposited with different sputtering times in three series: on the as received and ball milled magnesium hydride (Series 1); on the ball milled powder (Series 2) and on the ball milled powder with modified experimental setup (Series 3)

X-Ray diffraction pattern collected after the sputtering suffers of lack of reflections coming from the metal layers – obtained layers thickness is probably too low to get significant signal. XRD results showed that some of the samples are sensitive to oxidation. In case of the first group of materials, there is no significant oxidation/hydroxidation, but in case of second group, oxidation is strong because of higher reactivity of ball milled magnesium hydride. An amount of MgO in the sample varies from 20 to 30 wt. % for Nb-coated materials and 40-80 wt. % for nickel coated samples and is growing while increasing sputtering time. Nickel coating makes ball milled powders much more sensitive for oxidation. Problems spotted during the study of Series 2 powders were motivation to modify the experimental setup. Vacuum pumps were improved to give one order of magnitude better vacuum (10^{-4} mbar) and a special, remotely controlled cap was added, to cover the powder container while moving to argon filled glovebox. After such modifications amount of oxides was reduced to 20 wt. %. Other interesting observation is the partial decomposition of the MgH_2 to pure magnesium, which is stronger in case of ball milled powders. Coated hydride poses lower activation energy, which enhances desorption kinetics and magnesium hydride may partially decompose due to plasma heating.

SEM observations and EDS mapping shows nickel and vanadium completely covering the surface of as received magnesium hydride grains. Thanks to the proper mixing during the deposition, film thickness is uniform and reaches 320 nm and 170nm for the nickel and vanadium coatings respectively. Artefacts in shape of nanoparticles present on the grains surfaces are probably a part of the finest powder fraction sticked to the bigger grains. In case of coating of ball-milled powders huge problem of the agglomeration was spotted. Nanoparticles with ~100 nm are present in the sample and forms big (~50μm) conglomerates. Sputtering of metals on such structures is results in poor uniformity of thin films – some of particles are fully covered with niobium or nickel films and some of them remain clear. Such differences in local effective amount of the introduced dopants and their structure will cause poor and unclear results of thermodynamic and kinematic studies. The effective catalyst content obtained from EDS elemental analysis of large scale images stays between ~0.2-1.8 wt. %, only exception are niobium samples from Series 2, which contains up to 7 wt. % of Nb, but this values are probably overestimated due to not uniform coating. In addition, because of strong sputtering target erosion, last nickel sample from Series 3 contents around 5 times less nickel than expected.

Presence of thin nickel, vanadium and niobium films on the surface of magnesium hydride reduces the activation energy for hydrogen dissociation or recombination. The reductions is the largest for not-milled, nickel coated samples and can reach 150 kJ/mol. For ball milled powders the reduction is smaller, around 40 kJ/mol, but this is the effect of oxidation shells present on the hydride surface. In addition, owing to the surface modification, the effective hydrogen desorption temperature was decreased by about 50 K. Following model was proposed to describe above effects. The kinetic barrier can be reduced by coating to a level which has its limit at the full coverage of magnesium particles by catalyst layer. Further increase in coating thickness may affect the effective decomposition temperature by formation of magnesium alloys on the grain surface. Niobium and vanadium coating have smaller impact on the shift of decomposition temperature, that samples poses nearly the same, or even ~5-10 K higher point of desorption compared to the pure MgH_2. Because of the oxidation and partial decomposition of the magnesium hydride the analysis of the results obtained for Series 2 and Series 3, ball milled powders, is uncertain and not clear.

Hydrogen absorption and desorption kinetics studied using a Sieverts apparatus is greatly enhanced for most of the samples. Nickel coating on not milled powders can effectively enhances hydrogenation and dehydrogenation rates, reducing time needed for charging and discharging of the tank down from more than 12 hour to 70 and 15 min. The impact on

desorption kinetics is stronger than absorption. Vanadium coating, probably because of lower hydrogen permeability, causes small enhancement in dehydrogenation rate, but the absorption reaction it is slower than the pure MgH_2. The equilibrium hydrogen capacity is lower the theoretical value (7.5 wt. %), it reaches around 2 – 3.5 wt. %, due to only partial decomposition of magnesium hydride under that conditions. Ball milled magnesium hydride exhibits better reaction kinetics for absorption process. Times needed to react of 90% of hydrogen can reach 33-25 min for niobium coating and 11-4 min for nickel one, but nickel samples contains smaller amounts of the hydride (~11-5 wt. %) due to oxidation. More studies are needed to distinguish effects of amounts of the hydride and oxide to reaction kinetics. Effective measured hydrogen content is near 1.5-3.5 wt. % and 1.2 – 1.7 wt. % for niobium and nickel coated samples, which is far from the expected values (6-7.5 wt. %).

A reaction speed time dependence, defined as the derivative of reacted hydrogen content shows interesting behaviour. For absorption it has typical exponential shape - reaction starts rapidly and slowly extinguishes. On the other hand, the desorption poses a maximum efficiency after several minutes from the beginning of the process. Differences can be explained by the different heat transfer models: for desorption, it is necessary to deliver large amount of heat to the sample to star the reaction, which makes initial reaction speed low. In case of absorption, heat also have to be dissipated, but the active material can store some amount of heat until it is removed. Moreover, on beginning of the process it is in metallic form, so the thermal conductivity is much higher the hydride form, so heat can be removed faster. Both of nickel and niobium samples have higher rate for absorption but the difference (0.7 vs 0.04 wt. %/min for Nb and 0.5 vs 0.09 wt. %/min for Ni). Nickel doped materials poses also much better kinetics than niobium samples, but the absorption kinetics is slightly lower.

Despite the fact that the sorption kinetics is enhanced, the thermodynamics of the hydride did not change. Entropies and enthalpies of reaction stays on the similar level for nickel coated sample as in the as received magnesium hydride. The amount of nickel introduced to the hydride is not large enough to form an alloy in large part of the sample, not only on the surface, so typical alloying method of improvement cannot be applied. Hydrogen content saturates at 4.5-6.6 wt. % and the plateaus of coated samples are at 3-4 bars lower level than pure MgH_2. Because of the surface modifications, coated powders are characterized with slightly higher slopes, especially near saturation region. Ball milled powders coated with niobium poses the increase of both of entropy (to ~200 kJ/mol) and enthalpy of reaction (to ~110 kJ/mol), probably due to the oxidation effects.

Medium coated nickel sample from the first group was chosen to cycling measurements. After several cycles of absorption and desorption under 300 °C and with 1 MPa / 0.001 MPa pressure SEM observations, as well as DSC measurements were repeated. Metal coating is still present on the exemplary particle but the layer is cracked and partly detached. What is interesting, the decomposition peak tends to shift back to pure MgH_2 level, but the activation energy for the cycled sample is almost two times lower than for pure hydride and 45% lower than for initial run. We realize that, when the number ruptures on the layer surface grows and the interface between the magnesium and metal film is more open and exposed for the hydrogen gas, the dissociation, diffusion and penetration of hydrogen atoms through the nickel layer is more effective.

The study shows that magnetron coating of hydride powder can be considered as an effective way for introduction of the catalytic elements and desirable modification of properties of the hydride materials. Results give several options for future work. At first mixing methods can be enhanced by introducing ultrasonic vibrations or by adding anti-caking agents to allow uniform coating of nanopowders. Next, many different types of hydrides, as well as coating materials, including alloys can be tested and sputtered. An interesting application could be the coating of carbon structures in order to increase binding energy of hydrogen molecules on their surface to improve storage by physisorption.

5. HYDRIDE – GRAPHITE COMPOSITES WITH ALIGNED FILLER PARTICLES – RESULTS AND DISCUSSION

This chapter presents results of try of improvement of the heat transfer performance of magnesium hydride. A special, electric field aligned, composites of graphite, magnesium hydride and epoxy resin were prepared and examined with X-ray diffraction, Sieverts apparatus and on Thermal Transport option on PPMS device. In addition a trials of structure imaging were performed.

5.1. Samples overview

Three series of composite samples were prepared from different filler materials and with the different designation.

- Series 0 - The first one was used for the preliminary tests of aligning technology. Graphite was mixed with resin in three grades: 5, 10 and 15 vol. %. For each grade one isotropic sample and one sample aligned in 90V/mm electric field was prepared. Each experimental method (except of the Sievert's hydrogenation) was tested for that samples.
- Series 1 – Composites from this group consist of resin matrix filled with graphite and the magnesium hydride according to the proportion below. Both aligned and isotropic samples were prepared. The amount of graphite is increasing linearly while the resin content is kept constant. It was decided to produce samples with large resin content in order to avoid problems with samples mechanical strength – the aim of the study was to check the possibility of improvement of heat transfer performance by aligning of graphite flakes - materials with the higher hydride content can be produced in next step of the study.

Table 5.1. Proportions for preparation of series 1 composite materials.

Sample No	Resin [vol. %]	MgH_2 [vol. %]	Graphite [vol. %]	MgH_2 – graphite wt. ratio	Type
#1a	50	50	0	-	Isotropic
#1b	50	47.5	2.5	95 - 5	Isotropic
#1c	50	47.5	2.5	95 - 5	Aligned
#1d	50	45	5	90 - 10	Isotropic
#1e	50	45	5	90 - 10	Aligned

- Series 2 – Materials from this group are based on lanthanum-nickel alloy $LaNi_5$, graphite and silicone resin. The main motivation of using of this materials was to check how the

presence of metallic particles will influence on the aligning process. In the previous group of samples, we expected that dielectric magnesium hydride will not affect the electric field. Because the pure metallic magnesium easy undergo oxidation and is dangerous to use, more conventional, safe alloy was chosen. Three types of sample were prepared (Table 5.2), with pure lanthanum-nickel and with graphite addition, isotropic and aligned in electric field.

Table 5.2. Proportions for preparation of series 2 composite materials

Sample No	Resin [vol. %]	$LaNi_5$ [vol. %]	Graphite [vol. %]	$LaNi_5$ – graphite wt. ratio	Type
#2a	50	50	0	-	Isotropic
#2b	50	45	5	90 - 10	Isotropic
#2c	50	45	0	90 - 10	Aligned

5.2. X-Ray diffraction study of the structure of composites and its anisotropy

At first, the structure of the samples was examined with X-ray diffractions. Measurements were focused mainly on the analysis of structural anisotropy. In conventional powder diffraction it is assumed that crystallines have random orientation and the intensities are average on all angles. In presence of alignment (texture), peak intensities will be varied, depending on orientation between sample and scattering direction. By comparing their relative intensities the degree of the anisotropy can be derived. Graphite poses very specific XRD pattern - Fig. 5.1 presents an example of results for 10 vol. % graphite filled material. Because of planar, flakes structure, the [002] reflection is very high comparing to the other directions – [010] and [100].

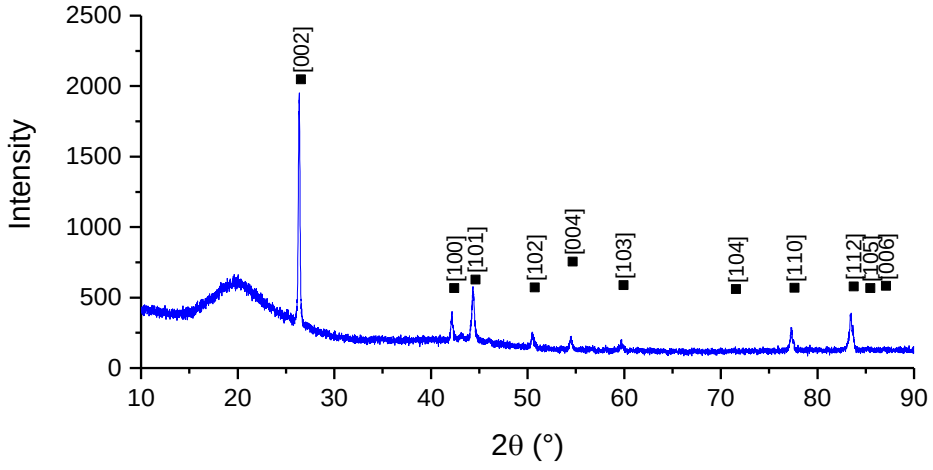

Fig. 5.1. X-ray diffraction pattern of isotropic, 10 vol. % graphite filled composite.

By choosing measuring proper orientation (Fig. 5.2) between the sample and incident X-rays, the [002] reflection intensity can be either boosted or reduced. If the scattering vector is perpendicular to the [002] direction (or, it is parallel to the flake/plate) the intensity is larger. But when the scattering vector is in parallel position, the [002] intensity is reduced.

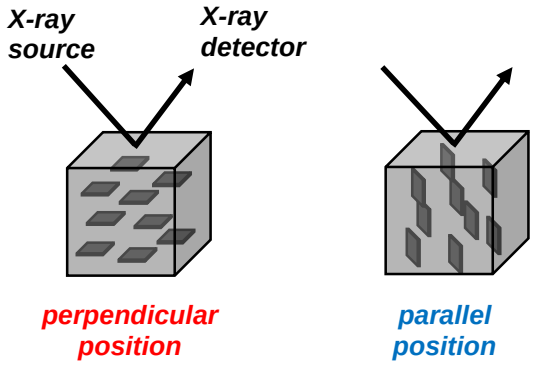

Fig. 5.2. Sample and X-ray orientation possibilities

Example of that phenomena is shown on the and Fig. 5.3, where the XRD spectra under different orientations of 10% graphite filled composite are presented. It can be observed that [002] line intensity is enhanced when the sample is measured in perpendicular direction. The intensity ratio, which can serve as the alignment degree measure, is decreasing while putting more filler. It suggest that the alignment is poorer for higher-filled samples. It may be caused by two reasons: At first, the interactions between induced dipole of particles are weaker than the interactions with external electric field. The second reason is fast increase of the mixture viscosity, which the wetting of particles more difficult and the resin is harder to cast. The solution for both problems can be use of resin with low viscosity, however product available on the market, especially silicon resins, usually have very high viscosity (>1 Pa ·s). Other option is to dilute the resin with the special thinner, also based on polysiloxane materials, which reduces viscosity of liquid resin and incorporates into the resin structure during curing process. However, poorer mechanical and curing performance of such diluted mixtures must be taken into account hardening time will be longer and cured composite may poses cracks and sample uniformity can be poorer. Some parts of the thinner may not react with the resin and can affect on experimental procedures. It could be removed by evaporation and vacuum heating, but then the effective composite composition will be changed and difficult to predict.

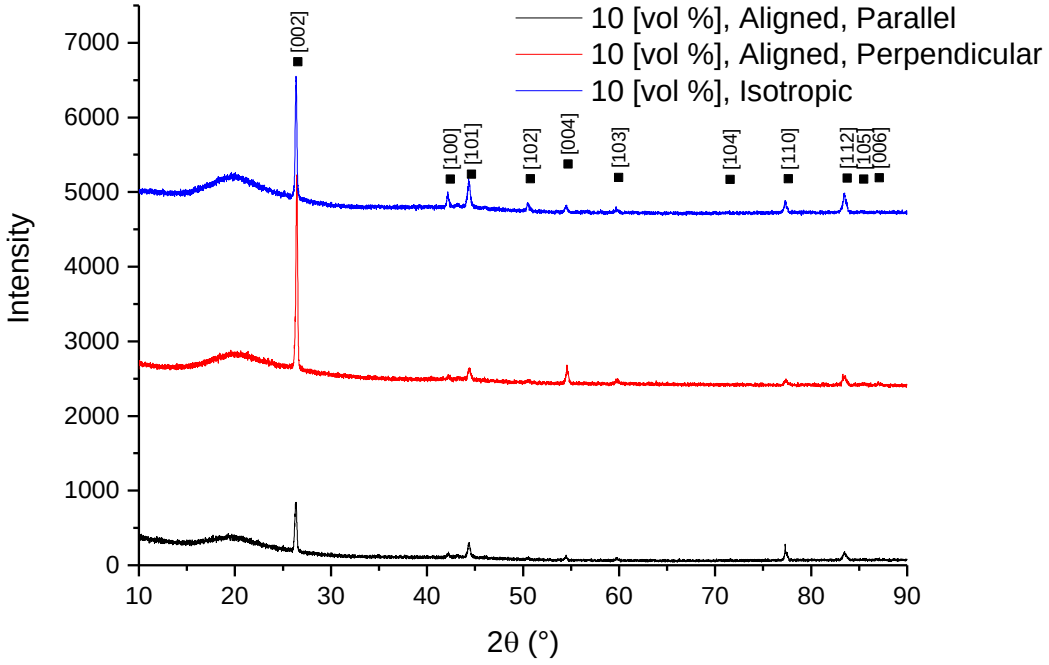

Fig. 5.3. Full X-ray diffraction pattern of 10% graphite filled composites

Direct comparison of peak intensities is not best way to analyse the structural anisotropy because the single peak intensity may depend on the background and sometimes it is difficult to keep constant conditions, such as sample size, beam intensity during the measurement. More accurate is to obtain the orientation factor prom Rietveld [107] refinement to the whole experimental data and to use March-Dollase factor of orientation [122]. For given [hkl] direction preferred orientation (r) value means:

- $r = 1$ means the orientation of [hkl] is completely random
- $r < 1$ means that the [hkl] direction is the preferred orientation of the crystallites
- $r > 1$ means that the [hkl] direction is preferentially avoided

Fig. 5.4 shows data obtained from pattern refinement for series 0 (only graphite) composites, calculated for both of isotropic and aligned samples. Full fitting results (data, calculated profile, background and difference plots) are listed in the Appendix. For oriented materials, XRD data was collected on the base surface of the cylindrical sample – which corresponds to _|_ orientation from previous analysis. March-Dollase factor is generally lower than unity for aligned samples and is getting closer to 1, while increasing the graphite content, which confirms previous analysis of the orientation degree. For isotropic samples, orientation coefficient is close to unity, but for the 10 vol. % graphite filled sample has value of 1.09, which may suggest

the needle alignment of graphite flakes. On the other hand, this effect could be caused by measurement or refinement errors.

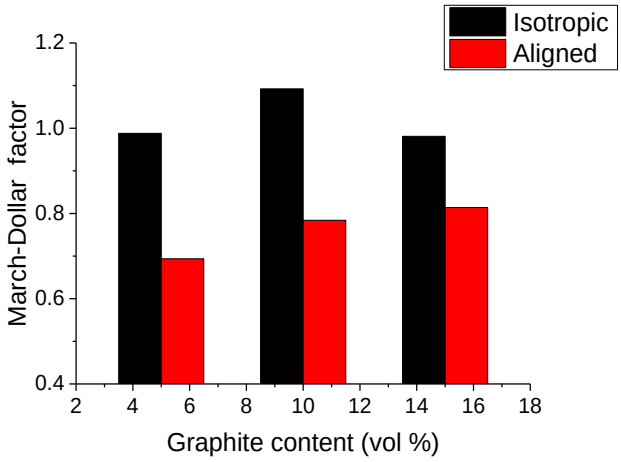

Fig. 5.4. March – Dollase preferred orientation parameter [002] for series 0 composites.

After testing of the analysis methods on graphite-silicone resin composites, the same steps was repeated for composites containing magnesium hydride and lanthanum-nickel alloy. Full diffraction pattern are presented on plots below. Fig. 5.5 presents results for composites without the graphite (#1a), and with 95-5 graphite-MgH_2 composition, both isotropic (#1b) and aligned (#1c). Fig. 5.6 shows data with 90-10 graphite-MgH_2 composition, isotropic (#1d) and aligned (#1e), compared with the results for composites without the graphite (#1a). Identified graphite and magnesium hydride reflection were marked on the plots with the square and triangle dots. The results are consistent with expectations – [002] reflection is increased, what suggest the presence of texture and aligning of the graphite flakes. March-Dollase factors (Fig. 5.7) are lower for oriented materials, only small difference between 2.5% and 5% graphite filled composites can be observed. It means, that 5% filling still can be effectively oriented and the problems with weaker influence of the electric field known from series 0 materials, probably will appear with higher graphite amount. Preferred orientation parameter for isotropic samples is close to zero, however there are again some deviations for 5% sample. What is important, for all samples neither of magnesium oxide or magnesium hydroxide reflections can be found. This is important observation from practical, technology point of view – magnesium hydride immersed in silicon resin can withstand ambient atmosphere and it is not necessary to perform curing process inside the neutral gas filled chamber.

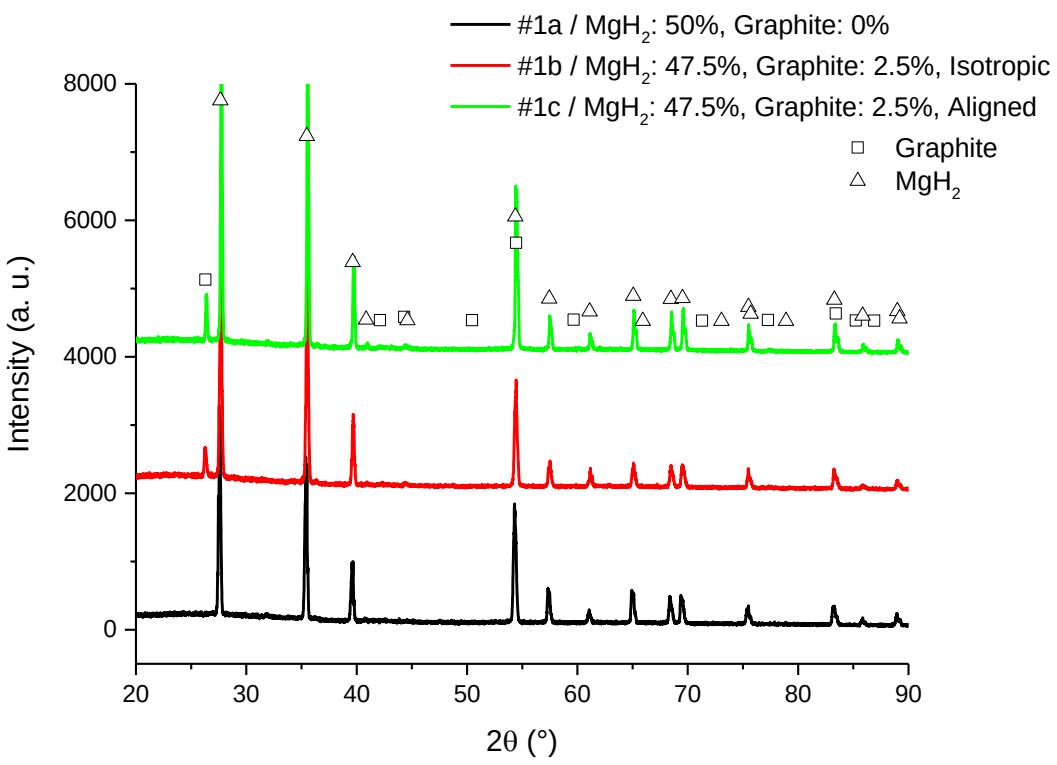

Fig. 5.5. Full X-ray diffraction pattern of magnesium hydride and graphite filled composites: samples #1a, #1b and #1c.

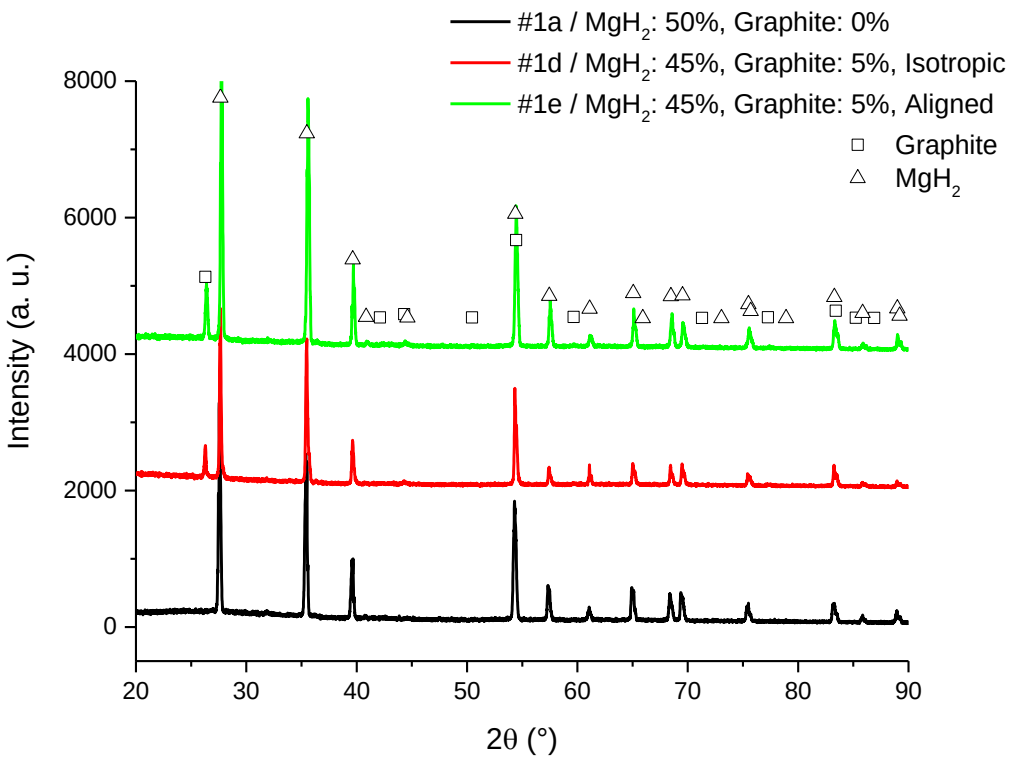

Fig. 5.6. Full X-ray diffraction pattern of magnesium hydride and graphite filled composites: samples #1a, #1d and #1e.

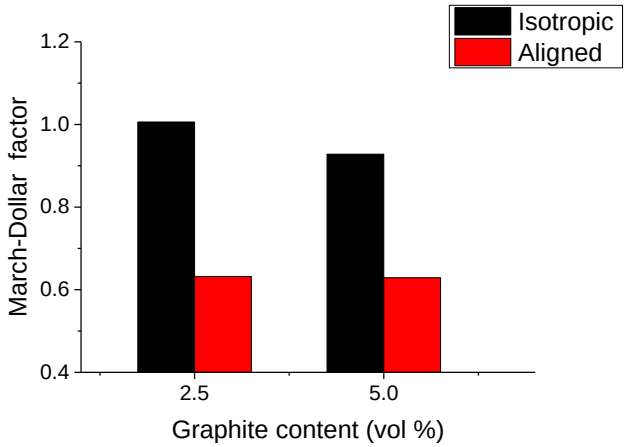

Fig. 5.7 March – Dollase preferred orientation parameter [002] for series 1 composites.

Analogic results were obtained for lanthanum-nickel based groups of composites (Fig. 5.8). No significant oxidation effects were found and the orientation parameters for isotropic and aligned sample was calculated as 0.9426 and 0.6479 respectively.

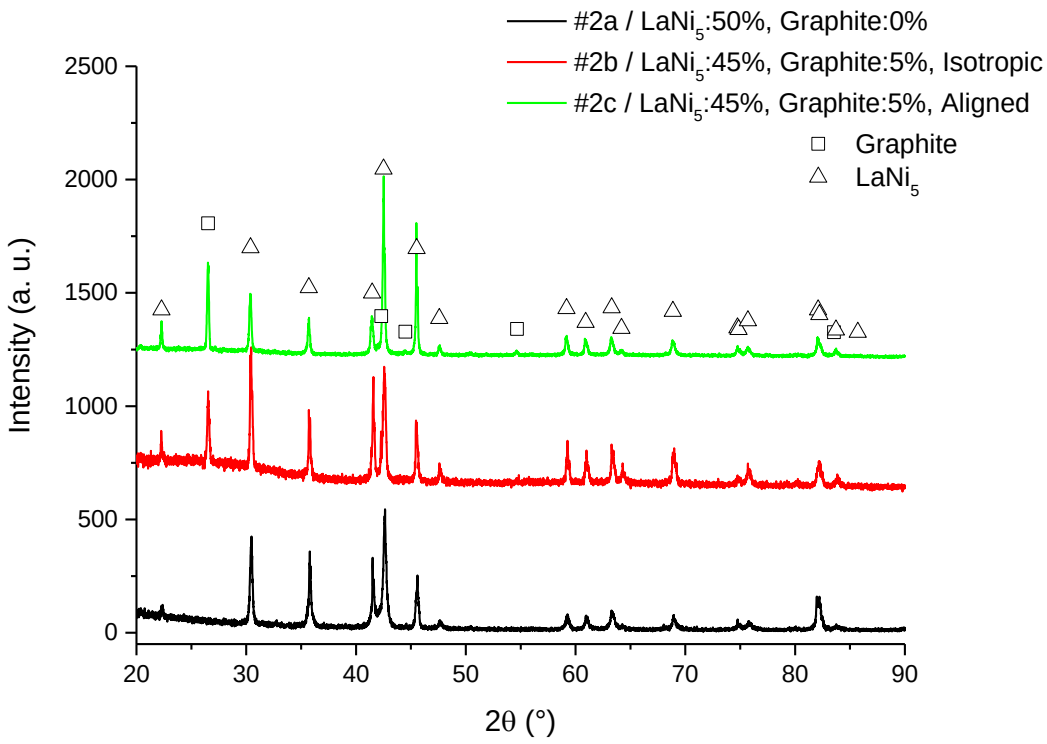

Fig. 5.8. Full X-ray diffraction pattern of lanthanum-nickel and graphite filled composites: samples #2a, #2b and #2c.

5.3. Thermal conductivity measurements

Next step of the research are the measurements of the thermal conductivity performed on PPMS Thermal Transport option. At first, study was focused on graphite-resin composites in order to analyse how alignment affects on the effective heat transfer parameters of composite. Thermal conductivity in room temperature was measured in different configurations (Fig. 5.9) parallel and perpendicular to the aligned flakes.

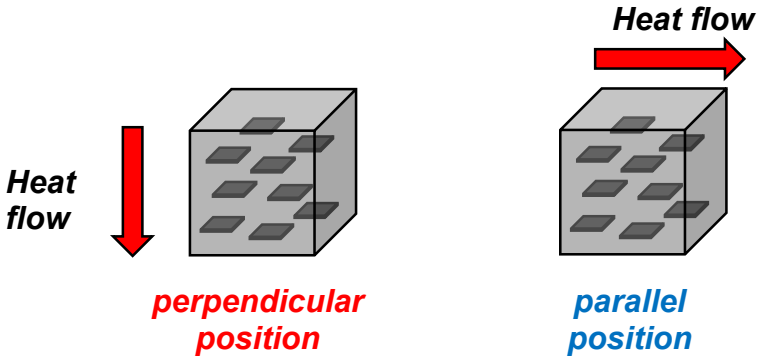

Fig. 5.9. Sample orientations configuration for thermal conductivity measurements.

The results are presented on Fig. 5.10. Effective thermal conductivity is increasing while introducing more graphite into the resin. It ranges from 0.5 W/m·K for 5 vol. % sample to 1.05 W/m·K for isotropic, 15 vol. % filled sample while the conductivity of pure resin is close to 0.2 W/m·K. The anisotropy of the thermal conductivity is easy observed – when measured along the plates it is around 0.3 W/m·K greater than measured across the plates.

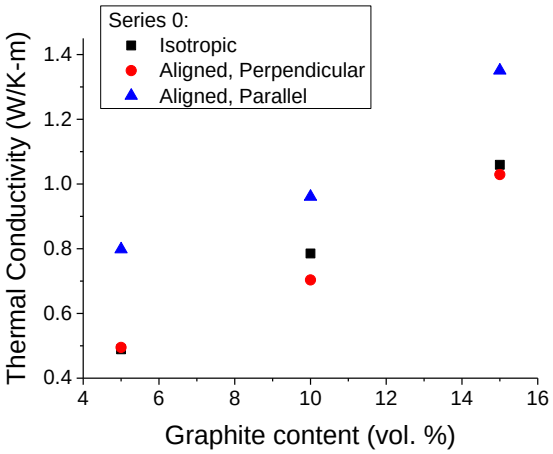

Fig. 5.10. Thermal conductivity versus graphite content measured for different sample orientation.

The difference is low compared to the difference between thermal conductivities along and across single graphite flake, but the graphite is only 15% vol. of the composite and large part of the heat flux flows through the resin matrix. What is interesting, the difference between the non-oriented and perpendicular results are much smaller, than the difference between the non-oriented and parallel ones, what is the positive results. Big enhancement of conductivity in one direction is compromised with only low reduction of conductivity in the other direction. Thermal Conductivity Enhancement, defined as a percentage growth of the TC in parallel direction in relation to the non-oriented sample. The largest improvement was achieved for 5 vol. % graphite composite (63%), which is the effect of the highest alignment. For higher filled materials, a percentage growth is lower, between 22% and 27% for 10 and 15% graphite composites respectively. The value obtained for the last sample is not the smallest one – what is unexpected, because from XRD refinement the lowest anisotropy was achieved. It may be caused by the fact, that the conductivity can be enhanced not only by alignment, but even by making the filler particles to become closer, to force them to form the conductive, net-like aggregates, what can happen in higher loaded composites.

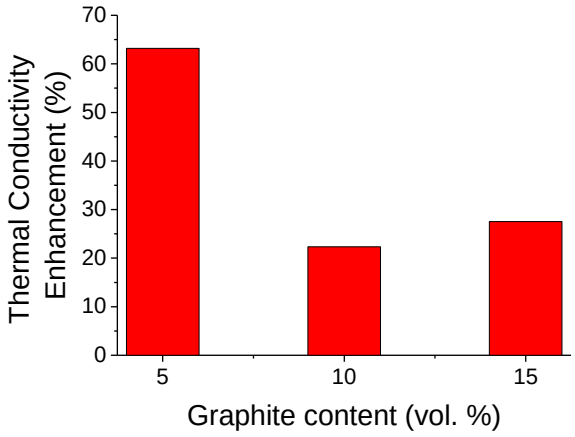

Fig. 5.11. The enhancement of the thermal conductivity vs the graphite content for series 0 composites.

Also electric resistivity measurements were carried out (Fig. 5.12). Samples conduct electricity better in direction along the flakes, and the differences are more than one order of magnetite high ($1.5 \cdot 10^4$ Ω·m to $2.2 \cdot 10^5$ Ω·m). When increasing filler content, the resistivity drops down to $2.4 \cdot 10^4$ Ω·m. Comparing with the thermal conductivity, the anisotropy is stronger, but this is the effect of much stronger anisotropy of electrical than thermal conductivity for single graphite flake.

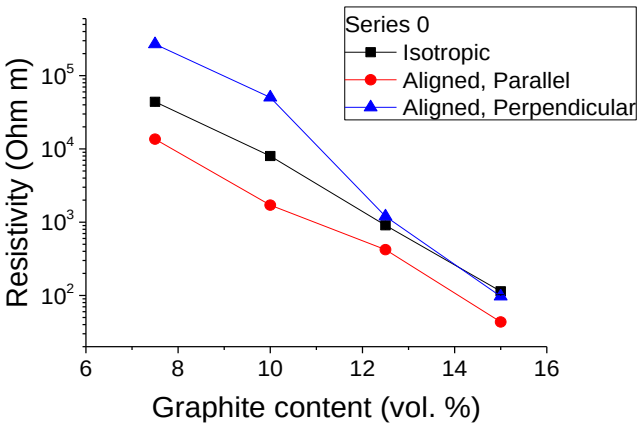

Fig. 5.12. Specific resistivity versus graphite content in composites measured for different sample orientation.

Except of the room temperature study, the measurements of temperature dependence (from 300 K to 4K) of the thermal conductivity was performed. Fig. 5.13 presents results obtained for the medium graphite filled material, both aligned || and isotropic sample. Typical polycrystalline/amorphous behavior of the composites, corresponding to the phonon scattering on crystallites boundaries, was found. The thermal conductivity is increasing fast and low temperatures and tend to saturate near to the ambient conditions. Because the literature reports the possibility of switching of electron part of conductivity in different materials with high magnetic field, measurements of in 8 Tesla field were performed. The results suggest limited change in the thermal conductivity, however it must be taken in to account, that heat conduction in graphite is based mainly on the phonons and the graphite loading in the composites (10% vol.) is relatively too low to observe the effect.

Before transferring to the next group of composites, a conductivity of pure resin was analyzed. At room temperature it reaches value of 0.2 W/m·K (Fig. 5.14) and its temperature dependence poses a specific bump near 180 K. It is the effect of glass transition of silicone polymer – since glass transition is the second order type of transition, change of the specific heat occurs and therefore, change of thermal conductivity. In lower temperatures, material behaves as typical polymer.

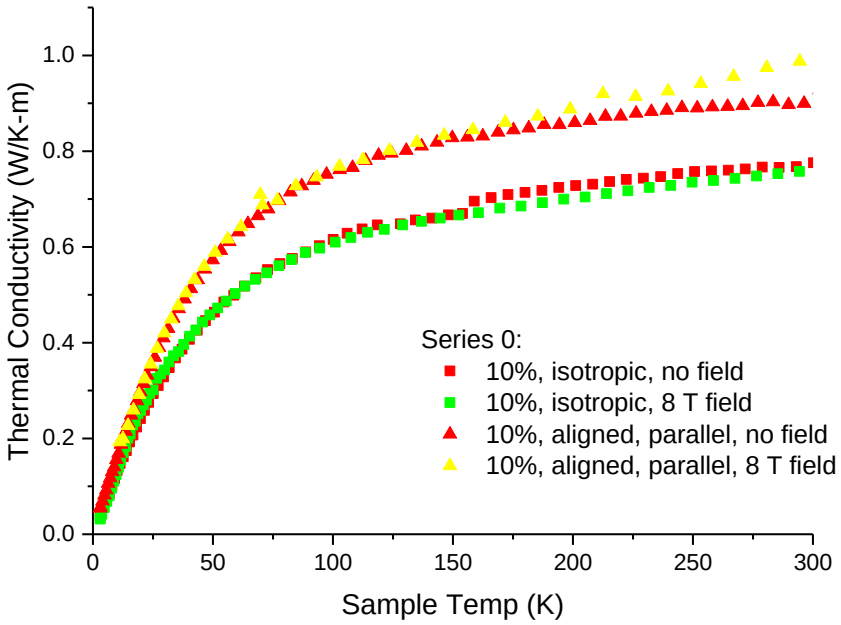

Fig. 5.13. Thermal conductivity versus temperature for 10% graphite composites (aligned and isotropic sample)

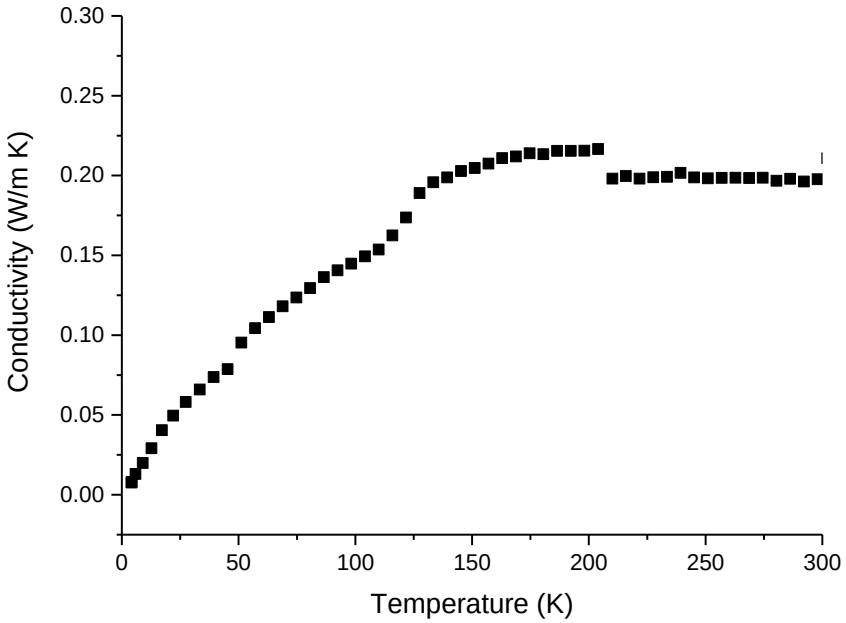

Fig. 5.14. Thermal conductivity versus the temperature for pure silicone resin.

Result of conductivity measurements for Series 1 (MgH_2 – based) materials are presented on Fig. 5.15. Temperature plot is similar to the pure resin, but the thermal conductivity is enhanced to the level of 0.8 -1.2 W/m·K, because of presence of magnesium hydride (bulk conductivity ~1.2 W/m·K) and graphite. What should be pointed out, the peak in conductivity

coming from the glass transition is present in 0% graphite composite (#1a), but it is getting smoothed while increasing graphite content. Graphite poses more dielectric character of thermal conductivity (Chapter 2), so it could enhance the thermal conductivity near temperatures 150-200K and reduce visible bump.

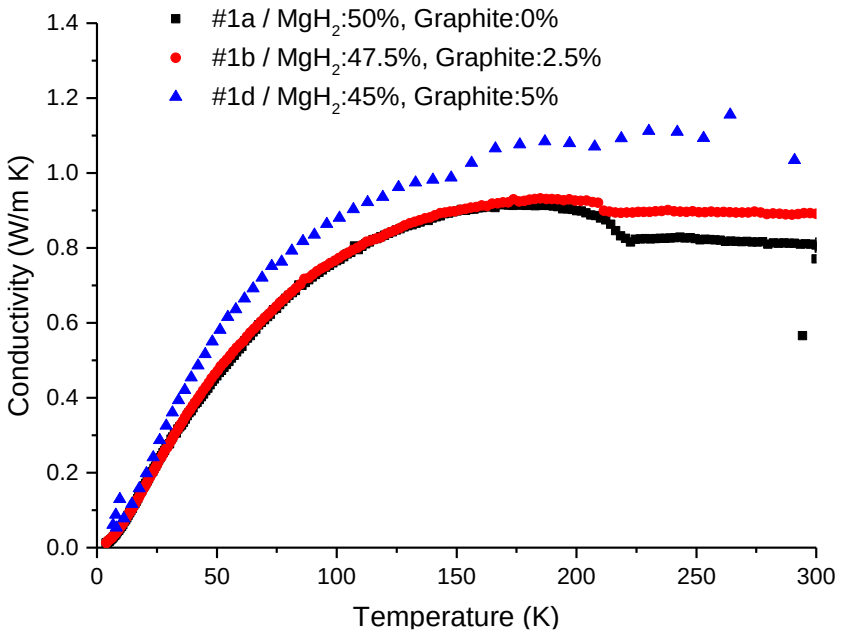

Fig. 5.15. Thermal conductivity versus the temperature for #1a, 1b and 1d composites

The room temperature thermal conductivity anisotropy and its enhancement of MgH_2 composites (Fig. 5.16) behaves as can be expected from study of Series 0 composites. The thermal conductivity is of isotropic materials is growing while increasing graphite content and it reaches 1.08 W/m·K for the last sample. By the alignment it can be enhance to the level of 1.24-1.28 W/m·K and the percentage growth related to the isotropic sample is 43% and 22% for samples #1c and 1#e respectively, so it is lower for more graphite loaded sample. A conductivity of material without the graphite (#1a) is around 4 times higher than the pure resin and around 80 times better than the values reported for the powdered magnesium hydride (Chapter 2). It is expected, that even preparing of composite without any high conductive fillers can improve the reaction ratio, just by keeping powder in bulk form. Powder can be made bulk by pelletizing, but the pellets of pure MgH_2 are unstable and cracks because of material expansion during the hydrogenation reaction. Rubber-like material, used as binder, can absorb active material expansion and reduce the tensions in the sample, keeping it bulk.

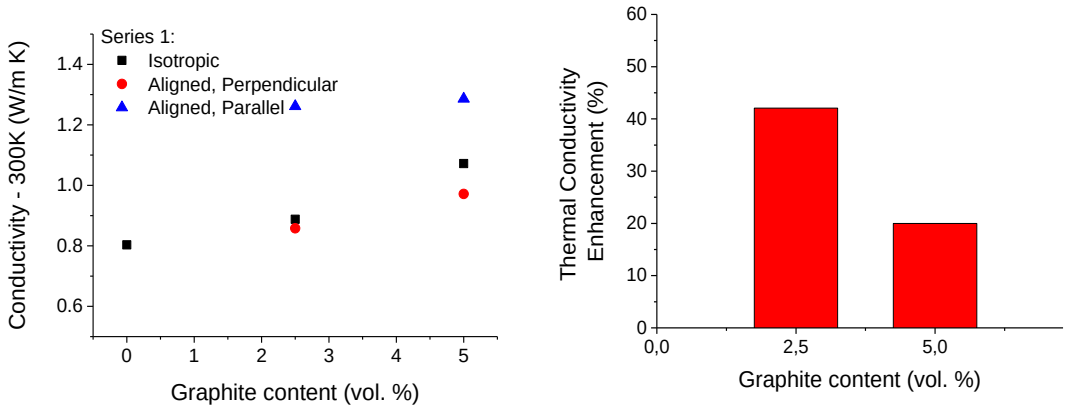

Fig. 5.16. Thermal conductivity of aligned and isotropic samples and its enhancement as a function on graphite content for series 1 composites.

Thermal conductivity of lanthanum – nickel composites is slightly larger (Fig. 5.17) because of metallic state of used filler. It reaches 1.35 W/m·K for sample without graphite addition. The anisotropy of the thermal conductivity of graphite filled material is also present (Fig. 5.18), measured across the graphite flakes gives 1.26 W/m·K and measured along the flakes gives 1.6 W/m·K. Measurements for isotropic sample could not be performed due to sample cracking.

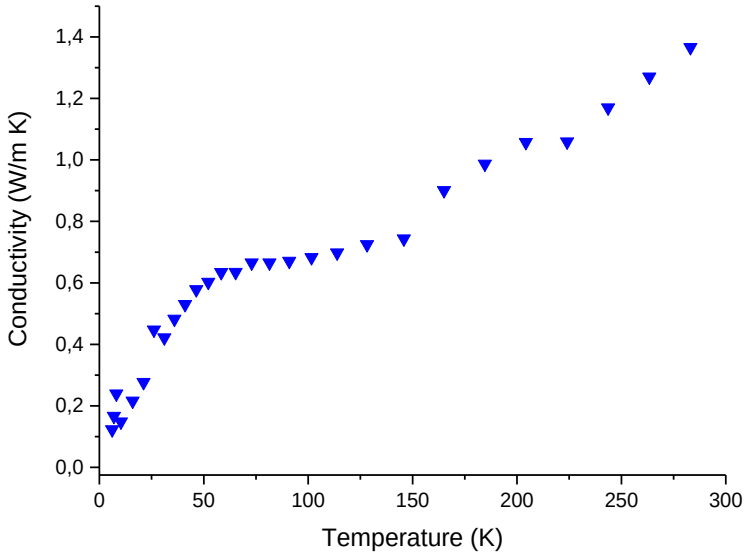

Fig. 5.17. Thermal conductivity versus the temperature for #2a (50% resin, 50% $LaNi_5$ and 5% graphite), #2b and #2c composites (50% resin, 45% $LaNi_5$ and 5% graphite)

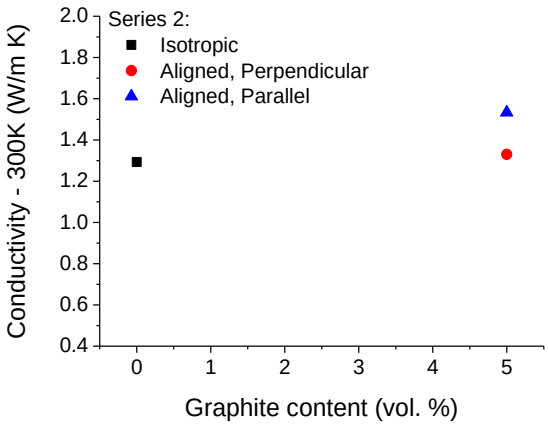

Fig. 5.18. Thermal conductivity of aligned and isotropic samples as a function on graphite content for Series 2 composites.

5.4. Analysis of the hydrogenation/dehydrogenation reaction rate

The most important part of the study were the measurements of hydrogenation and dehydrogenation rate on Sievert –type apparatus (Chapter 3). Samples were cut to shape o cylinders, with 6 mm diameter and 200 mg mass (Fig. 5.19). Cylinders side surfaces were wrapped with copper foil to provide tighter fitting and better contact with the wall of sample chamber (pipe). Thanks to such sample mounting heat is exchanged on side walls and the main parameter responsible for effective heat dissipation is radial conductivity of the sample, which is basically the thermal conductivity along the oriented flakes in case of aligned samples.

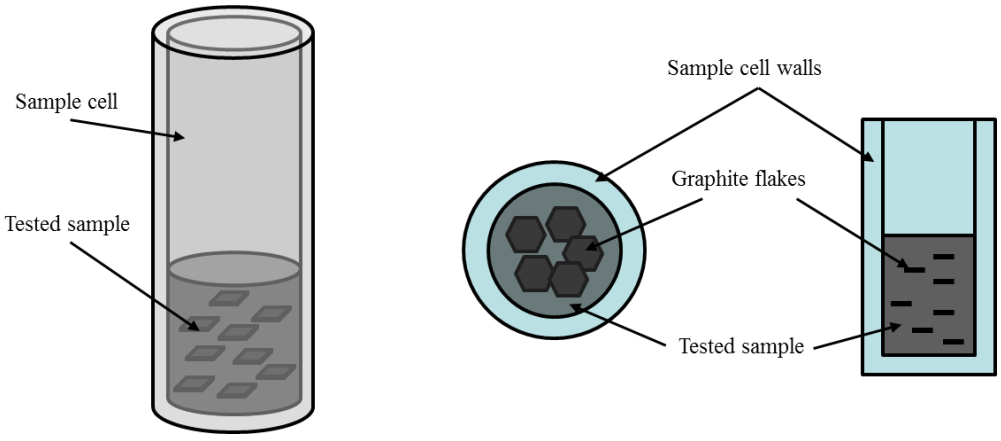

Fig. 5.19. Scheme of the sample mounting inside the sample cell.

After the activation of the sample (in 300 °C, for 20h, under vacuum), an absorption test was performed, under 300 °C, with initial pressure of 1 MPa. Experiment was carried out until the

equilibrium was reached, then hydrogen was removed from the sample cell and desorption of hydrogen was studied with initial pressure of 0.001 MPa. Fig. 5.21 and Fig. 5.21 present results obtained for MgH_2 based composites. An amount of reacted (absorbed or desorbed) hydrogen is plotted against the reaction time. Aligned and more conductive samples have slightly improved kinetics (details discussed later). All samples saturates after 250-400 or 80-120 min of reaction for absorption and desorption respectively and reaches hydrogen capacities around 3.5 wt. %. An accurate maximal capacity values are listed in Table 5.3 and they stay close to the theoretical capacity calculated from the composites composition. Shape of reaction curve is different for hydrogenation and dehydrogenation reactions. Absorption has typical exponential dependence – it starts rapidly when the hydrogen pressure is applied and slowly saturates. On the other hand release of hydrogen starts slowly, then goes through close to linear curve and then saturate and the end the reaction. It could be effect of slightly different heat transfer model for absorption and desorption. We propose the next model: At beginning of the desorption heat is conducted slower, because material is composed of resin and dielectric hydride. But at beginning the absorption thermal conductivity is higher, because composite is made of resin and metallic magnesium. Thus at start hydrogen is released slowly, then reaction goes faster thanks to better conductivity when hydride is transferring to the metal and again is slower when last molecules of hydrogen are released and reaction ands. The absorption process starts very fast, because heat is effectively transferred in metallic magnesium, then goes slower and slower when metal is exchanged by the hydride.

Table 5.3. Maximal hydrogen capacities of magnesium hydride composites

Reaction	Sample code	Graphite content [vol. %]	Max. capacity [%]		
			Isotropic	Aligned	Theoretical
Desorption	#1a	0	3.82	-	4.41
	#1b, #1c	2.5	3.63	3.69	4.12
	#1d, #1e	5	3.47	3.45	3.84
Absorption	#1a	0	3.96	-	4.41
	#1b, #1c	2.5	3.77	3.82	4.12
	#1d, #1e	5	3.51	3.45	3.84

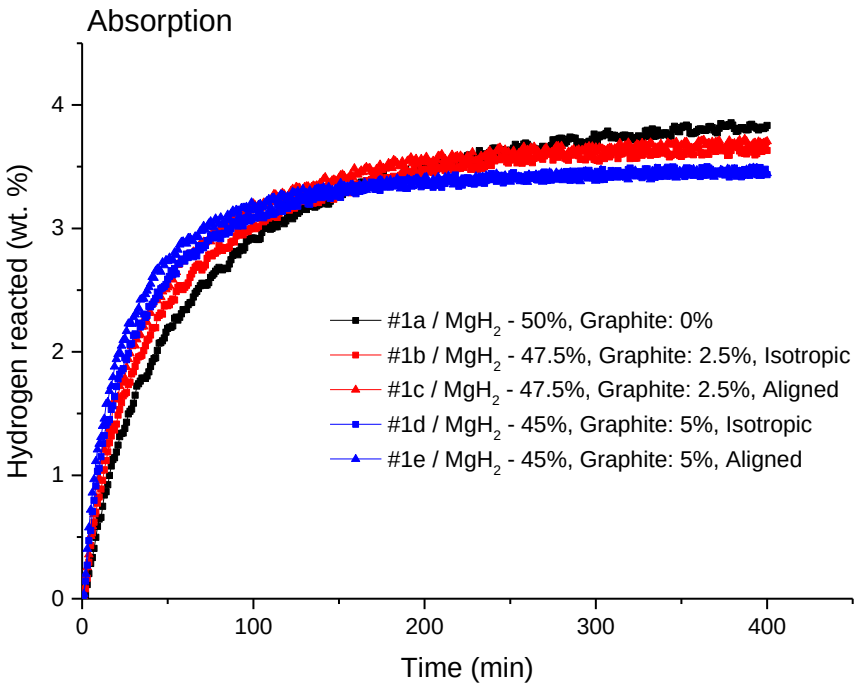

Fig. 5.20. Hydrogenation curves for series 1 composites under 1 MPa and 300 °C.

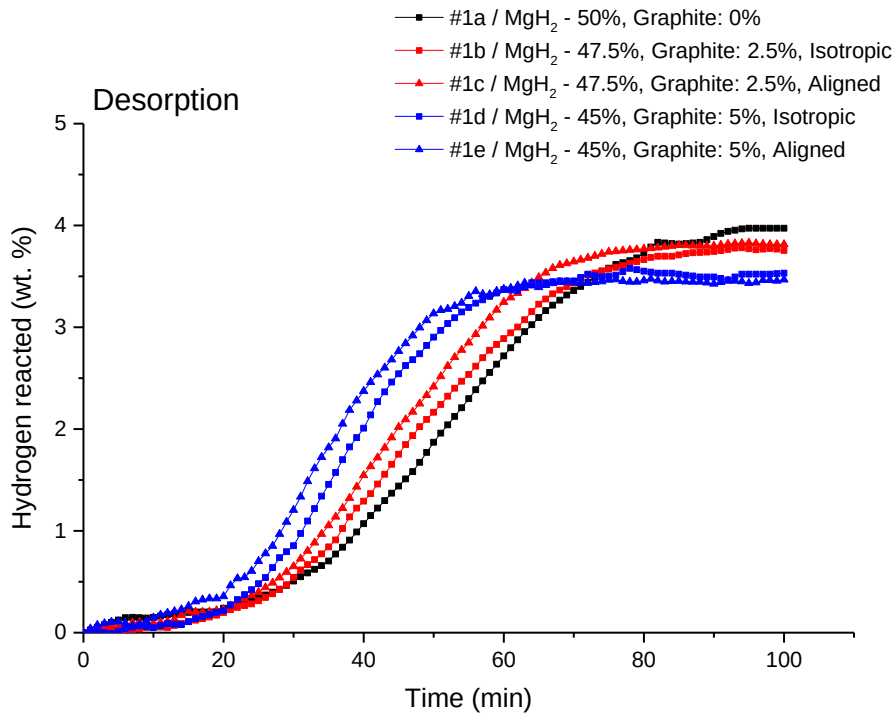

Fig. 5.21. Dehydrogenation curves for series 1 composites under 0.001 MPa and 300 °C.

Such behavior of reaction kinetics is clearly seen when the derivatives of the reacted hydrogen, versus time were calculated, which can serve as measure of reaction rate (Fig. 5.22 and Fig. 5.23). For absorption obtained values are the highest on the beginning of reaction and they decrease exponentially with time. On the other hand, desorption derivative poses maximum in the middle of reaction time. It is worth to notice, that despite the longer saturation time values of maximal reaction rate are higher for absorption process. Graphite filled, aligned samples with better thermal conductivity have better reaction rates. In addition, for desorption process, maximum shifts in time – it reached earlier while improving heat transfer parameters. It is interesting, that despite similar conductivities (Fig. 5.16) both aligned samples exhibits different reaction rates. It is probably because the fact, that sample have different composition – sample with smaller amount of MgH_2 will have faster kinetics.

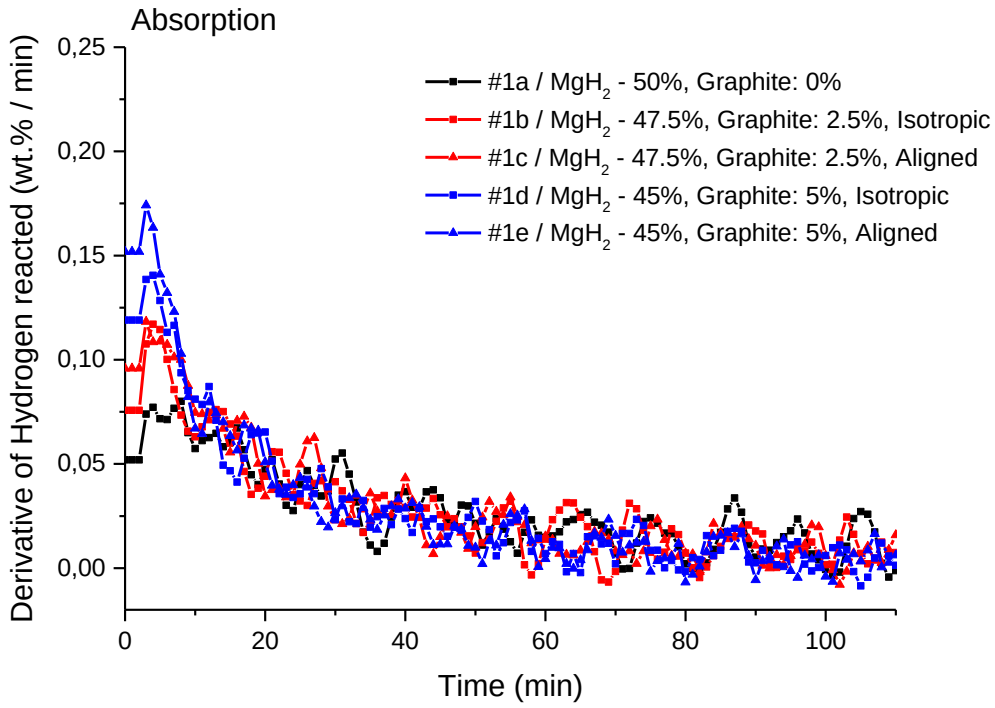

Fig. 5.22. Absorption speed, calculated as derivative of hydrogenation curves for series 1 composites.

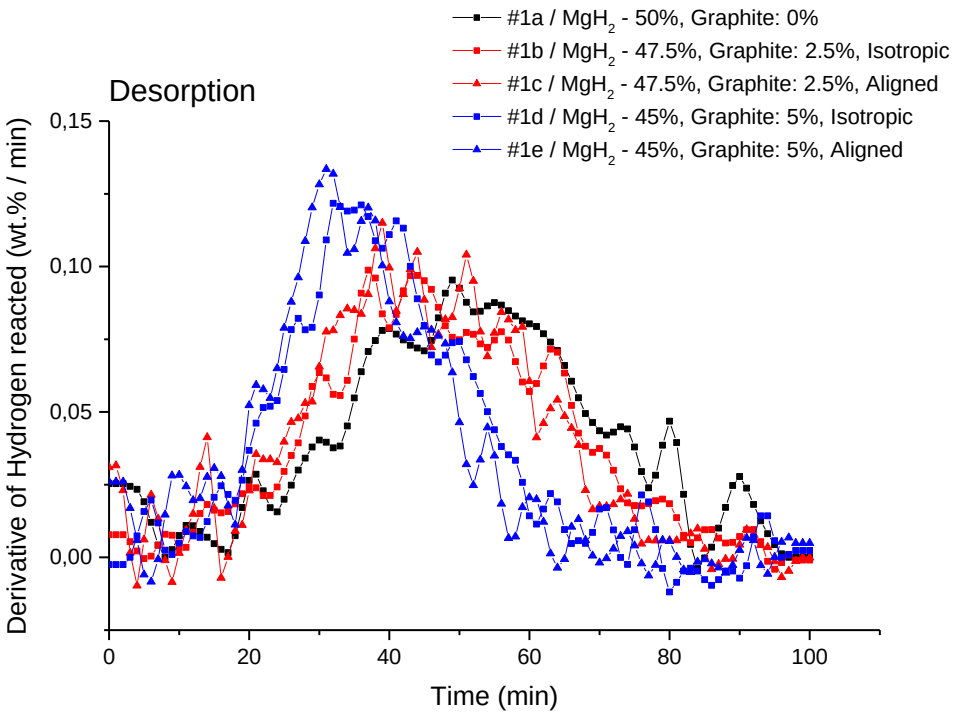

Fig. 5.23. Desorption speed, calculated as derivative of dehydrogenation curves for series 1 composites.

The other parameter used for comparison of reaction rate is time to reach 90% of maximal capacity. Fig. 5.24 presents date for absorption and desorption process. For both the time effectively reduced: during absorption - from 195 min for pure magnesium hydride to 92 min for 5% graphite filled aligned material, and during desorption- from 74 min to 54 min.

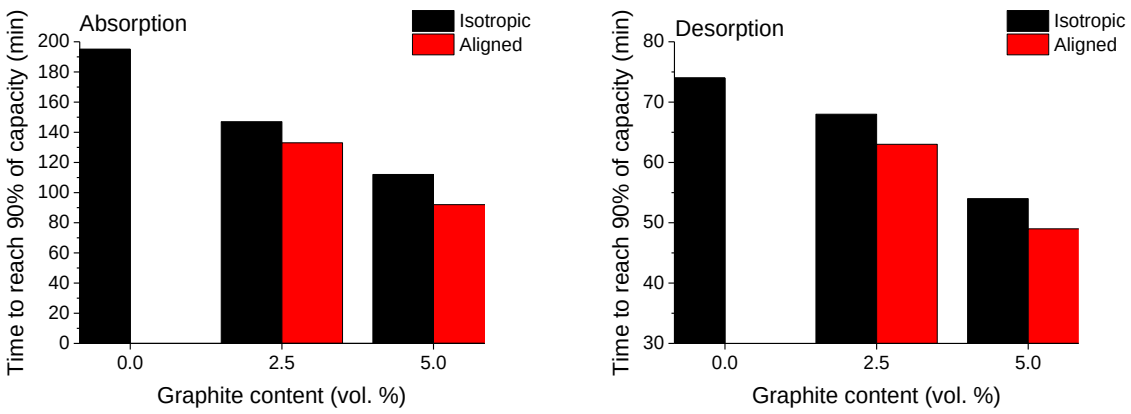

Fig. 5.24. Time to absorb and desorb of 90% of hydrogen as a function on graphite content for series 1 composites.

Results for lanthanum nickel based composites are presented below. Conditions of reaction were set to temperature 30 °C and pressure 1 MPa for absorption and 0.001 MPa for desorption. The reaction kinetics is faster than MgH_2 materials, because of general better performance of LaNi5. At this conditions, it takes 6-4 min to absorb and 16-12min to desorb of 90% of hydrogen (Table 5.4) and the improvement introduced by aligning of graphite particles is clearly observed. Composites filled with poses hydrogen capacity around 1.32 wt. %, which is close to the theoretical value coming from fillers content. The reduction of capacity compared to the pure hydride powder is much lower for $LaNi_5$ (1.5 to 1.32) than MgH_2 materials (7.5 to 3.45), due to higher density of alloy compared to magnesium.

Shape of reaction plots is slightly different from magnesium composites. Both desorption and absorption starts rapidly and there is not slow, flat beginning known from MgH_2 samples. A time dependence is exponential in both cases. Initial reaction rates (Fig. 5.26) are higher for absorption (~0.3 wt. %/min) and for aligned samples, but after few minutes they are falling below level of the pure samples due to saturation of hydrogen content.

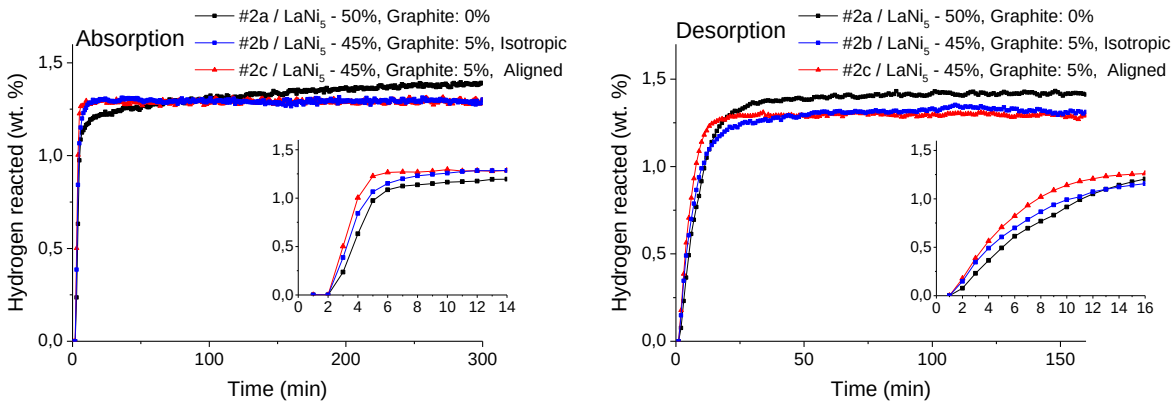

Fig. 5.25. Hydrogenation and dehydrogenation curves for series 2 composites

Table 5.4. Time to absorb and desorb of 90% of hydrogen as a function on graphite content for series 2 composites

Type	Sample code	Graphite content [vol. %]	Time to reach 90% of capacity [min]	
			Isotropic	Aligned
Absorption	#2a	0	39	-
	#2b, #2c	5	6	4
Desorption	#2a	0	20	-
	#2b, #2c	5	16	12

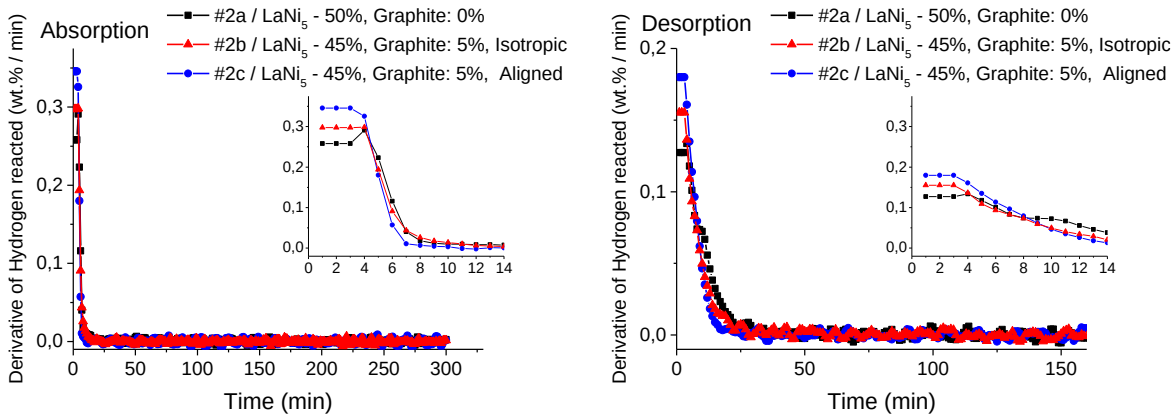

Fig. 5.26. Absorption and desorption speed, calculated as derivative of de/hydrogenation curves for series 2 composites.

5.5. Influence of reaction cycling on the changes of properties of the composites

Sample with the best performance (#1e – MgH_2: 45%, Graphite: 5%, aligned) was chosen to be tested under cycling reactions. Ten cycles of hydrogenation and dehydrogenation were performed using Japan Metals & Chemicals Co. Ltd (JMC) experimental machine (Chapter 2), under pressure of 1 MPa and temperature 300 °C. Cycles absorption are shown on Fig. 5.27 – experimental machine do not allow to register desorption data, during the desorption sample is under continuous vacuum. All cycles poses similar kinetics, but he most important information is that saturation amount of absorbed hydrogen decreasing with cycle number (Fig. 5.1), from 3.43 wt. % for the initial reaction to 1.68 wt. % for last one. In order to examine this problem, XRD measurements on cycled sample were taken.

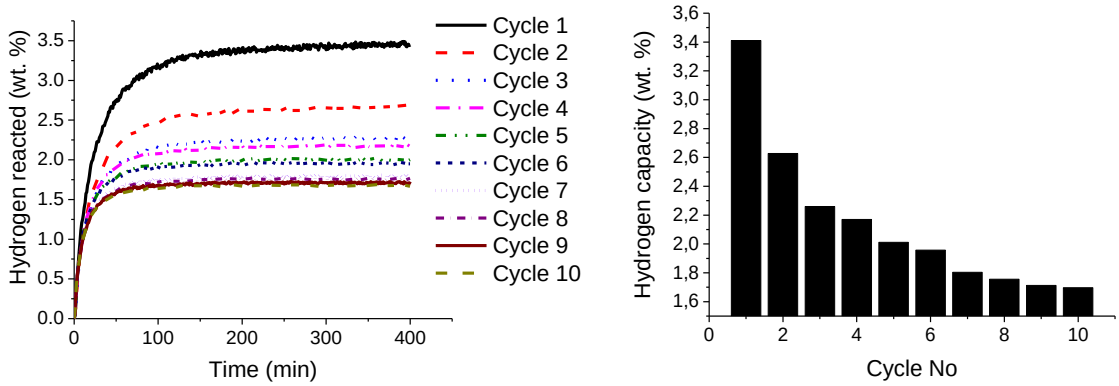

Fig. 5.27. Hydrogenation curve for ten cycles of reaction for sample #1e (MgH_2: 45%, Graphite: 5%, aligned) and maximum capacity of the composite versus cycle number.

Results are plotted in Fig. 5.28. Sample was in dehydrogenated state. Except of expected metallic magnesium and graphite reflections, peaks of magnesium oxide and magnesium silicate. It turns out, that during the experiment highly reactive magnesium atoms reacts with silicone resin's siloxane bonds (-SiO-). The products of that reaction are magnesium oxide MgO and magnesium silicate Mg_2Si. Magnesium oxide peaks are much wider than other phase, what suggest strong tensions and small crystalline size, typical for surface oxidation effects on magnesium hydride. An oxidation is not the effect of air/oxygen exposition, because at measurement time sample was under vacuum/hydrogen atmosphere. Because forming of magnesium oxide is irreversible under this conditions, its presence limits effective hydrogen capacity of hydrogen. Rietveld refinement was performed in order to determine cycled sample phase content. Magnesium in reactable form (metallic Mg and from Mg_2Si) is only ~56% of composites mass, the rest is neutral magnesium oxide and graphite, so it is the main reason for decrease in the hydrogen capacity of composites. What is interesting, one of the product is the magnesium silicate, which was considered as one of the magnesium alloys with good kinetic performance (Chapter 2), however its amount is relatively small (~10%) and its properties are limited by the presence of oxide layers.

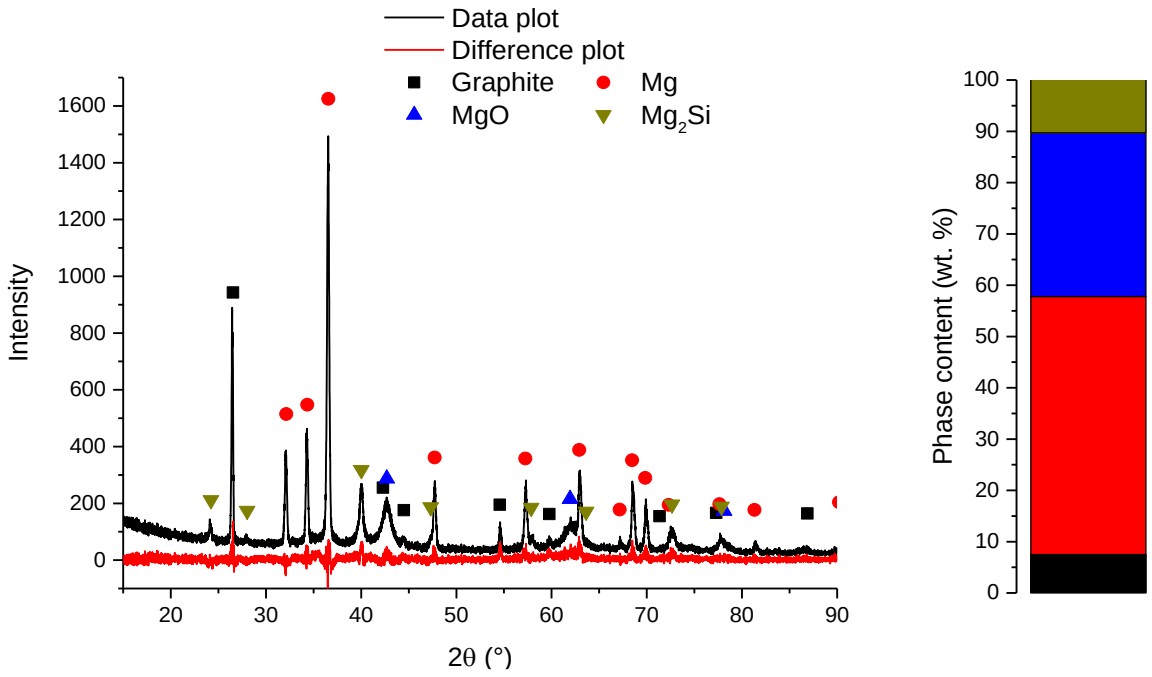

Fig. 5.28. XRD pattern after 10 reaction cycles for sample #1e – MgH_2: 45%, Graphite: 5%, aligned.

5.6. Scanning electron microscopy study of morphology of composites

Microstructure observations and element distribution mapping was carried out to analyse fillers particles distribution and orientation. Samples were cut in plane perpendicular to flake orientation to see axial cross section of cylinder sample. Samples were immersed in epoxy resin, cured and their surface was polished with different grade sandpapers. It must be told, that polishing process was difficult because of rubber-like properties of composite samples. In result samples surface is very rough and a lot of filler particles are ripped out from matrix or distorted. Because of that problems, accurate, high magnification images could not be obtained, however results for magnesium hydride, graphite filled samples no. #1d and #1e are presented on figures on the next pages. Photos of the other samples can be found in Appendix. A low magnification (90x) and medium magnification (500x) are posted on the top of the figure. The EDS mapping results for silicon, magnesium and carbon are presented below together with the EDS spectrum. It must be noticed, that carbon is an artefact in EDS method, but when the amount of carbon are high, or confined in form of grains or particles some qualitative results can be discussed. Magnesium hydride is displaced uniformly inside the material, no sedimentation effects are visible, which often problem for long curing liquid resins. Silicone polymer matrix surrounds the magnesium islands on EDS maps what suggest good wetting of the hydride particles during the mixing of liquid and powders. Only small aggregates of MgH_2 particles can be observed. Graphite particles are visible as small particles in background of carbon maps, but because of the quality of the image the alignment cannot be observed.

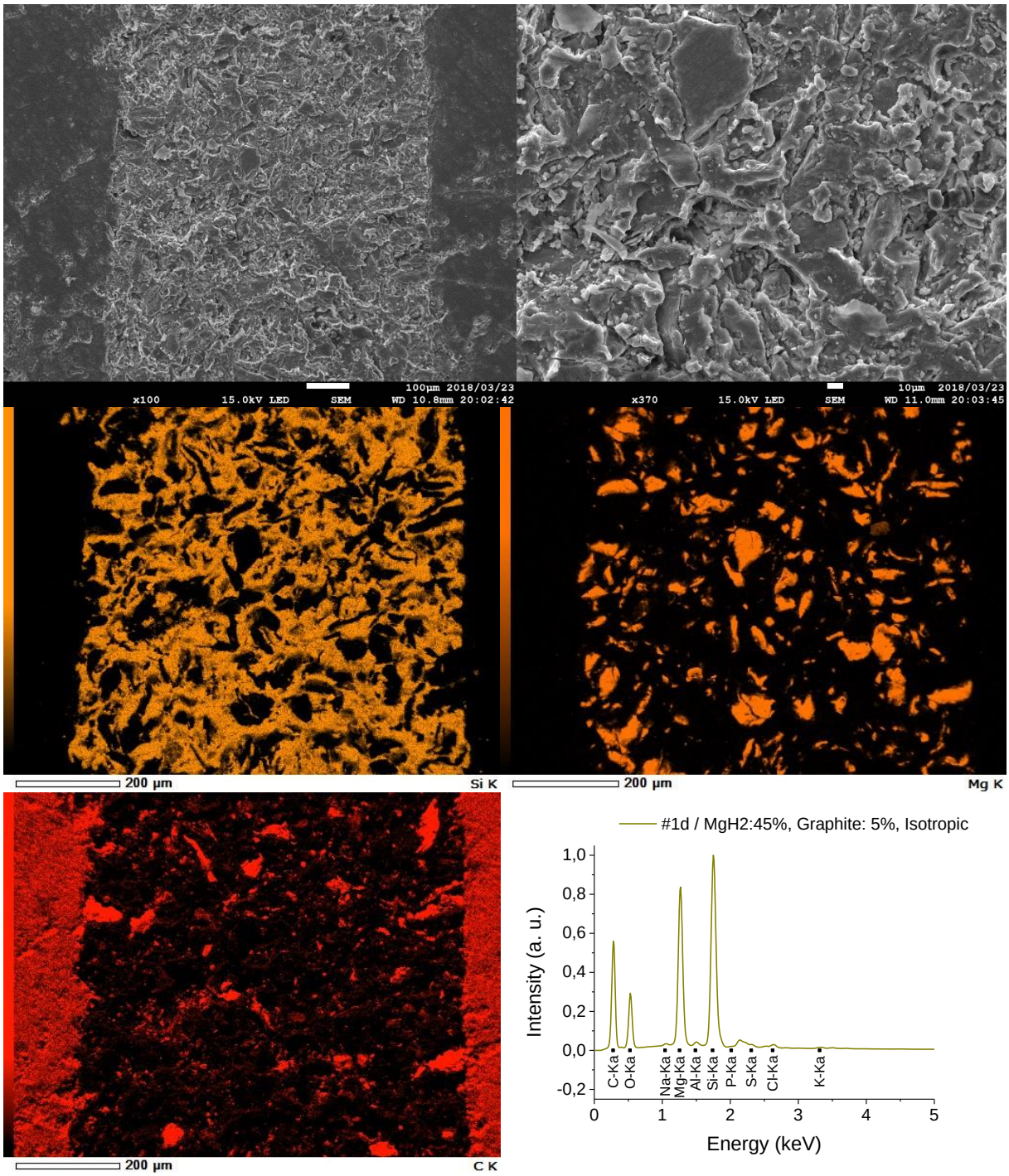

Fig. 5.29. SEM images, EDS element distribution maps for Si (from matrix), Mg and C (from fillers) and EDS spectra for composite sample #1d (MgH_2: 50%, Graphite: 5%, isotropic)

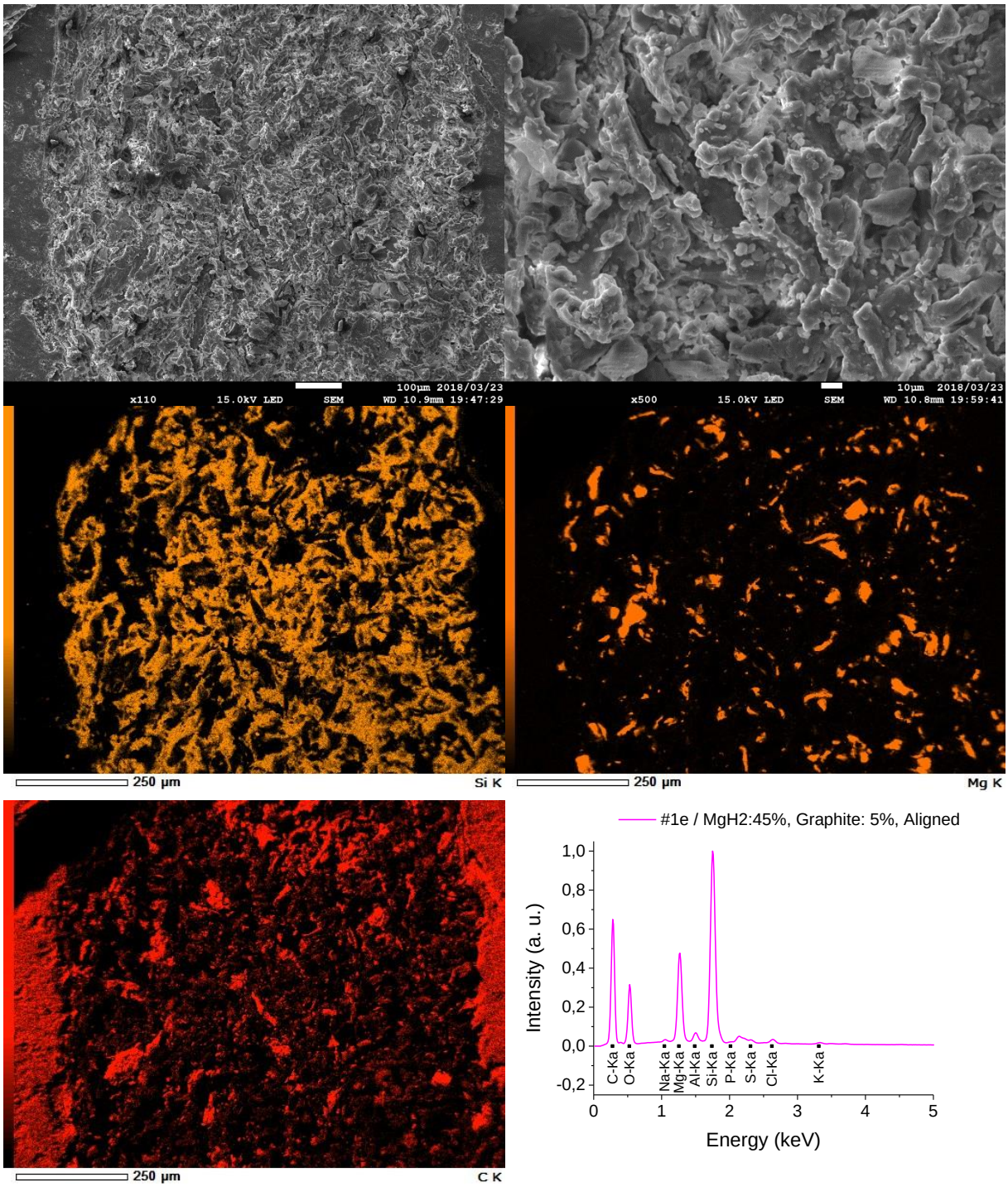

Fig. 5.30. SEM images, EDS element distribution maps for Si (from matrix), Mg and C (from fillers) and EDS spectra for composite sample #1e (MgH_2: 45%, Graphite: 5%, aligned)

5.7. Summary of the results obtained for composites

To sum up, samples of composite materials based on silicone resin and metal hydrides with graphite fillers was prepared in order to test how the enhancement of thermal conductivity by aligning graphite flakes will affect on reaction kinetics. Initial testing of materials tested without active material (only resin and graphite) shows that it is possible to introduce orientation of graphite particles in uncured, liquid resin by using electric field produced torque. The alignment was confirmed with X-ray diffraction method and by measurements of thermal and electric resistivity in different directions in relation to applied electric field vector.

A preferred orientation parameter of [002] (c axis) direction, calculated with March-Dollase method, is near 0.6-0.8 for aligned samples, which means that this is preferred direction of orientation. In case of isotropic, non-electrically tailored samples that parameter stays close to unity. Orientation is poorer for higher loaded samples because of weaker interactions with external field and higher mixture viscosity. Thermal conductive measured along the flakes is around 0.3 W/m·K better than across the flake and increases from 0.2 W/m·K for pure resin to 1-1.2 W/m·K for 15% graphite filled material. Specific difference between the conductivities across the flake, along and of isotropic sample suggests that large enhancement of conductivity in one direction is compromised with only low reduction of conductivity in the other direction. The enhancement of thermal conductivity, expressed as percentage growth of conductivity in parallel direction in relation to the isotropic conductivity is lower for more graphite content materials, but still exist, because particles are forced them to form the conductive, net-like aggregates, what increases effective thermal conductivity despite lower anisotropy.

Similar results were found for magnesium hydride and lanthanum-nickel based composites. March-Dollase factors stays around 0.6, what suggest good alignment and the thermal conductivity is enhanced by 45-20% comparing to isotropic samples. Effective thermal conductivity ranges from 0.8 W/m·K for resin-hydride sample to 1.08 W/m·K for graphite filled composites. A conductivity of material is around 4-6 times higher than the pure resin and around 80-120 times better than the values reported for the powdered hydride.

Improve in effective thermal conductivity results in observed improve of the reaction kinetics. absorption time of magnesium composites can be reduced from 195 min to 92 min for aligned, graphite filled sample and desorption is accelerated from 74 to 54 min. In case of LaNi5 materials, absorption and desorption time drops from 39 to 4 and 20 to 12 min respectively. It must be noticed, that despite the longer time, improvement of reaction rate in absorption process is higher. Due to of changes in thermal conductivity caused by change of

active material character during the reaction (from metallic to dielectric and reverse), shape of hydrogenation curves is slightly different for hydrogenation and dehydrogenation. Hydrogen is absorbed with the highest speed at the beginning of the process, then reaction rate decreases because of reducing of thermal conductivity by transferring of metallic magnesium to magnesium hydride. On the other hand the desorption is the fastest in the middle of reaction - when it starts, the heat transfer and reaction is slow then reaction goes faster thanks to better conductivity when hydride is transferring to the metallic magnesium. The maximum of reaction rates is higher graphite filled, aligned materials and for desorption process, maximum shifts in time – it reached earlier while improving heat transfer parameters.

SEM observations of particles alignment were impossible to perform because of rubber character of composites forcing sample preparation problems, but obtained images provide information about uniform magnesium particles distribution, which is important and suggest no sedimentation problems during curing process. Moreover, liquid silicone resin is well mixed with powders and no addition processing or adding a thinner is necessary.

Future work should be focusing on increasing of the amount of active material (hydride) in the composite and choosing proper matrix. It could be achieved by using low viscosity binders, such as polyester and epoxy resins. On the other hand, their operating temperature usually does not exceed 100 ºC, so they can be applied only to lanthanum-nickel alloy and other moderate temperature materials. High temperature inorganic binders, based on silicates and phosphates can withstand temperatures over 800-1000 ºC, but all of the systems are based on water solution, so the can be used only with metallic (non-hydrided) fillers. In case of active metals, such as magnesium, oxidation and passivation problems may easy occur. Thermal conductivity can be enhanced more by using stronger electric field or using other anisotropic carbon materials, such as graphene or nanotubes.

6. SUMMARY AND CONLUSIONS

In the Dissertation designing and development of new methods of introducing catalytic elements to the magnesium hydride was presented. The main idea was to use the catalyst in the form of a thin film uniformly covering the surface of bulk magnesium hydride grains. Such surface modification reduces the activation energy barrier on the magnesium surface and improves the reaction rate while keeping dopant amount low. The advantage is a precise control of film thickness and amount of the dopant, uniform coating and possibility of deposition of different elements, alloys and compounds.

Within the work a special equipment for sputtering on powdery substrates was designed and constructed. The powder is placed there in a special, round shaped container, set in circular motion in vertical plane in order to mix the powder during the deposition to get uniform coating.

Owing to that, thin films of nickel and vanadium, fully covering the surface of grains of the as purchased magnesium hydride were successfully deposited. Film thickness was reaching 320 nm and 170nm for the Ni- and V-coatings, respectively. The effective dopant amount for most of the samples between ~ 0.2 and ~1.8 wt. % was obtained. An attempt was also undertaken to coat ball milled powders, making use of additional nanostructurization effect, but the particle agglomeration effect caused a poor uniformity of thin films. Due to their nanocrystallinity the deposited nanolayers give too low X-ray diffraction signal to observe their diffraction peaks.

XRD measurements have shown that ball milled powders are very sensitive to oxidation. The amount of MgO in such samples was exceeding 40 wt. %. Large differences in local effective amount of the introduced dopants and oxidation effect cause poor and inconclusive results of thermodynamic and kinetic studies. On the other hand, there was no significant oxidation effects observed for not milled powders.

The reduction of the activation energy for hydrogen dissociation/recombination has been observed with DSC measurements, being the largest for the not-milled, nickel coated samples and reaching 150 kJ/mol. For ball milled powders the reduction is smaller, of 40 kJ/mol, but this is affected by oxide shells present on the hydride surface there. The decomposition temperature was decreased by about 50 K for nickel coatings, but for niobium and vanadium samples it stays on the same level or is slightly increased. A special model was proposed to describe the influence of the coatings on the activation energy and desorption temperature. Within it the kinetic barrier can be reduced by coating to a level which has its limit at the full coverage of magnesium particles by catalyst layer. Further increase in coating thickness may

negatively affect the effective decomposition temperature, i.e. increase it, by formation of magnesium alloys on the grain surface.

Nickel coating on the as purchased powders can effectively enhance reaction rates, reducing the time needed for charging and discharging from more than 12 hours to 70 and 15 min, respectively. The impact on the desorption kinetics is stronger than on the absorption one. Vanadium coatings have smaller influence on the reaction kinetics, but there is still slight enhancement of them visible.

Ball milled magnesium hydride exhibits better reaction kinetics for absorption process, the time needed to react of 90% of hydrogen is as short as 11-4 min for nickel samples, but the samples exhibit a much smaller effective content of the hydride (~11-5 wt. %) due to oxidation. The equilibrium hydrogen capacity was lower than the expected value (7.5 wt. %), and reached 1.2 – 3.5 wt. %, due to only partial decomposition of magnesium hydride under these conditions and because of the presence of magnesium oxide. Coated samples show also generally higher reaction rates than pure magnesium hydride. Despite the fact that the sorption kinetics is enhanced, the thermodynamics of the hydride did not change. Entropies and enthalpies of reaction stay on the similar level for nickel coated sample as in the as received magnesium hydride. The amount of nickel introduced to the hydride is not large enough to form an alloy in high part of the sample, not only on the surface.

The materials obtained show an interesting behavior during the cycling of hydrogenation/dehydrogenation reactions. Metal coating is still present on the particle surface, but the layer gets cracked and partly detached. The decomposition temperature goes back to the value for pure MgH_2, but the activation energy for the cycled sample is almost two times lower than for pure hydride and by 45% lower than that in the initial run. This is probably due to growth of ruptures and micro-cracks on the layer surface, so that the interface between the magnesium and metal film is more open and exposed to the hydrogen gas. Thus, the dissociation, diffusion and penetration of hydrogen atoms through the nickel layer is more effective.

A study towards improvement of the heat transfer in the composites of hydride materials resembling those to be used in real hydrogen tanks has also been carried out. For that, special composites of magnesium hydride and graphite with thermal conductivity enhanced through their anisotropy were prepared. Initial tests showed that it is possible to introduce orientation of graphite particles in uncured, liquid resin by using electric field produced torque. The successful alignment was confirmed with X-ray diffraction method and by measurements of

thermal and electrical resistivity in different directions with respect to the aligning electric field vector. The preferred orientation parameter of [002] (*c* axis) direction, determined with March-Dollase method, was near 0.6 for aligned samples, which means that this was the preferred direction of orientation. The alignment was poorer for higher loaded samples because of the lower effectiveness of the interaction with external field and higher viscosity of the mixture. The thermal conductivity was found to be enhanced by 20-45% comparing to isotropic samples and ranged from 0.8 W/m·K for resin-hydride material to 1.08 W/m·K for graphite doped composites. The conductivity of the material was 4 to 6 times higher than that of the pure resin and 80 to 120 times better than the values reported for the powdered hydride.

Improved heat transfer was found to enhance reaction rates. Reaction times of MgH_2 – graphite composites were shortened from 195 min to 92 min and 74 to 54 min for absorption and desorption, respectively. Despite the longer absorption time, the improvement of reaction rate in absorption process was greater.

Changes in the effective thermal conductivity of the composite caused by transformation of the active material from metallic to dielectric (and reverse) made shape of dehydrogenation curves is slightly different than for hydrogenation. Hydrogen is absorbed faster at the beginning of the process, because of the high thermal conductivity of metallic magnesium. The desorption is the fastest in the middle of reaction; when it starts, the heat transfer and reaction are slow, but after several minutes it goes faster owing to better conductivity when hydride is transforming to the metallic magnesium. The maximum of reaction rates was higher for graphite filled, aligned materials. For them, in the desorption, the maximum was reached earlier owing to the improved heat transfer.

Detailed SEM observations were difficult to perform on the composites because of sample preparation problems (too soft materials to polish), but the crude images obtained show no sedimentation problems during curing process and good mixing of the silicone resin with powders giving uniform composite materials.

The research carried out shows that magnetron sputtering on powder substrates can be an effective way to introduce catalytic elements to metal hydrides. Electric field driven aligning of highly conductive carbon structure in the composite can be used to improve heat transfer in metal hydride system without introducing additional amount of dopants. Although the research presented in the Thesis was performed mostly on the magnesium hydride, the conclusions drawn and technical issues can be easily applied to other materials.

7. APPENDIX

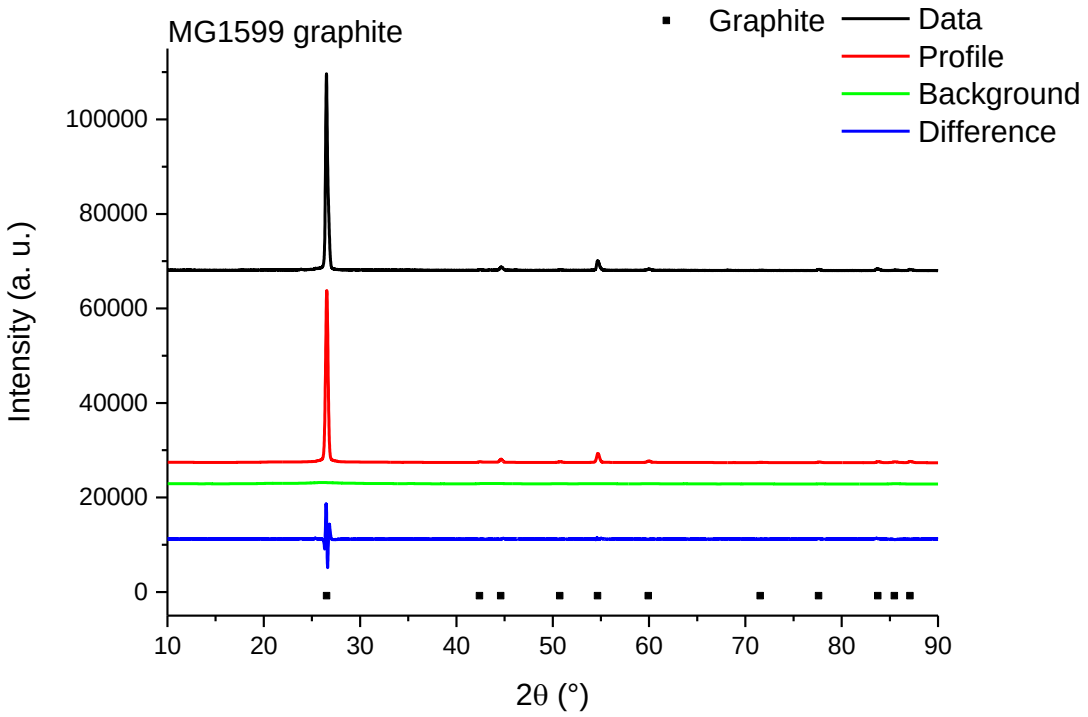

Fig. 7.1. XRD pattern, calculated profile, background profile and difference plot for pure graphite powder .

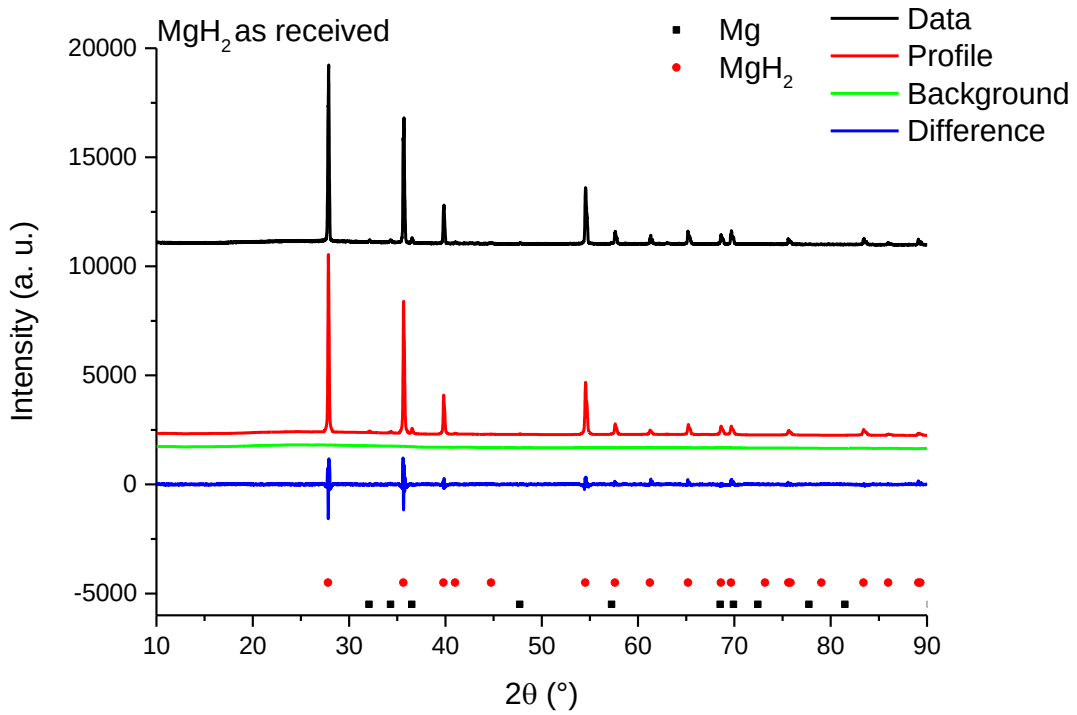

Fig. 7.2. XRD pattern, calculated profile, background profile and difference plot for as received magnesium hydride .

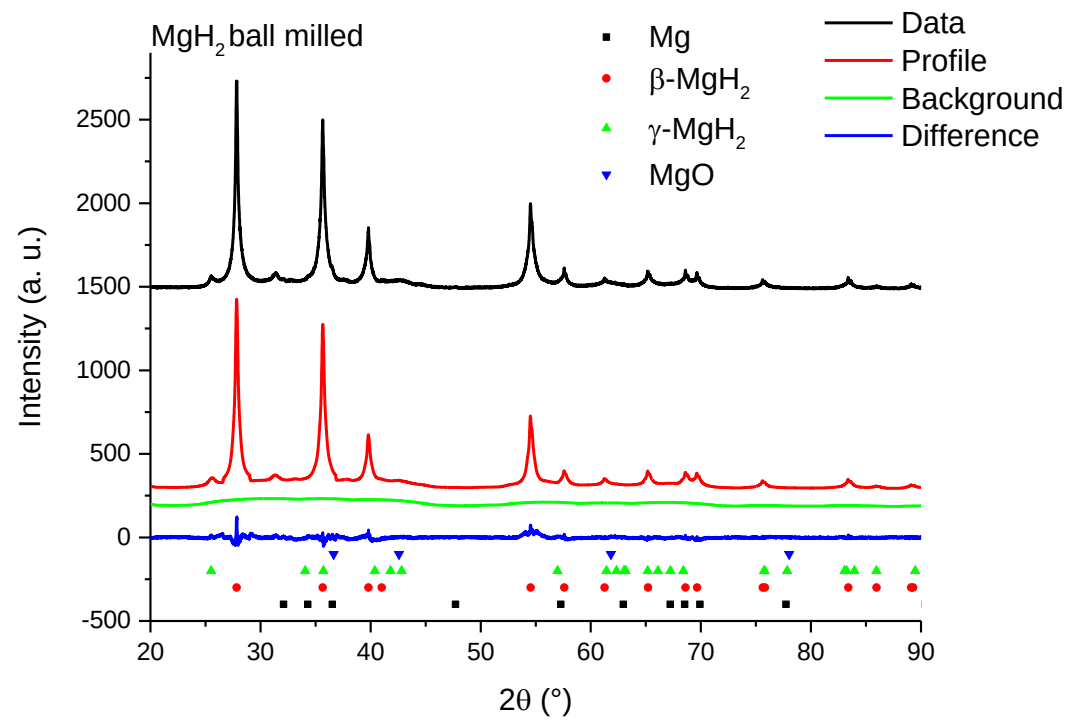

Fig. 7.3. XRD pattern, calculated profile, background profile and difference plot for ball milled magnesium hydride .

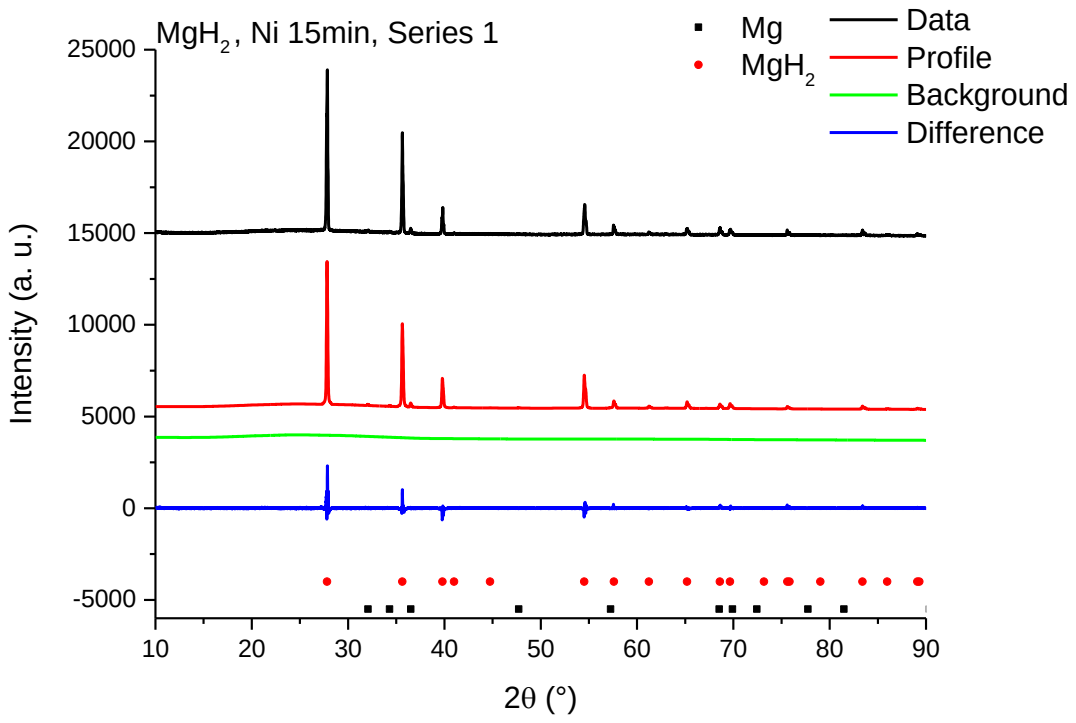

Fig. 7.4. XRD pattern, calculated profile, background profile and difference plot for sample MgH_2, Ni 15min, Series 1.

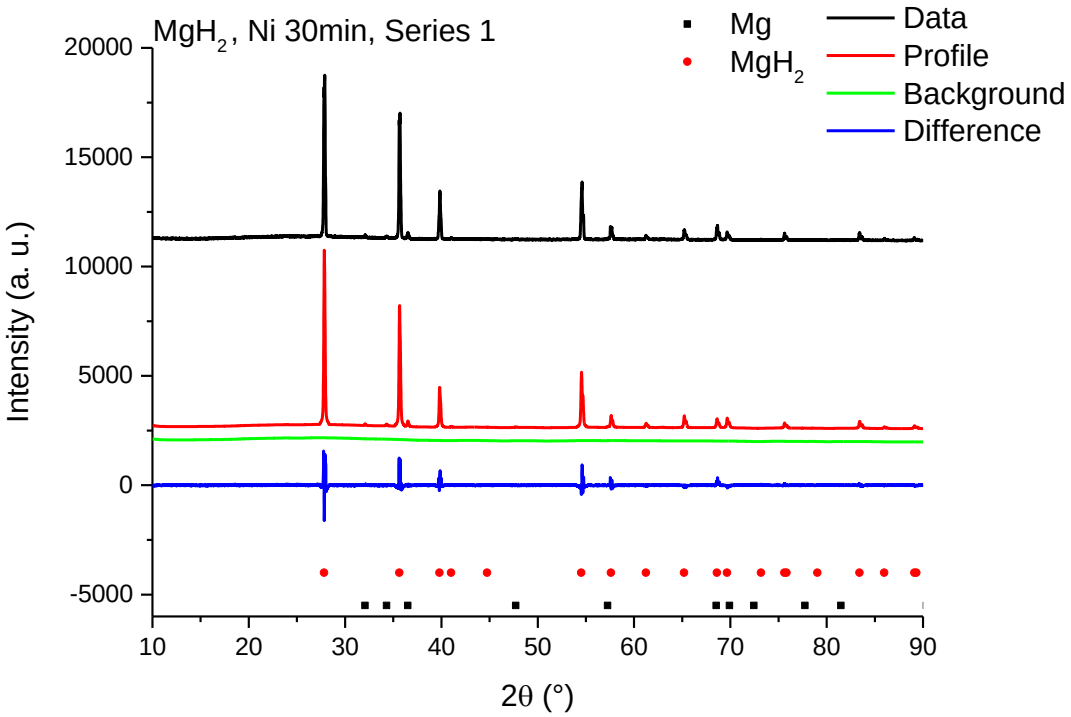

Fig. 7.5. XRD pattern, calculated profile, background profile and difference plot for sample MgH_2, Ni 30min, Series 1.

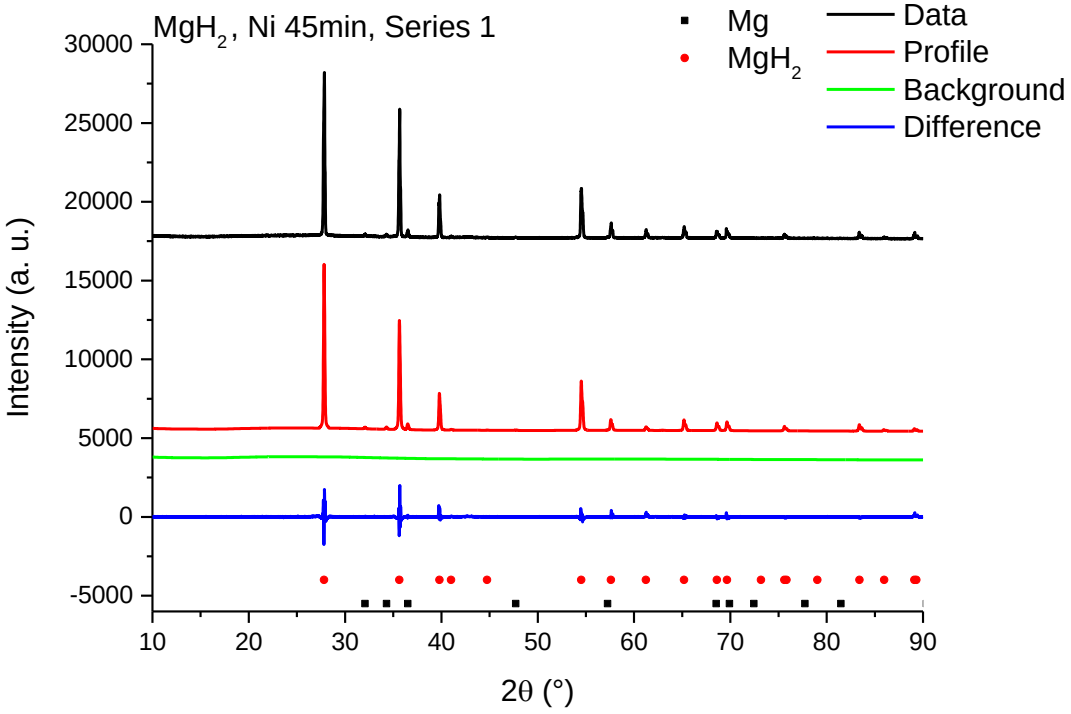

Fig. 7.6. XRD pattern, calculated profile, background profile and difference plot for sample MgH_2, Ni 45min, Series 1.

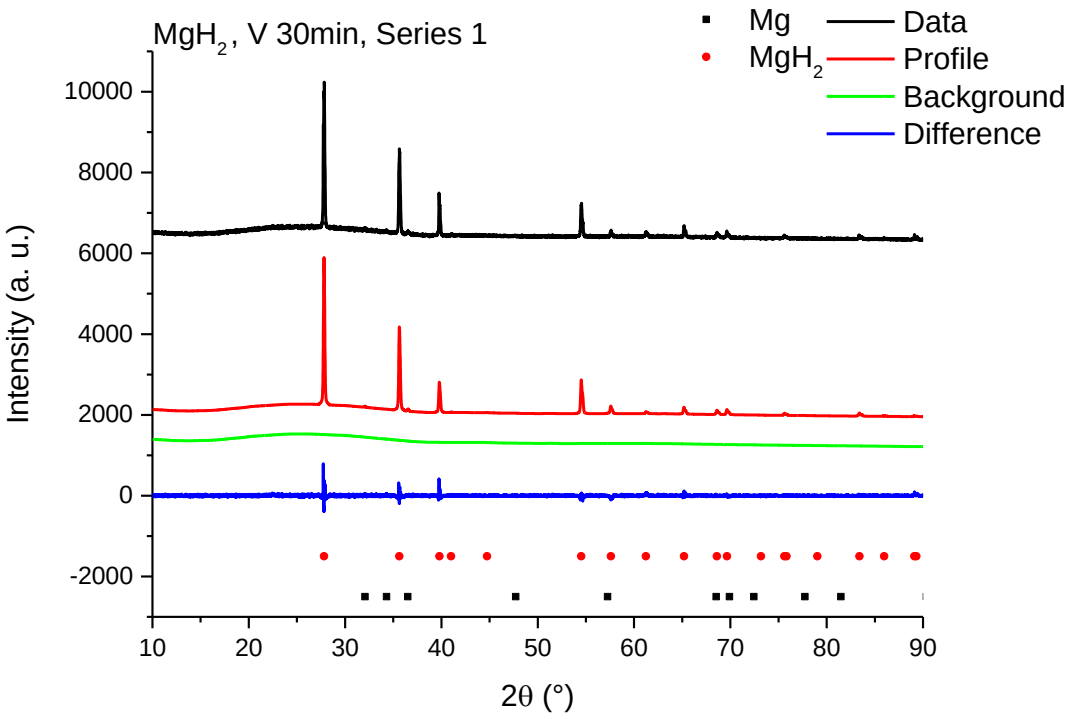

Fig. 7.7. XRD pattern, calculated profile, background profile and difference plot for sample MgH_2, V 30min, Series 1.

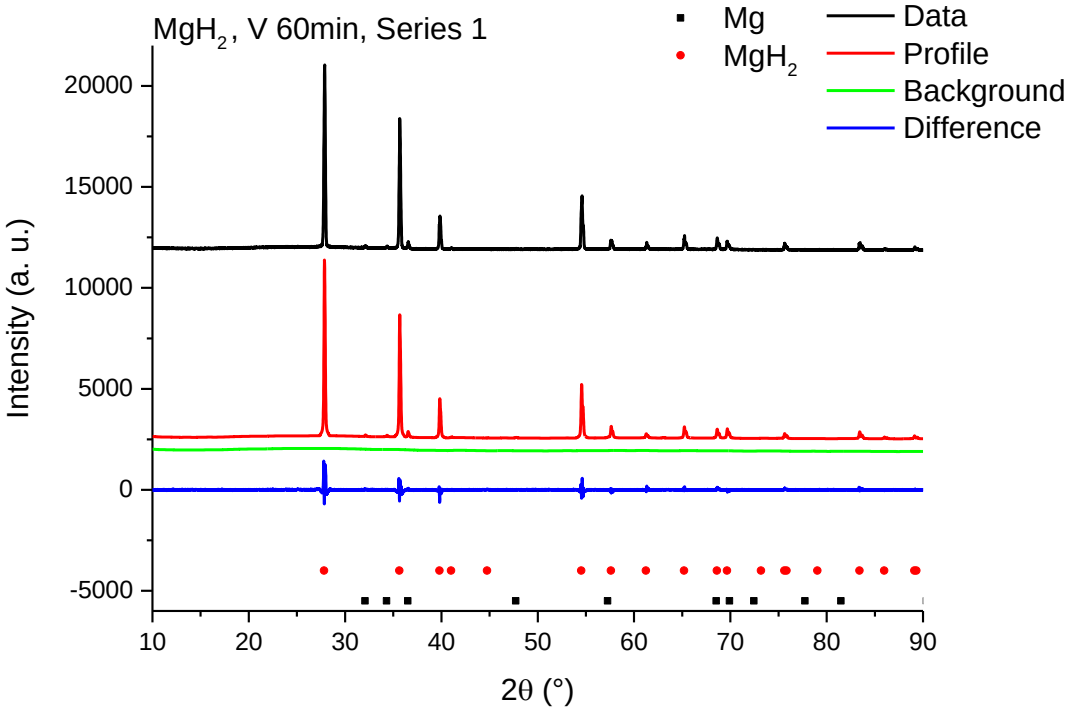

Fig. 7.8. XRD pattern, calculated profile, background profile and difference plot for sample MgH_2, V 60min, Series 1.

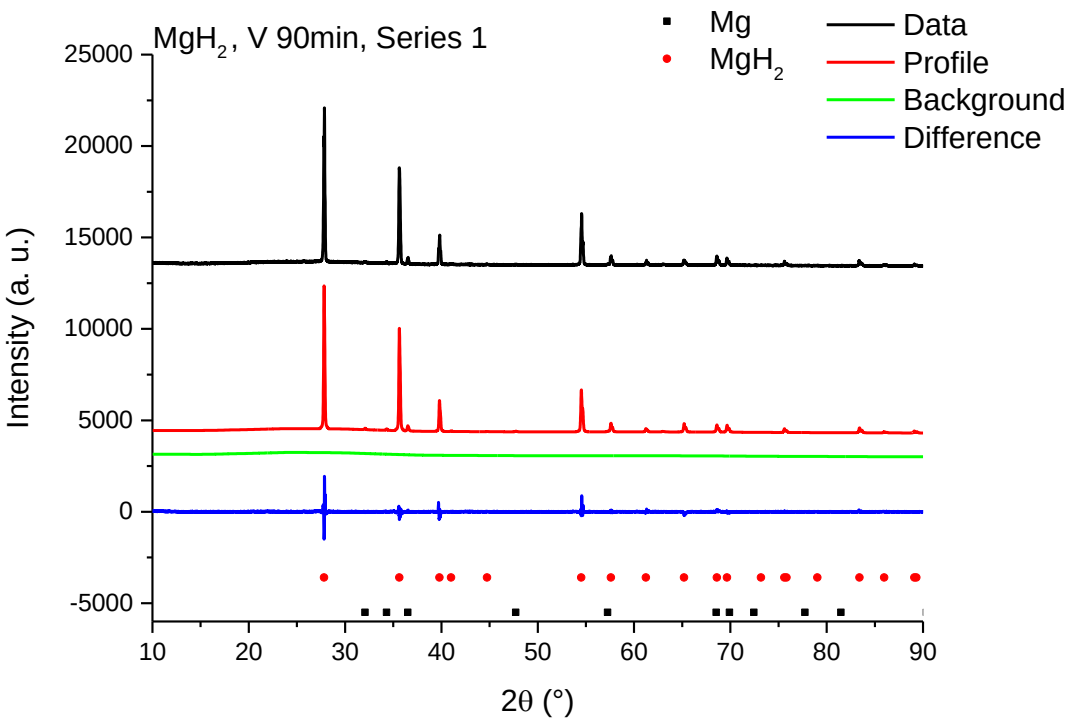

Fig. 7.9. XRD pattern, calculated profile, background profile and difference plot for sample MgH_2, V 90min, Series 1.

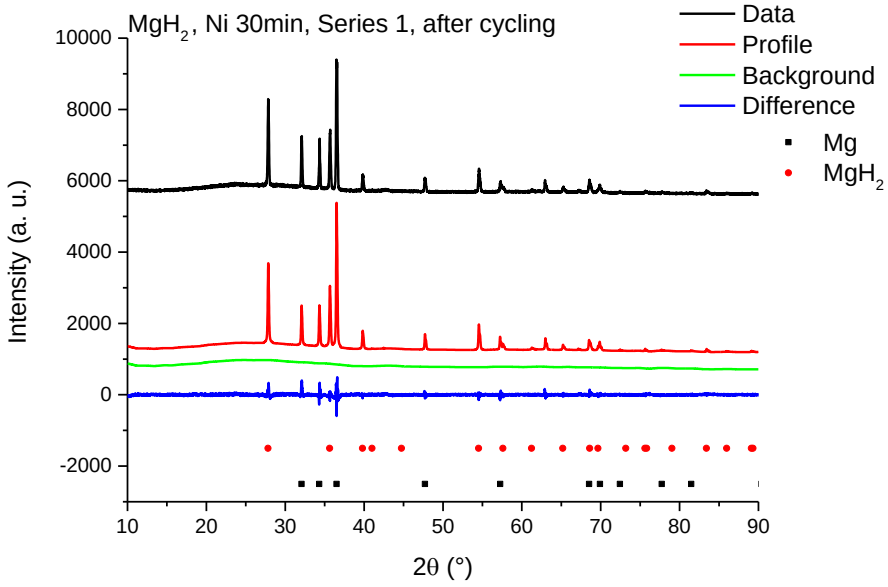

Fig. 7.10. XRD pattern, calculated profile, background profile and difference plot for sample MgH_2, Ni 30min, Series 1, after the cycling.

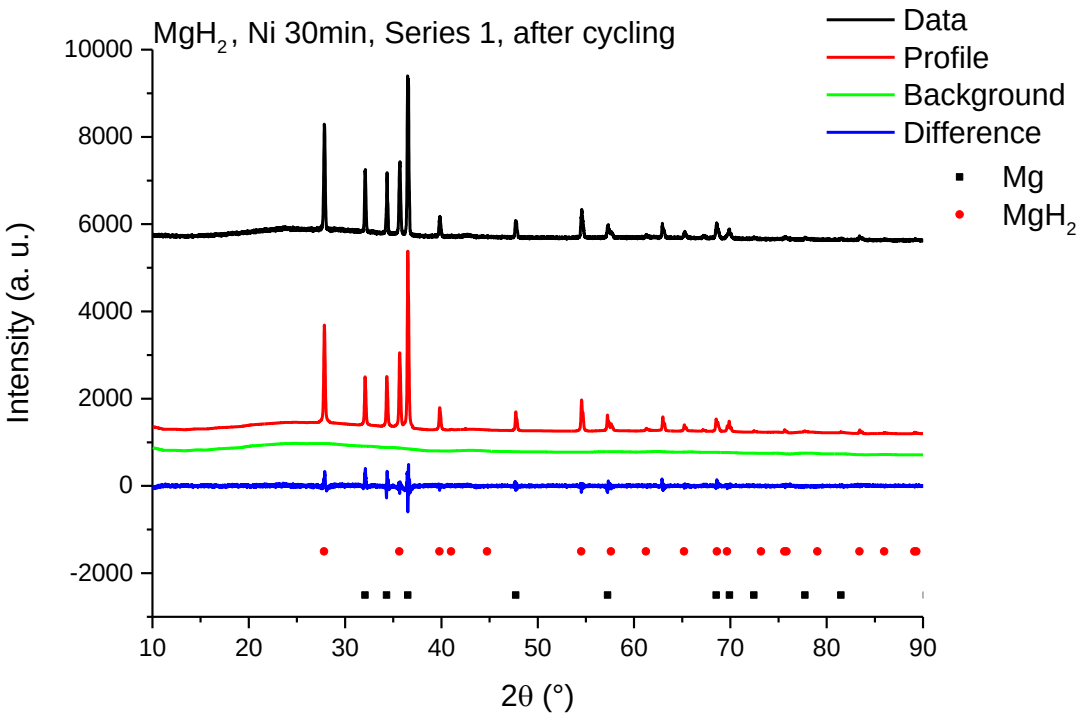

Fig. 7.11. XRD pattern, calculated profile, background profile and difference plot for sample MgH_2 - BM, Nb 30min, Series 2.

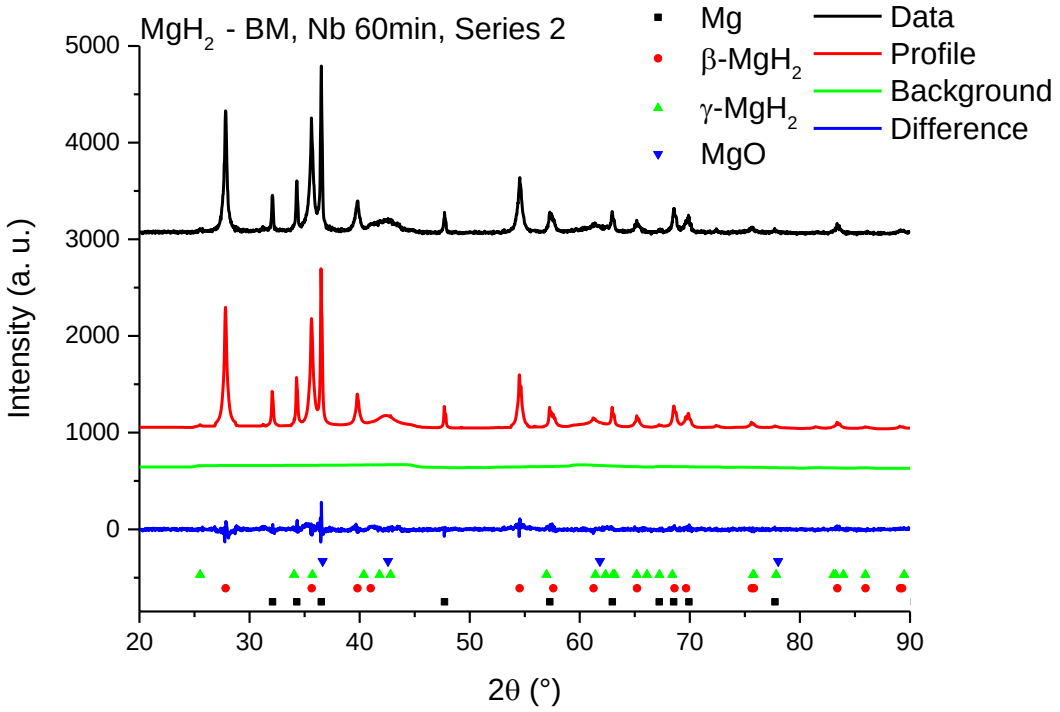

Fig. 7.12. XRD pattern, calculated profile, background profile and difference plot for sample MgH_2 - BM, Nb 60min, Series 2.

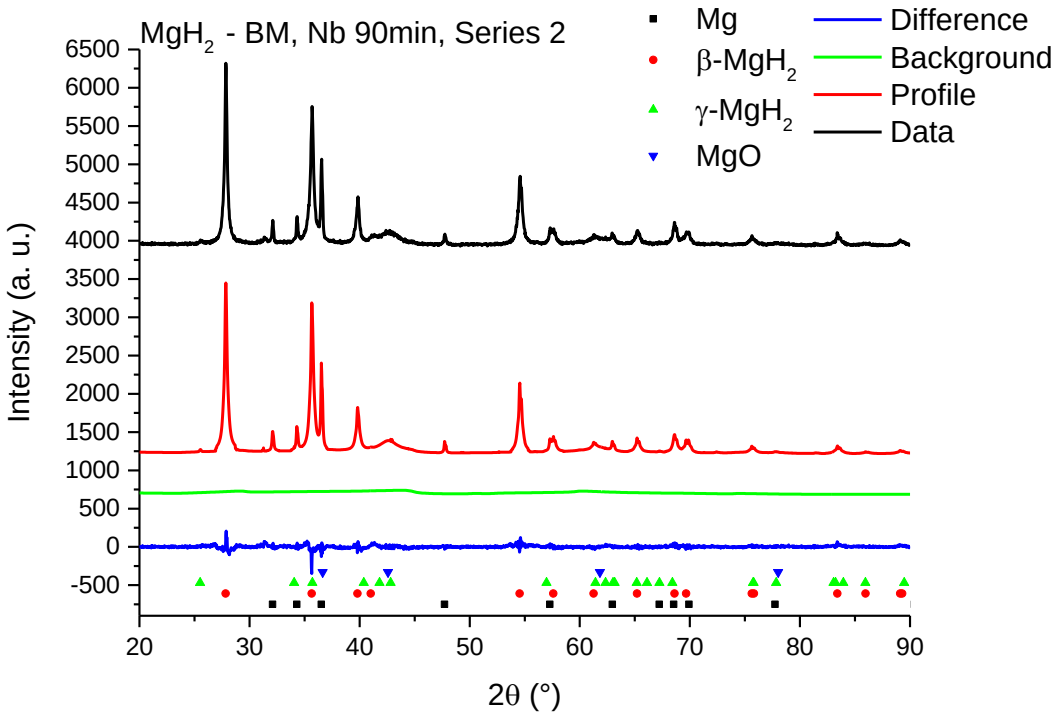

Fig. 7.13. XRD pattern, calculated profile, background profile and difference plot for sample MgH_2 - BM, Nb 90min, Series 2.

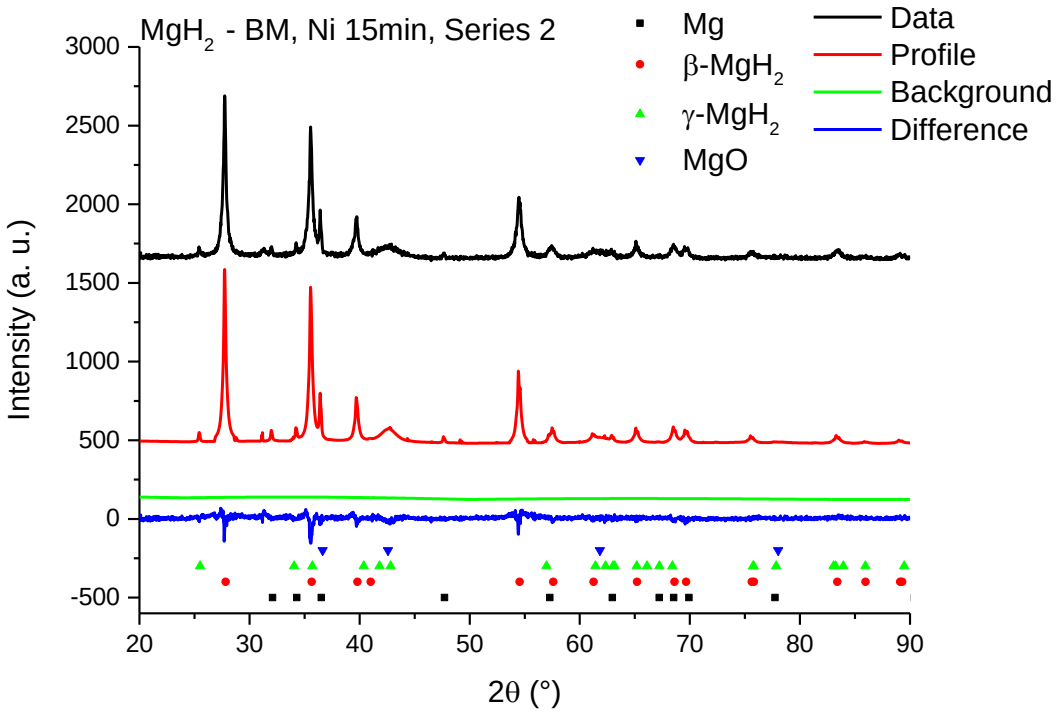

Fig. 7.14. XRD pattern, calculated profile, background profile and difference plot for sample MgH_2 - BM, Ni 15min, Series 2.

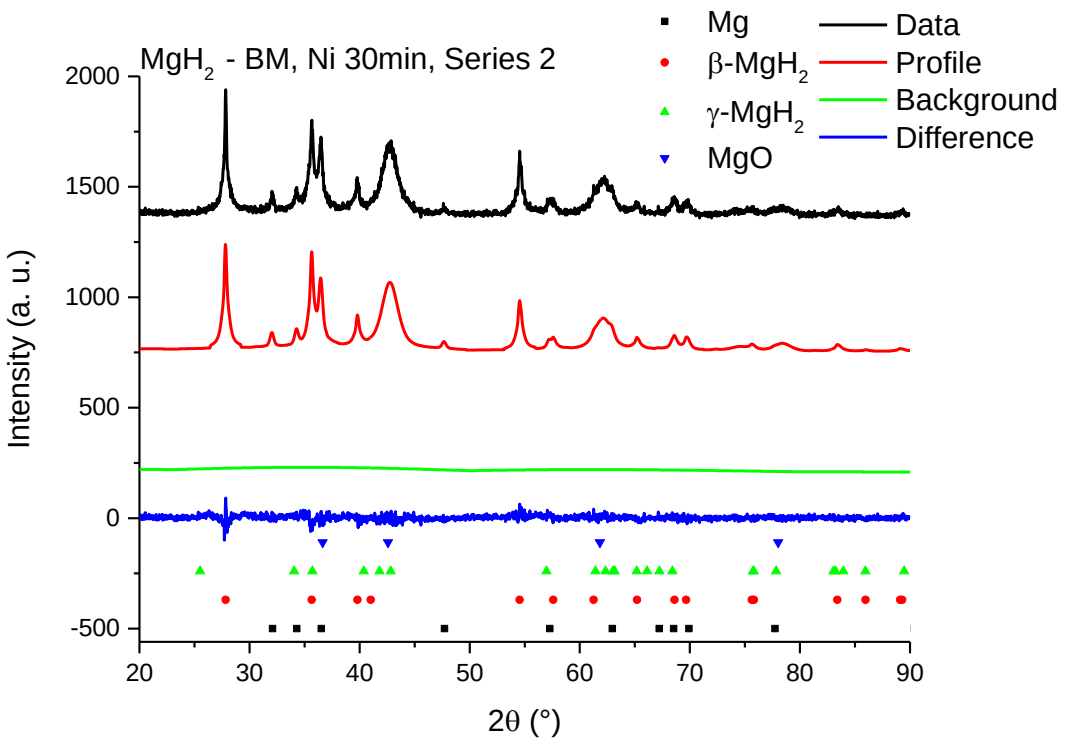

Fig. 7.15. XRD pattern, calculated profile, background profile and difference plot for sample MgH_2 - BM, Ni 30min, Series 2.

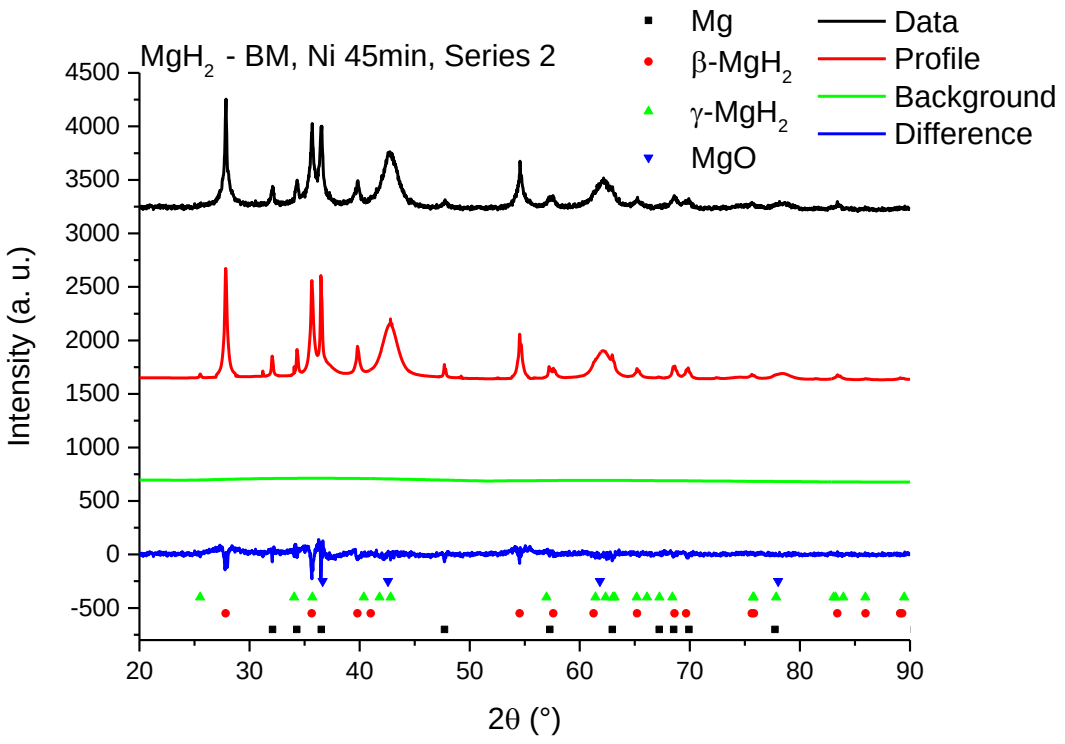

Fig. 7.16. XRD pattern, calculated profile, background profile and difference plot for sample MgH_2 - BM, Ni 45min, Series 2.

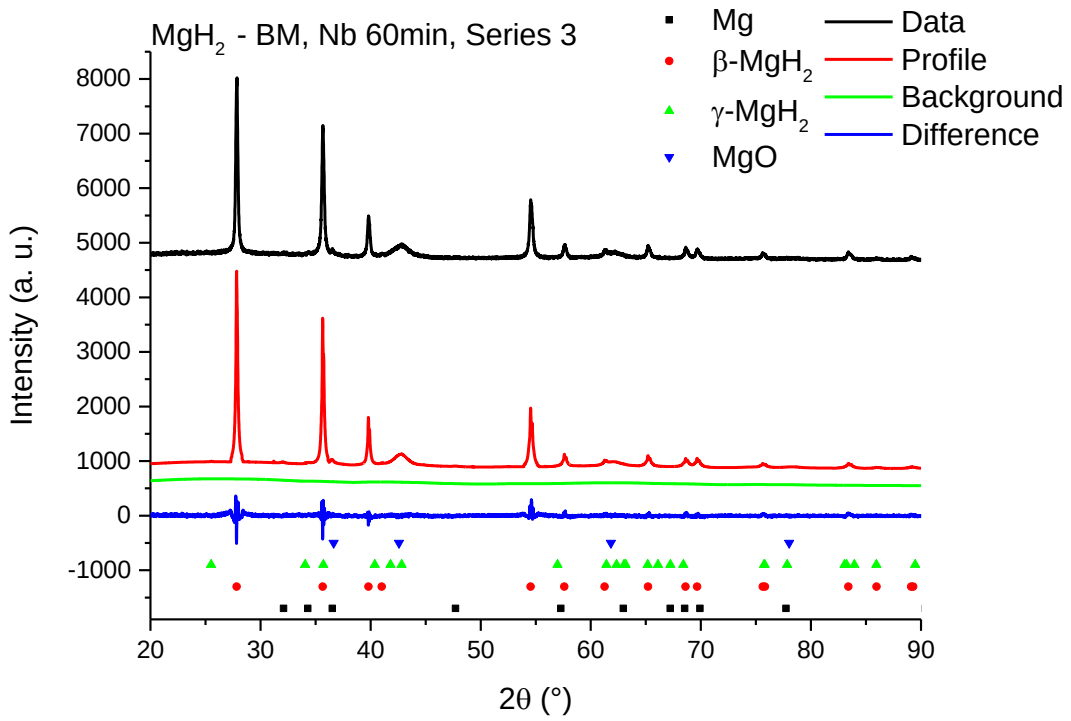

Fig. 7.17. XRD pattern, calculated profile, background profile and difference plot for sample MgH_2 - BM, Nb 60min, Series 3.

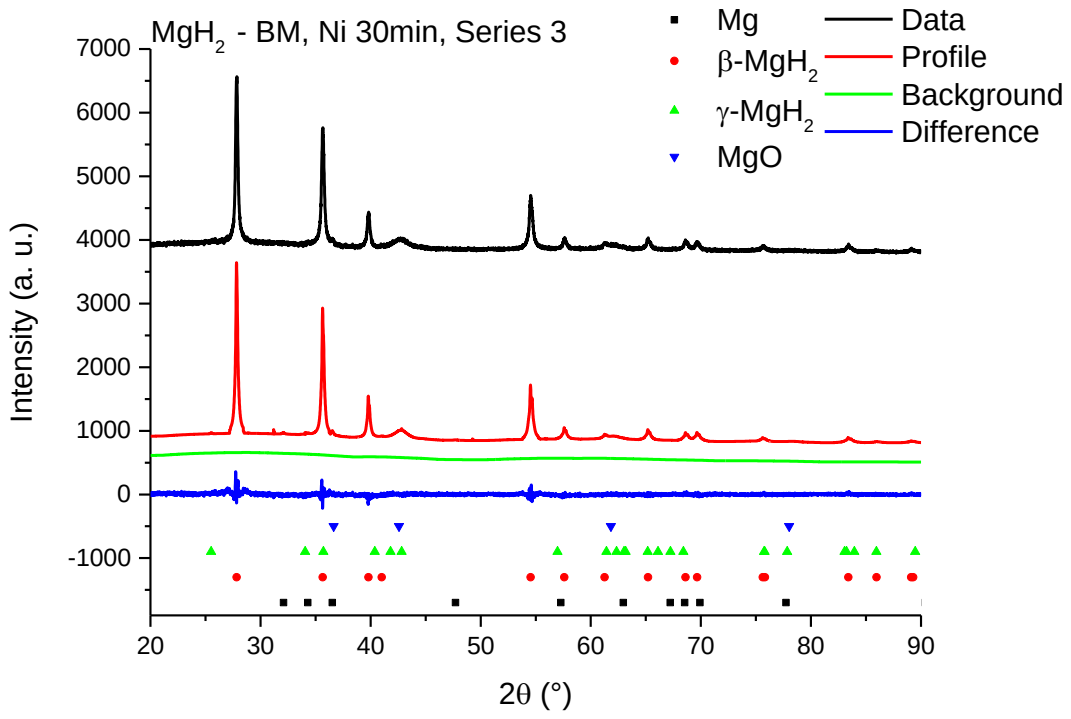

Fig. 7.18. XRD pattern, calculated profile, background profile and difference plot for sample MgH_2 - BM, Ni 30min, Series 3.

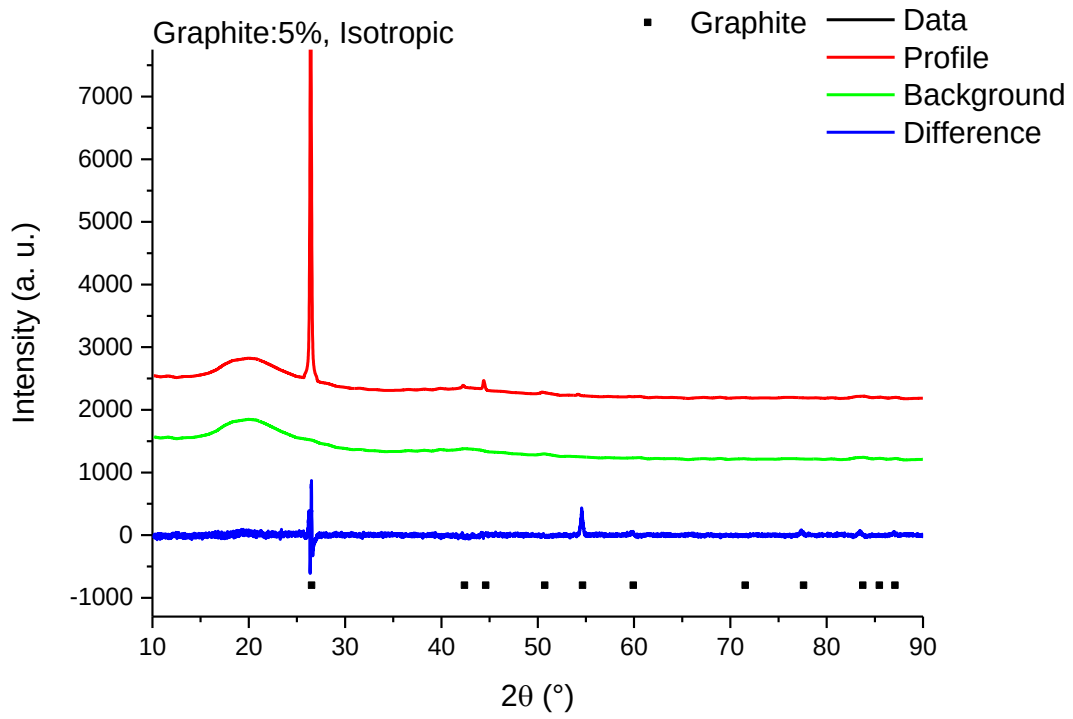

Fig. 7.19. XRD pattern, calculated profile, background profile and difference plot for sample of 5 vol.% isotropic graphite composite.

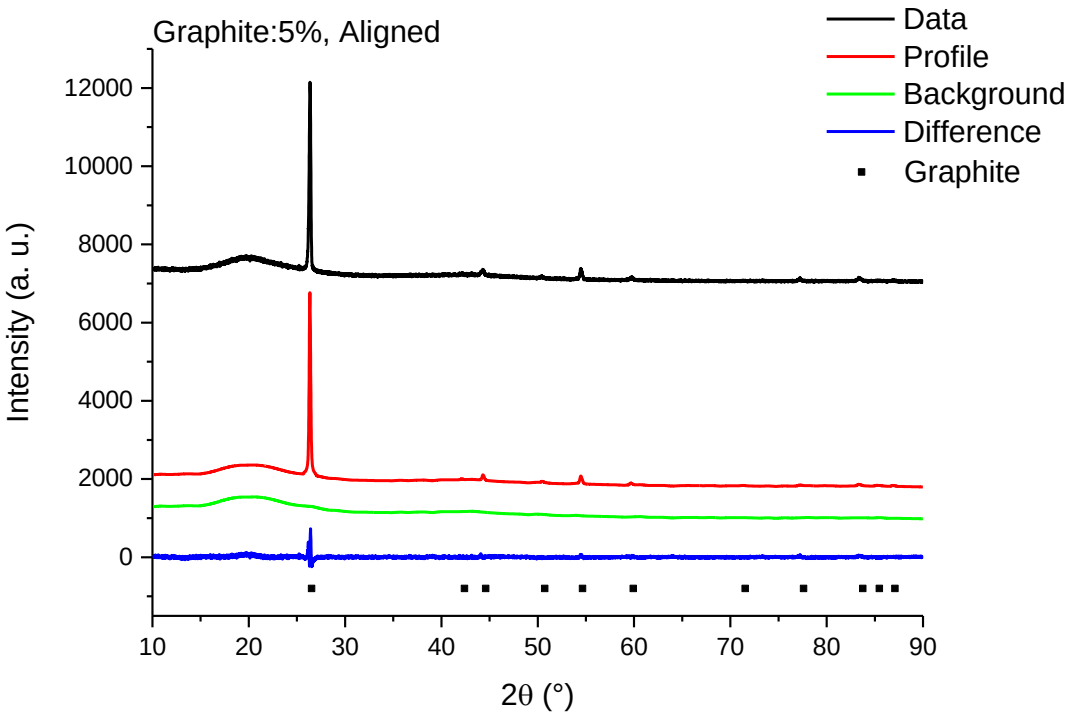

Fig. 7.20. XRD pattern, calculated profile, background profile and difference plot for sample of 5 vol.% aligned graphite composite.

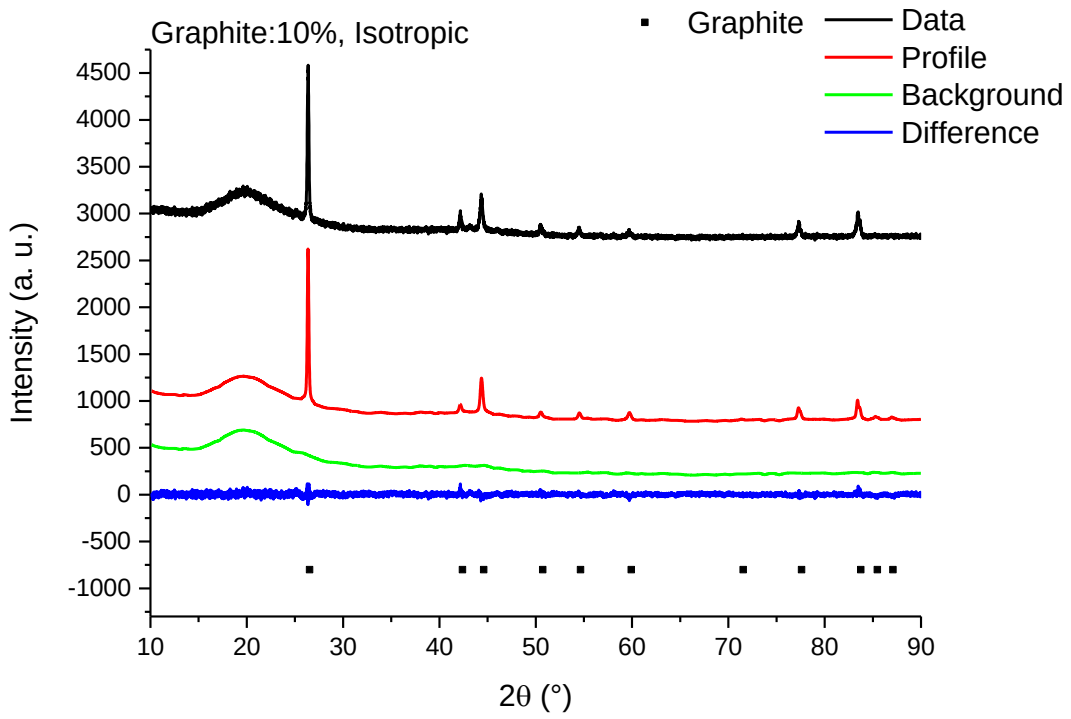

Fig. 7.21. XRD pattern, calculated profile, background profile and difference plot for sample of 10 vol.% isotropic graphite composite.

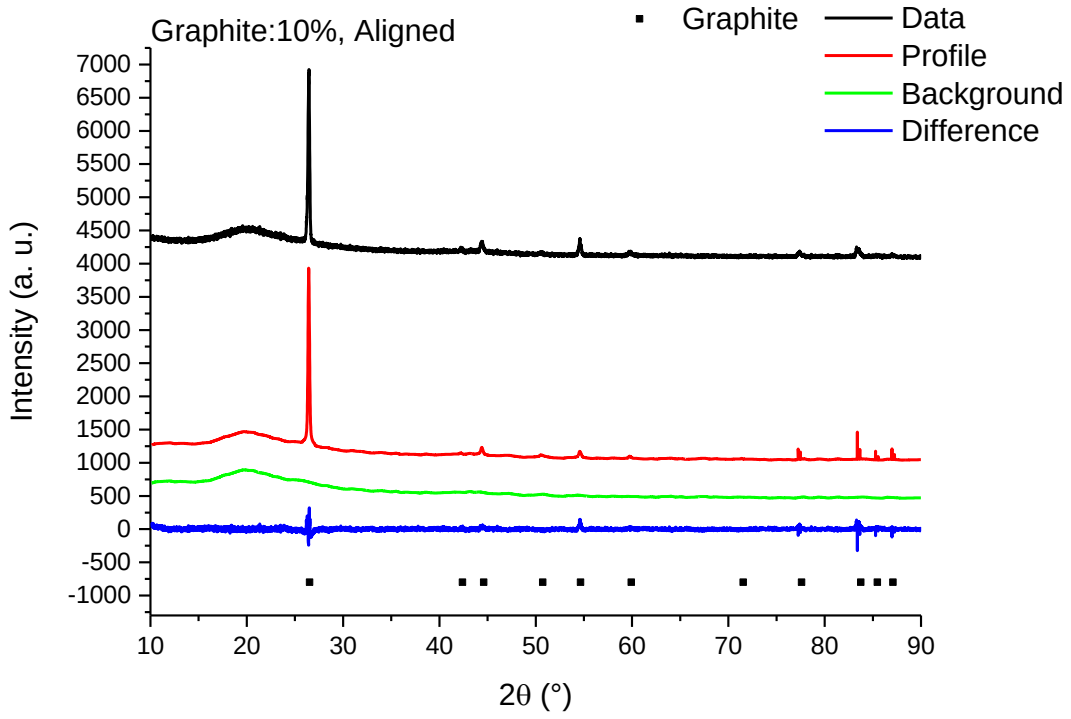

Fig. 7.22. XRD pattern, calculated profile, background profile and difference plot for sample of 10 vol.% aligned graphite composite.

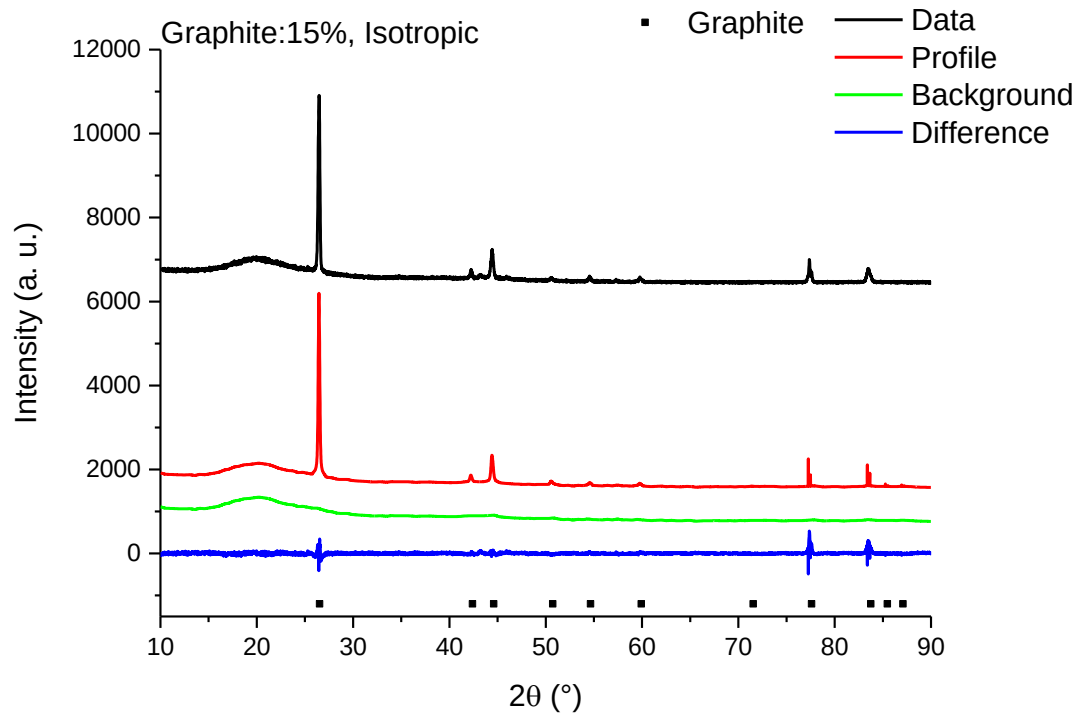

Fig. 7.23. XRD pattern, calculated profile, background profile and difference plot for sample of 15 vol.% isotropic graphite composite.

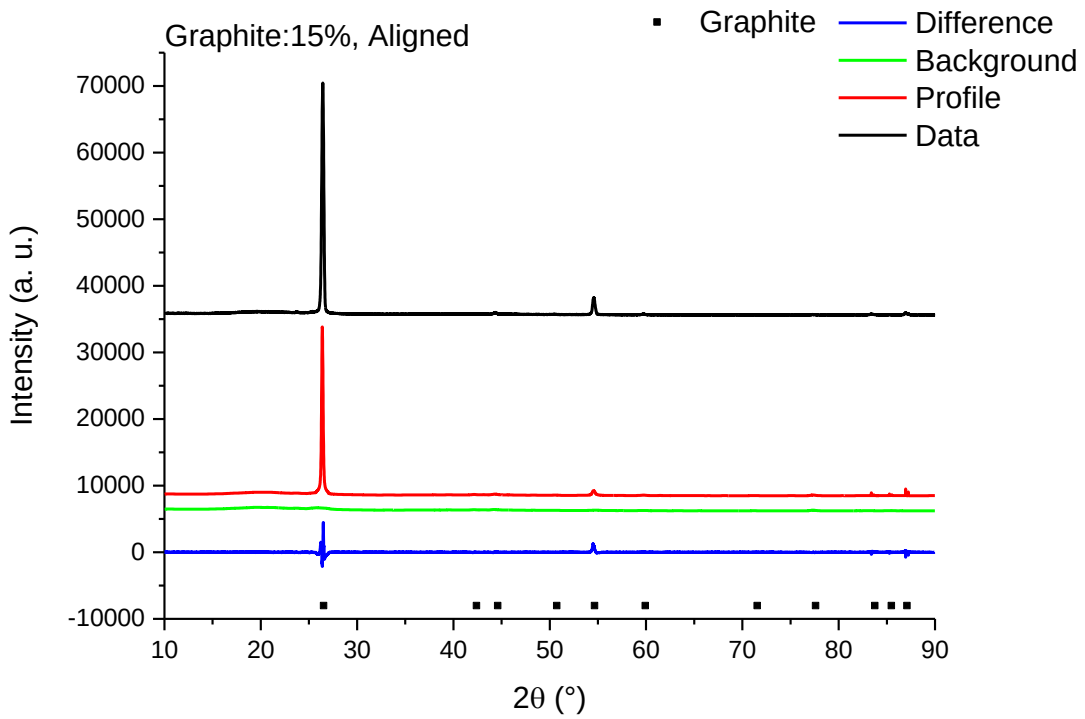

Fig. 7.24. XRD pattern, calculated profile, background profile and difference plot for sample of 15 vol.% aligned graphite composite.

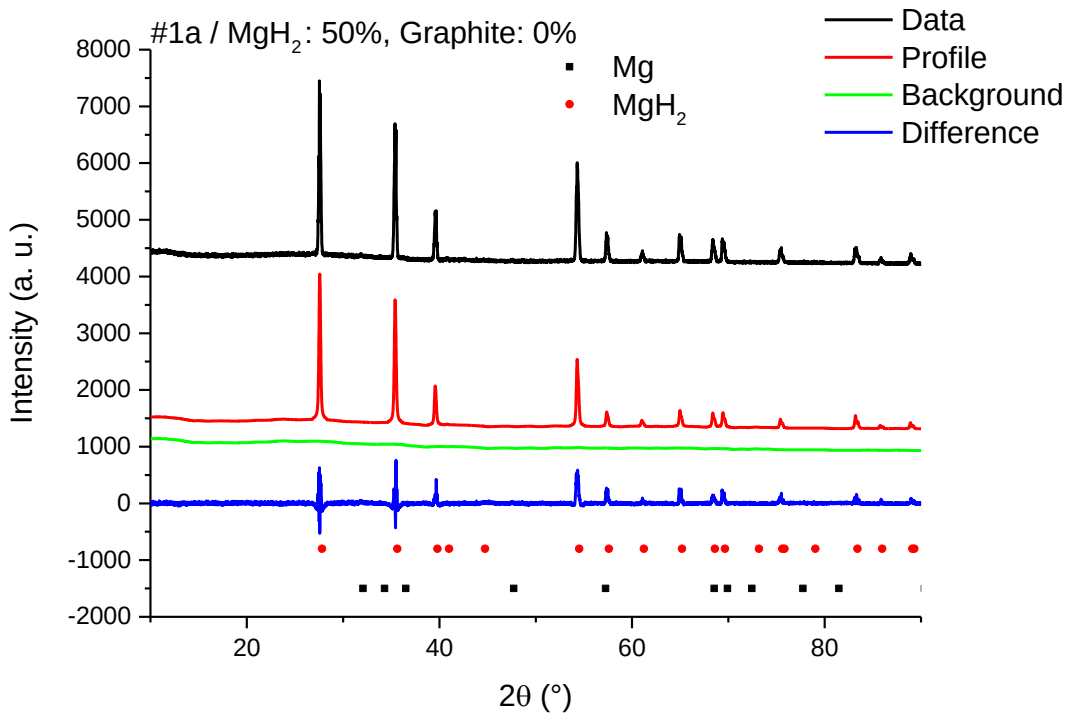

Fig. 7.25. XRD pattern, calculated profile, background profile and difference plot for sample #1a / MgH_2 : 50%, Graphite: 0%.

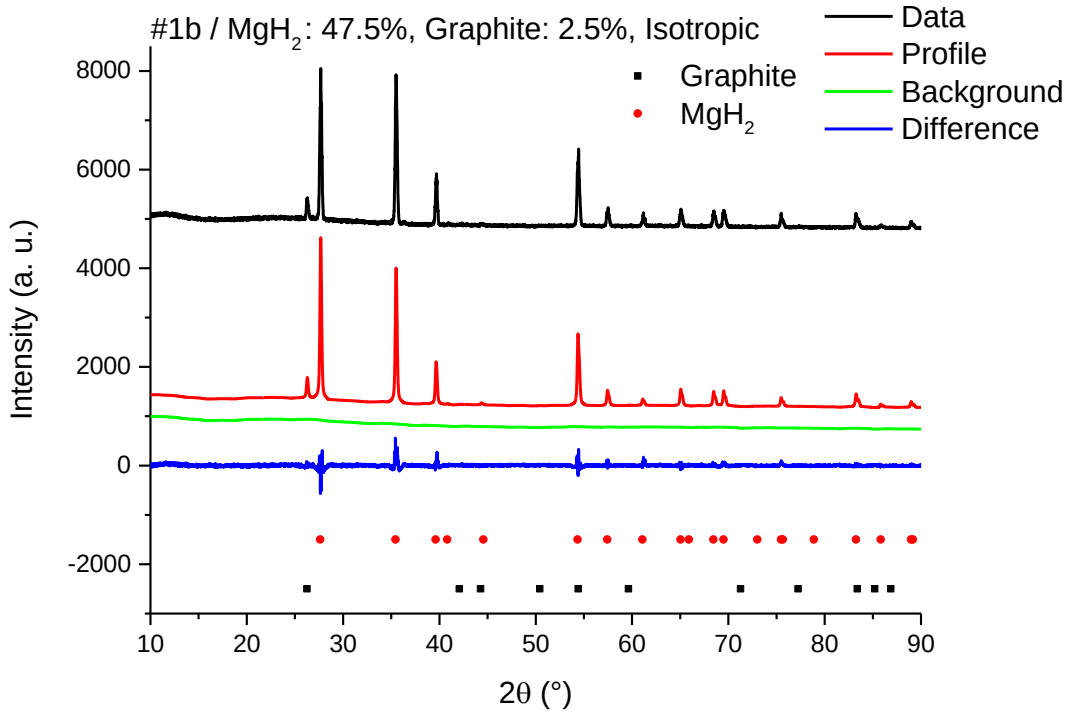

Fig. 7.26. XRD pattern, calculated profile, background profile and difference plot for sample #1b / MgH_2 : 47.5%, Graphite: 2.5%, Isotropic.

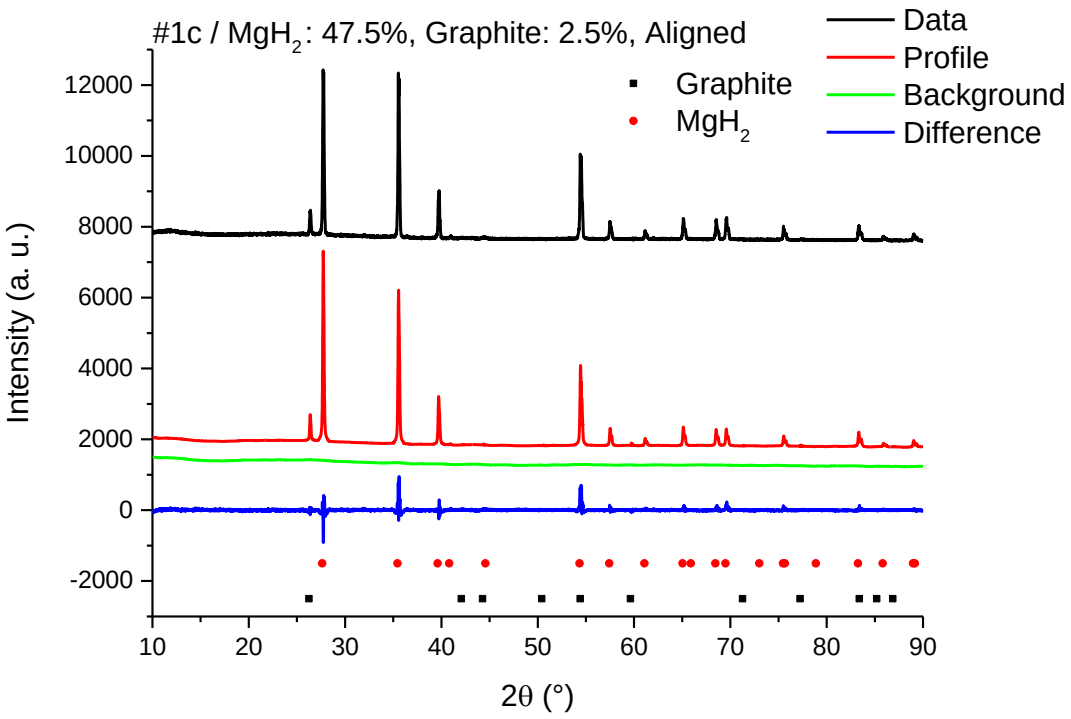

Fig. 7.27. XRD pattern, calculated profile, background profile and difference plot for sample #1c / MgH_2 : 47.5%, Graphite: 2.5%, Aligned.

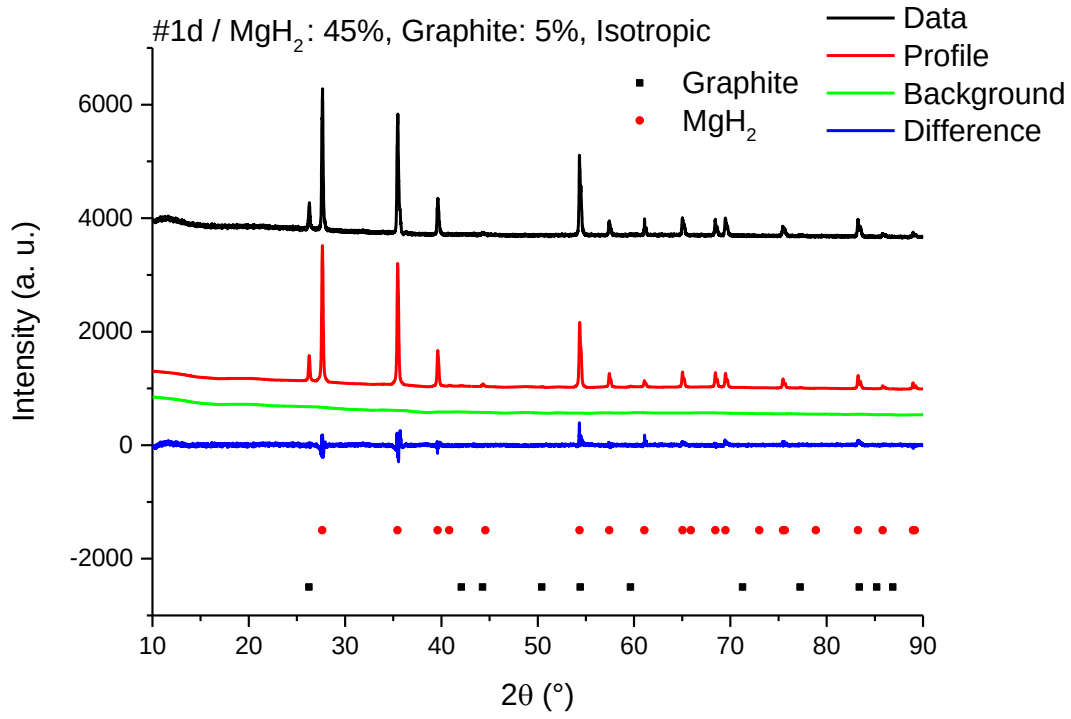

Fig. 7.28. XRD pattern, calculated profile, background profile and difference plot for sample #1d / MgH_2 : 45%, Graphite: 5%, Isotropic.

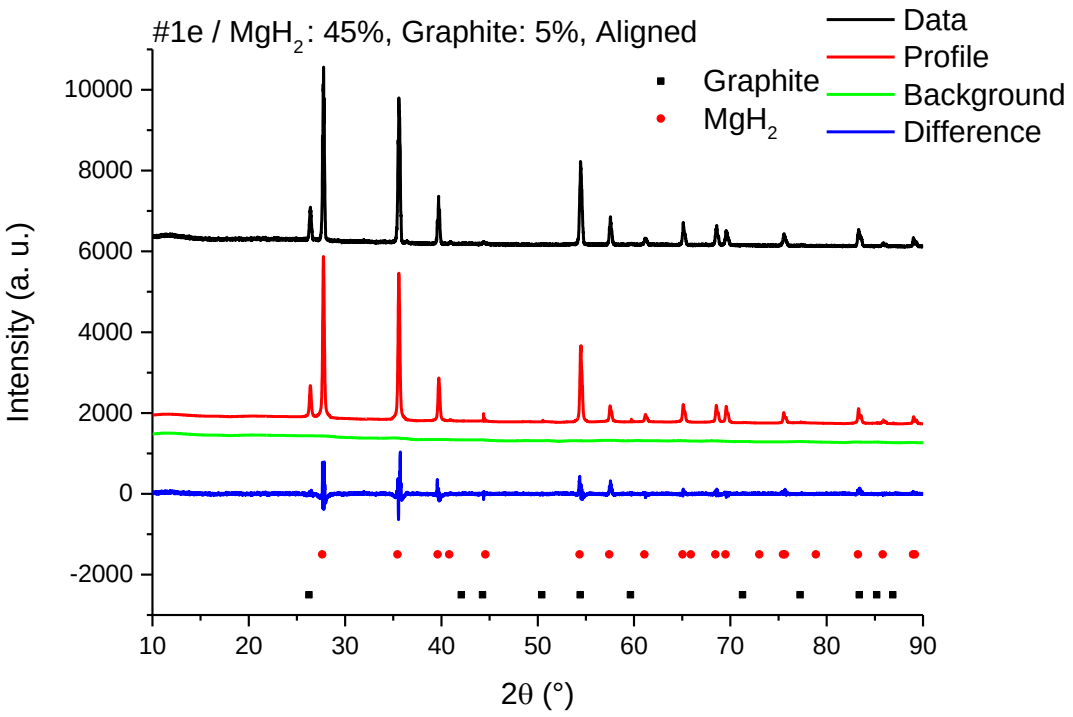

Fig. 7.29. XRD pattern, calculated profile, background profile and difference plot for sample #1e / MgH_2 : 45%, Graphite: 5%, Aligned.

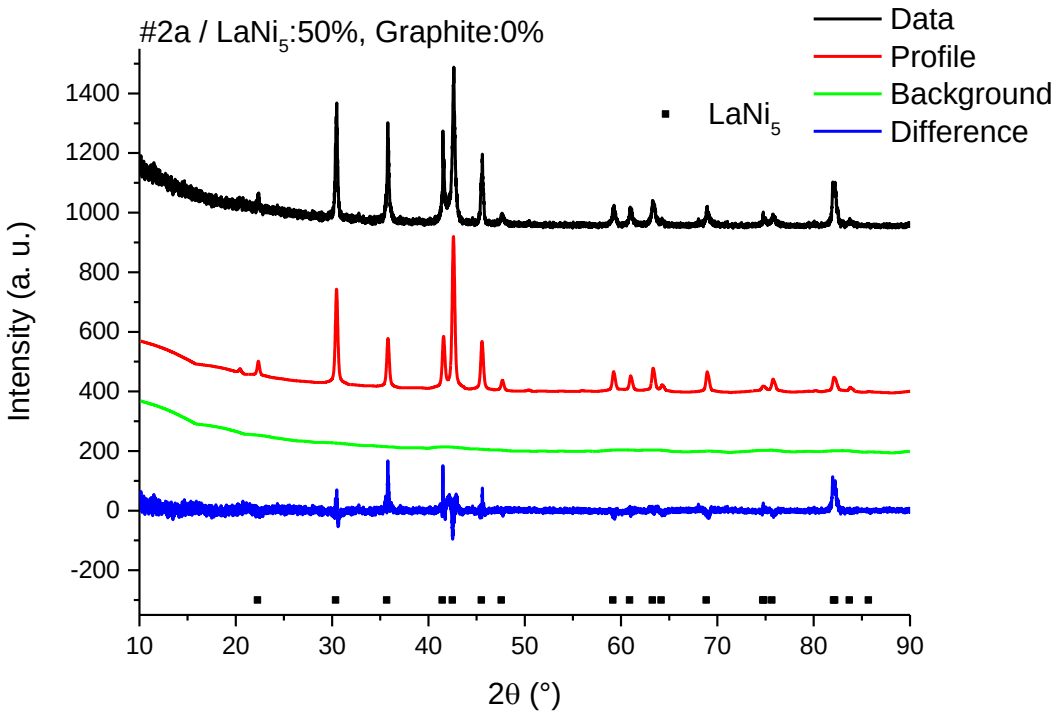

Fig. 7.30. XRD pattern, calculated profile, background profile and difference plot for sample #2a / $LaNi_5$: 50%, Graphite: 0%.

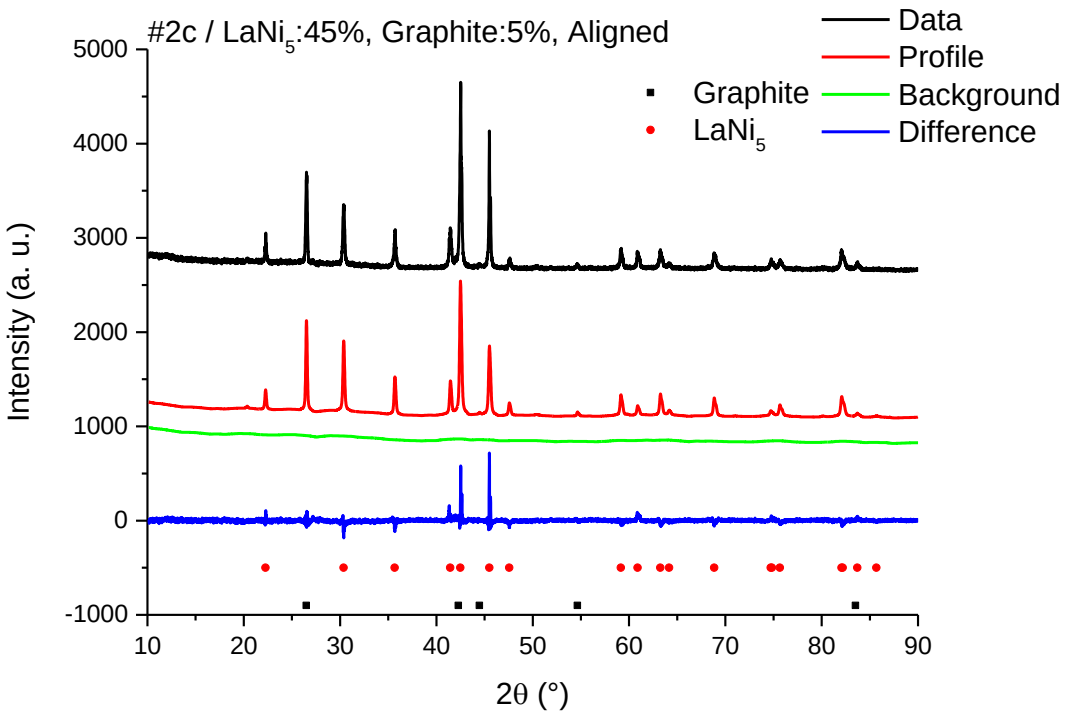

Fig. 7.31. XRD pattern, calculated profile, background profile and difference plot for sample #2b / $LaNi_5$: 45%, Graphite: 5%, Isotropic.

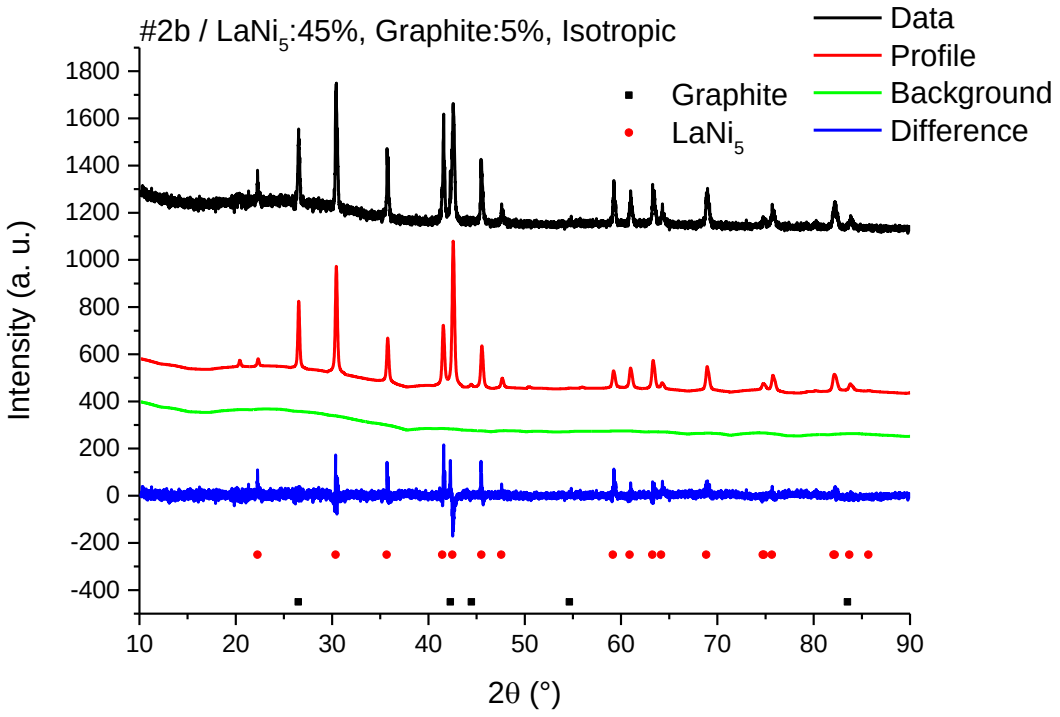

Fig. 7.32. XRD pattern, calculated profile, background profile and difference plot for sample #2c / $LaNi_5$: 45%, Graphite: 5%, Aligned.

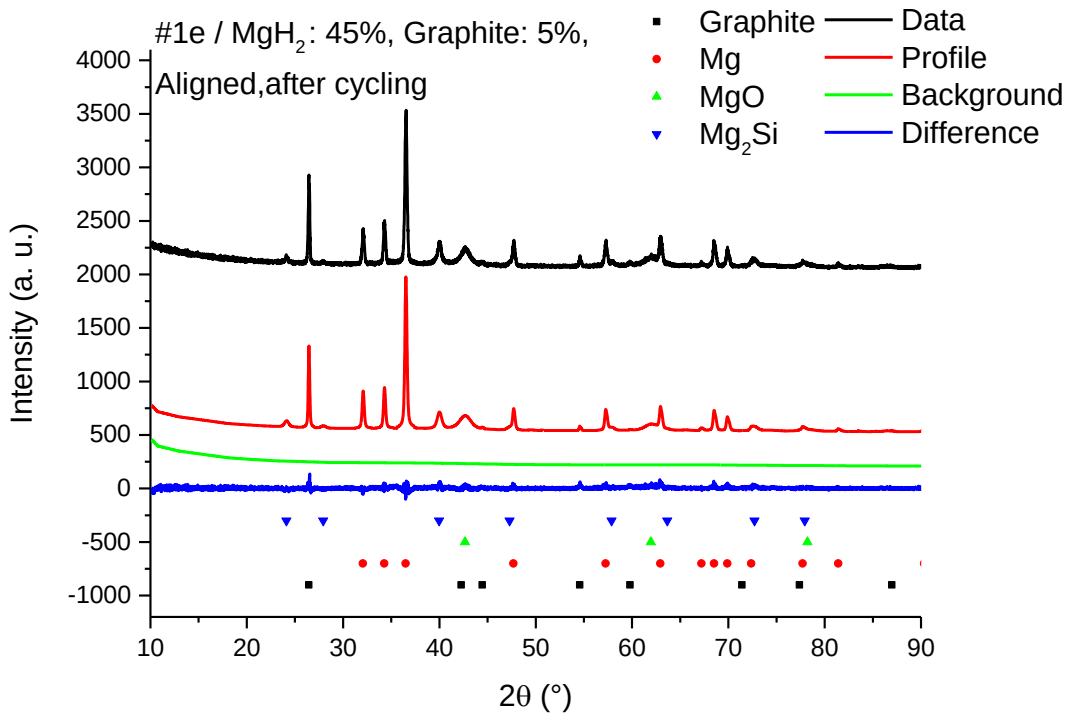

Fig. 7.33. XRD pattern, calculated profile, background profile and difference plot for sample #1e / MgH_2 : 45%, Graphite: 5%, Aligned, after the cycling.

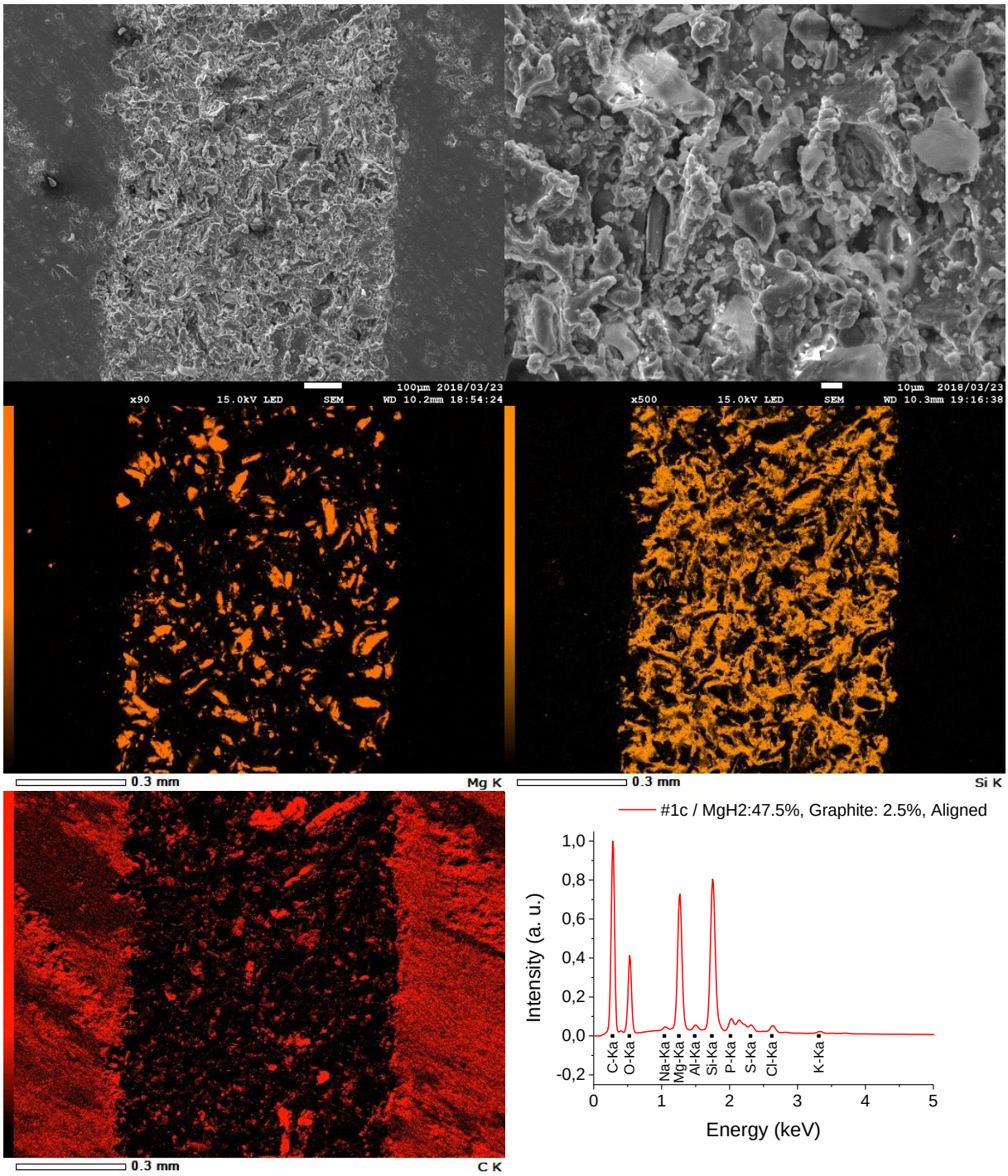

Fig. 7.34. SEM images, EDS element distribution maps for Si (from matrix), Mg and C (from fillers) and EDS spectra for composite sample #1c (MgH_2: 47.5%, Graphite: 2.5%, aligned)

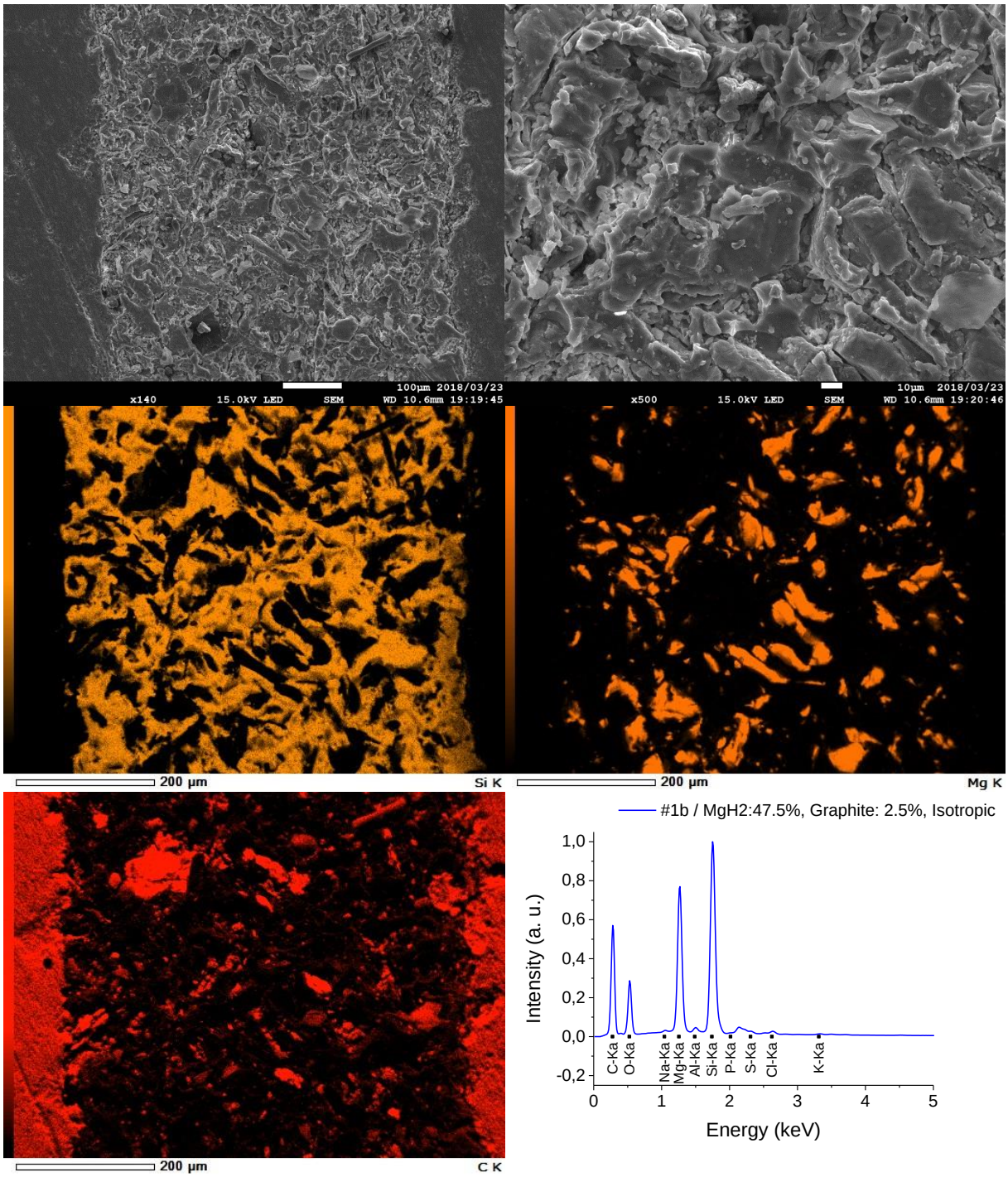

Fig. 7.35. SEM images, EDS element distribution maps for Si (from matrix), Mg and C (from fillers) and EDS spectra for composite sample #1b (MgH_2: 47.5%, Graphite: 2.5%, isotropic)

REFERENCES

[1] "DOE Technical Targets for Onboard Hydrogen Storage for Light-Duty Vehicles | Department of Energy." [Online]. Available: https://www.energy.gov/eere/fuelcells/doe-technical-targets-onboard-hydrogen-storage-light-duty-vehicles. [Accessed: 11-Jul-2018].

[2] H. Barthelemy, M. Weber, and F. Barbier, "Hydrogen storage: Recent improvements and industrial perspectives," *Int. J. Hydrog. Energy*, vol. 42, no. 11, pp. 7254–7262, Mar. 2017.

[3] K. T. Møller, T. R. Jensen, E. Akiba, and H. Li, "Hydrogen - A sustainable energy carrier," *Prog. Nat. Sci. Mater. Int.*, vol. 27, no. 1, pp. 34–40, Feb. 2017.

[4] Y. Sun, C. Shen, Q. Lai, W. Liu, D.-W. Wang, and K.-F. Aguey-Zinsou, "Tailoring magnesium based materials for hydrogen storage through synthesis: Current state of the art," *Energy Storage Mater.*, vol. 10, pp. 168–198, Jan. 2018.

[5] P. Preuster, A. Alekseev, and P. Wasserscheid, "Hydrogen Storage Technologies for Future Energy Systems," *Annu. Rev. Chem. Biomol. Eng.*, vol. 8, pp. 445–471, 07 2017.

[6] V. A. Blagojević, D. G. Minić, and J. G. N. and D. M. Minic, "Hydrogen Economy: Modern Concepts, Challenges and Perspectives," *Hydrog. Energy - Chall. Perspect.*, 2012.

[7] A. Züttel, A. Remhof, A. Borgschulte, and O. Friedrichs, "Hydrogen: the future energy carrier," *Philos. Trans. R. Soc. Lond. Math. Phys. Eng. Sci.*, vol. 368, no. 1923, pp. 3329–3342, Jul. 2010.

[8] A. Züttel, "Materials for hydrogen storage," *Mater. Today*, vol. 6, no. 9, pp. 24–33, Sep. 2003.

[9] N. Takeichi *et al.*, "'Hybrid hydrogen storage vessel', a novel high-pressure hydrogen storage vessel combined with hydrogen storage material," *Int. J. Hydrog. Energy*, vol. 28, no. 10, pp. 1121–1129, Oct. 2003.

[10] J. Yang, A. Sudik, C. Wolverton, and D. J. Siegel, "High capacity hydrogen storage materials: attributes for automotive applications and techniques for materials discovery," *Chem. Soc. Rev.*, vol. 39, no. 2, pp. 656–675, Feb. 2010.

[11] W. Luo, P. G. Campbell, L. N. Zakharov, and S.-Y. Liu, "A single-component liquid-phase hydrogen storage material," *J. Am. Chem. Soc.*, vol. 133, no. 48, pp. 19326–19329, Dec. 2011.

[12] "(6) Hydrogen storage and delivery by reversible hydrogenation of liquid-phase hydrogen carriers," *ResearchGate*. [Online]. Available: https://www.researchgate.net/publication/289541800_Hydrogen_storage_and_delivery_by_reversible_hydrogenation_of_liquid-phase_hydrogen_carriers. [Accessed: 01-Aug-2018].

[13] M. Dornheim, "Thermodynamics of Metal Hydrides: Tailoring Reaction Enthalpies of Hydrogen Storage Materials," *Thermodyn. - Interact. Stud. - Solids Liq. Gases*, 2011.

[14] A. Andreasen, Risø National Lab, and Roskilde (DK). Materials Research Department, *Predicting formation enthalpies of metal hydrides.* 2004.

[15] Y. Wang and Y. Wang, "Recent advances in additive-enhanced magnesium hydride for hydrogen storage," *Prog. Nat. Sci. Mater. Int.*, vol. 27, no. 1, pp. 41–49, Feb. 2017.

[16] K.-F. Aguey-Zinsou and J.-R. Ares-Fernández, "Hydrogen in magnesium: new perspectives toward functional stores," *Energy Environ. Sci.*, vol. 3, no. 5, pp. 526–543, May 2010.

[17] A. Zaluska, L. Zaluski, and J. O. Ström–Olsen, "Nanocrystalline magnesium for hydrogen storage," *J. Alloys Compd.*, vol. 288, no. 1, pp. 217–225, Jun. 1999.

[18] W. Liu and K.-F. Aguey-Zinsou, "Size effects and hydrogen storage properties of Mg nanoparticles synthesised by an electroless reduction method," *J. Mater. Chem. A*, vol. 2, no. 25, pp. 9718–9726, Jun. 2014.

[19] W. Li, C. Li, H. Ma, and J. Chen, "Magnesium Nanowires: Enhanced Kinetics for Hydrogen Absorption and Desorption," *J. Am. Chem. Soc.*, vol. 129, no. 21, pp. 6710–6711, May 2007.
[20] C. Zhu and T. Akiyama, "Zebra-Striped Fibers in Relation to the H_2 Sorption Properties for MgH_2 Nanofibers Produced by a Vapor–Solid Process," *Cryst. Growth Des.*, vol. 12, no. 8, pp. 4043–4052, Aug. 2012.
[21] Y. S. Au, M. K. Obbink, S. Srinivasan, P. C. M. M. Magusin, K. P. de Jong, and P. E. de Jongh, "The Size Dependence of Hydrogen Mobility and Sorption Kinetics for Carbon-Supported MgH2 Particles," *Adv. Funct. Mater.*, vol. 24, no. 23, pp. 3604–3611, Jun. 2014.
[22] G. Xia *et al.*, "Monodisperse Magnesium Hydride Nanoparticles Uniformly Self-Assembled on Graphene," *Adv. Mater.*, vol. 27, no. 39, pp. 5981–5988, Oct. 2015.
[23] M. S. El-Eskandarany, E. Shaban, and B. Al-Halaili, "Nanocrystalline β-γ-β cyclic phase transformation in reacted ball milled MgH_2 powders," *Int. J. Hydrog. Energy*, vol. 24, no. 39, pp. 12727–12740, 2014.
[24] M. Bortz, B. Bertheville, G. Böttger, and K. Yvon, "Structure of the high pressure phase γ-MgH_2 by neutron powder diffraction," *J. Alloys Compd.*, vol. 287, no. 1, pp. L4–L6, Jun. 1999.
[25] J.-C. Crivello *et al.*, "Review of magnesium hydride-based materials: development and optimisation," *Appl. Phys. A*, vol. 122, no. 2, p. 97, Jan. 2016.
[26] S. Zhou *et al.*, "Crystalline structure, energy calculation and dehydriding thermodynamics of magnesium hydride from reactive milling," *Int. J. Hydrog. Energy*, vol. 40, no. 35, pp. 11484–11490, Sep. 2015.
[27] J. M. Sander, L. Ismer, and C. G. Van de Walle, "Point-defect kinetics in α- and γ-MgH_2," *Int. J. Hydrog. Energy*, vol. 41, no. 13, pp. 5688–5692, Apr. 2016.
[28] S. X. Tao *et al.*, "First principle study of hydrogen diffusion in equilibrium rutile, rutile with deformation twins and fluorite polymorph of Mg hydride," *Int. J. Hydrog. Energy*, vol. 36, no. 18, pp. 11802–11809, Sep. 2011.
[29] X. Xiao, Z. Liu, S. Saremi-Yarahmadi, and D. H. Gregory, "Facile preparation of β-/γ-MgH_2 nanocomposites under mild conditions and pathways to rapid dehydrogenation," *Phys. Chem. Chem. Phys.*, vol. 18, no. 15, pp. 10492–10498, Apr. 2016.
[30] W. Liu, E. J. Setijadi, and K.-F. Aguey-Zinsou, "Tuning the Thermodynamic Properties of MgH_2 at the Nanoscale via a Catalyst or Destabilizing Element Coating Strategy," *J. Phys. Chem. C*, vol. 118, no. 48, pp. 27781–27792, Dec. 2014.
[31] J. J. Reilly and R. H. Wiswall, "Reaction of hydrogen with alloys of magnesium and nickel and the formation of Mg_2NiH_4," *Inorg. Chem.*, vol. 7, no. 11, pp. 2254–2256, Nov. 1968.
[32] J. J. Vajo, F. Mertens, C. C. Ahn, Bowman Robert C., and B. Fultz, "Altering Hydrogen Storage Properties by Hydride Destabilization through Alloy Formation: LiH and MgH_2 Destabilized with Si," *J. Phys. Chem. B*, vol. 108, no. 37, pp. 13977–13983, Sep. 2004.
[33] P. C. H. Mitchell, A. J. Ramirez-Cuesta, S. F. Parker, J. Tomkinson, and D. Thompsett, "Hydrogen Spillover on Carbon-Supported Metal Catalysts Studied by Inelastic Neutron Scattering. Surface Vibrational States and Hydrogen Riding Modes," *J. Phys. Chem. B*, vol. 107, no. 28, pp. 6838–6845, Jul. 2003.
[34] R. Krishna *et al.*, "Hydrogen Storage for Energy Application," *Hydrog. Storage*, 2012.
[35] G. Liang, J. Huot, S. Boily, A. Van Neste, and R. Schulz, "Catalytic effect of transition metals on hydrogen sorption in nanocrystalline ball milled MgH_2–Tm (Tm=Ti, V, Mn, Fe and Ni) systems," *J. Alloys Compd.*, vol. 292, no. 1, pp. 247–252, Nov. 1999.

[36] A. Patah, A. Takasaki, and J. S. Szmyd, “Influence of multiple oxide (Cr_2O_3/Nb_2O_5) addition on the sorption kinetics of MgH_2,” *Int. J. Hydrog. Energy*, vol. 34, no. 7, pp. 3032–3037, Apr. 2009.
[37] T. Kobayashi and A. Takasaki, “Ab initio study of the role of niobium oxides as catalysts in magnesium hydride,” *J. Alloys Compd.*, vol. 580, pp. S229–S232, Dec. 2013.
[38] G. Barkhordarian, T. Klassen, and R. Bormann, “Kinetic investigation of the effect of milling time on the hydrogen sorption reaction of magnesium catalyzed with different Nb_2O_5 contents,” *J. Alloys Compd.*, vol. 407, no. 1, pp. 249–255, Jan. 2006.
[39] M. Song, J.-L. Bobet, and B. Darriet, “Improvement in hydrogen sorption properties of Mg by reactive mechanical grinding with Cr_2O_3, Al_2O_3 and CeO_2,” *J. Alloys Compd.*, vol. 340, no. 1, pp. 256–262, Jun. 2002.
[40] Z. Jalil, A. Rahwanto, I. Ismail, H. Sofyan, and E. Handoko, “The use of nano-silicon carbide and nickel as catalyst in magnesium hydrides (MgH_2) for hydrogen storage material application,” *Mater. Res. Express*, vol. 5, no. 6, p. 064002, 2018.
[41] Z. Jalil, A. Rahwanto, F. Mulana, and M. Mustanir, “Desorption Temperature Characteristic of Mg-based Hydrides Catalyzed by Nano-SiO2 Prepared by High Energy Ball Milling,” *Int. J. Technol.*, vol. 7, no. 8, p. 1301, Dec. 2016.
[42] Y. Wang, Q. Zhang, Y. Wang, L. Jiao, and H. Yuan, “Catalytic effects of different Ti-based materials on dehydrogenation performances of MgH_2,” *J. Alloys Compd.*, vol. 645, pp. S509–S512, Oct. 2015.
[43] J. Cui *et al.*, “Remarkable enhancement in dehydrogenation of MgH_2 by a nano-coating of multi-valence Ti-based catalysts,” *J. Mater. Chem. A*, vol. 1, no. 18, pp. 5603–5611, Apr. 2013.
[44] Y. Chen and Y. Liu, “Preparation of porous carbon with high dispersion of Ru nanoparticles by sol–gel method and its application in hydrogen storage,” *J. Mater. Chem. A*, vol. 2, no. 24, pp. 9193–9199, May 2014.
[45] Y. Liu, J. Zou, X. Zeng, X. Wu, D. Li, and W. Ding, “Hydrogen Storage Properties of a Mg–Ni Nanocomposite Coprecipitated from Solution,” *J. Phys. Chem. C*, vol. 118, no. 32, pp. 18401–18411, Aug. 2014.
[46] M. A. Lillo-Ródenas, Z. X. Guo, K. F. Aguey-Zinsou, D. Cazorla-Amorós, and A. Linares-Solano, “Effects of different carbon materials on MgH_2 decomposition,” *Carbon*, vol. 46, no. 1, pp. 126–137, Jan. 2008.
[47] “Improvement in hydrogen cycling properties of magnesium through added graphite,” *Mater. Lett.*, vol. 61, no. 14–15, pp. 3163–3166, Jun. 2007.
[48] “Hydrogenation characteristics of air-exposed magnesium films,” *J. Alloys Compd.*, vol. 345, no. 1–2, pp. 158–166, Oct. 2002.
[49] “Imaging the hydrogenation of Mg thin films,” *Int. J. Hydrog. Energy*, vol. 42, no. 35, pp. 22411–22416, Aug. 2017.
[50] L. Ouyang *et al.*, “Express penetration of hydrogen on Mg(10T3) along the close-packed-planes,” *Sci. Rep.*, vol. 5, p. 10776, Jun. 2015.
[51] H. Fujii, K. Higuchi, K. Yamamoto, H. Kajioka, S. Orimo, and K. Toiyama, “Remarkable Hydrogen Storage, Structural and Optical Properties in Multi-layered Pd/Mg Thin Films,” *Mater. Trans.*, vol. 43, no. 11, pp. 2721–2727, 2002.
[52] C.-J. Chung, S.-C. Lee, J. R. Groves, E. N. Brower, R. Sinclair, and B. M. Clemens, “Interfacial alloy hydride destabilization in Mg/Pd thin films,” *Phys. Rev. Lett.*, vol. 108, no. 10, p. 106102, Mar. 2012.
[53] P. Vermeulen, R. a. H. Niessen, and P. H. L. Notten, “Hydrogen storage in metastable MgyTi(1-y) thin films,” *Electrochem. Commun.*, vol. 8, no. 1, pp. 27–32, 2006.

[54] P. Vermeulen *et al.*, “In situ electrochemical XRD study of (de)hydrogenation of MgyTi100−y thin films,” *J. Mater. Chem.*, vol. 18, no. 31, pp. 3680–3687, Jul. 2008.
[55] “Heat transfer techniques in metal hydride hydrogen storage: A review,” *Int. J. Hydrog. Energy*, vol. 42, no. 52, pp. 30661–30682, Dec. 2017.
[56] “Magnesium based metal hydride reactor incorporating helical coil heat exchanger: Simulation study and optimal design,” *Appl. Energy*, vol. 130, pp. 712–722, Oct. 2014.
[57] “Optimization of hydrogen storage in metal-hydride tanks,” *Int. J. Hydrog. Energy*, vol. 34, no. 2, pp. 897–905, Jan. 2009.
[58] “Performance analysis of cylindrical metal hydride beds with various heat exchange options,” *J. Alloys Compd.*, vol. 645, pp. S89–S95, Oct. 2015.
[59] “Hydrogen desorption from a hydride container under different heat exchange conditions,” *Int. J. Hydrog. Energy*, vol. 38, no. 30, pp. 13352–13359, Oct. 2013.
[60] “Role of heat pipes in improving the hydrogen charging rate in a metal hydride storage tank,” *Int. J. Hydrog. Energy*, vol. 39, no. 20, pp. 10552–10563, Jul. 2014.
[61] “Accelerating hydrogen absorption in a metal hydride storage tank by physical mixing,” *Int. J. Hydrog. Energy*, vol. 39, no. 21, pp. 11035–11046, Jul. 2014.
[62] J. Lang, M. Eagles, M. S. Conradi, and J. Huot, “Hydrogenation rate limiting step, diffusion and thermal conductivity in cold rolled magnesium hydride,” *J. Alloys Compd.*, vol. 583, no. Supplement C, pp. 116–120, Jan. 2014.
[63] E. Martínez-Franco, T. Klassen, D. Jaramillo-Vigueras, and R. Bormann, “Propiedades de ab-desorción de hidrógeno del intermetálico Mg2Ni obtenido empleando un molino de bolas Simoloyer,” *Ing. Investig. Tecnol.*, vol. 11, no. 3, pp. 325–332, Sep. 2010.
[64] “Simulation of heat transfer in a metal hydride reactor with aluminium foam,” *Int. J. Hydrog. Energy*, vol. 32, no. 14, pp. 2957–2964, Sep. 2007.
[65] “Expanded graphite as heat transfer matrix in metal hydride beds,” *Int. J. Hydrog. Energy*, vol. 28, no. 5, pp. 515–527, May 2003.
[66] “Simulation and experimental validation of a hydrogen storage tank with metal hydrides,” *Int. J. Hydrog. Energy*, vol. 33, no. 1, pp. 98–104, Jan. 2008.
[67] “Metal hydride beds and hydrogen supply tanks as minitype PEMFC hydrogen sources,” *Int. J. Hydrog. Energy*, vol. 28, no. 3, pp. 329–333, Mar. 2003.
[68] “Heat and gas transport properties in pelletized hydride–graphite-composites for hydrogen storage applications,” *Int. J. Hydrog. Energy*, vol. 38, no. 3, pp. 1685–1691, Feb. 2013.
[69] “Solid-state hydrogen storage in Hydralloy–graphite composites,” *J. Power Sources*, vol. 231, pp. 97–105, Jun. 2013.
[70] “Enhancement of hydrogen sorption in magnesium hydride using expanded natural graphite,” *Int. J. Hydrog. Energy*, vol. 34, no. 20, pp. 8589–8596, Oct. 2009.
[71] “Effective thermal conductivity of MgH2 compacts containing expanded natural graphite under a hydrogen atmosphere,” *Int. J. Hydrog. Energy*, vol. 39, no. 1, pp. 349–355, Jan. 2014.
[72] “Microstructure and morphology changes in MgH2/expanded natural graphite pellets upon hydrogen cycling,” *Int. J. Hydrog. Energy*, vol. 38, no. 4, pp. 1918–1924, Feb. 2013.
[73] “Handbook of Carbon, Graphite, Diamonds and Fullerenes - 1st Edition.” [Online]. Available: https://www.elsevier.com/books/handbook-of-carbon-graphite-diamonds-and-fullerenes/pierson/978-0-8155-1339-1. [Accessed: 31-Aug-2018].
[74] A. A. Balandin, “Thermal properties of graphene and nanostructured carbon materials,” *Nat. Mater.*, vol. 10, no. 8, pp. 569–581, Aug. 2011.

[75] S. Akamaru, M. Inoue, and T. Abe, “Surface Modification of NaCl Particles with Metal Films Using the Polygonal Barrel-Sputtering Method,” *Mater. Sci. Appl.*, vol. 04, no. 07, p. 29, Jul. 2013.
[76] O. K. Alexeeva and V. N. Fateev, “Application of the magnetron sputtering for nanostructured electrocatalysts synthesis,” *Int. J. Hydrog. Energy*, vol. 41, no. 5, pp. 3373–3386, Feb. 2016.
[77] D. M. Baechle, J. D. Demaree, J. K. Hirvonen, and E. D. Wetzel, “Magnetron sputter deposition onto fluidized particle beds,” *Surf. Coat. Technol.*, vol. 221, no. Supplement C, pp. 94–103, Apr. 2013.
[78] A. A. Dameron *et al.*, “Pt–Ru Alloyed Fuel Cell Catalysts Sputtered from a Single Alloyed Target,” *ACS Catal.*, vol. 1, no. 10, pp. 1307–1315, Oct. 2011.
[79] W. Ensinger and H. R. Müller, “Noble metal deposition on aluminum oxide powder surfaces by ion beam sputtering,” *Nucl. Instrum. Methods Phys. Res. Sect. B Beam Interact. Mater. At.*, vol. 141, no. 1, pp. 693–698, May 1998.
[80] A. A. Fedotov, S. A. Grigor’ev, A. S. Glukhov, K. A. Dzhus’, and V. N. Fateev, “Synthesis of nanostructured electrocatalysts based on magnetron ion sputtering,” *Kinet. Catal.*, vol. 53, no. 6, pp. 753–758, Nov. 2012.
[81] M. Inoue, Y. Takahashi, M. Katagiri, T. Abe, and M. Umeda, “Addition of electrical conductivity to metal oxide particles using the polygonal barrel-sputtering method,” *J. Alloys Compd.*, vol. 670, no. Supplement C, pp. 170–174, Jun. 2016.
[82] G. Schmid, C. Eisenmenger-Sittner, J. Hell, M. Horkel, M. Keding, and H. Mahr, “Optimization of a container design for depositing uniform metal coatings on glass microspheres by magnetron sputtering,” *Surf. Coat. Technol.*, vol. 205, no. 7, pp. 1929–1936, Dec. 2010.
[83] J. Sun *et al.*, “Fabrication of active Cu–Zn nanoalloys on H-ZSM5 zeolite for enhanced dimethyl ether synthesis via syngas,” *J. Mater. Chem. A*, vol. 2, no. 23, pp. 8637–8643, May 2014.
[84] G. M. Veith, A. R. Lupini, S. J. Pennycook, G. W. Ownby, and N. J. Dudney, “Nanoparticles of gold on γ-Al_2O_3 produced by dc magnetron sputtering,” *J. Catal.*, vol. 231, no. 1, pp. 151–158, Apr. 2005.
[85] H. Yamamoto, K. Hirakawa, and T. Abe, “Surface modification of carbon nanofibers with platinum nanoparticles using a ‘polygonal barrel-sputtering’ system,” *Mater. Lett.*, vol. 62, no. 14, pp. 2118–2121, May 2008.
[86] C. Zeng *et al.*, “Highly selective and multifunctional Cu/ZnO/Zeolite catalyst for one-step dimethyl ether synthesis: Preparing catalyst by bimetallic physical sputtering,” *Fuel*, vol. 112, no. Supplement C, pp. 140–144, Oct. 2013.
[87] “Politechnika Wrocławska - WEMiF - Laboratorium Technologii Próżniowych i Plazmowych.” [Online]. Available: http://www.w12.pwr.wroc.pl/ltpp/sites/lab_mag.htm. [Accessed: 04-Sep-2018].
[88] M. A. Z.-A. R. A. Medina-Esquivel, “Thermal characterization of composites made up of magnetically aligned carbonyl iron particles in a polyester resin matrix,” *J. Appl. Phys.*, vol. 111, no. 5, pp. 054906–7, 2012.
[89] K. Goc *et al.*, “Influence of magnetic field-aided filler orientation on structure and transport properties of ferrite filled composites,” *J. Magn. Magn. Mater.*, vol. 419, pp. 345–353, Dec. 2016.
[90] K. Gaska, G. Kmita, A. Rybak, R. Sekula, K. Goc, and C. Kapusta, “Magnetic-aligned, magnetite-filled epoxy composites with enhanced thermal conductivity,” *J. Mater. Sci.*, vol. 50, no. 6, pp. 2510–2516, Jan. 2015.

[91] N. Ganguli and K. S. Krishnan, “Magnetic and other properties of the free electrons in graphite,” *Proc R Soc Lond A*, vol. 177, no. 969, pp. 168–182, Jan. 1941.
[92] F. Lin *et al.*, “Orientation Control of Graphene Flakes by Magnetic Field: Broad Device Applications of Macroscopically Aligned Graphene,” *Adv. Mater.*, vol. 29, no. 1, Jan. 2017.
[93] Y. Ominato and M. Koshino, “Orbital magnetism of graphene flakes,” *Phys. Rev. B*, vol. 87, no. 11, p. 115433, Mar. 2013.
[94] T. Kimura, H. Ago, M. Tobita, S. Ohshima, M. Kyotani, and M. Yumura, “Polymer Composites of Carbon Nanotubes Aligned by a Magnetic Field,” *Adv. Mater.*, vol. 14, no. 19, pp. 1380–1383, Oct. 2002.
[95] M. Abdalla, D. Dean, M. Theodore, J. Fielding, E. Nyairo, and G. Price, “Magnetically processed carbon nanotube/epoxy nanocomposites: Morphology, thermal, and mechanical properties,” *Polymer*, vol. 51, no. 7, pp. 1614–1620, Mar. 2010.
[96] E. Camponeschi, R. Vance, M. Al-Haik, H. Garmestani, and R. Tannenbaum, “Properties of carbon nanotube–polymer composites aligned in a magnetic field,” *Carbon*, vol. 45, no. 10, pp. 2037–2046, Sep. 2007.
[97] M. A. Correa-Duarte *et al.*, “Alignment of Carbon Nanotubes under Low Magnetic Fields through Attachment of Magnetic Nanoparticles,” *J. Phys. Chem. B*, vol. 109, no. 41, pp. 19060–19063, Oct. 2005.
[98] I. T. Kim, A. Tannenbaum, and R. Tannenbaum, “Anisotropic conductivity of magnetic carbon nanotubes embedded in epoxy matrices,” *Carbon*, vol. 49, no. 1, pp. 54–61, Jan. 2011.
[99] H. Yan, Y. Tang, W. Long, and Y. Li, “Enhanced thermal conductivity in polymer composites with aligned graphene nanosheets,” *J. Mater. Sci.*, vol. 49, no. 15, pp. 5256–5264, May 2014.
[100] W. Zhao, H. Wang, H. Tang, and G. Chen, “Facile preparation of epoxy-based composite with oriented graphite nanosheets,” *Polymer*, vol. 47, no. 26, pp. 8401–8405, Dec. 2006.
[101] “Preparation of polymer/oriented graphite nanosheet composite by electric field-inducement,” *Compos. Sci. Technol.*, vol. 68, no. 1, pp. 238–243, Jan. 2008.
[102] G. Chen, H. Wang, and W. Zhao, “Fabrication of highly ordered polymer/graphite flake composite with eminent anisotropic electrical property,” *Polym. Adv. Technol.*, vol. 19, no. 8, pp. 1113–1117, Aug. 2008.
[103] S. Wu *et al.*, “Aligning multilayer graphene flakes with an external electric field to improve multifunctional properties of epoxy nanocomposites,” *Carbon*, vol. 94, pp. 607–618, Nov. 2015.
[104] “Structure Characterization of Unsaturated Polyester/Graphite Nanosheet Composite under Electric Field,” *dokumen.tips*. [Online]. Available: https://dokumen.tips/documents/structure-characterization-of-unsaturated-polyestergraphite-nanosheet-composite.html. [Accessed: 03-Sep-2018].
[105] “Preparation of polystyrenegraphite nanosheet composite - Szukaj w Google.” [Online]. Available: https://www.google.com/search?q=Preparation+of+polystyrenegraphite+nanosheet+composite&ie=utf-8&oe=utf-8&client=firefox-b-ab. [Accessed: 03-Sep-2018].
[106] Y.-F. Zhu, L. Shi, C. Zhang, X.-Z. Yang, and J. Liang, “Preparation and properties of alumina composites modified by electric field-induced alignment of carbon nanotubes,” *Appl. Phys. A*, vol. 89, no. 3, pp. 761–767, Nov. 2007.
[107] H. M. Rietveld, “A profile refinement method for nuclear and magnetic structures,” *J. Appl. Crystallogr.*, vol. 2, no. 2, pp. 65–71, Jun. 1969.

[108] “Automated multipurpose X-ray diffractometer (XRD) with Guidance software | Rigaku.” [Online]. Available: https://www.rigaku.com/en/products/xrd/smartlab. [Accessed: 05-Sep-2018].
[109] “Quantum Design, Inc. - Products - Physical Property Measurement System PPMS®.” [Online]. Available: https://www.qdusa.com/products/ppms.html. [Accessed: 03-Sep-2018].
[110] “Physical Property Measurement System - Thermal Transport Option User’s Manual.” .
[111] “Thermogravimetry / Differential Thermal Analyzer TGD-9000 series | ADVANCE RIKO, Inc.” [Online]. Available: https://advance-riko.com/en/products/tgd-9000/. [Accessed: 05-Sep-2018].
[112] S. S. Instruments, “DSC-60/60A Differential Scanning Calorimeters,” 22-Jan-2018. [Online]. Available: https://www.ssi.shimadzu.com/. [Accessed: 05-Sep-2018].
[113] H. E. Kissinger, “Variation of peak temperature with heating rate in differential thermal analysis,” *J. Res. Natl. Bur. Stand.*, vol. 57, no. 4, p. 217, Oct. 1956.
[114] H. E. Kissinger, “Reaction Kinetics in Differential Thermal Analysis,” *Anal. Chem.*, vol. 29, no. 11, pp. 1702–1706, Nov. 1957.
[115] C. J. Webb and E. M. Gray, “Analysis of the uncertainties in gas uptake measurements using the Sieverts method,” *Int. J. Hydrog. Energy*, vol. 39, no. 1, pp. 366–375, Jan. 2014.
[116] “Electronics Materials Department | 日本重化学工業株式会社.” [Online]. Available: http://www.jmc.co.jp/en/products/battery.html. [Accessed: 05-Sep-2018].
[117] “Gas sorption station: PCTPro, gas analyzer - Setaram Instrumentation.” [Online]. Available: https://www.setaram.com/setaram-products/gas-sorption/pctpro-8/. [Accessed: 05-Sep-2018].
[118] “Grafit Płatkowy | GRAFIT NATURALNY | SINOGRAF SA.” [Online]. Available: http://www.sinograf.home.pl/sinograf/pl/Grafit-Platkowy.html. [Accessed: 10-Sep-2018].
[119] “MG-1599 High Purity Micronized Graphite Graphite - Matmatch.” [Online]. Available: https://matmatch.com/materials/glgr002-novocarbon-mg-1599-high-purity-micronized-graphite. [Accessed: 10-Sep-2018].
[120] G. Graffius, F. Bernardoni, and A. Y. Fadeev, “Covalent Functionalization of Silica Surface Using ‘Inert’ Poly(dimethylsiloxanes),” *Langmuir*, vol. 30, no. 49, pp. 14797–14807, Dec. 2014.
[121] “Specialize In Thin Film Materials | Xinkang Adavanced Materials.” [Online]. Available: http://www.xk-sputteringtarget.com/index.html. [Accessed: 09-Sep-2018].
[122] W. A. Dollase, “Correction of intensities for preferred orientation in powder diffractometry: application of the March model,” *J. Appl. Crystallogr.*, vol. 19, no. 4, pp. 267–272, Aug. 1986.

LIST OF TABLES

LIST OF FIGURES